TRANSPORTATION RESEARCH

RECORD

No. 1415

Soils, Geology, and Foundations

Field Performance of Structures and Nondestructive Evaluation of Subsurface Infrastructure

A peer-reviewed publication of the Transportation Research Board

TRANSPORTATION RESEARCH BOARD
NATIONAL RESEARCH COUNCIL

NATIONAL ACADEMY PRESS
WASHINGTON, D.C. 1993

Transportation Research Record 1415
ISSN 0361-1981
ISBN 0-309-05564-4
Price: $25.00

Subscriber Category
IIIA soils, geology, and foundations

TRB Publications Staff
Director of Reports and Editorial Services: Nancy A. Ackerman
Associate Editor/Supervisor: Luanne Crayton
Associate Editors: Naomi Kassabian, Alison G. Tobias
Assistant Editors: Susan E. G. Brown, Norman Solomon
Production Coordinator: Sharada Gilkey
Office Manager: Phyllis D. Barber
Senior Production Assistant: Betty L. Hawkins

Printed in the United States of America

Sponsorship of Transportation Research Record 1415

GROUP 2—DESIGN AND CONSTRUCTION OF TRANSPORTATION FACILITIES
Chairman: Charles T. Edson, Greenman Pederson

Soil Mechanics Section
Chairman: Michael G. Katona, Air Force Civil Engineering Laboratory

Committee on Soils and Rock Instrumentation
Chairman: John L. Walkinshaw, FHWA, U.S. Department of Transportation
Loren R. Anderson, Richard J. Bathurst, Harold E. Beeston, Douglas A. Blankenship, Joseph A. Caliendo, Barry R. Christopher, Brian J. Dawes, Charles N. Easton, David J. Elton, Kenneth A. Jackura, W. Allen Marr, P. Erik Mikkelsen, Anthony Minnitti, Soheil Nazarian, Dawit Negussey, John L. Nieber, Gary W. Rhodes, A. J. Simmonds, Nader Tabatabaee, Thomas C. Tonkins, David E. Weatherby, Duncan C. Wyllie

Committee on Subsurface Soil-Structure Interaction
Chairman: Thomas D. O'Rourke, Cornell University
Arnold Aronowitz, Timothy J. Beach, Jeffrey Enyart, Lester H. Gabriel, James B. Goddard, William A. Grottkau, John Owen Hurd, D. T. Iseley, Jey K. Jeyapalan, Michael G. Katona, Salah Y. Khayyat, Kenneth K. Kienow, Steven R. Kramer, Samuel C. Musser, Priscilla P. Nelson, Thomas C. Sandford, Shad M. Sargand, James C. Schluter, Ernest T. Selig, Sunil Sharma, Mehdi S. Zarghamee

Geology and Properties of Earth Materials Section
Chairman: Robert D. Holtz, University of Washington

Committee on Soil and Rock Properties
Chairman: Mehmet T. Tumay, National Science Foundation
Robert C. Bachus, Dario Cardoso de Lima, Don J. De Groot, David J. Elton, Kenneth L. Fishman, Paul M. Griffin, Jr., Robert D. Holtz, An-Bin Huang, Mary E. Hynes, Steven L. Kramer, Rodney W. Lentz, Emir Jose Macari, Paul W. Mayne, Kenneth L. McManis, Victor A. Modeer, Jr., Priscilla P. Nelson, Peter G. Nicholson, Norman I. Norrish, Sibel Pamukcu, Carl D. Rascoe, Kaare Senneset, Sunil Sharma, Timothy D. Stark

G. P. Jayaprakash, Tranportation Research Board staff

Sponsorship is indicated by a footnote at the end of each paper. The organizational units, officers, and members are as of December 31, 1992.

Transportation Research Record 1415

Contents

Foreword

The 13 papers in this volume are related to geotechnical and structural engineering. The first eight papers present recent findings on soil-structure interaction as evaluated on the basis of field behavior. Diverse structures are covered, including bridge abutments, pipelines, cut-and-cover tunnels, and large span culverts. In aggregate, these papers provide an excellent review of the stresses and deformations experienced by instrumented subsurface structures and the most appropriate analytical techniques for qualifying and predicting the stresses and deformations induced in similar structures.

The next four papers present information on nondestructive testing of infrastructure, including emerging and advanced technologies and case histories.

The last paper describes the development and evaluation of the Tensioned Wire System for monitoring horizontal and vertical movement in a tunnel.

Skew Effects on Backfill Pressures at Frame Bridge Abutments

THOMAS C. SANDFORD AND MOHAMED ELGAALY

The abutments of frame bridges are integrally connected to the deck without expansion joints. Active soil pressures are normally considered in design despite the movement of the abutments into the soil from thermal expansion of the deck. Many abutments are located on a skew, but possible effects of this skew on the backfill soil pressures are not considered in design. To improve the knowledge of soil pressures behind a skewed integral abutment for use in designing this type of bridge, soil pressures were measured on an installed project for 33 months. The soil pressure measurements were taken using total pressure cells in the backfill on each side of the centerline for both abutments of a 20-degree skewed bridge in Maine. A total of 16 pressure cells plus temperature indicators have been monitored four times a day using a data acquisition system since October 1989. Expansion of the deck causes the pressure to increase well above the active conditions on the upper part of the abutment wall. Skew effects on the pressures that develop near the deck level behind the abutment wall of an integral abutment are substantial. When the greatest deck expansion occurs, the pressures at 3 m (10 ft) from centerline on the obtuse side reach almost three times the value at the corresponding distance on the acute side. The horizontal variation of pressure is greater than the vertical variation. A design envelope is proposed.

The typical bridge is designed with expansion joints to accommodate the deck movements related to temperature change. Abutments on shallow foundations are then able to rotate during construction and for a limited amount during operation under the action of the lateral soil pressure of the approach fill. Thus active pressure coefficients (K_A) as determined by the Rankine, Coulomb, or log-spiral method, as given by Naval Facilities Engineering Command (NAVFAC) (*1*) and elsewhere, are used in abutment design to determine soil pressures from the approach fill. In some abutments, there is restraint to movement due to wingwalls, pile foundations, or cantilevering. In these cases, higher lateral soil pressures may develop on the wall (*2–5*), and some designers (*1*) recommend the at-rest pressure coefficients (K_0) instead of the active coefficients. In all these designs, the lateral soil pressures vary with depth (see Figure 1), and a single profile is used across the abutment.

Bridges with the abutment rigidly connected to the deck slab are also being widely used. Dagher et al. (*6*) found in a survey that 11,500 bridges of this type with and without skew exist in 22 states. The elimination of the expansion joint allows thermal changes in the deck slab to move the abutment into or away from the fill. On the basis of field measurements, Broms and Ingleson (*7*) proposed a pressure envelope that combines a passive pressure envelope using Rankine passive pressure coefficients (K_P) in the upper third of the wall and a transition to the Rankine active case at the base of the wall (see Figure 1). This recognizes the abutment movement into the backfill at the top and the lack of movement at the base of the abutment. In these cases, the lateral pressure distribution varies with height, but the same distribution is used across the abutment. Most states that use pile-supported abutments ignore the effects of thermal expansion. Greimann et al. (*8*) indicate that "the survey responses show that most states ignore the thermally induced bending stress due to transverse thermal movement" and that "only a few states consider thermal, shrinking, and soil pressure forces when calculating pile loads." However, it is unclear that these soil forces can be ignored in all designs with pile foundations or any designs with shallow foundations.

For bridges with integral abutments on a skew, concerns are expressed about the effects of skew in the survey summarized by Greimann et al. (*8*). Some of the concerns included "rotational action caused by the active soil pressure on skewed bridges," as well as "rotational forces from the lateral earth pressure on the end walls [which] cause a failure of the pier anchor bolts on the exterior girders." However, the survey indicated that no special considerations are given to skew in determining pressures behind the abutment. For abutments on piles, Greimann et al. (8) state: "When the abutment is skewed, some twisting may be induced in the piles when the structure deflects, but this can be assumed to be of a minor nature and may be neglected. . . . No special treatments are usually given to backfill and pile cap on skewed bridges, and they might be constructed in the same way as on nonskewed bridges."

STUDY OBJECTIVE

The objective of the study was to determine if there are effects of skew of an integral bridge on the backfill pressures and how these relate to the deck movements arising from thermal changes and to develop a design guideline covering this effect. To accomplish this objective, the pressures occurring behind a skewed integral bridge abutment were continuously monitored.

INTEGRAL BRIDGE DESIGN

The Forks Bridge between the plantations of The Forks and West Forks in western Maine was opened to traffic in late

T. C. Sandford, Civil Engineering Department, University of Maine, 103 Boardman Hall, Orono, Maine 04469. M. Elgaaly, Civil Engineering Department, University of Maine, 103 Boardman Hall, Orono, Maine 04469; current affiliation: Civil and Architectural Engineering Department, Drexel University, 32nd and Chestnut Streets, Philadelphia, Pa. 19104.

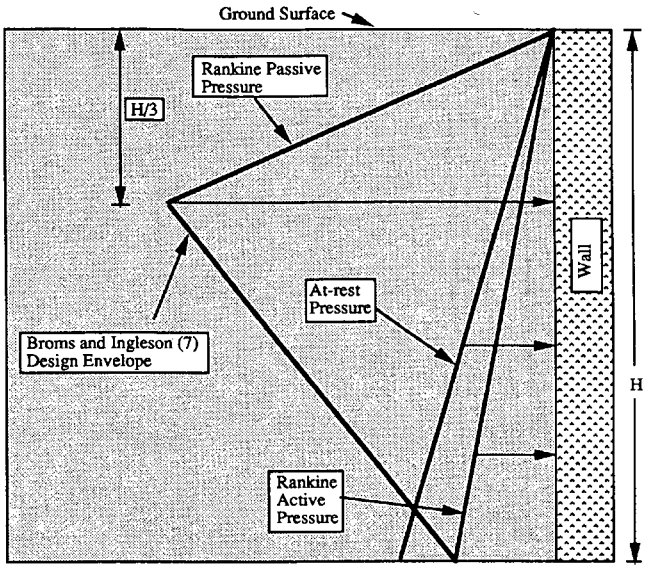

FIGURE 1 Design pressure distributions behind abutments.

1989. The stiff-legged, steel rigid frame bridge spans the Kennebec River. The bridge (see Figure 2) is a 20-degree skewed bridge with a 50.3-m (165-ft) span and an 11.5-m (37.67-ft) overall width. It consists of five steel frames resting on shallow foundations. The steel legs are encased in concrete to form the abutments (see Figure 3). The composite reinforced concrete deck is connected to the steel legs of the frames and the abutment encasement. The bridge design is described in more detail by Roberts (*9,10*).

The Maine Department of Transportation used a Rankine passive pressure in the upper third of the wall transitioning to an at-rest case at the base of the wall as described by Roberts (*10*) and shown in Figure 3. Thus the effect of expansion of the deck as found by Broms and Ingleson (*7*) was incorporated into the design. No effect of the skew on the soil pressures was considered. However, even this envelope raises questions. Because the Rankine passive coefficients neglect the effects of wall shear, could wall shear have a substantial effect on the passive resistance? For this length of bridge, will enough movement occur to develop full passive pressure? Does a skew of only 20 degrees affect the soil pres-

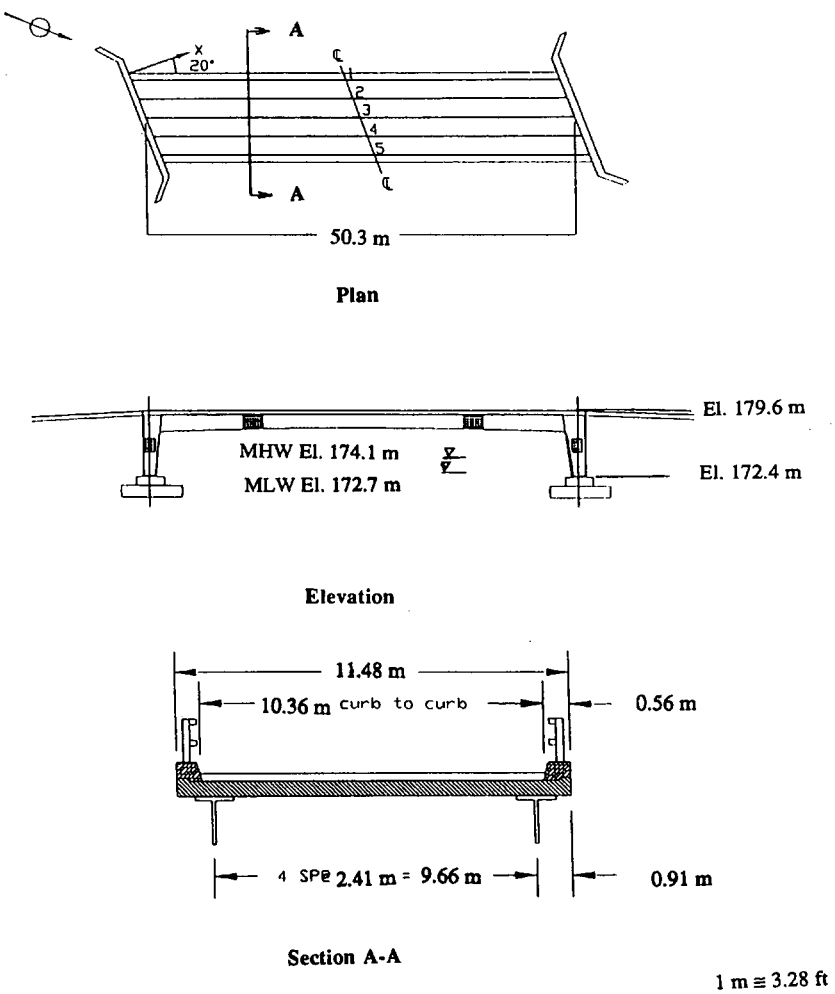

FIGURE 2 Plan, elevation, and section of The Forks Bridge.

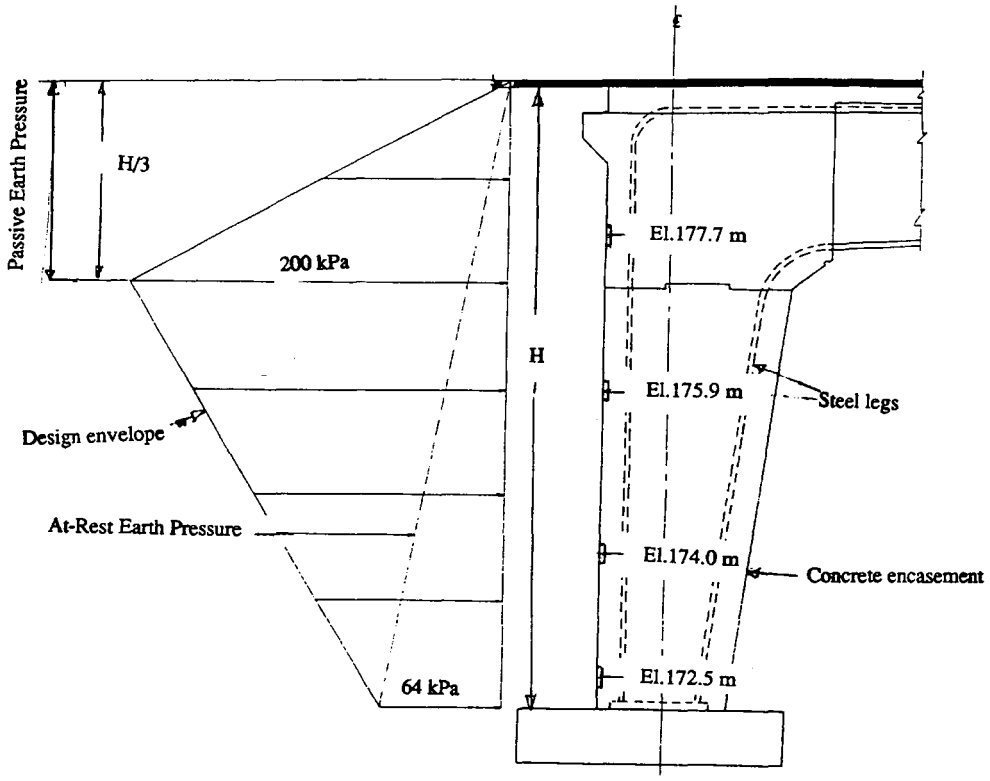

FIGURE 3 Design earth pressure for The Forks Bridge [after Roberts (*10*)].

sures? Will passive resistance increase with reloading in subsequent years? Because it had little experience with this size and type of bridge, the Maine Department of Transportation decided to monitor the soil pressures at the back of the abutment.

BACKFILL

The backfill was a coarse to fine sand and gravel with practically no fines as shown on a typical gradation in Figure 4. Triaxial tests using material compacted to 90 percent of AASHTO T99 gave a friction angle of 37 degrees for two different samples. The maximum dry density according to AASHTO T99 was 19.3 kN/m^3 (123 lbf/ft^3), and, after correction for oversize, the maximum dry density was 20.5 kN/m^3 (130.3 lbf/ft^3) with an optimum water content of 7.0 percent. The backfill was required to meet a minimum compaction dry density of 90 percent of the maximum, whereas the subbase was required to meet 95 percent of the maximum. The measured dry unit weights of the backfill averaged 94.9 percent of maximum, and the subbase averaged 96.4 percent.

INSTRUMENTATION

A total of 16 pressure cells were mounted at the back of the concrete abutments to monitor soil pressures for vertical variation and the effects of skew. Two temperature indicators monitored air temperature near the structure. The cells and other instrumentation were connected to a data acquisition system that could be remotely accessed by telephone to retrieve data or change the reading schedule on the instruments. The instruments are described in more detail by Elgaaly et al. (*11,12*).

The presence of a pressure cell alters soil pressure to some degree, and it is usually impossible to match the stiffness of the cell to that of the soil. Weiler and Kulhawy (*13*) and Dunnicliff (*14*) describe problems in obtaining reliable earth pressure readings. Thus a number of provisions were made to maximize the reliability of the readings. These included selecting a 228.6-mm (9-in.) diameter fluid-filled cell with a diameter-to-thickness ratio of 23. A vibrating wire transducer was used to measure pressures, and thermistors within the cells were used to correct the pressure signal for temperature effects. A bedding for each cell was prepared by casting a concrete block in the laboratory and setting the cell as nearly flush as possible into the wet concrete. After the concrete had set, the cell was removed, and the recess was ground as needed on the edges to remove concrete shrinkage pressures on the cell edges. Each cell was calibrated in this preformed bed in the concrete block, and then the cell and its concrete block were installed flush to the back of the abutment in the field as described in more detail by Elgaaly et al. (*11,12*). The backfill within 150 mm (6 in.) of each cell was restricted to a maximum size of 5 mm (0.2 in.) so that pressure concentrations would be reduced. The precast block containing the bedded cell protected the cell during concreting operations. The direct burial type cable was embedded in the abutment concrete and further protected with polyvinyl chloride tubing. Redundancy of readings was provided by installing instruments in both abutments as shown in Figure 5. All 16 cells

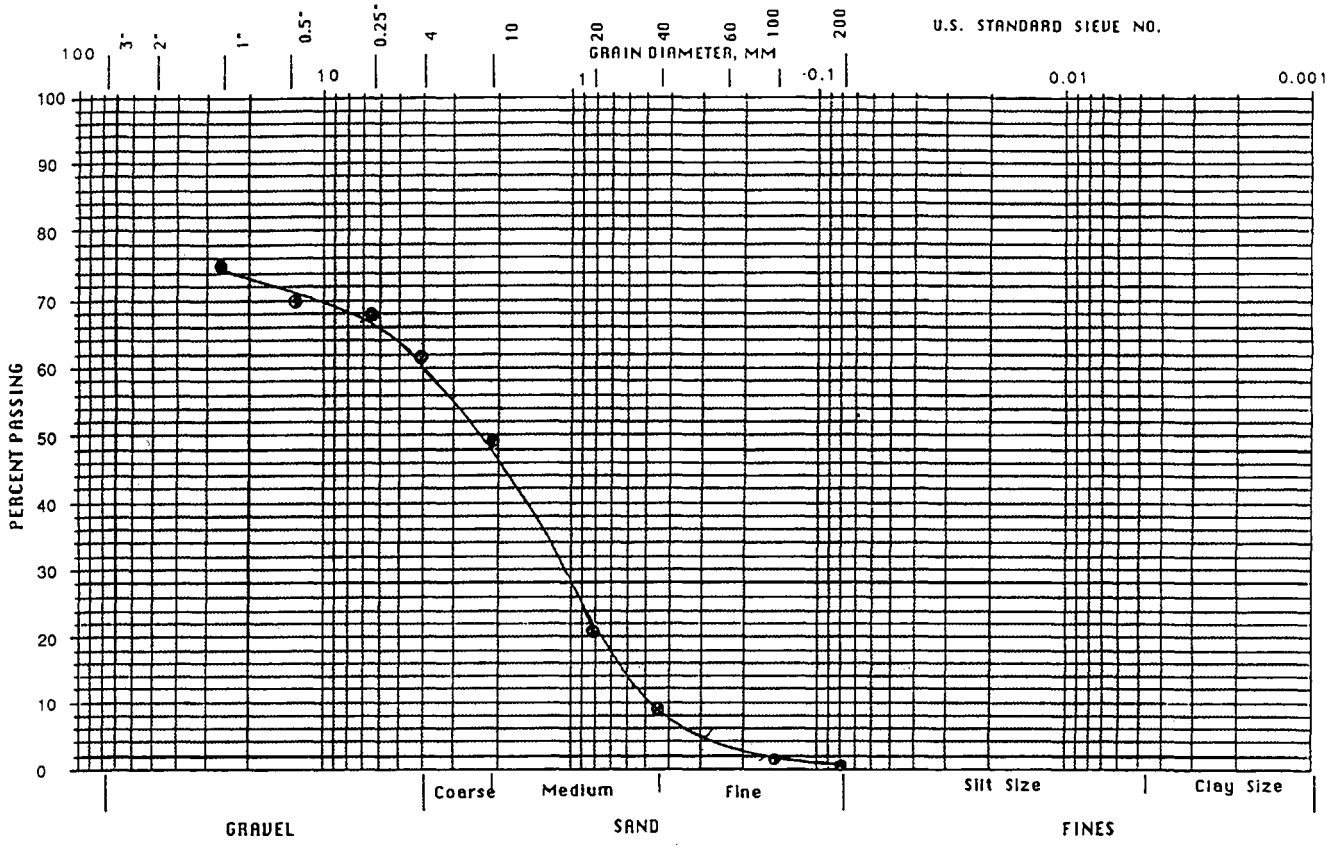

FIGURE 4 Grain size of approach fill.

were mounted 3 m (10 ft) from the centerline as shown in Figure 5. The elevations of the pressure cells with respect to the girders are shown in Figure 3.

Two resistance temperature indicators (RTDs) were located beneath the deck and measured the air temperature near the structure. The RTDs were calibrated in the field. The soil temperatures at the back of the abutment were available from thermistors located in each pressure cell. However, only six soil temperature locations at the back of the abutment were monitored because of channel availability on the datatakers. One of these locations was below river level. Because the in situ material was free draining, the temperature measured at this location was likely close to the river water temperature. The RTD air temperature indicators ceased operating on June 29, 1991 (Day 909), but the thermistors in the cells continued to monitor temperatures behind the abutment.

TEMPERATURES

The temperature of the structure determines how much expansion or contraction the structure will undergo. The structure temperature varies with seasons, weather changes, and diurnally as the sun heats the structure and with temperature changes in the air, adjacent soil, and water. Thus, a structure like The Forks Bridge continuously moves in response to these changes.

Two indicators of the superstructure temperature plus the water temperature in Maine over 33 months of monitoring are shown in Figure 6, in which the days are numbered beginning with 1 on January 1, 1989. The indicators of the superstructure temperature are the midday air temperature below the deck and the midday temperature at the back of the abutment near the girder level at Elevation 177.7 m (583 ft) in Cell 1 as shown in Figure 5. Midday water temperature as measured in Cell 7 shown in Figure 5 is also given in Figure 6. Despite three gaps where data were lost and the loss of the air temperature indicator on Day 909, the profile of temperatures at the bridge was obtained and is shown in Figure 6.

The seasonal changes in the air, soil, and water temperatures shown in Figure 6 are the largest temperature changes. This is important because seasonal temperature changes will result in a more or less uniform rise in the structure temperature. Therefore the air and soil temperatures should be good indicators for seasonal temperature change of the structure. Although data from every fifth day are plotted, the weather front changes are reflected in the variability of the air temperature. The magnitude of this variability is considerably less than the seasonal changes. Diurnal air temperature changes are not shown because only midday temperatures are plotted, but the effects are generally less than the weather front changes. The short-term changes will result in nonuniform temperatures in the structure. The temperatures in the structure are not uniform because of the rate of heat transfer, the heat capacity, heat sources and sinks at various locations on the structure, and a complicated geometry. For example, during the day, the top of the deck with an asphalt cover will reach a higher temperature than most of the steel, which is covered by the concrete deck. The most westerly girder will likely be

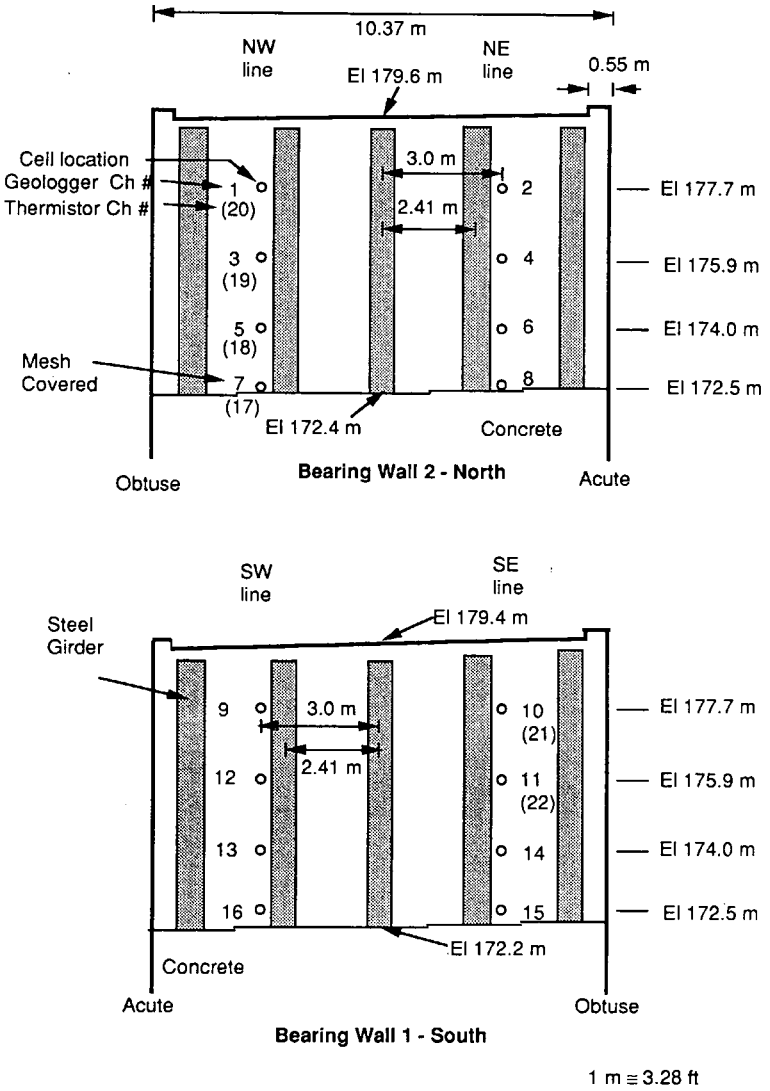

FIGURE 5 Pressure cell locations.

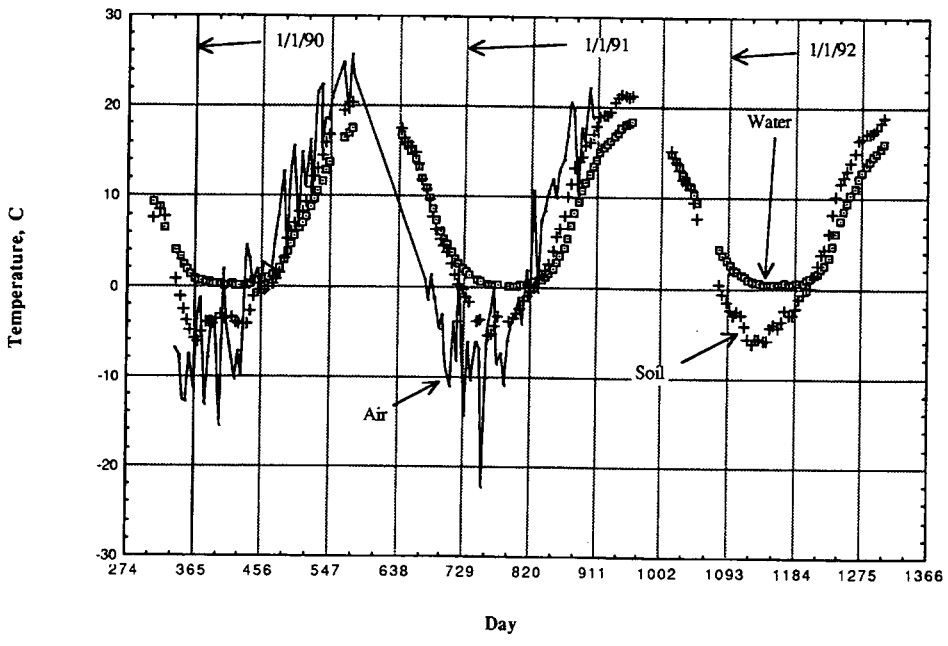

FIGURE 6 Temperatures at The Forks Bridge.

warmer in the afternoon than the other four girders. Air temperatures below the deck and soil temperatures behind the abutment may have shortcomings for predicting distortions from short-term temperature fluctuations. Although the plots of midday temperatures do not show the diurnal variation of temperature, they do include the higher diurnal temperatures occurring at the bridge.

The seasonal air, soil, and water temperatures and patterns of change that were monitored do not appear unreasonable for this location in Maine. The summer of 1992 was cooler than the two previous summers, as indicated by lower soil temperatures. The river current is too swift at the bridge for freezing to occur even though the air temperature in the winter is often well below freezing. Because the measured water temperatures go right to freezing but not below freezing, this increases the confidence in the water temperature readings. Freezing was indicated in the soil at a depth of 1.9 m (6.23 ft). This is ordinarily below the maximum depth of frost penetration. However, the cell is located at the back of the concrete wall. Although the concrete is about 2.5 m (8.20 ft) thick at this point, the freezing front penetrates the concrete rapidly.

LATERAL SOIL PRESSURE DISTRIBUTION IN VERTICAL PLANE

Because the bridge has no expansion joints, thermal expansion of the deck due to temperature rise during the summer will push the abutments into the approach fills; winter contraction will then relieve the pressure. Soil pressure results for approximately 7 months were given by Elgaaly et al. (*11*). Additional results for a period of 33 months of the average pressures at each elevation behind the backfill are shown in Figure 7. At each level, with the exception of Elevation 172.5 m (566 ft), the plotted pressure is the average of four pressure cells. At Elevation 172.5 m (566 ft), one cell has been covered with a porous screen and measures only water pressure. This water pressure is used to find an effective pressure at that level and at Elevation 174.0 m (571 ft). The effective pressure at Elevation 172.5 m (566 ft) is thus the average of only three cells. These average midday pressures thus combine results from both the acute and obtuse sides of the centerline.

Despite the precautions taken during their installation, the pressure cells may give misleading results (*13,14*), but the results shown in Figure 7 do not appear unreasonable. Soil pressures vary vertically close to at-rest pressure or slightly lower when the bridge contracts during colder weather as shown in Figure 8. Near the footing at Elevation 172.5 m (566 ft), the pressures stay relatively constant throughout the year, reflecting little movement at that depth. Because these are effective pressures, there is some change in the results due to higher water levels in the spring. During warmer weather, the superstructure pushes into the soil at higher levels, and then the pressures at the higher elevations increase. For Elevation 174.0 m (571 ft), which is located in a zone of fluctuating water level of 1.4 m (4.7 ft) caused by upstream dam releases, there are spikes in pressures from about January 1 to mid-March of each year. It is believed that this is frost buildup due to the fluctuating water level at this location combined with an air temperature below freezing. This is a separate phenomenon from pressure buildup due to thermal changes. Considering the movement of the abutment from thermal expansion or contraction of the deck, the level of pressures in all seasons is not unreasonable. However, recent values at Elevation 172.5 m (566 ft) do show some erratic behavior in one cell.

Clearly, the active or even the at-rest pressures are inadequate for predicting the pressures that are generated in the upper levels of the abutment during expansion. On average, the results were similar to those found by Broms and Ingleson (*7*). The Rankine passive pressure down to one-third of the

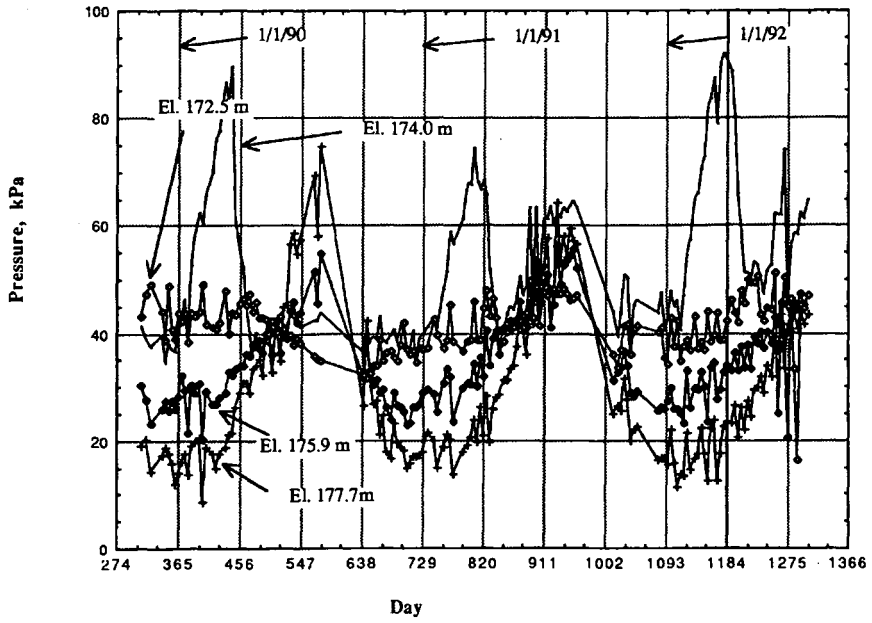

FIGURE 7 Pressure averages behind abutment.

wall height, which transitions to the at-rest condition at the base, forms an envelope for the results of the average pressures in this bridge, as shown in Figure 8. For locations other than Maine, the temperature changes will be different. Elgaaly et al. (*12*) found for this 50.3-m (165-ft) bridge that at Elevation 177.7 (583 ft), the change of pressure per degree change in temperature was 1.46 kPa/°C (17 lbf/ft²/°F) for seasonal, 0.51 kPa/°C (5.9 lbf/ft²/°F) for weather fronts, and 0.28 kPa/°C (3.3 lbf/ft²/°F) for diurnal temperature changes. There was concern that the soil reaction during the seasons following the first season would show stiffening and thus give higher pressures for the same expansion. The pressure cells do not indicate that this is happening.

SKEW EFFECTS ON PRESSURE

If pressures are affected by skew, then laterally nonuniform pressures will be exerted on abutment walls that may have implications for structural design of the abutment walls. To measure the effects of the skew on the soil pressures, pressure cells were installed on both abutments on both sides of the centerline as shown in Figure 5. Under a uniform temperature change with no constraint of the soil, it was anticipated that the skewed superstructure with a span of 50.3 m (165 ft) would expand or contract uniformly parallel to the roadway centerline as the temperature changed.

As shown in Figure 5, at Elevation 177.7 m (583 ft) two total pressure cells were installed on the acute side (Cell 2 on the northeast line and Cell 9 on the southwest line) at 3 m (10 ft) from the centerline and two pressure cells on the obtuse side (Cell 1 on the northwest line and Cell 10 on the southeast line) at the same distance from centerline.

The average pressures of the two obtuse cells are compared with those of the two acute cells in Figure 9. The pressures are about the same when the bridge contracts from November through February of each year. The pressures are close to the anticipated at-rest pressure of 13.3 kPa (280 lbf/ft²) and appear to sometimes reach the anticipated active pressure of 8.3 kPa (175 lbf/ft²). This is not unexpected and gives confidence that the pressure cells are reading at an appropriate level. During March of each of the three years, the seasonal temperature increase begins to increase the pressure at all cells. However, there is a distinct difference at this elevation of the superstructure between the pressures on the acute side and the pressures on the obtuse side. By the end of July, which is the peak temperature in Maine (as shown in Figure 6), the pres-

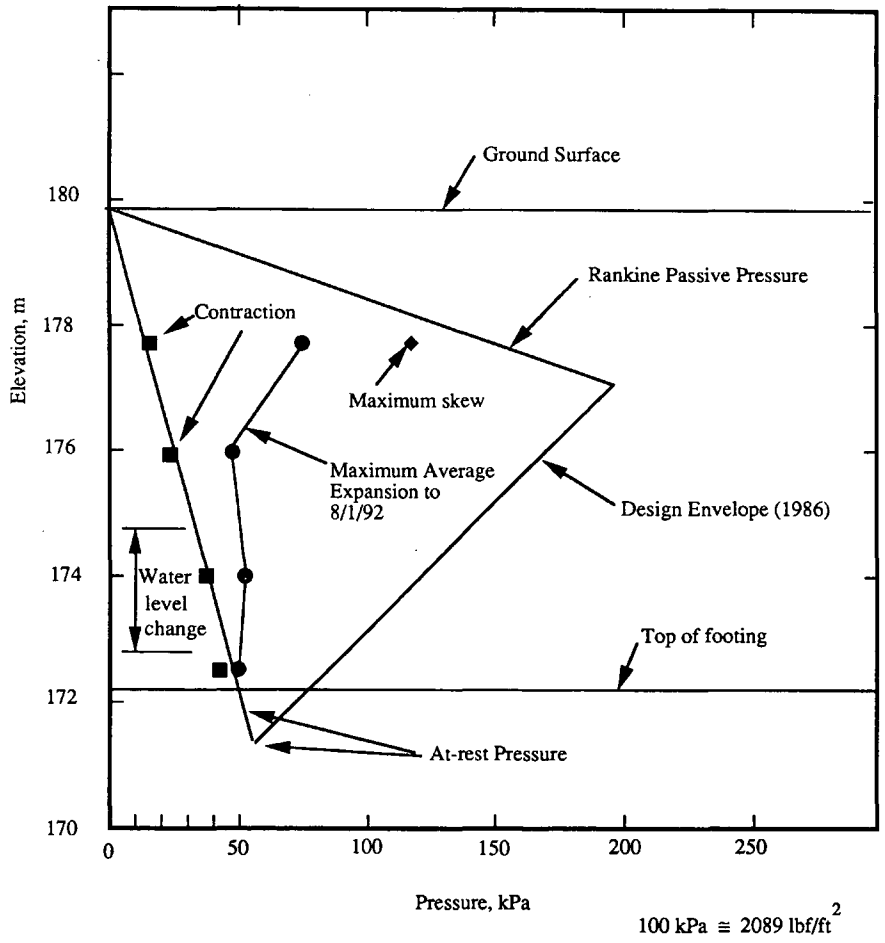

FIGURE 8 Measured earth pressures versus depth with integral abutment envelope.

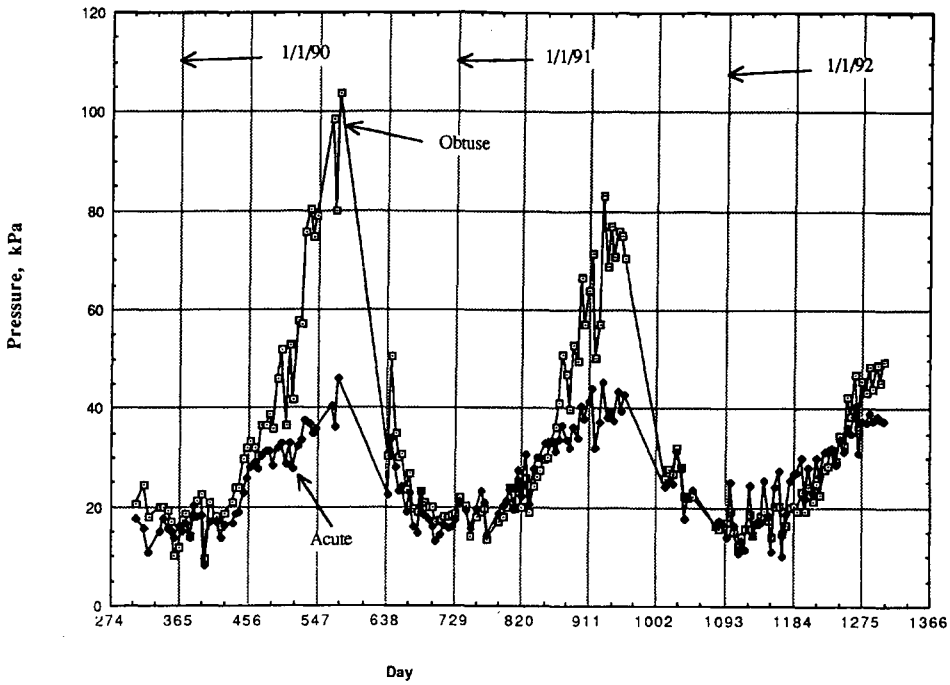

FIGURE 9 Skew effects on pressures, elevation 177.7 m.

sures on the obtuse side have increased by four to six times the cold weather value, whereas the pressures on the acute side have increased only two to three times.

The difference in pressure between the cells on the obtuse side and those on the acute side is shown in Figure 10. For 4 to 5 months during the warmest weather, there are consistent differences in pressure between the obtuse side and the acute side of this skewed bridge. The difference occurs seasonally and thus indicates that the skew effect is not a reflection of distortions caused by nonuniform temperatures in the structure from short-term changes in temperature. The effect of the skew appears to be diminishing with time, and thus there

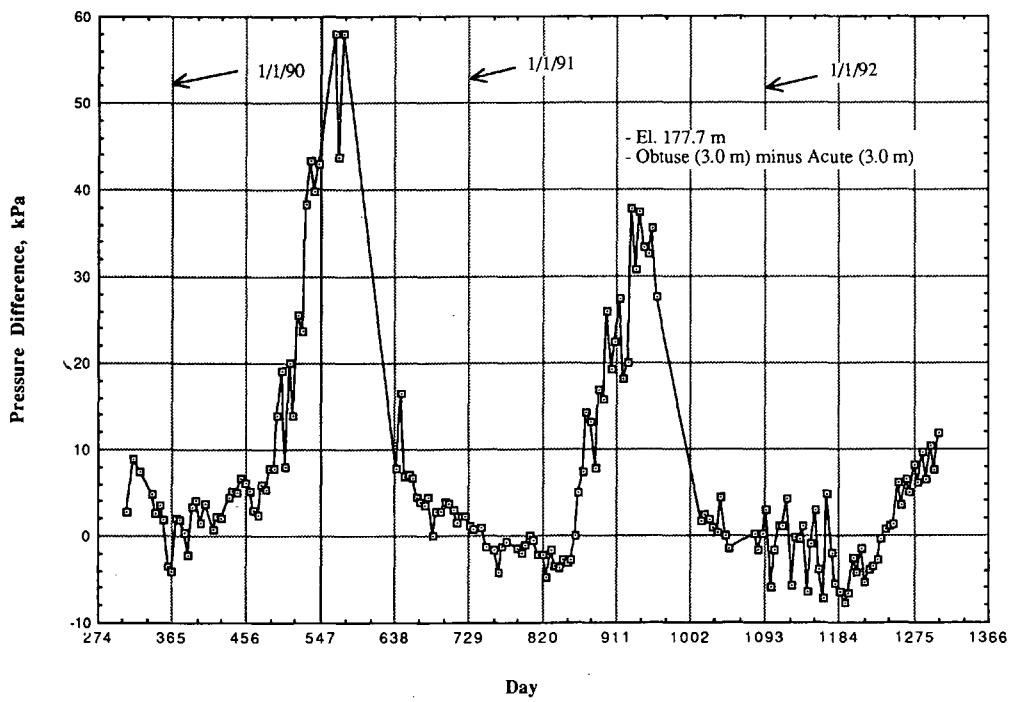

FIGURE 10 Lateral pressure difference at girder elevation.

is no indication that the effects of the cyclic stiffening of the soil are increasing skew differences.

The pressure difference across the centerline indicates that a greater movement is possibly occurring on the obtuse side than on the acute side; that is, a rotation of the abutment at the level of the superstructure is occurring. When the air temperature increases, the bridge deck experiences thermal expansion, which is restrained by the massive abutments. This restrained thermal expansion will result in thermal stresses and strains, which have been found to be larger at the obtuse corner than at the acute corner (*6*). Hence, the bridge has the potential to push more on the soil at the obtuse corners and cause higher pressures at the obtuse corner. The diminishing of the skew effects with time indicates that the expansions may have caused more permanent deformation of the backfill on the obtuse side than on the acute side.

For a linear rotation of the abutment, the pressures near the ends at 4.88 m (16 ft) from the centerline are estimated and given in Table 1. The estimated pressure difference across the skewed abutment at Elevation 177.7 m (583 ft) is almost 96 kPa (2000 lbf/ft^2). This is a larger difference than occurs from top to bottom during contraction or expansion.

It is possible that some of the skew effects arise from differences in stiffness of the soil. However, the magnitude of difference that was measured was more than could be expected from soil property variations. The average unit weight of the backfill on the acute side was 19.4 kN/m^3 (123.6 lbf/ft^3) on the basis of 14 tests. On the obtuse side, the average unit weight was 19.5 kN/m^3 (124.2 lbf/ft^3) on the basis of 21 tests. The behavior was replicated on each abutment, which makes it less likely to be caused by soil property variations. There is more apparent confinement of the soil on the acute side than on the obtuse side, which would give the opposite effect from that measured.

At the next lower level of cells at Elevation 175.9 m (577 ft), which is below the girder level, there is substantial buildup of pressure as expansion occurs in the warm months, as shown in Figure 7. However, when the obtuse and acute cells are distinguished, there are some differences, as seen in Figure 11, but it is not the same pattern as for the girder elevation in Figure 10. The magnitude of pressure differences is small at Elevation 175.9 m (577 ft) and can almost be considered as having no skew effect. This indicates that the thermal expansion restraining effects are diminishing below the deck-abutment junction, as would be expected.

CONCLUSIONS

For integral abutment bridges, thermal expansion will be resisted by abutment soil pressures, which will rise above the active or at-rest conditions according to the magnitude of movement depending on the length of the bridge, the temperature change, and the sharing of the resistance with the foundation piling. Measurements taken on a 50.3 m (165 ft) span bridge in Maine showed that average soil pressures at the girder level reached five times the at-rest condition (Figure 8).

For this 50.3-m (165-ft) span bridge, the Maine Department of Transportation proposed a modification to the Broms and Ingleson (*7*) design envelope incorporating passive pressures (Figure 3). Monitoring indicated that these design pressures were an envelope for the actual soil pressures. Most designers of these abutments now use active pressures (*8*), which can be significantly less than the actual pressures.

With a 20-degree skew, measurements showed a variation in soil pressure laterally at a height near the base of the girder. The pressure at 3.0 m (10 ft) from the centerline on the obtuse side at this level was measured to be more than two times the pressure at the same distance on the acute side (Table 1 and Figure 12). It is anticipated that the pressure ratio of the obtuse to the acute at the ends of the abutment 4.88 m (16 ft) from the centerline could reach a ratio of 4. The lateral variation of pressure for the deck expansion is higher than the vertical variation of pressure due to the expansion. This lateral variation has apparently not been considered by designers of these abutments (*8*).

RECOMMENDATIONS

As a result of this study, the authors recommend the following:

- For design of integral abutments, a vertical pressure envelope similar to that of Broms and Ingleson (*7*) or that of the Maine Department of Transportation (Figure 3) should be considered.
- For skewed abutments, a horizontal soil envelope that has the Rankine passive pressure at the obtuse end of the wall and the Rankine active pressure at the acute end should be considered (Figure 12). This should be analyzed to the

TABLE 1 Pressures at Skewed Abutment, The Forks, Maine

Distance from Centerline, m (ft)	Maximum Pressure, kPa (lbf/ft^2)	Pressure[d] Difference, kPa (lbf/ft^2)
4.88 (16), Obtuse	121 (2530)[c]	104 (2170)
3.0 (10), Obtuse	103 (2160)[a]	86 (1800)
0.0	75 (1560)[b]	57 (1200)
3.0 (10), Acute	46 (960)[a]	29 (600)
4.88 (16), Acute	28 (590)[c]	11 (230)

(a) Measured value in late July 1990
(b) Interpolated value
(c) Extrapolated value (linear extrapolation)
(d) Maximum pressure minus measured pressure for cold weather of 17 kPa (360 lbf/ft^2).

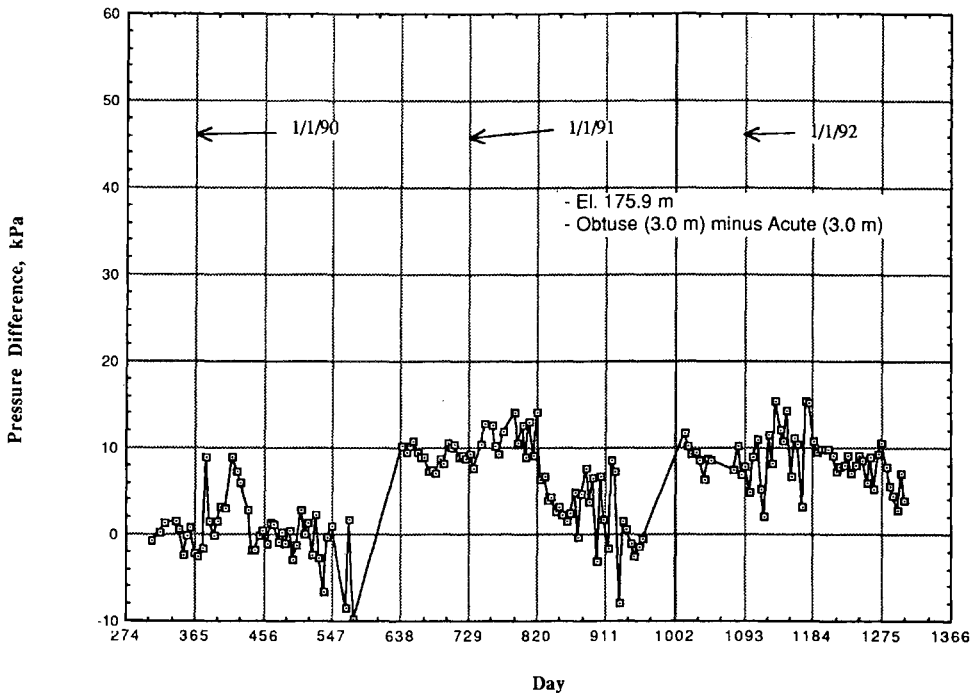

FIGURE 11 Lateral pressure difference below girder level.

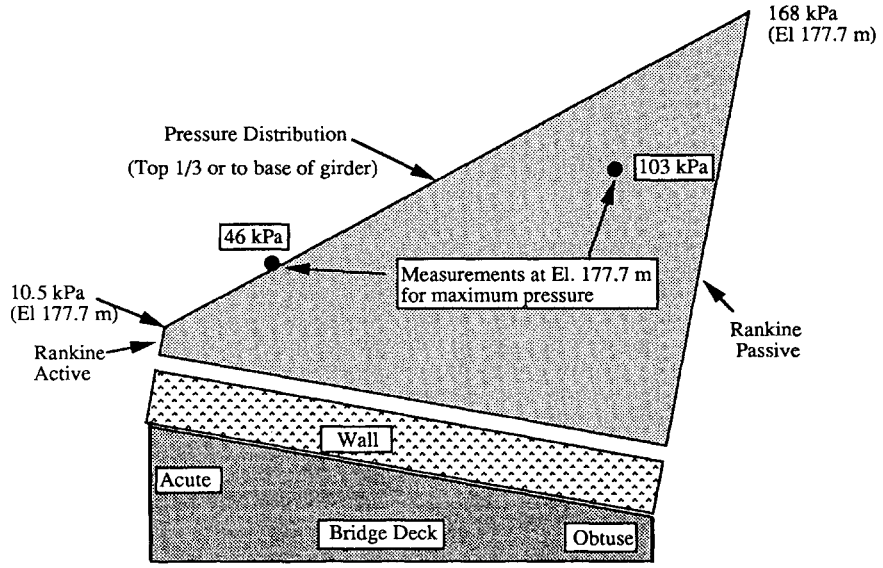

FIGURE 12 Design lateral pressure distribution for skewed abutments.

maximum depth of either the upper third of the height of the wall or the distance to the base of the girder.

ACKNOWLEDGMENTS

The authors wish to extend their appreciation to the Maine Department of Transportation for sponsoring this research. James Chandler is the MDOT Engineer of Design, and Larry L. Roberts is the MDOT Bridge Design Engineer.

REFERENCES

1. *Foundations and Earth Structures*. Design Manual 7.02. Naval Facilities Engineering Command, 1986.
2. Coyle, H., and R. E. Bartoskewitz. Earth Pressure on Precast Panel Retaining Wall. *Journal of Geotechnical Engineering*, ASCE, May 1976, pp. 441–456.
3. Jones, C. J. F. P., and F. A. Sims. Earth Pressures Against the Abutments and Wing Walls of Standard Motorway Bridges. *Géotechnique*, 1975, pp. 731–742.
4. Ingold, T. S. Retaining Wall Performance during Backfilling. *Journal of Geotechnical Engineering*, ASCE, May 1979, pp. 613–626.

5. Smoltczyk, U., K. Hilmer, E. Franke, and B. Schuppener. Earth Pressure Variations due to Temperature Change. *Proc., 9th International Conference on Soil Mechanics and Foundation Engineering*, Tokyo, Vol. 1, 1977, pp. 725–733.
6. Dagher, H. J., M. Elgaaly, and J. Kankam. Analytical Investigation of Slab Bridges with Integral Wall Abutments. In *Transportation Research Record 1319*, TRB, National Research Council, Washington, D.C., 1991, pp. 115–125.
7. Broms, B. B., and I. Ingleson. Earth Pressure Against the Abutments of a Rigid Frame Bridge. *Géotechnique*, Vol. 21, No. 1, 1971, pp. 15–28.
8. Greimann, L. F., A. M. Wolde-Tinsae, and P. S. Yang. Skewed Bridges with Integral Abutments. In *Transportation Research Record 903*, TRB, National Research Council, Washington, D.C., 1983, pp. 64–72.
9. Roberts, L. Two State-of-the-Art Bridges for Maine. *Modern Steel Construction*, January–February 1990, pp. 45–47.
10. Roberts, L. Evolution of Steel Bridge Design in Maine. *Proc., National Symposium on Steel Bridge Construction*, Washington, D.C., October 19, 1989, pp. 21-1—21-16.
11. Elgaaly, M., T. C. Sandford, and C. B. Colby. Testing an Integral Steel Frame Bridge. In *Transportation Research Record 1371*, TRB, National Research Council, Washington, D.C., 1993.
12. Elgaaly, M., T. C. Sandford, and C. B. Colby. *Monitoring of The Forks Bridge to June 6, 1990*. Research Report ST 91-1, GT 91-2. Department of Civil Engineering, University of Maine, Dec. 1991.
13. Weiler, Jr., W. A., and F. H. Kulhawy. Factors Affecting Stress Cell Measurements in Soil. *Journal of Geotechnical Engineering*, ASCE, Dec. 1982, pp. 1,529–1,548.
14. Dunnicliff, J. *NCHRP Report 89: Geotechnical Instrumentation for Monitoring Field Performance*. TRB, National Research Council, Washington, D.C., April 1982, pp. 16–18.

Publication of this paper sponsored by Committee on Subsurface Soil-Structure Interaction.

Pipeline Response to Undermining at Excavation Crossings

HARRY E. STEWART AND THOMAS D. O'ROURKE

A series of field tests was conducted to investigate the response of cast-iron pipelines subjected to cross-trench construction and to identify conditions that might lead to brittle failure. Static strains were measured for various trench widths, backfill conditions, and both static and dynamic construction vehicle loadings. Tests also were conducted to evaluate the increases in rolling wheel loads that would be caused by surface irregularities. Design recommendations for maximum excavation width and a limiting pipeline strain of 500 microstrain are presented. The recommendations consider the static response of the pipe during backfill and construction vehicle loadings as well as the dynamic response following restoration of the roadway. Design recommendations for maximum allowable trench widths are given for 102-, 152-, and 203-mm diameter cast-iron pipelines that have depths of burial from 0.6 to 1.5 m.

The vulnerability of pipelines and conduits to undermining excavations is dominated by the most vulnerable piping materials. Among the most brittle and aged piping in the U.S. infrastructure are cast-iron pipelines, which are critical for water supplies and gas distribution systems. Although cast-iron piping has provided consistent and dependable service for many years, it is nonetheless a brittle material that fails at strains substantially less than those damaging the ductile pipe materials in modern installations.

Because cast-iron pipelines frequently are undermined by trench construction for other utilities, it is of considerable importance to understand the mechanics of soil-pipeline interaction under these conditions. Special field testing was conducted at a site near Cornell University to investigate pipeline response to cross-trench construction (*1*). The tests were organized to assess pipeline strains caused by backfilling and construction vehicle loads.

The experimental setup and field measurements are described here, and the static strains measured for various trench widths, truck wheel loads, and the locations of cast-iron joints with respect to the loads are reported. The development and verification by experimental data of theoretical models to predict pipeline response are discussed, followed by an explanation of how pipeline deformations under static and dynamic loading were combined to provide a comprehensive model for engineering and planning. Recommendations are made pertaining to the maximum width of cross-trench construction for maintaining pipeline integrity, based on the theoretical models and field test verification program.

School of Civil and Environmental Engineering, Cornell University, Ithaca, N.Y. 14853-3501.

EXPERIMENTAL SETUP

The location and soil conditions at the field test site are described. Detailed information pertaining to the regional setting and geology, characteristics of the soil profile at site, and laboratory tests for soil classification are given elsewhere (*1*).

Soil Profile

A typical soil profile for the test site consisted of approximately 25 to 50 mm of asphalt overlying approximately 200 to 250 mm of a subbase composed of glacial till. In general, at depths greater than 0.3 m and up to 2.7 m, the predominant soil was a heterogeneous mixture of silt, clay, sand, gravel, and cobbles, which is typical of glacial till. Rock consisting mainly of shale and sandstone was encountered at a depth of approximately 2.7 m. The water table was located approximately 1.2 to 2.0 m below the ground surface.

The material used to backfill the pipeline was a poorly graded, coarse-to-medium fluvial glacial sand. It was composed by weight of approximately 99 percent sand and approximately 1 percent fine-grained material. This material was selected because it is similar to select backfill often used in pipeline construction. The moisture-density relationship of the sand backfill was determined according to ASTM D698-78. The optimum moisture content was found to be approximately 10 percent, with a corresponding dry unit weight of 18.8 kN/m^3.

Backfilling, Pipe Installation, and Surfacing

A profile view of the soil and pavement at the test pipeline is shown in Figure 1(*a*). A plan view of the site, which also outlines the north and south test bays, is shown in Figure 1(*b*). The in situ material was excavated to a minimum depth of 1.2 m in the areas outside the two test bays and was removed to a minimum 1.8-m depth within the two test bay areas. The test bays were the locations where the trenches were excavated perpendicular to the experimental pipeline. The trenches for the pipeline and test bays were backfilled with sand in 150- to 200-mm lifts and compacted. The backfill was compacted at a water content of 7 percent and to a relative compaction (RC) of 93 percent. The pipeline was installed so that the top of the pipe was approximately 0.75 m below the top of pavement. The trench then was backfilled with sand to a depth approximately 380 mm below the top of the pavement.

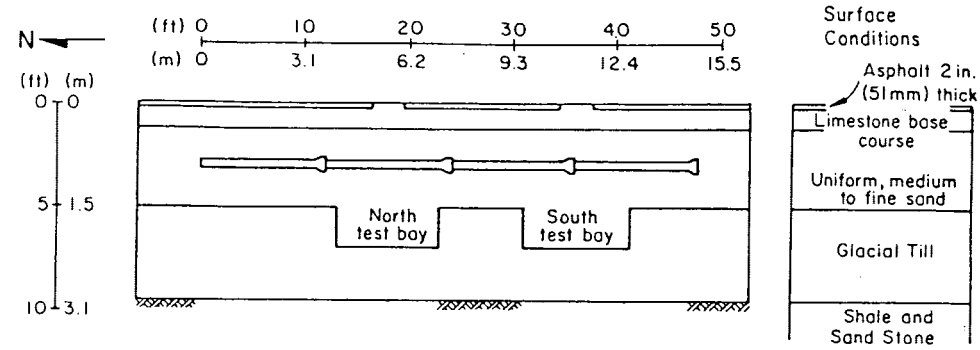

(a)

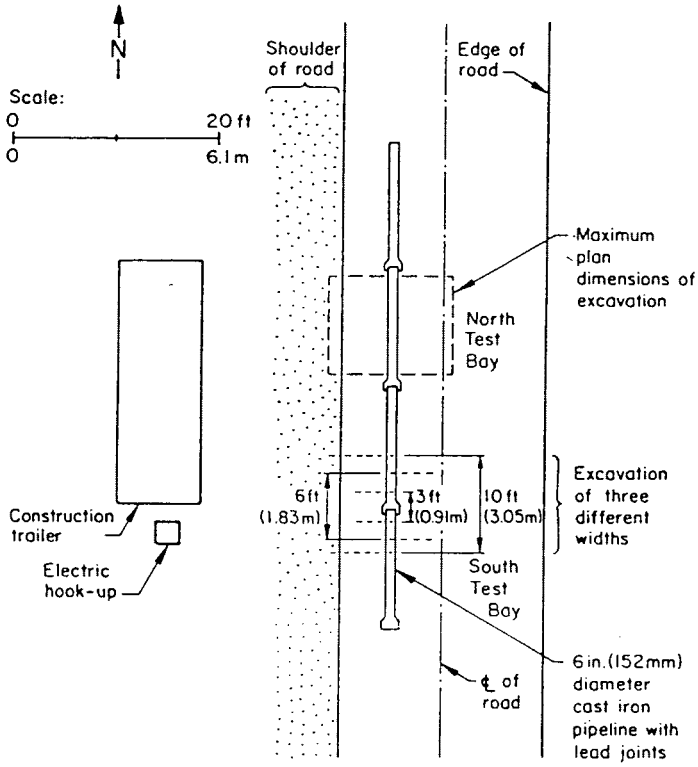

(b)

FIGURE 1 Test site layout: (*a*) profile; (*b*) plan view.

The experimental pipeline was composed of four pit cast-iron pipe segments obtained from an existing line that was installed in 1905 and taken out of service in spring 1986. Each segment had an approximate length of 3.7 m and nominal inside and outside diameters of 152 and 178 mm, respectively. The exterior diameter of the pipe was 176 mm with a standard deviation of 0.76 mm, and the pipe wall thickness was 11.3 mm with a standard deviation of 1.02 mm. The pipeline was installed with the assistance of personnel from the Brooklyn Union Gas Company in a manner consistent with the construction practices that had been used for cast-iron gas mains currently in service.

Following pipeline installation, the roadway was surfaced. The finished roadway surface consisted of a crushed limestone base course 255- to 330-mm thick covered by 75 to 100 mm of 3–2A binder.

PIPELINE INSTRUMENTATION

Field experiments and instrumentation were designed to obtain a comprehensive data set of pipeline strains generated by loads during trench construction as well as by dynamic impact loads from heavy vehicles traversing the site after the backfilling of undermining excavations. Of principal importance were the strain measurements. Other measurements included pavement surface displacement, soil settlements, stresses in the soil, temperature of the pipeline, joint rotation,

and ground and pipeline accelerations. Because of space limitations, the discussion in this paper is limited to strain gauge data. A complete description of the pipeline instrumentation and full field measurements are provided by Stewart et al. (*1*).

FIELD MEASUREMENTS

Strain gauge measurements are reported here for the test pipeline undermined by 0.9-m, 1.8-m, and 3.0-m wide trenches. For each trench width, the test pipeline was undermined by a combination of mechanical and hand excavation, generally to depths of 0.6 to 0.8 m beneath the pipe. The trench then was backfilled by loose-dumping sand. The sand was not compacted to allow the backfilling procedure to represent the worst field conditions. Crushed No. 2 stone was placed in the upper 0.3 m of the backfilled trench. A truck was then backed into specific positions along the test bay so that its wheels were directly over the pipe.

Surface loads were generated using an "overloaded" six-wheel, single rear-axle dump truck. The loads of the truck were 111.2 kN (25 kips) on the rear axle and 55.7 kN (12.5 kips) on the front axle. The suspension of the truck was not balanced, and unequal loads of 44.5 and 66.7 kN (10 and 15 kips) were measured on the left and right rear wheel sets, respectively. In addition, a 10-wheel, double rear-axle, 12.2-m^3 dump truck also was used for comparison loading conditions. The respective loads of the 10-wheel truck were 205.5 kN (46.2 kips) on the rear axle and 70.3 kN (15.8 kips) on the front axle.

Two pipeline configurations were investigated with respect to trench loads in which the wheel load was centered on (a) the middle of a pipe segment (referred to as LCP—load centered on pipe), and (b) a cast-iron joint (referred to as LCJ—load centered on joint). The LCP and LCJ configurations represent bounding conditions for response of a pipeline to localized surface load. The lead-caulked joints tend to have a low moment capacity such that the LCJ configuration is similar to a cantilever loading condition. In contrast, the LCP configuration is similar to a simply supported beam loading condition.

Figure 2 shows pipeline strains measured in response to backfilling, truck loading, and truck removal for both the LCP and LCJ configurations. The graphs are organized so that longitudinal strains averaged between the top and bottom of the pipe are plotted relative to the top chord of the pipeline. The absolute values of compressive and tensile bending strains at each gauge location were approximately equal. Average strains are plotted at each gauge station, referenced according to the distance along the pipeline. All plotted measurements are incremental strains referenced to the pipeline condition after the trench had been excavated. It was found that trench excavation tended to reduce pipeline strains to minimum values. The maximum strains in response to the truck load in each plot are for truck orientations in which the 66.7-kN (15-kip) rear wheels were positioned directly over the center of the undermined and backfilled pipeline.

Figure 3(*a*) and (*b*) show the maximum pipe strain as a function of trench width for the LCP and LCJ configurations, respectively. The increments due to backfilling and construction vehicle loading are shown along with the combined maximum strains. The peak strains in both test sections are similar in magnitude, although the locations at which they occurred are different. Peak pipe strains developed in the central portion of the test pipe for the LCP configuration. The LCJ configuration had a joint in the excavation center, resulting in maximum strains near the edges of the excavations. The maximum pipe strains due to combined backfilling and construction vehicle loading for both configurations were on the order of 200 $\mu\varepsilon$ for 0.9-m-wide trenches, 500 $\mu\varepsilon$ for 1.8-m-wide trenches, and 800 $\mu\varepsilon$ for 3.0-m-wide trenches.

THEORETICAL MODEL

Pipeline deformations caused by backfilling and construction vehicle loads, as well as by rolling and impact loads, are included in the models. The models used in this method are, by design, simple. The pipe moments computed using the models represent upper-bound predictions against which the field results are compared.

Pipeline Response to Backfilling

Figure 4(*a*) shows settlement and deformation mechanisms for the test configurations. Note that only the LCJ model contains the joint and pin. As backfill is placed on the pipe, the underlying soil compresses and moves away from the bottom of the pipe. The soil load then becomes concentrated on top of the pipe. This type of loading is analogous to a situation in which the pipeline is being lifted through the soil.

The additional load transmitted to the pipeline because of the relative movement can be characterized by a dimensionless load factor, N_v (*2*,*3*). The load imposed on the pipeline (ω), in terms of force per unit length, is given by

$$\omega = N_v \gamma Z D \tag{1}$$

where

N_v = dimensionless load factor,
γ = soil unit weight, and
Z,D = depth to pipeline centerline and outside pipe diameter, respectively.

Figure 4(*b*) shows the analogues used to calculate the strains in the pipeline, which was modeled as a pin-ended beam for the LCP configuration and as two fixed, cantilever beams connected by a hinge at the location of the joint in the LCJ configuration. The hinge cannot transfer moments. No support was considered from the poorly compacted backfill beneath the pipe. This condition was justified by stress cell readings below the invert of the pipe in the center of the LCP configuration, which showed virtually no increase in stress during the backfilling process. The effective trench width was assumed to be 0.3 m wider than the edges of the excavation to account for spalling and loosening of soil along the sides. The field data showed that the maximum strains in the LCJ configuration and the locations of zero strain in the LCP configuration were approximately 150 mm outside the edges of the trench excavation. The maximum moment (M_{max}) for both configurations, based on the conceptualized loadings

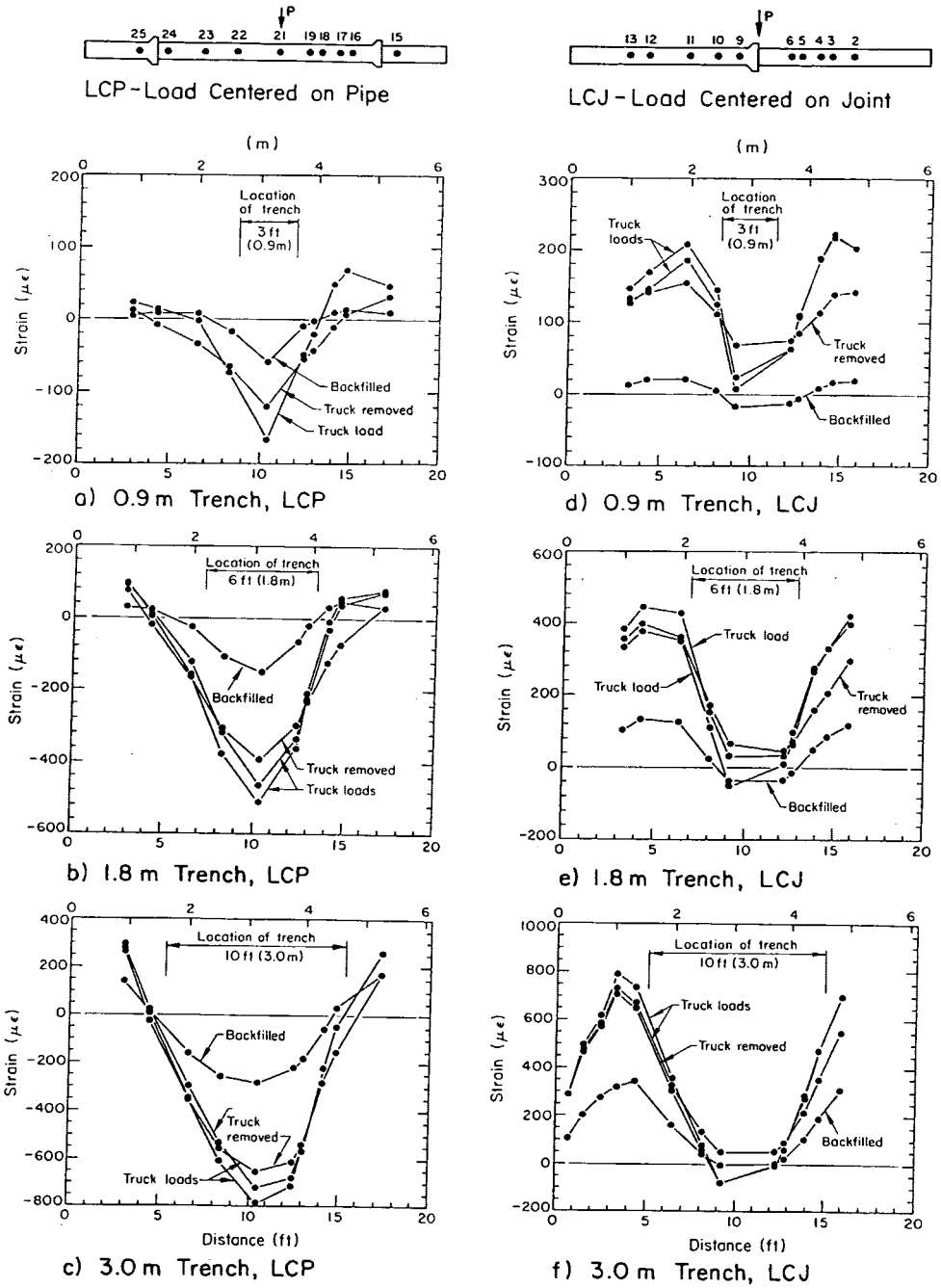

FIGURE 2 Pipeline strains measured in response to backfilling and surface loads.

shown in Figure 4(*b*), is given by

$$M_{max} = \frac{\omega \ell^2}{8} \quad (1)$$

where ω is the force per unit pipeline length and ℓ is the trench width (W) plus 0.3 m. The soil load, ω, was calculated using Equation 1 with a dimensionless load factor of $N_v = 2$ as appropriate for a loose backfill condition.

The comparisons between the maximum strains predicted by these models and those measured in the field test sections for the 3.0-m-wide trenches are shown in Figure 5. (Space limitations preclude the inclusion of comparisons for the narrower trenches.) The theoretical strains were calculated on the basis of the measured pipe geometric and material properties and soil properties described previously. In both graphs, the theoretical plots are shown by a solid curved line.

Pipeline Response to Construction Surface Loads

The strains generated by truck loads over the pipeline immediately after trench backfilling were considerably higher than those recorded during the backfilling. Figure 6 shows

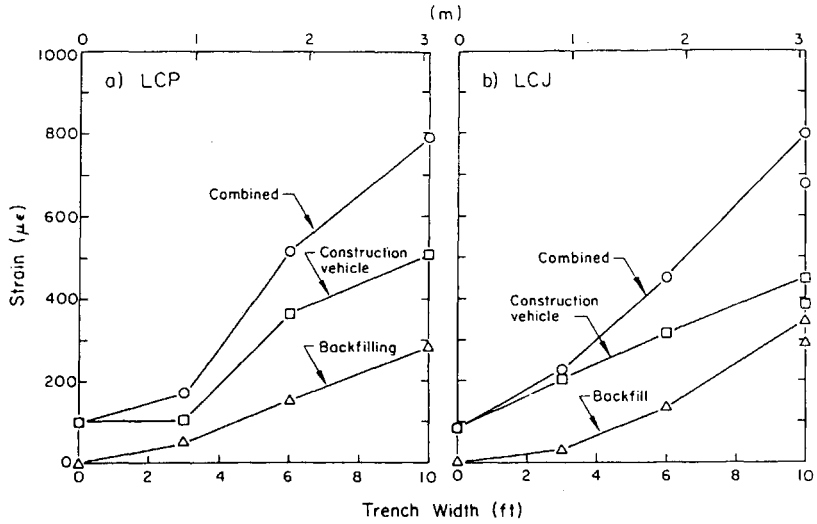

FIGURE 3 Maximum pipe strains for LCP and LCJ configurations.

the conceptual loading model for the distribution of a surface wheel load onto an underlying pipeline. A point load model (*4*) was used to evaluate the distribution of stress with depth. The locations at which the theoretical incremental stresses become negligible, on the basis of the test section geometry and predicted stresses, correspond roughly to intersections of downward-sloping lines from the surface having 1H to 1V slopes. The predicted stresses have a characteristic shape similar to that shown in Figure 6(*a*). This characteristic shape, or Boussinesq distribution, can be simplified further as a triangular stress distribution acting over a length defined by the 1H:1V projections from the surface, as shown in Figure 6(*b*).

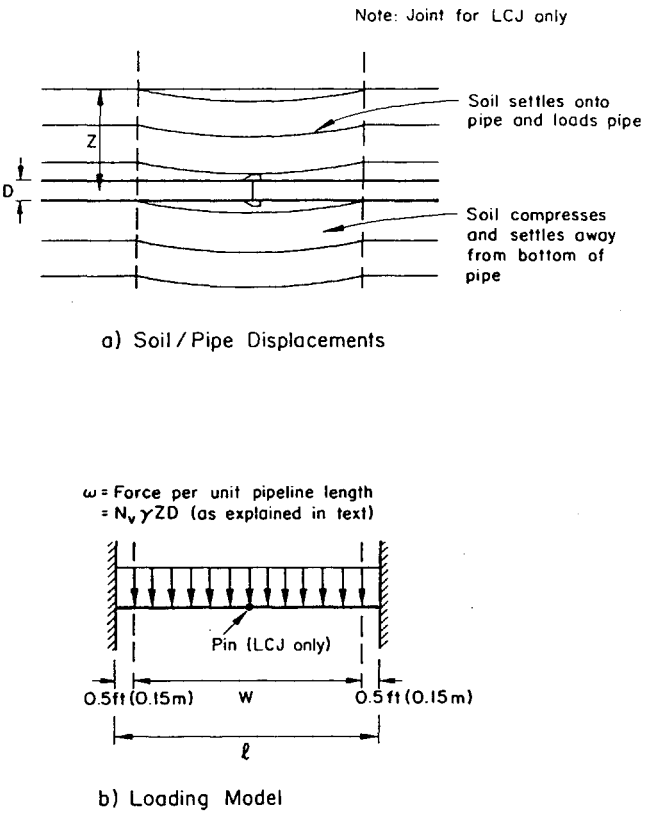

FIGURE 4 Soil/pipe displacement and loading models.

Stress cells located 75 mm above the center of the pipe in the north test bay registered stresses that were 3 to 3.5 times higher than those predicted. Measurements performed under similar conditions at the U.K. Transport Research Laboratory (*5*) have shown that the vertical stress distribution was more sharply peaked and approximately 1.9 times greater than that predicted by elastic theory.

There is theoretical justification for the increased level of stress. Backfill settlement and compaction during surface loading increase the backfill density from a loose to medium-dense condition. The increased density results in additional friction load, which should be consistent with a dimensionless load factor (N_v) of 3 for medium-dense granular soil (*2,3*). The stress cell recordings showed vertical soil loads in agreement with the theoretical load factor. A triangular stress distribution was therefore assumed with a base length equal to 1.50 m (two times the depth to the crown of the pipe) and a peak stress equal to three times that predicted by the point load Boussinesq-type distribution.

A simply supported beam analogue of this loading condition is shown in Figure 6(*c*). For most conditions, this model overpredicts the pipeline strains when compared with field measurements and does not account properly for the distribution of pipeline strains beyond the sides of the undermining trench. Although this type of model is helpful in setting an upper bound on pipeline response, additional refinements were needed to develop a more robust model for analytical predictions.

The pipe test sections were modeled as partially supported beams on elastic foundations, with the backfill providing support beyond the triangular load distribution. The soil reaction is characterized in Figure 6(*b*) as a series of springs on either side of the undermining trench. The subgrade reaction zones were modeled as short, pin-ended truss elements with a spring stiffness equal to a coefficient of subgrade reaction.

The coefficients of subgrade reaction (k_s) were derived from bearing capacity analyses and considerations of the pipe dis-

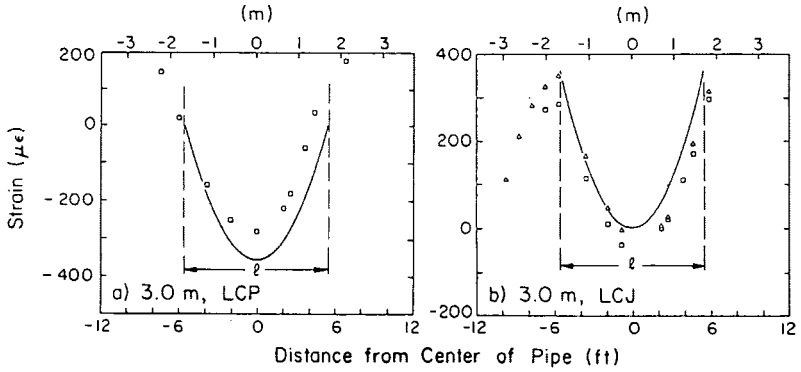

FIGURE 5 Measured and predicted pipe strains, 3.0-m trench.

placements. The values used for loose and dense backfill were k_s = 2270 and 22 500 kN/m², respectively. These values fall within those given by (*6*), which are in the range of 1090 to 3280 kN/m² for loose fill, and 16 400 to 54 700 kN/m² for dense fill.

Because the trench excavations were symmetrical about the trench centerlines, only half of the pipe geometry and support conditions required modeling. A schematic of the beam on elastic foundation (BOEF) model used for the 3.0-m trench excavations is shown in Figure 7. Details of the narrower trench excavation models are given by Stewart et al. (*1*). For the LCP pipe sections, a pipe joint element was placed 1.8 m from the trench centerline. A pipe joint element also was placed at the trench centerline for the LCJ configuration. The influence length for the triangular stress distribution extended 0.75 m on either side of the trench centerline. The equivalent reaction spring stiffnesses beyond the excavation limits and 150-mm loosened soil zones were those corresponding to dense soil. Spring stiffnesses based on a loose soil support condition were placed beneath the pipe within the excavation limits and the loosened soil zones. Short beam sections (25 mm) were used to model the lead-caulked joints and were given a bending stiffness (EI) of 1 percent of the pipe bending stiffness.

The comparisons between the measured pipeline strains in the north test bay and those computed using the BOEF models are shown in Figure 8. The BOEF model predictions were in good agreement with the measured strains. The critical strain locations for the LCJ configuration occur near edges of the trenches, and the strains are shown as tensile on the pipe crown.

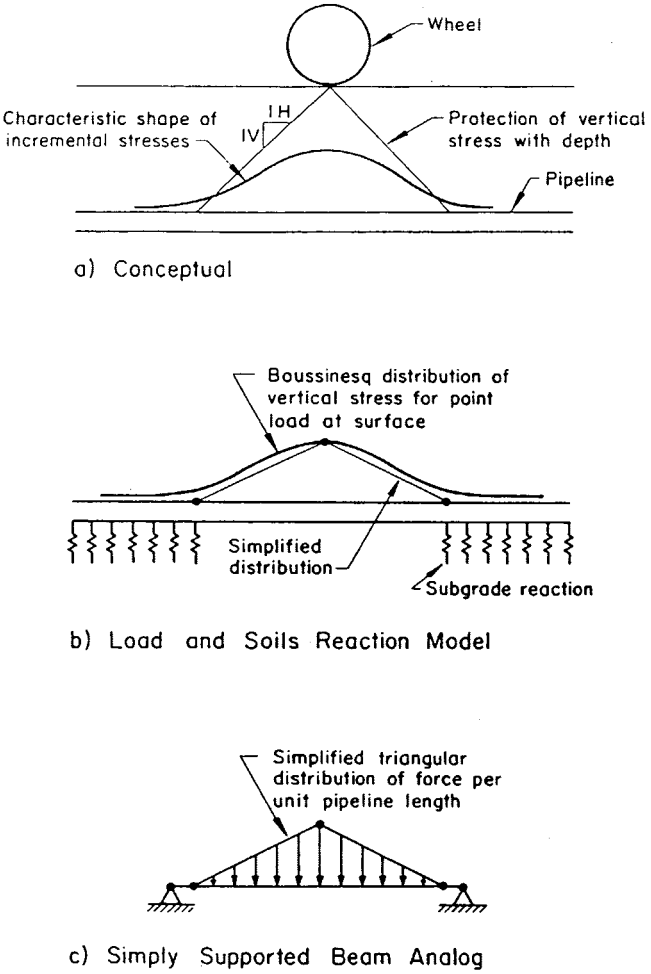

FIGURE 6 Vertical stress transfer from vehicle loads.

Combined Soil and Construction Vehicle Loading

The strains due to trench backfilling followed by construction vehicle loading are the algebraic sum of the strains for each of the two phases. The maximum strains due to trench backfilling are shown in Figure 9(*a*).

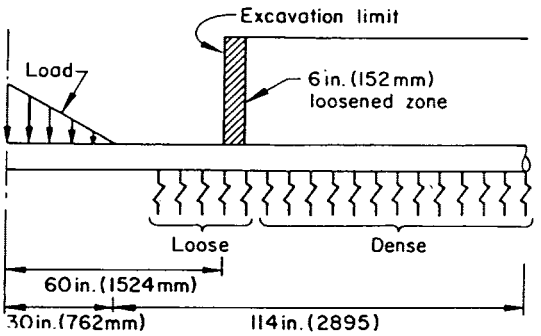

FIGURE 7 Generalized BOEF model used for characterizing vehicle loadings, 3.0-m trench.

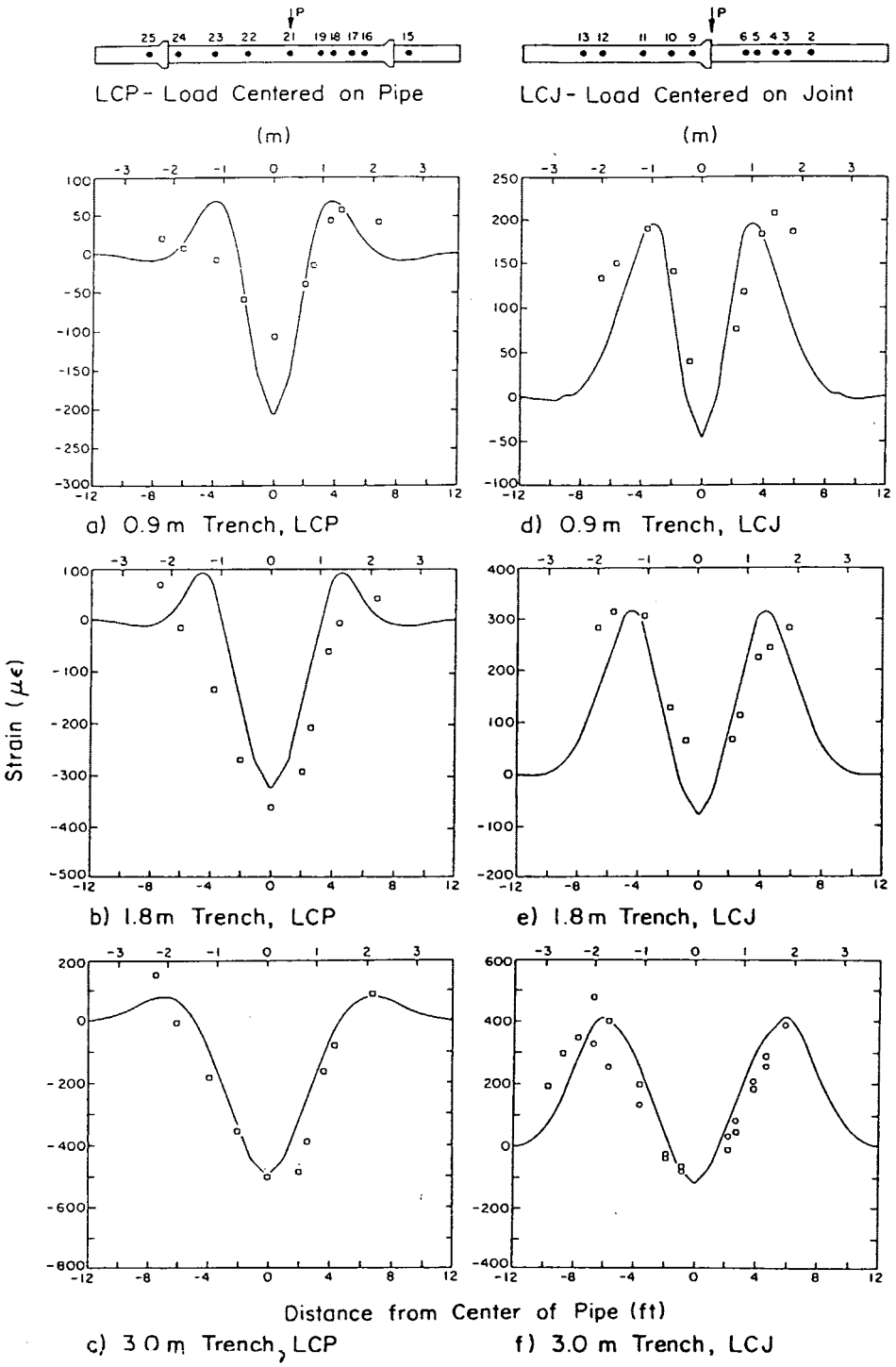

FIGURE 8 Measured and predicted strains due to vehicle loading.

Figure 9(*b*) shows the maximum pipeline strains due to construction vehicle loading only, which are dependent on trench width. The graph shows the predicted strains based on the simple beam model as well as the more refined BOEF models for both pipeline configurations. For trench widths up to 1.8 m, the simplified model appears reasonable; however, it is overly conservative for trench widths beyond 1.8 m, and the BOEF models result in better agreement between the predicted values and those measured in the field tests.

Analyses indicated that there is a trench width beyond which the vehicle-induced strains no longer increase. This limiting trench width is on the order of 2.7 to 4.6 m. Trench widths greater than this could result in entire 3.7-m-long pipe sections lying between the excavation limits. Because the joints transfer little moment, the effective pipe length over which moments would develop would be controlled by the length of the pipe sections between the nearest exposed joint and the edge of the excavation.

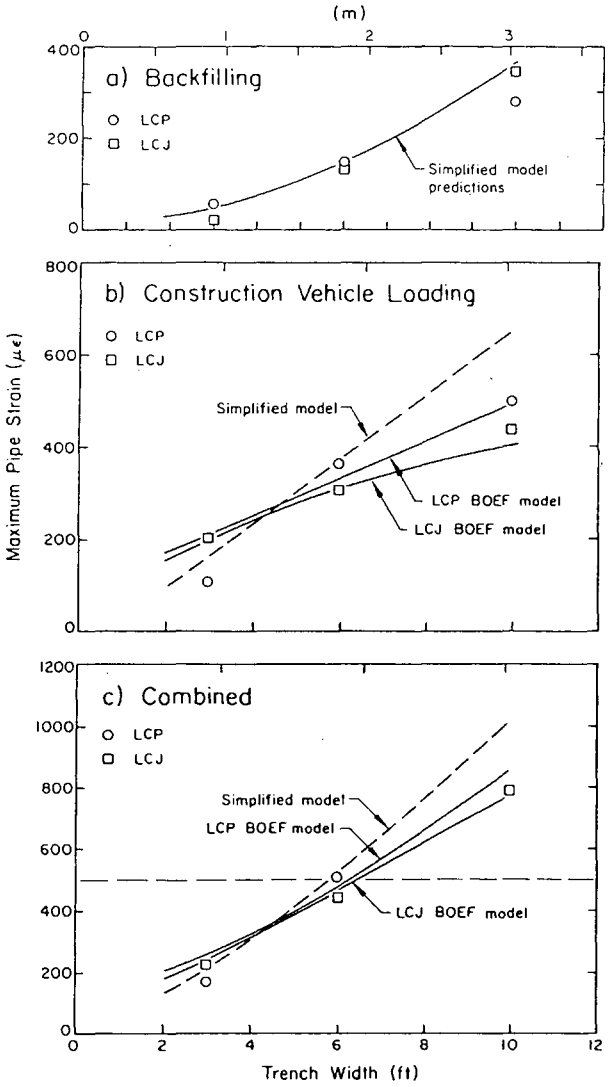

FIGURE 9 Maximum pipeline strains.

The strains resulting from combined backfill and surface vehicle loading are shown in Figure 9(*c*). These maximum strains were obtained by adding the maximum measured and predicted strains from the two separate cases. It should be recognized that the field data and analytical model predictions represented in this graph cover the worst, or upper-bound, loading conditions in the field. The measured and predicted pipe responses both show that 500 με is exceeded for trenches greater than 1.8 m wide. In addition, the simplified loading models give reasonably accurate and conservative results for trench widths in the range of 0.9 to 1.8 m.

COMBINED STATIC AND DYNAMIC LOADING

Factors that must be considered in addition to those generated by backfilling and construction vehicle loading are the strains due to the impact of traveling surface traffic following pavement resurfacing. Rolling-wheel loads and impacts caused by surface irregularities were considered for pipeline loading. A complete description of the dynamic tests is given elsewhere (*1*), and only a brief treatment of the primary results is provided here. Impact conditions in the dynamic tests were represented by an uneven roadway and various surface obstructions with dimensions similar to those associated with temporary asphalt patching of streets. Vehicle speeds ranged roughly between 14.5 and 53.0 km/hr.

The average rolling-wheel load strain in the LCP configuration was roughly 88 ± 14 με and for the LCJ configuration, 67 ± 18 με. The combined average rolling-wheel load strain developed in both test sections for the types of surface irregularities used in the rolling-wheel tests was 79 ± 19 με. An upper limit, then, to be used in the impact design methodology for a rolling-wheel load, was taken as 100 με (79 + 19 ≈ 100). This strain level compares favorably with the values reported for similar bedding conditions (*7,8*).

Average impact factors were calculated as the ratio of strain with impact divided by the average strains under static loading conditions. The combined average impact factor for these data was 1.42 with a standard deviation of 0.24. The impact factor that was selected for use in the impact formulation presented here was 1.65, which is roughly equivalent to the combined average of 1.42 plus one standard deviation of 0.24. This impact factor is consistent with other recommendations (*9,10*).

The final result of these quasi-static rolling-wheel loads and measured dynamic impact factors can be used to estimate a reasonable upper bound of expected dynamic strains. For the field test sections then, an expected dynamic strain would be calculated at 165 με, which is the product of the upper-bound rolling-wheel increment of 100 με multiplied by the upper-bound dynamic impact factor of 1.65.

The field experiments were conducted for a 0.75-m burial depth. However, mains may be found in the depth range of 0.6 to 1.5 m. For pipelines buried deeper than 0.75 m, the dynamic stress increments would be reduced, resulting in decreased dynamic strains. For this design methodology, the stresses predicted using the point load model (*4*) at depths from 0.6 to 1.5 m were normalized by the predicted stresses at a depth of 0.75 m. The dynamic strains at other depths were then predicted relative to the strains at 0.75-m depth multiplied by the normalized stresses for the given depth. Thus, the incremental dynamic strains at a depth of 0.6 m would be approximately 1.5 times greater than the strains at 0.75 m. Likewise, the expected strains at a depth of 1.1 m would be roughly one-half of those at a depth of 0.75 m. The rolling-wheel load strains at depths then are estimated by using the 100 με upper bound, measured in the field experiments at 0.75-m depth, and the appropriate stress ratio. For the previous example depths of 0.6 and 1.1 m, this would result in rolling-wheel strains of 150 and 50 με, respectively.

The final step in determining pipeline strains must consider all contributors, that is, backfill loading, construction vehicle loading, and dynamic traffic-induced strain. Because the residual strains following unloadings of the construction vehicles were on the order of 75 to 90 percent of the peak strains under load, no reduction in backfill and construction vehicle-related strains was considered, which adds a reasonable level of conservatism to the design methodology. The total allowable pipeline strain has been limited to 500 με. Because the dynamic strain decreases with increasing depth, the backfill and construction vehicle-related strains can be a greater percentage of a total allowable design strain of 500 με as pipe burial

depth increases. Parametric studies were performed to determine the expected pipe strains as a function of trench width for 102-, 152-, and 203-mm pit cast-iron mains at various burial depths ranging from 0.6 to 1.5 m. Complete details are provided by Stewart et al. (*1*).

RECOMMENDATIONS FOR PRACTICE

The methodology given here has been followed for 102-, 152-, and 203-mm nominal pipe diameters. Figure 10 shows the maximum trench widths as dependent on a depth of burial that would result in a 500-με pipe strain. As the depth of burial increases from 0.6 to 1.5 m, the maximum trench width increases but reaches limiting values. At typical minimum depths of 0.75 m, the maximum trench widths would be approximately 0.9, 1.2, and 1.7 m for 102-, 152-, and 203-mm diameter mains, respectively. At burial depths of 1.2 m or more, the maximum trench widths would be limited to approximately 1.2, 1.8, and 2.4 m for pipes having diameters of 102, 152, and 203 mm, respectively.

The design chart shown in Figure 10 is based on several observations that require additional interpretations. As trench width increases, the pipe-unsupported span increases, resulting in higher backfill-related strains as well as increased strains caused by construction vehicle loading. The combined effect is that pipeline strains increase for constant burial depth as the trench width increases. For constant pipe burial depth, two interactions must be considered. The backfill-related strains increase as the depth of burial increases. However, the imposed construction vehicle load and resulting pipe strains decrease as burial depth increases. At depths larger than roughly 1.2 m, the increase in backfill strains is compensated for by the decrease in construction vehicle strain, resulting in, for constant trench width, about the same level of combined pipe strain.

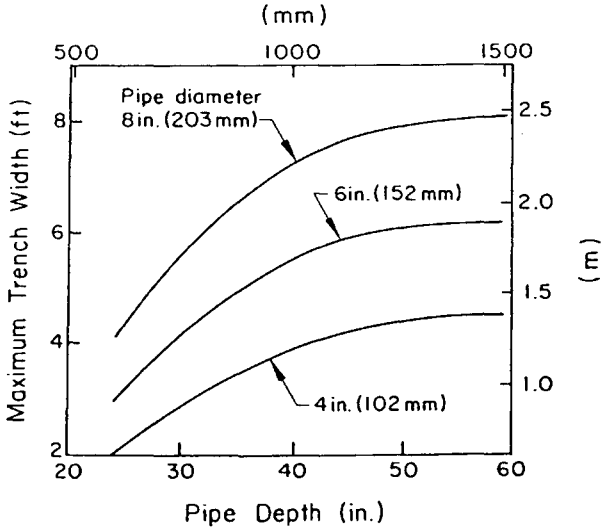

FIGURE 10 Maximum trench width versus pipe depth.

CONCLUSIONS

Field tests were conducted to evaluate the static and dynamic responses of cast-iron mains undermined by perpendicular excavations. A 14.6-m long instrumented pipeline was installed using four 3.7-m lengths of 152-mm nominal diameter pit cast-iron pipe sections with lead-caulked joints. Excavations of 0.9, 1.8, and 3.0 m widths were made, centered on a lead-caulked joint and also at the middle of a pipe section. A poorly graded, coarse-to-medium sand was used as backfill. This type of backfill is similar to materials commonly used in pipeline construction, particularly urban excavations. Pipeline strains were measured due to backfilling and construction vehicle loading and under impact conditions. Analytical models were developed on the basis of the field test results to evaluate pipe strains due to excavation crossings.

Pipe strains due to backfilling and construction vehicle loading increased as trench width increased for both test sections. The locations of maximum pipe bending strains in the LCP configuration were in the mid-portion of the pipe in the center of the excavation. In the LCJ configuration, the excavations were centered on a pipe joint, and the maximum strains occurred near the excavation margins.

Simple beam models were developed, along with more complete BOEF-type solutions. The simple beam models accurately predicted the strain measured in the pipeline for the 0.9- and 1.8-m excavations, but were overly conservative for 3.0-m trenches. The BOEF models accurately predicted the pipeline response for all trench widths.

The final design recommendations were based on a combination of static and dynamic effects. Design recommendations for maximum excavation width and a limiting strain of 500 με were presented and considered the effects of pipe diameter and burial depth. For typical minimum burial depths of 0.75 m, the maximum allowable trench widths would be 0.9, 1.2, and 1.7 m for 102-, 152-, and 203-mm diameter mains, respectively. At burial depths of 1.2 m or more, the maximum trench width would be limited to 1.2, 1.8, and 2.4 m for pipes having diameters of 102, 152, and 203 mm, respectively.

ACKNOWLEDGMENTS

The work presented in this paper was performed as part of research sponsored by the New York Gas Group (NYGAS). Appreciation is extended to Robert B. Meade, the NYGAS RD&D Program Manager and Contract Administrator, and to George M. Kok and Arthur A. Shapiro, Project Managers from Brooklyn Union Gas Company. Thanks are extended to B. J. O'Rourke, K. M. Kohl, B. M. New, and I. Ahmed for their participation in the work. A. Avcisoy and K. J. Stewart, who prepared the drawings and the manuscript, respectively, are duly recognized for their skills and contributions.

REFERENCES

1. Stewart, H. E., B. J. O'Rourke, and T. D. O'Rourke. *Evaluation of Cast Iron Response at Excavation Crossings*. Geotechnical Engineering Report 89-1. School of Civil and Environmental Engineering, Cornell University, Ithaca, N.Y., Jan. 1989.

2. Trautman, C. H., and T. D. O'Rourke. Behavior of Pipe in Dry Sand Under Lateral and Uplift Loading. *Geotechnical Engineering Report 83-7*. School of Civil and Environmental Engineering, Cornell University, Ithaca, N.Y., May 1983.
3. Trautman, C. H., T. D. O'Rourke, and F. H. Kulhawy. Uplift Force-Displacement Response of Buried Pipe. *Journal of Geotechnical Engineering*, ASCE, Vol. 111, No. 9, Sept. 1985, pp. 1061-1067.
4. Carder, D. R., P. Nath, and M. E. Taylor. *A Method of Modeling the Effect of Traffic on Undermined Buried Pipelines*. Laboratory Report 1028. U.K. Transport and Road Research Laboratory, Crowthorne, Berkshire, England, 1981.
5. Crabb, G. I., and D. R. Carder. *Loading Tests on Buried Flexible Pipes to Validate a New Design Model.* Research Report 28. U.K. Transport and Road Research Laboratory, Crowthorne, Berkshire, England, 1985.
6. Terzaghi, K. Evaluation of Coefficients of Subgrade Reaction. *Géotechnique*, Vol. 5, No. 4, Dec. 1955, pp. 297-326.
7. Pocock, R. G., G. J. L. Lawrence, and M. E. Taylor. *Behavior of a Shallow Buried Pipeline Under Static and Rolling Wheel Loads.* Laboratory Report 954. U.K. Transportation and Road Research Laboratory, Crowthorne, Berkshire, England, 1980.
8. Taylor, M. E., G. J. L. Lawrence, and D. R. Carder. *Behavior of a Shallow Buried Pipeline Under Impact and Abnormal Loads.* Laboratory Report 1129. U.K. Transport and Road Research Laboratory, Crowthorne, Berkshire, England, 1984.
9. *Recommended Practice for Liquid Petroleum Pipelines Crossing Railroads and Highways.* API Recommended Practice 1102, 6th ed. American Petroleum Institute, 1992.
10. Committee on Pipeline Crossings of Railroads and Highways. *Interim Specifications for the Design of Railroads and Highways.* American Society of Civil Engineers, New York, 1964.

Publication of this paper sponsored by Committee on Subsurface Soil-Structure Interaction.

Cut-and-Cover Tunnel Subgrade Modeling

JOHN S. HORVATH

Mathematical models that can be used to construct reinforced-concrete "box" tunnels using the cut-and-cover method are reviewed and critiqued. Newer models consistently provide better agreement between calculated and observed behavior than traditional ones do (the "rigid method" and Winkler's hypothesis with a constant coefficient of subgrade reaction). In addition, determining the appropriate model parameters is conceptually straightforward with the newer models. With current computer analysis capabilities, there is no reason to continue using traditional models that were reasonable alternatives when only manual calculations could be performed. Detailed recommendations for modeling subgrades in practice are presented with consideration given to the capabilities of commercially available structural analysis computer software. Other factors that influence the structural analysis of this type of tunnel are also discussed.

Reinforced-concrete "box" tunnels constructed using the cut-and-cover method have been used for decades for transportation applications and are an important part of several major projects currently under design. This latter fact has resulted in renewed interest in the way to model the soil subgrade underlying the base slabs of box tunnels, especially in consideration of the dramatic advances in the computational capability of microcomputers within the past few years. Mathematical models, also called subgrade models, used for constructing reinforced-concrete box tunnels are reviewed and critiqued. Models that can realistically be used in routine engineering practice are emphasized, although other models are noted for the sake of completeness.

CURRENT PRACTICE: REVIEW AND DISCUSSION

Parameters of Interest

A subgrade model is not necessarily a general soil model. It is intended to approximate only the important aspects of a particular soil-structure interaction problem. Therefore, the accuracy of subgrade models should be judged on consideration of the parameters that are important to a particular type of structure. Bending moments in the base slab and slab settlements, both total and differential, are of primary importance in box-tunnel design. The slab-subgrade contact stress, which will be referred to as the "subgrade reaction stress" or simply "subgrade reaction" as suggested by Liao (*1*), is generally of secondary interest, as is shear within the base slab.

A key premise of this paper is that an acceptable subgrade model should produce accurate estimates of both moments and settlements from a single analysis. This is consistent with other problems in modern structural analysis in which accurate estimates of loads and deformations of structural members are expected from the same analysis. However, this philosophy has not, in general, been used in past analyses of tunnels.

Civil Engineering Department, Manhattan College, Bronx, N.Y. 10471-4099.

Problem Components

A base slab and the subgrade that supports it are integral parts of the overall tunnel structure (see Figure 1). The reason is that the load-deformation behavior of any one component (roof slab and walls, base slab, or subgrade) depends on the behavior of the other two. Therefore, these three components should be analyzed as a single composite unit. This renders the problem highly indeterminate. With modern computer software, the structural components can be accurately analyzed. However, the way in which the subgrade effects are modeled has generally not improved by using computer applications. Therefore, this paper focuses on the issue of improving the subgrade modeling.

It is useful to define the coefficient of subgrade reaction:

$$k(x) = \frac{p(x)}{w(x)} \tag{1}$$

This parameter is completely general and independent of a particular subgrade model. An important point is that $k(x)$ is an observed result and not an assumption. However, this fact has not been emphasized in the past and will be used subsequently as one way of evaluating the accuracy of subgrade models.

Traditional Methods of Analysis

Rigid Method

Although numerous subgrade models have been developed over the years (*2*), only two have been used extensively in U.S. practice. The simpler one, which assumes that the base slab is perfectly rigid and has a straight-line distribution of subgrade reaction, is the Conventional Method of Static Equilibrium (CMSE). It is often referred to as the "rigid method." The CMSE is not a true subgrade model because it does not produce an estimate of total settlement of the base slab, although it does imply that there is no differential settlement. The base slab is treated as a footing and settlements are estimated separately using any one of several methods developed for footings. This is a classic example of the traditional approach in which separate analyses are used to estimate moments and settlements.

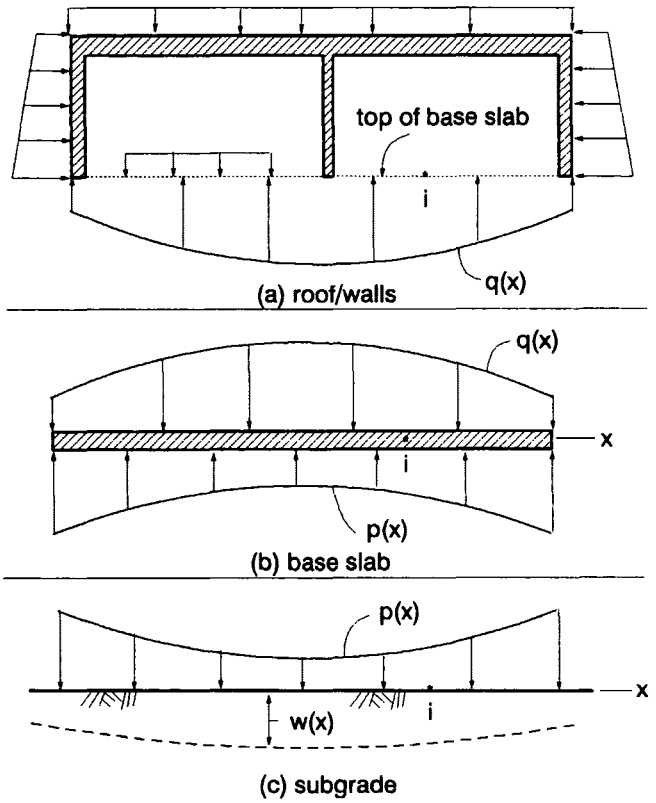

FIGURE 1 Components of typical box tunnel.

The concept that a base slab is essentially a large footing has unfortunately created a persistent perception that design requires only some "allowable bearing pressure." This is incorrect because footings and base slabs are significantly different in this regard. For example, for a footing supporting a building wall, the width is varied to match some "allowable bearing pressure" that is based on consideration of allowable settlement and the safety factor against a bearing failure under service load. On the other hand, the width dimension of a base slab is predetermined by the width of the tunnel. Thus the designer has relatively little control over the magnitude of the total settlement and bearing stresses that will result and must decide whether these parameters are of acceptable magnitude. If not, either a deep foundation alternative is used or the design of the structure is modified.

Winkler's Hypothesis

The other traditional subgrade model is Winkler's hypothesis. In its basic form, it is simply an assumption that the settlement (w_i) at some point i on the subgrade surface is caused only by the applied vertical normal stress (subgrade reaction) (p_i) at that point [see Figure 1(*c*)]. Mathematically, this is expressed as

$$p_i = k_{w_i} w_i \tag{2}$$

where k_{w_i} is the Winkler coefficient of subgrade reaction at Point i. The parameter k_{w_i} is sometimes referred to as the "soil spring constant" or by a similar term because the most common physical interpretation of the abstract behavior defined by Equation 2 is that of an independent spring oriented vertically. For an arbitrary number of contiguous points along the x-axis, the general form of Winkler's hypothesis is

$$p(x) = k_w(x) w(x) \tag{3}$$

where $k_w(x)$ is Winkler's coefficient of subgrade reaction for the general case. An important point is that Winkler's hypothesis forces the coefficient of subgrade reaction to become a known problem input rather than a calculated problem result. This was not emphasized in the past.

There is nothing inherent in Winkler's hypothesis that requires the Winkler coefficient of subgrade reaction to be constant in the x-direction, nor is there any reason why the value of $k_w(x)$ at some point cannot vary with the magnitude of applied load at that point. However, a constant value of $k_w(x)$, independent of load magnitude, is assumed traditionally. This evolved from pre-computer days when the only chart or tabular solutions available for a beam on a Winkler subgrade ("beam on elastic foundation") were based on a constant value of Winkler's coefficient of subgrade reaction. Assuming a constant value, Equation 3 becomes

$$p(x) = k_{w_0} w(x) \tag{4}$$

where k_{w_0} is a constant.

A contentious issue that has interested both practicing engineers and researchers for decades is the appropriate value for k_{w_0} in a specific problem. Methods for estimating k_{w_0} fall into two broad categories: (*a*) tabular or chart values and (*b*) those with some link to the theory of elasticity. The most widely referenced table or chart is from Terzaghi (*3*). Elasticity-based methods are generally based on collocation (matching) of Equation 2 with a p_i and w_i from some closed-form solution for an elastic continuum. A detailed discussion and comparison of several of these methods are provided by Horvath (*4*). However, any discussion of the accuracy of different methods for estimating k_{w_0} is relative because Winkler's hypothesis with a constant value of the Winkler coefficient of subgrade reaction is a poor model of the behavior of an actual soil subgrade, a fact recognized for more than 50 years. This is illustrated using the two limiting cases of a flexible and rigid foundation as shown in Figure 2. For an actual subgrade, the resulting coefficient of subgrade reaction, $k(x)$, is not uniform in either case. This is because of the mechanism of "load spreading," which is primarily the result of vertical shearing within the soil. Using the spring analogy, the springs in actual soil are not independent (as Winkler's hypothesis implies); they are coupled or linked together so that an applied load at one point produces settlement at many points. Conversely, the settlement at some point is influenced by applied loads at other points.

There are many reasons why Winkler's hypothesis with a constant coefficient of subgrade reaction is still used extensively in routine design practice despite its poor representation of actual subgrade behavior. Probably the most significant, practical reason (even in the current computer age) is that it allows the subgrade reaction, $p(x)$, to be eliminated as a variable in the problem solving. For example, the behavior of the

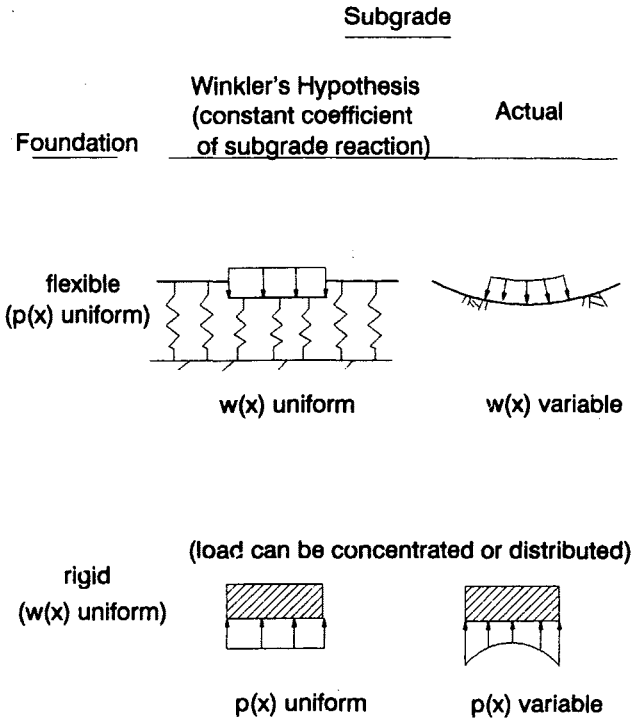

FIGURE 2 Comparison of subgrade response.

base slab shown in Figure 1(*b*) is given by

$$D\frac{d^4w(x)}{dx^4} + p(x) = q(x) \tag{5}$$

where D is the flexural stiffness of the slab (assumed constant). Combining Equations 4 and 5 yields the behavior of the combined base slab and subgrade:

$$D\frac{d^4w(x)}{dx^4} + k_{w_0}w(x) = q(x) \tag{6}$$

Thus the subgrade effects are easily accounted for in the stiffness matrix of the base slab as the external, independent springs transverse to the slab (*5*). Commercially available structural analysis software that is used in practice can easily accommodate such a model.

Although Winkler's hypothesis does produce an estimate of total and differential settlements, traditional practice is to "believe" only the moments calculated using this subgrade model. The calculated settlements are often ignored, which means that a separate analysis must be performed to estimate the expected settlements. This is based on recommendations by Terzaghi (*3*).

New Methods of Analysis

Pseudo-Coupled Concept

In an effort to retain the accustomed mathematical and modeling simplicity of Winkler's hypothesis with a constant coefficient of subgrade reaction, yet provide results closer to reality, "pseudo-coupled" subgrade models have been developed relatively recently (*5*). Examination reveals that this is not a new type of subgrade model at all but simply a return to the general form of Winkler's hypothesis (Equation 3). The assumption of a variable Winkler coefficient of subgrade reaction mimics the effects of coupling of the soil springs without explicitly doing so mathematically. Therefore, existing software can be used because the soil springs are still independent; they just vary in magnitude.

Any number of variations in $k_w(x)$ might be assumed when the pseudo-coupled subgrade concept is used. As a result, several versions of this concept have been proposed to date. They can be grouped into two categories:

- Generic variations that can be applied to any problem and
- Problem-specific variations.

The generic variations now in use assume an increase in $k_w(x)$ near the edges of the base slab. This comes from Figure 2 where, for relatively simple loading, the coefficient of subgrade reaction will always increase at the edges of the foundation, regardless of the relative foundation-subgrade stiffness. The simplest suggestion is to double the traditional constant value of Winkler's coefficient of subgrade reaction, k_{w_0}, along the edges of the base slab (*5*). The basic value of k_{w_0} would have to be determined using the methods discussed by Horvath (*4*). A somewhat more sophisticated version of this, which is discussed by Bowles (*5*), is to use a variation in the Winkler coefficient of subgrade reaction based on the theory of elasticity (usually the solution for a uniformly loaded flexible area). Typically, this produces a Winkler coefficient of subgrade reaction that is also about twice as large along the edges of the base slab than in the center, but with a gradual change in between. Again, the basic value at the center of the base slab to which this empirical variation would be applied would have to be determined from the methods discussed by Horvath (*4*).

Examples of the problem-specific category are provided by Liao (*1*) (a summary of key aspects are also provided by Liao [*6*]) and the Discrete Area Method (*7*). In these methods, both the magnitude and variation of $k_w(x)$ are predicted. Liao developed a solution for a variable Winkler coefficient of subgrade reaction that is based on a uniformly loaded slab of different relative stiffnesses and widths under plane-strain conditions and is supported on an isotropic, homogeneous linear-elastic continuum of finite thickness. He developed his solution specifically for analyzing tunnel base slabs.

The Discrete Area Method is completely general in the type of foundation to which it can be applied, although it has been used primarily for building mat foundations. This method requires separate but parallel structural and geotechnical analyses in which the foundation element (base slab, mat, etc.) and subgrade are divided into the same checkerboard of areas (discrete areas), using an arbitrary number and shape of areas. In the structural analysis, each arbitrary area of the foundation is supported on an independent spring of potentially different stiffness from the others. In the geotechnical analysis, an elastic continuum is subjected to perfectly flexible loaded areas on its surface, with each load uniform but potentially different in magnitude. Spring stiffnesses (in the structural analysis) and applied surface loads (in the geotechnical analysis) of each discrete area are varied in an iterative, trial-and-error

process until the deformation patterns from the two analyses match within some acceptable difference. It is assumed that this match provides the unique solution to the problem. Thus the major difficulty inherent in the pseudo-coupled concept is overcome because the variable Winkler coefficient of subgrade reaction used in the structural analysis (*a*) is determined specifically and uniquely for a given problem by matching the patterns of one analysis to those of a separate, rigorous analysis of the subgrade and (*b*) does not depend on some generic solution. Although the Discrete Area Method is perhaps the ultimate pseudo-coupled method and appears to give good results consistently for building mats (*7*), its inherent iterative, trial-and-error nature has discouraged its widespread use in practice.

Although the pseudo-coupled concept appears to be the long-sought improvement to the traditional use of Winkler's hypothesis with a constant coefficient of subgrade reaction, the actual improvement in a given problem is subject to significant variability that can be difficult to assess. The reason for the difficulty is that the degree of improvement depends on how closely the actual problem being analyzed matches the assumed problem that was used to develop the variation in the values of $k_w(x)$. Thus, the fundamental deficiency of the pseudo-coupled concept is that the correct answer must be known beforehand to be able to choose values of $k_w(x)$ that will result in calculating the correct answer. The reason for this circular logic is that the pseudo-coupled concept, which is just Winkler's hypothesis, does not incorporate soil-spring coupling inherently so it is incumbent on the engineer to input the coupling effects. Thus, the accuracy of results depends on how accurately the actual coupling effects can be estimated beforehand.

Multiple-Parameter Models

Because of the uncertainties inherent in the pseudo-coupled concept, there is a need for a subgrade model that incorporates spring coupling in the model's mathematics and is easy to implement and use in routine practice. Of all such models investigated, the most promising appear to be in the general category of multiple-parameter models. In addition to including spring coupling, these models are attractive because they are surface-element (two-dimensional) models whose governing equations do not require explicit consideration of the subgrade depth. The depth effects are built into the derivation of the equation defining the behavior of the subgrade model. A detailed discussion of multiple-parameter subgrade models identified to date is provided by Horvath (*2*).

The most accurate multiple-parameter model that has been identified and studied in detail to date is the Reissner Simplified Continuum (RSC) (*8*). Its governing equation is

$$p(x) - C_{R_1}\frac{d^2p(x)}{dx^2} = C_{R_2}w(x) - C_{R_3}\frac{d^2w(x)}{dx^2} \tag{7}$$

where C_{R_1}, C_{R_2}, and C_{R_3} are constants. Spring coupling comes from the terms involving the second derivatives of $w(x)$ and $p(x)$. Unfortunately, implementing this model into practice has been slow. The primary reason is that the solution requires consideration of subgrade boundary conditions that involve the first derivatives of both $w(x)$ and $p(x)$. The structural analysis software now used in practice cannot accommodate the latter condition directly. Work is in progress to develop an indirect method for implementing the RSC subgrade model within the capabilities of existing software. As an interim improvement, a recent suggestion (*9*) is to use a multiple-parameter model that is intermediate in accuracy between Winkler's hypothesis and the RSC. This model is usually referred to as Pasternak's hypothesis. Its governing equation is

$$p(x) = C_{P_1}w(x) - C_{P_2}\frac{d^2w(x)}{dx^2} \tag{8}$$

where C_{P_1} and C_{P_2} are constants. Spring coupling comes from the term involving the second derivative of $w(x)$. Of importance here is that not only is there no boundary condition involving the first derivative of $p(x)$, but $p(x)$ itself can be eliminated as a variable by combining Equations 5 and 8 so that the behavior of the combined base slab and Pasternak subgrade is defined by

$$D\frac{d^4w(x)}{dx^4} - C_{P_2}\frac{d^2w(x)}{dx^2} + C_{P_1}w(x) = q(x) \tag{9}$$

This is recognized as the equation defining the behavior of a beam-column with constant column tension of magnitude C_{P_2} supported on independent vertical springs of stiffness C_{P_1}. Therefore, the combined model of the base slab plus Pasternak subgrade will be referred to as the "beam-column analogy." The spring coupling inherent in Pasternak's hypothesis can be visualized as a pseudo-column tension that, from a structural-behavior perspective, effectively increases the base-slab stiffness. Most important, the modeling simplicity of a foundation supported on independent springs is preserved. Because structural-analysis software can model a spring-supported beam-column under constant tension, implementing the beam-column analogy into practice is simple. General recommendations for evaluating the coefficients C_{P_1} and C_{P_2} are presented in detail by Horvath (*9*). An example is included in this paper.

True Continua

Two categories of subgrade models are more accurate than multiple-parameter models. The first is boundary-element solutions of an elastic continuum in which the subsurface conditions are not modeled explicitly. The depth effects are built into a two-dimensional equation applicable only over the surface of the continuum. This is identical conceptually to the multiple-parameter surface-element models discussed previously, but the boundary-element method is more accurate because it involves more rigorous (and complex) mathematics.

The other category is explicit modeling of the continuum depth. As summarized by Horvath (*8*), closed-form elastic solutions have very limited use because of the large number of variables involved; therefore true continuum modeling is generally limited to using the finite-element method. In this case, a variety of soil models might be used, including linear-elastic and hyperbolic stress-strain models. Because of the

effort involved in developing and debugging finite-element meshes, using this method, although perhaps offering the closest analytical match to reality, is generally impractical on a routine basis.

CASE HISTORY: BACKGROUND DATA

Introduction

A goal of this paper is to illustrate the accuracy of various types of subgrade models using a case history. Because of the dearth of suitable published data for cut-and-cover tunnels, the case history used in this paper involves a mat foundation for a building. However, the geometric and physical conditions for this mat are almost identical to those of a typical tunnel section, including the application of an uplift water pressure on the base slab. Consequently, use of this case history is relevant to cut-and-cover tunnels.

The building is the Whitaker Laboratory, which was constructed at the Massachusetts Institute of Technology campus in Cambridge, Massachusetts, in the 1960s. A detailed compilation of relevant structural and geotechnical data and observed settlements was published previously by DeSimone and Gould (*10*).

Structural Analyses and Properties

The Whitaker Laboratory mat is significantly longer than it is wide and orders of magnitude stiffer at foundation level in the longitudinal direction compared with the transverse direction. As a result, mat flexure was essentially limited to the transverse direction, which is identical to the behavior of a typical tunnel base slab. This restriction was taken advantage of in the current study by performing only a plane-strain analysis in the transverse direction. This also simplifies the presentation of results and the assessment of the accuracy of the subgrade models considered.

A transverse section through the Whitaker Laboratory mat is shown in Figure 3. It is 1.14 m (3.75 ft) thick. Note the great physical similarity to a center-wall box tunnel. Also shown are the service loads from an analysis of the superstructure frame neglecting any differential settlement. The moment loading along the exterior below-grade walls, which coincide with Column Lines A and C, is the result of the lateral earth and water pressures on these walls. Not shown is the 292-kN/m (20-kip/ft) axial compressive force per unit width on the mat from these loads. The flexural stiffness of the mat alone in the transverse direction was given as 2.58 $\times$ 10^6 kN-m^2/m (1.9 $\times$ 10^6 kip-ft^2/ft). The superstructure stiffness, using the simple additive method discussed by the American Concrete Institute (*11*), was 2.31 $\times$ 10^5 kN-m^2/m (1.7 $\times$ 10^5 kip-ft^2/ft). Note that the mat is relatively much stiffer than the superstructure. Because the settlement data used to compare actual and calculated mat behavior were obtained about 6½ years after the superstructure was poured, one-third of these stiffness values was used to account for assumed time-dependent effects on the Young's modulus of the concrete. Cracked-section behavior of the mat was considered and modeled using Branson's equation. The cracking moment for this mat was estimated to be 667 kN-m/m (150 kip-ft/ft).

Subsurface Conditions and Subgrade Model Parameters

The key soil parameter in tunnel base slab analysis is generally the compressibility (Young's modulus). Below the foundation level for this mat there is approximately 21 m (70 ft) of Boston blue clay. This is underlain by glacial outwash sands and till that were assumed to act as a rigid base. When dealing with a fine-grained soil (i.e., clay) as at this site, there are two limiting cases of soil behavior: the immediate (undrained) condition and the long-term (drained) condition. Only the drained condition was studied because the most complete settlement data published were for a time well after primary

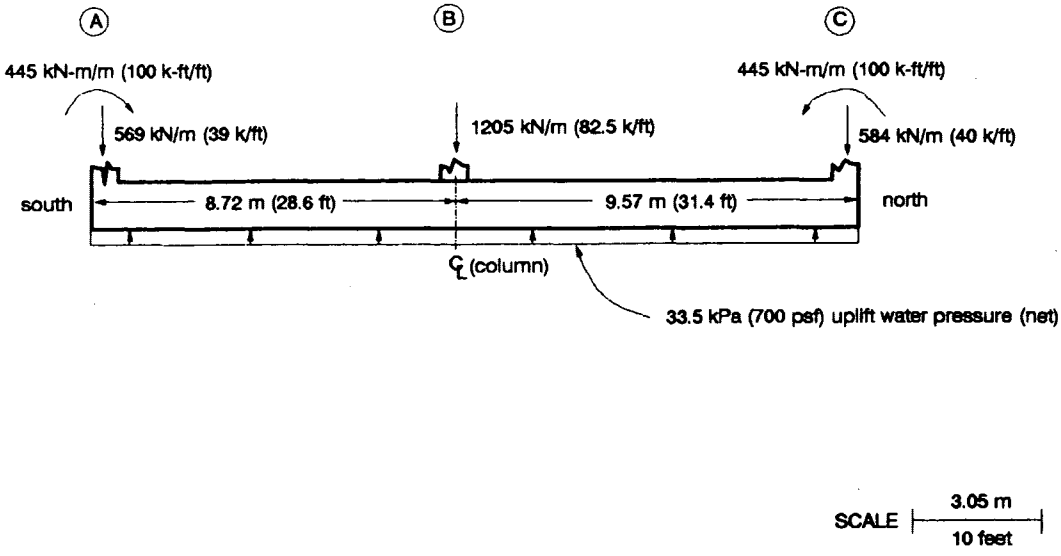

FIGURE 3 MIT Whitaker Laboratory—Transverse section through mat foundation.

consolidation was complete. This is not necessarily the more critical condition in terms of bending moments in the mat.

The procedure followed to arrive at a value of Young's modulus of the soil is detailed by Horvath (*12*). The equivalent average drained Young's modulus was calculated to be 38 MPa (800 ksf). The drained Poisson's ratio was assumed to be 0.25. The shear modulus was calculated to be 15 MPa (320 ksf). Using these elastic parameters, the coefficients for the various subgrade models compared in this study were calculated as follows:

- *Winkler's hypothesis/constant coefficient of subgrade reaction*. The Winkler-type simplified continuum has been found to be the most consistent method for calculating a constant value of Winkler's coefficient of subgrade reaction, k_{w_0} (*4*). Horvath (*13*) derived the following equation for an isotropic, homogeneous layer:

$$k_{w_0} = \frac{E_s}{H} \tag{10}$$

where E_s is the Young's modulus of the layer [38 MPa (800 ksf)] and H is the layer thickness [21.3 m (70 ft)].

- *Winkler's hypothesis/variable coefficient of subgrade reaction (pseudo-coupled concept) using generic solution*. The simplest generic pseudo-coupled solution is to use the value from Equation 10 everywhere except to double its value along the edges of the base slab.
- *Winkler's hypothesis/variable coefficient of subgrade reaction using Liao's method*. Liao's results provide a uniform value for $k_w(x)$ within the middle 60 percent of the foundation, with increasing values of $k_w(w)$ between there and the edges of the base slab. The elastic parameters and problem geometry were used to estimate the appropriate values from charts and tables by Liao (*1*);
- *Beam-column analogy*. As discussed by Horvath (*2*), there are at least five different ways to interpret the coefficients in Equation 8, which defines the behavior of this model. Of these, the Pasternak-Type Simplified Continuum appears to be the most logical. Horvath (*14*) derived the following for an isotropic, homogeneous layer:

$$C_{P_1} = \frac{E_s}{H} \tag{11}$$

$$C_{P_2} = \frac{G_s H}{2} \tag{12}$$

Equation 11 is identical to Equation 10 and represents the compression (spring) component of the subgrade. Equation 12 represents the shear (spring coupling) component, which is visualized as a fictitious tensile column force.

- *Reissner Simplified Continuum*. Horvath (*8*) derived the following for an isotropic, homogeneous layer:

$$C_{R_1} = \frac{G_s H^2}{12 E_s} \tag{13}$$

$$C_{R_2} = \frac{E_s}{H} \tag{14}$$

$$C_{R_3} = \frac{G_s H}{3} \tag{15}$$

Equation 14 is identical to Equations 10 and 11 and represents the compression component of the subgrade. Equations 13 and 15 represent the shear effects (Equation 15 is a pseudo beam-tension similar to Equation 12).

PRESENTATION AND DISCUSSION OF RESULTS

Introduction

For all parameters studied, it was found that using a constant Winkler coefficient of subgrade reaction and the simplest variable Winkler (pseudo-coupled) analysis where the coefficient of subgrade reaction was simply doubled along the edges produced nearly identical results. Consequently, the results for the latter analysis have been omitted from figures for clarity. In all figures, the results labeled "Winkler/variable" are those for Liao's pseudo-coupled solution.

Settlements

The comparison of calculated with average observed settlements is shown in Figure 4. The mat exhibited a slight overall dishing, although it was relatively stiff, even in the transverse direction, and exhibited only modest differential settlement. The RSC model provided good agreement with observed behavior and the best of all models considered. The results from Liao's pseudo-coupled solution were also good. The results from the beam-column analogy (Pasternak subgrade) and using a constant Winkler coefficient of subgrade reaction were similar and compared less well with observed behavior.

Bending Moments

The comparison of calculated moments is shown in Figure 5. Also included here are the results for the traditional method of assuming a rigid mat. Because of the known theoretical accuracy of the RSC model and the good comparison of observed settlements with values calculated using the RSC model, the RSC results were assumed to be correct for relative comparisons. As is typical, the relative range in calculated moments is less than that in settlements. Of particular note is the excellent agreement between the RSC and Liao methods as well as the significant underestimation of positive moments near the center using the rigid method. It is of interest to note that the theoretical cracking moment [667 kN-m/m (150 k-ft/ft)] would be exceeded only near the center of the mat.

Coefficient of Subgrade Reaction

As defined in Equation 1, the coefficient of subgrade reaction, $k(x)$, is the ratio of subgrade reaction to settlement. It is an observed result. However, using a subgrade model as simple as Winkler's hypothesis (with either a constant or variable Winkler coefficient of subgrade reaction) requires knowing

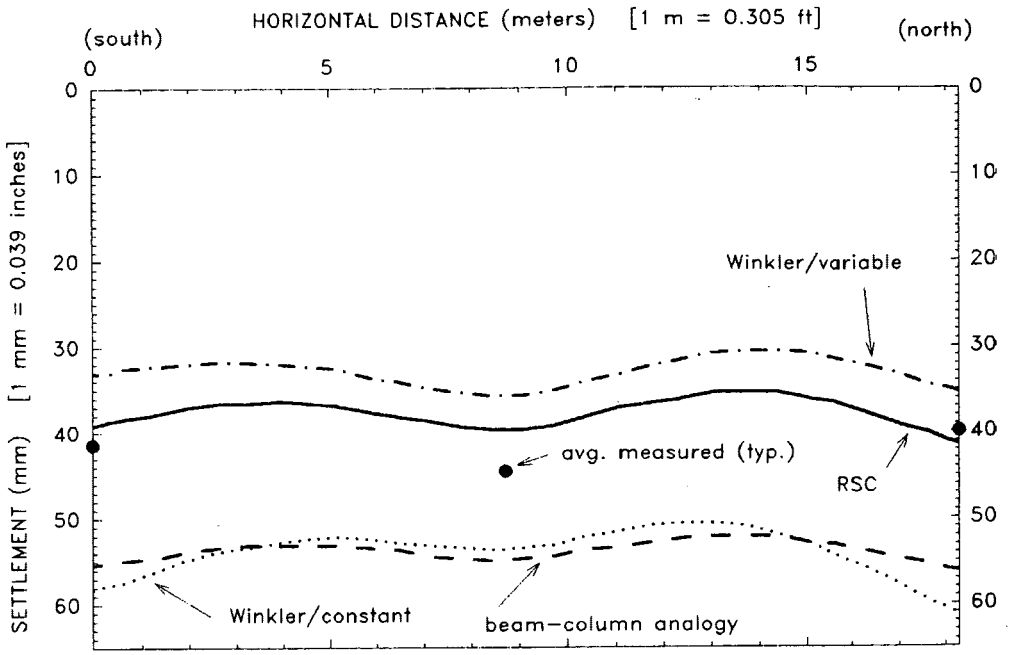

FIGURE 4 Whitaker Laboratory—Settlement comparison.

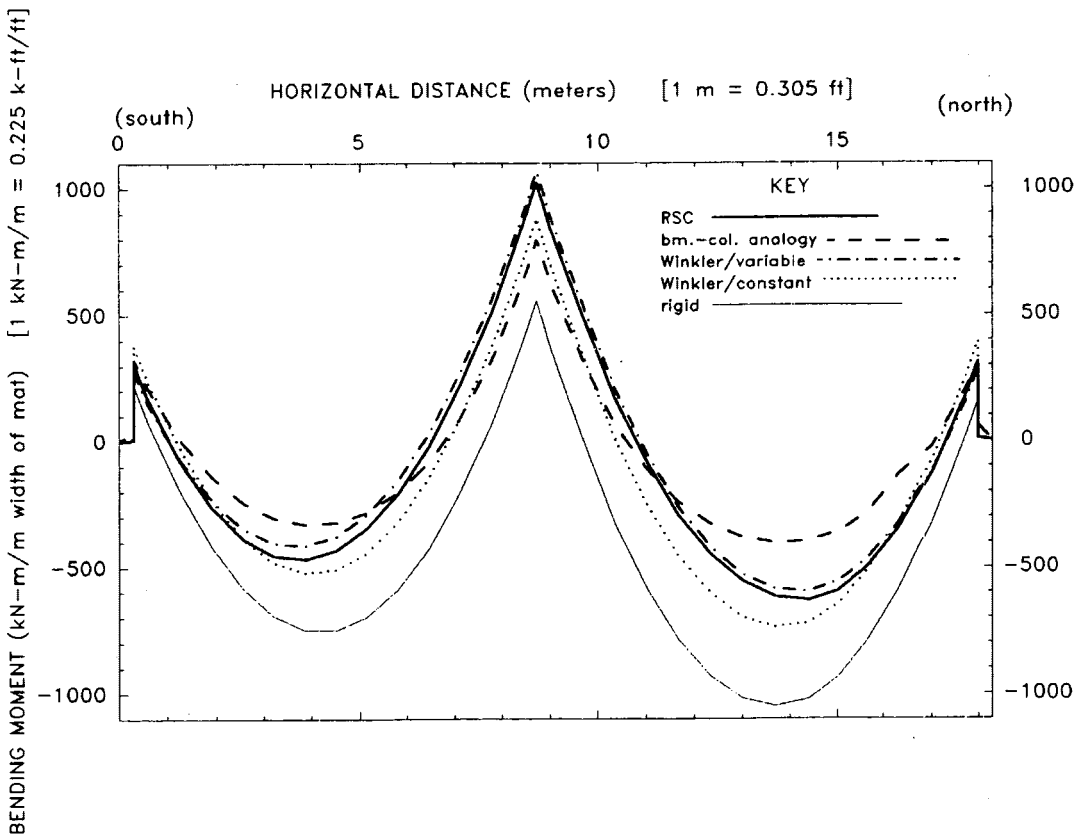

FIGURE 5 Whitaker Laboratory—Calculated bending moments in mat.

the $k(x)$ input beforehand. Therefore, one way to evaluate the accuracy of analyses performed using Winkler's hypothesis is to compare both the magnitude and variation of that assumed with the actual. Because contact stresses were not measured for this mat, the actual value is unknown. However, the value calculated using the RSC model was considered to be correct. Because the RSC model inherently incorporates spring coupling, the coefficient of subgrade reaction does not have to be assumed beforehand when using this subgrade model.

The comparison is shown in Figure 6. The generally good agreement between the values assumed in Liao's pseudo-coupled method and the RSC model explain why Liao's method produced good estimates of settlements and moments as shown previously. Similarly, the fact that the "actual" (RSC model) coefficient of subgrade reaction is not constant (nor does simply doubling the edge values provide significant improvement) explains why the traditional use of Winkler's hypothesis with a constant coefficient of subgrade reaction (or simply doubling the edge values) does not provide as good an estimate of settlement and moments.

CONCLUSIONS

Although only one case history was illustrated, the results are consistent with theoretical work (*8*); parametric studies involving foundation elements of numerous combinations of thickness, loading, and subgrade stiffness (*8*); and other case histories (*12,15*). Therefore, the following conclusions with respect to subgrade models are based on a collective evaluation of all work and not just the one case history:

- The Conventional Method of Static Equilibrium, which implies a perfectly rigid base slab, provides poor approximation of observed behavior. Virtually all base slabs exhibit some flexibility relative to the subgrade. Because moments of both signs will occur in base slabs, moments calculated assuming mat rigidity can be unconservatively in error in at least one sign.
- Using Winkler's hypothesis with a constant coefficient of subgrade reaction does not produce accurate estimates of both moments and settlements from a single value of Winkler's coefficient of subgrade reaction.
- The accuracy of results from using a variable Winkler coefficient of subgrade reaction (pseudo-coupled concept) are variable. The simplest approach of doubling the otherwise-constant value of k_{w_0} along the edges of the mat produced very little difference compared to using Winkler's hypothesis with a constant value for k_{w_0}. On the other hand, Liao's method produced results that agreed very well with the observed behavior and those calculated using the RSC subgrade model.
- The accuracy of results from Winkler's hypothesis is, in general, directly related to how well the assumed magnitude and variation of Winkler's coefficient of subgrade reaction matches the actual.
- The accuracy of results of the recently suggested beam-column analogy (which incorporates the Pasternak subgrade model) is also variable. In the case history shown, the results were only slightly better than those using Winkler's hypothesis with a constant coefficient of subgrade reaction. For other case histories (*9*), the improvement was considerably better. Based on work performed to date, the degree of improvement offered by the beam-column analogy appears to depend on the stiffness of the foundation relative to the subgrade. This is because the spring coupling represented by the pseudo column tension simply adds to the flexural stiffness of the foundation element. If, as with the case history in this paper, the foundation is already quite stiff, the improvement will be modest. For cases where the foundation element is relatively

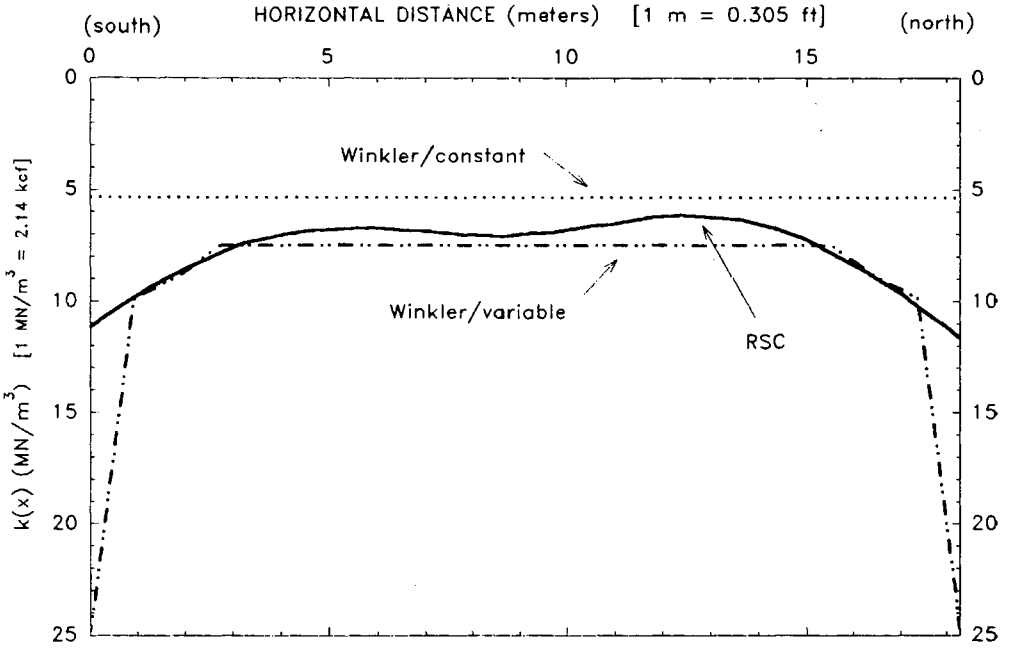

FIGURE 6 Whitaker Laboratory—Coefficient of subgrade reaction comparison.

more flexible (either a thinner element, stiffer subgrade, or both), the improvement would be greater.

- Of the subgrade models considered, the RSC provided the best agreement between observed and calculated settlements.

RECOMMENDATIONS

Subgrade Models

As with the above conclusions, the following recommendations are based on work in addition to the results presented in this paper. The overall recommendation is that a single subgrade model is used to calculate all parameters of interest in the design of a cut-and-cover tunnel (moments, settlements, etc.). Within this context, the following specific recommendations are made:

- Use of the Conventional Method of Static Equilibrium ("rigid method") should be discontinued.
- Use of the traditional form of Winkler's hypothesis with a constant coefficient of subgrade reaction should be discontinued.
- The general form of Winkler's hypothesis with a variable coefficient of subgrade reaction (the pseudo-coupled concept) can produce acceptable results provided that the reference analysis used to produce the values of $k_w(x)$ matches the problem of interest in terms of geometry, loading, and foundation stiffness. Thus the simple methods of doubling the Winkler coefficient of subgrade reaction at the edges or using a generic variation based on an elastic solution should not be used. Liao's method appears to be quite promising, and it is expected that the charts and tables provided by Liao (*1*) will be published soon so that designers of cut-and-cover tunnels will have access to this useful method [Liao has provided limited plots (*6*)]. The Discrete Area Method consistently produces good results, but it appears to be too cumbersome for routine practice, especially on smaller projects. This will likely continue to limit its use to those who are familiar and comfortable with the method.
- As an interim general-purpose method, the beam-column analogy should be used because it incorporates the Pasternak multiple-parameter subgrade model, which is fundamentally more accurate than Winkler's hypothesis. However, a boundary condition involving $w'(x)$ [the first derivative of $w(x)$] at the edges of the base slab must be dealt with. This issue is discussed by Horvath (*9*). Based on a limited study of this model to date, it is recommended that the continuity of $w'(x)$ be assumed. This can be achieved by specifying a zero-column-tension boundary condition at the edges of the base slab. It is also recommended that zero-horizontal-deformation boundary conditions be imposed at each edge of the base slab. This is to prevent calculation of fictitious horizontal deformations of the mat of a very large magnitude.
- Recommendations 3 and 4 should be considered only interim measures until such time that consistently more accurate subgrade models, such as the Reissner Simplified Continuum, can be implemented using structural analysis software that is available to practicing engineers. As stated previously, methods for accomplishing this are already under development.
- On large projects, at least one comprehensive model of the entire structure and subgrade should be developed and analyzed using a finite-element program such as *SOILSTRUCT* (*14*), which can model all stages of excavation, construction, and loading. The results from such an analysis, if conducted in the beginning of the project and, ideally, in conjunction with an instrumented test section, can be used to calibrate simpler models for project-specific conditions.

It is important to note that all of the recommended methods require knowledge of Young's modulus for the subgrade materials as well as the depth to an effective "rigid base" beneath the tunnel. Because there is considerable judgment involved in determining both parameters, any problem in practice will require studying the sensitivity of the calculated results to some reasonable range in both parameters. In addition, the final structural design should be based on an evaluation of the range in calculated bending moments.

Structural Analysis

Although this paper has focused on subgrade models, other structural aspects that should be considered include the following:

- The well-known behavioral aspects of the tunnel concrete, such as modulus reduction, with time and cracked section behavior;
- Seasonal temperature variations of tunnel roofs that can cause lateral expansion of the roof and increased lateral earth pressures on the side walls. As a result, this will influence the loading on the base slab (*15*). Geothermal analyses should be performed to evaluate the thermal variation to determine whether they are significant (*16*). If they are, as an alternative to designing a heavier tunnel section to withstand the higher stresses, an economic evaluation of more-modern design strategies should be performed. Specifically, a newly-identified geosynthetic product, "geofoam," could be used to provide several functions (*17*). For example, geofoam could be used above the tunnel roof as thermal insulation or along the exterior side walls to cushion the effects of expansion and contraction.
- The use of "thick" elements (in which the effect of shear on flexural stiffness is considered) for modeling the foundation element versus the usual "thin" elements based on simple beam theory (Horvilleur and Patel, unpublished data). The conclusion of these studies suggest that shear effects are significant in some cases. Therefore, it would appear to be prudent to always model a base slab using thick elements if the analysis software used has this capability.

REFERENCES

1. Liao, S. S. C. *Estimating the Coefficient of Subgrade Reaction for Tunnel Design*. Parsons Brinckerhoff, Inc., 1991.
2. Horvath, J. S. Subgrade Models for Soil-Structure Interaction Analysis. In *Foundation Engineering: Current Principles and Practices*, ASCE, New York City, 1989, pp. 599–612.
3. Terzaghi, K. Evaluation of Coefficients of Subgrade Reaction. *Géotechnique*, Vol. 5, No. 4, 1955, pp. 297–326.
4. Horvath, J. S. *Further Evaluation of the Coefficient, or Modulus, of Subgrade Reaction, k, Using an Extension of Reissner's Sim-*

plified Elastic Continuum Concept. Research Report CE/GE–88–2. Manhattan College, Bronx, N.Y., 1988.
5. Bowles, J. E. *Foundation Analysis and Design*, 4th ed. McGraw-Hill Book Company, New York, 1988.
6. Liao, S. S. C. Using Finite Element Analysis to Derive the Coefficient of Subgrade Reaction. *Proc., Fifth International Conference on Computing in Civil Engineering*, Anaheim, Calif., 1993.
7. Ulrich, E. J. Subgrade Reaction in Mat Foundation Design. *Concrete International*, Apr. 1991, pp. 41–50.
8. Horvath, J. S. New Subgrade Model Applied to Mat Foundations. *Journal of Geotechnical Engineering*, ASCE, Vol. 109, No. 12, 1983, pp. 1567–1587.
9. Horvath, J. S. Beam-Column-Analogy Model for Soil-Structure Interaction Analysis. *Journal of Geotechnical Engineering*, ASCE, Vol. 119, No. 2, 1993, pp. 358–364.
10. DeSimone, S. V., and J. P. Gould. Performance of Two Mat Foundations on Boston Blue Clay. *Proc., Specialty Conference on Performance of Earth and Earth-Supported Structures*, 1972, pp. 953–980.
11. American Concrete Institute Committee 336. Suggested Analysis and Design Procedures for Combined Footings and Mats. *ACI Structural Journal*, Vol. 85, No. 3, 1988, pp. 304–324.
12. Horvath, J. S. Mat Foundation Analysis: A Review and Critique Based on Case Histories. Preprint paper, ACI Spring Convention, 1992.
13. Horvath, J. S. Modulus of Subgrade Reaction: New Perspective. *Journal of Geotechnical Engineering*, ASCE, Vol. 109, No. 12, 1983, pp. 1591–1596.
14. Horvath, J. S. *A Study of Analytical Methods for Determining the Response of Mat Foundations to Static Loads*. Ph.D. thesis. Polytechnic Institute of New York (currently Polytechnic University), Brooklyn, N.Y., 1979.
15. Horvath, J. S. *Base Pressure and Earth Pressure Measurements; Nürnberg Subway*. Research Report CE/GE–89–1. Manhattan College, Bronx, N.Y., 1989.
16. Horvath, J. S. Computer Software for Load-Deformation and Geothermal Analyses in Problems Involving Geosynthetics. *Geotextiles and Geomembranes*, Vol. 12, No, 5, 1993, pp. 425–433.
17. Horvath, J. S. Dark, No Sugar: A Well-Known Material Enters the Geosynthetic Mainstream. *Geotechnical Fabrics Report*, Oct. 1992, pp. 18–23.

Publication of this paper sponsored by Committee on Subsurface Soil-Structure Interaction.

Evaluation of Culvert Deformations Using the Finite Element Method

SUNIL SHARMA AND JAMES H. HARDCASTLE

A finite element analysis was performed to study the stability of a rib-reinforced, low-profile, long-span steel arch culvert located at Hayden Creek, Hayden Lake, Northern Idaho. The culvert, which is 3.42 m high and has a span of 10.52 m, was designed on the basis of empirical methods. The culvert suffered some unexpected deformations (sag) during the first few months after installation. Because of the limitations of conventional, empirical analysis methods, the finite element method was used to model the complex soil-structure interaction conditions at the culvert and to assess the ability of the culvert to accommodate future design loads safely. The CANDE program, which was developed for the Federal Highway Administration, was selected for this study because it was adjudged as providing the most flexible and realistic treatment of the culvert soil interaction. The soil-structure model used to analyze the Hayden Creek culvert is described. Factors of safety for compression and plastic hinge formation (inelastic buckling) are computed from the finite element analysis results; the limitations of the approach are presented. A nonlinear, finite element analysis requires a large amount of processing time. Previously this was an expensive proposition, but with the availability of fast desktop computers, the finite element method may be used regularly with appropriately selected linear or nonlinear parameters to gain a general insight into the deformation behavior of culverts.

A rib-reinforced, low-profile, long-span steel arch culvert was installed at Hayden Creek, Hayden Lake, Northern Idaho, in January 1986. The culvert, which is 3.42 m high and has a span of 10.52 m, was designed on the basis of empirical methods. Initially the dimensions of the structure were well within the 2-percent limit recommended by the steel supplier's specifications (*1*). Between January 13, 1986, and March 19, 1986, a sag or flattening developed in the plates located in the eastern half of the structure's roof (L. E. Wolf, unpublished data).

The maximum amount of deformation occurred at a location approximately 9 m from the inlet of the structure (S. D. Powell, unpublished data). These deformations indicated a maximum deflection of about 0.175 m at the crown and about 0.100 m to 0.125 m of foundation settlement. The calculations made by the steel supplier using the AASHTO criteria and the estimated longer top radius of 8.60 m in place of the 7.14-m design radius indicated that the flattened arch retained a factor of safety (FOS) against plastic hinge formation of 3.0 (S. D. Powell, unpublished data). A substantial part of the dimensional and elevation changes were experienced in the first 68 days after construction, and at no time since the measurements were initiated has the apparent rate of settlement exceeded the initially observed rate. As the rate of deformation had reduced considerably, a study to determine the design capacity of the deformed culvert was initiated to determine whether the existing culvert could perform satisfactorily. Because of the limitations of conventional empirical analysis methods, the finite element method was used to model the complex soil-structure interaction conditions at the culvert and to assess the future ability of the culvert to accommodate the design loads safely.

Several finite element computer programs are available to perform this type of analysis, including FINLIN (*2*), SSTIP, NLSSIP (*3,4*). However, the CANDE program (*5–8*), which was developed for the Federal Highway Administration, was selected for this study because it was adjudged as providing the most flexible and realistic treatment of the culvert soil interaction (*9,10*). The soil-structure model used to analyze the Hayden Creek culvert is described. In addition, the factors of safety for compression and plastic hinge formation are computed from the finite element analysis results, and a discussion of the limitations of the approach follows.

NUMERICAL MODEL

Figure 1 shows the mesh that was used to analyze the full section for cases where differential settlement of the foundation could be appropriately simulated. A half-section mesh, shown in Figure 2, was also used for some preliminary analyses because solutions could be obtained much more quickly than with the full section. The plane strain meshes used in this study were not investigated for solution convergence and accuracy because they have a form that is similar to meshes used for previous analyses by Katona et al. (*7,11*). Both meshes are fixed at the lower boundary, that is, the location of bedrock, and are restrained in the horizontal directions at the two side boundaries. The meshes for the full and half sections consisted of 352 and 167 elements and 360 and 176 nodes, respectively.

CONSTRUCTION SEQUENCE

It has been shown by Katona (*7*), Leonards et al. (*10*), and McVay and Selig (*12*) that the construction sequence must be modeled during the analysis phase to obtain a realistic assessment of deformations and stresses. This is simulated by "adding" the soil above the springline in layers, thus effectively accounting for the modulus—the overburden stress dependency. The sequential construction effects generally dom-

Department of Civil Engineering, University of Idaho, Moscow, Idaho 83843.

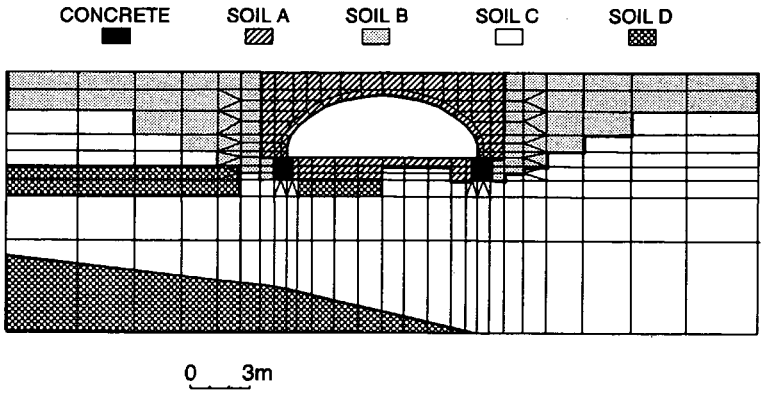

FIGURE 1 Full-section mesh and soil units used for finite element analysis.

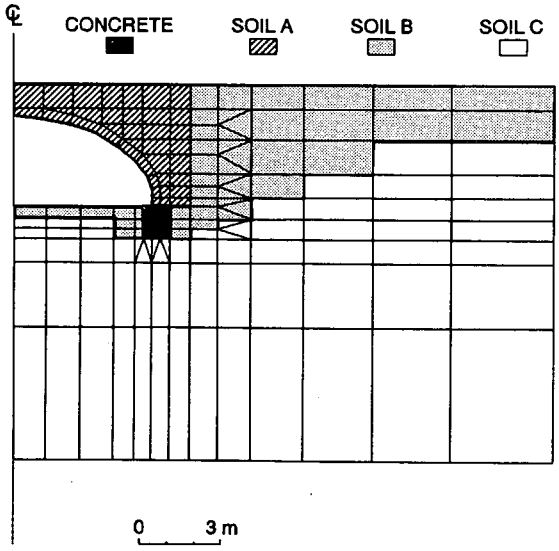

FIGURE 2 Half-section mesh and soil units used for finite element analysis.

inate the behavior of large span culverts with a shallow cover similar to the Hayden Creek culvert (*13*).

In this study the construction sequence was simulated by the following six steps, which are illustrated in Figure 3:

1. "Build" soil to foundation level (Level A in Figure 3);
2. Erect the culvert;
3. Place the compacted soil to the level of the springline (Level B);
4. Place the compacted soil to Level C;
5. Place the compacted soil to just above the crown (Level D); and
6. Place the compacted soil to the final grade (Level E).

Additional steps were included in the analysis to apply the live loads simulated by a line load applied above the crown at finished grade elevation.

ANALYSIS

For this study, the analysis considered three sets of model parameters corresponding to good, average, and poor soil conditions. This range was selected to investigate the possible influence of a variety of potential soil conditions that may be expected to affect the behavior of the installed culvert.

Model of Subsurface Profile

The subsoil profile was developed from the data collected from three soil borings performed at the site. Figures 1 and 2 show the distribution of soils used to analyze the full and half sections, respectively. Estimated model parameters for the soil zones are presented in Table 1. The model parameters were selected for three different soil conditions from the values suggested by Duncan et al. (*14*) for the appropriate soil types as follows:

- Good conditions were selected on the basis of optimum conditions during the compaction and backfilling operation. This category is considered to be an upper bound for the strength and compressibility of the soils. With these values, lower stresses and deformations are expected in the culvert.
- Average conditions were based on an estimate of the actual conditions that may exist at the site. These values were based on studies of similar soils from the area and results of the laboratory tests performed on disturbed or remolded samples obtained from the soil borings. The deformation results from the analysis are expected to be similar to values that may have been predicted during the design of the culvert.
- Poor conditions were based on the assumption that the subsoils and the compacted backfill have low strength and high compressibility. Such parameters are expected to generate large stresses and deformations in the culvert due to a lack of lateral support that is essential for such large-span structures.

These ranges of parameters (Table 1) were selected on the basis of a soil classification and simple laboratory tests that had been reported during the initial site exploration program.

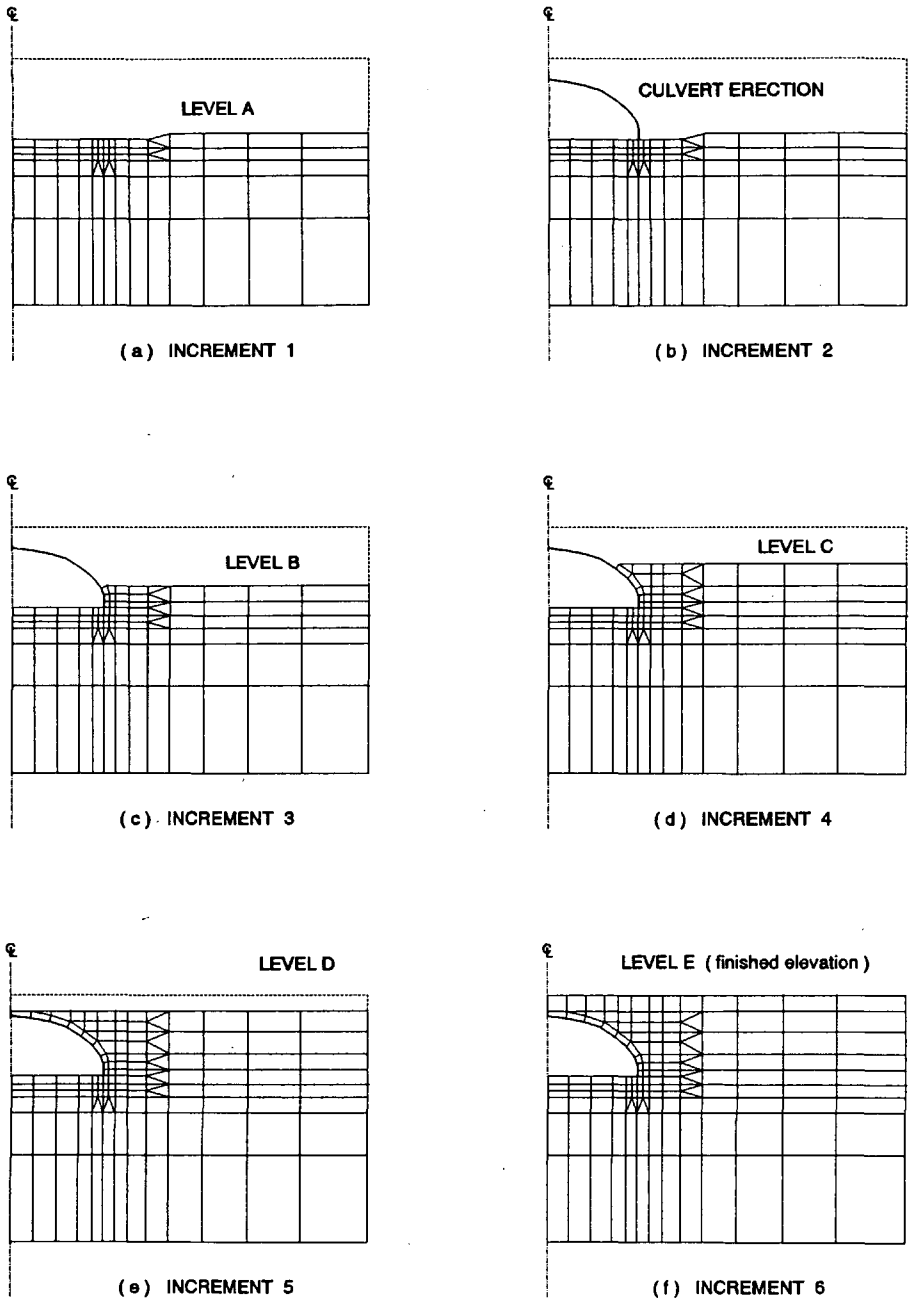

FIGURE 3 Incremental sequence used to simulate construction for finite element analysis.

The general parameters were initially selected for a preliminary assessment. A more elaborate and complete soil sampling and testing program would have been undertaken if the initial analyses had suggested marginal factors of safety.

LIVE LOADS

The AASHTO live load may typically be represented by a line load of 88 or 68 kN/m for a culvert with a 0.300-m or 0.600-m cover as suggested by Duncan (*13*). These line loads are estimated using the Boussinesq elastic theory and will produce the same peak stress at the top of the culvert as do two HS–20 truck trailers with single rear axles side by side on a two-lane road (*13*). For this study, several different line loads were selected to investigate the influence of possible overloading during or soon after construction.

RESULTS

The finite element analysis provides the following results at the pipe element nodes: displacements, thrust forces, bending moments, and shear forces. The thrusts and bending moments

TABLE 1 Soil Parameters for Duncan-Chang Model (*15*)

PARAMETER	SOIL A			SOIL B			SOIL C			SOIL D
	Good	Average	Poor	Good	Average	Poor	Good	Average	Poor	Average
K Modulus No.	800.0	700.0	450.0	600.0	500.0	300.0	600.0	500.0	300.0	200.0
n Modulus Exponent	0.5	0.4	0.45	0.5	0.35	0.4	0.5	0.35	0.4	0.35
c (kPa) Cohesion Intercept	0.0	0.0	0.0	0.0	0.0	0.0	0.0	0.0	0.0	0.0
$\phi°$ Friction Angle	50.0	50.0	50.0	45.0	40.0	40.0	45.0	38.0	38.0	30.0
R_f Failure Ratio	0.55	0.7	0.6	0.6	0.7	0.65	0.6	0.7	0.65	0.85
G Poisson's Ratio	0.25	0.3	0.3	0.3	0.33	0.35	0.3	0.33	0.35	0.35
F Poisson's Ratio Parameter	0.05	0.05	0.1	0.07	0.05	0.1	0.07	0.07	0.1	0.1
d Poisson's Ratio Parameter	10.0	5.0	5.0	5.0	5.0	4.0	5.0	5.0	4.0	4.0
γ (kN/m^3) Unit Weight	19.65	19.65	19.65	18.39	15.51	16.51	9.43	9.43	9.43	7.86

controlled the ability of the culvert to support the gravitational and design live loads. The shear forces were not expected to affect the stability of the culvert and thus were excluded in the computation of the factors of safety. The factor-of-safety values were calculated as follows:

Factor of safety against "pure" compression failure:

$$\text{FOS} = \frac{P}{A\sigma_y} \tag{1}$$

Factor of safety against plastic hinge formation (*13*):

$$\text{FOS} = \frac{1}{2} F_1[\sqrt{(F_1^2F_2^2 - 4)} - F_1F_2] \tag{2}$$

where

A = cross-sectional area of culvert,
S = section modulus,
σ_y = yield stress of culvert,
$F_1 = P_p/P$,
$F_2 = M/M_p$,
P = thrust force in culvert,
$P_p = A\sigma_y$, the axial force at yield,
M = bending moment, and
M_p = plastic moment resistance, $1.5\sigma_y S$ (estimated).

More than one plastic hinge is required for the formation of an unstable mechanism. In this case, the factor of safety against the formation of the *first* hinge is expected to give a conservative estimate of a plastic failure that will be caused by the formation of several such hinges. The possibility of *elastic buckling* was not considered for this analysis because it was not expected to be a controlling factor for a culvert of this size and a cover of about 0.600 m (*13*).

Results of the full sections analyses are presented according to the pipe node numbering system shown in Figure 4. The numbering of the nodes increases in a clockwise direction or from the left to the right.

Nonlinear Analyses

To obtain a general understanding of the effects of reasonable variation in soil parameters and culvert geometry (deformed versus ideal) within a reasonable expenditure of computational effort, a series of preliminary "runs" were performed using constant elastic moduli. However, nonlinear analyses are expected to provide a better simulation of the anticipated behavior of the culvert and supporting soils. Thus, following the preliminary elastic analysis, nonlinear analyses were performed using the subsoil models presented in Figures 1 and 2 and the parameters given in Table 1. A summary of the computed FOS values is presented in Table 2, and the results are discussed later.

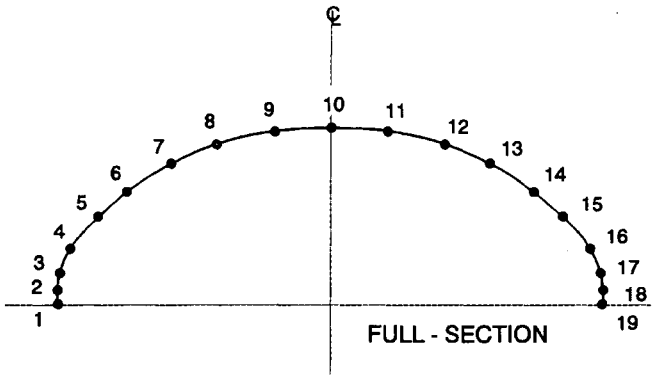

FIGURE 4 Location of pipe nodes for the full-section analyses.

DISCUSSION OF RESULTS

Half-Section Analyses

The nonlinear cases represent a realistic simulation of the culvert-soil interaction and are expected to provide the most reliable results. These results, summarized in Table 2, indicate FOS values ranging from 6.2 to 6.7 for thrust failure and 3.8 to 5.4 for plastic hinge formation with zero live loads. In the case of the half section, the poor soil conditions generated the lowest FOS values.

Full-Section Analyses

On the basis of results from the half-section analysis, two full-section cases were also analyzed to investigate the effects of a soft layer under the west footing. The FOS values are summarized in Table 2, and a discussion of the predicted deflections, thrust forces, and bending moments follows.

Good Soil Conditions

The horizontal and vertical deflections of the culvert for the good soil conditions are presented in Figure 5. For the full-section case, the effect of the soft layer leads to nonsymmetric deflections and further complicates their interpretation. However, the "peaking" is again evident from the y-deflection values. Also, the inclusion of the soft layer results in larger vertical settlements at the west footing, as expected, in comparison with that of the east footing. This differential settlement amounts to about 32 mm. The horizontal deflections are complex and difficult to interpret due to the inherent interaction between the culvert and surrounding soils.

The thrust forces are presented in Figure 6 (*top*) for the last two construction sequences and for a live load of 88 kN/m (Inc −7). For the dead load case (Inc −6), a minimum thrust force of 1000 kN/m is predicted at the crown, and a maximum force of 277 kN/m occurs at node 17, which is close to the west springline. Generally, the dead load thrust increases from the crown (node 10) to nodes 5 and 15, and then reduces slightly down to the footing level. This variation may be caused by the differential settlement which results in the development of positive arching and an apparent reduction in the dead loads. The application of the 88-kN/m live load increased the thrust at all nodes. A maximum increase of 93 kN/m was predicted at node 14, and the overall maximum thrust of 339 kN/m was computed at node 17, which is close to the east springline.

The bending moments for this case are shown in Figure 6 (*bottom*) and indicate that the west portion of the culvert near the springline has the higher bending stresses. (*Positive bending moments are defined as those generating tension on the outside face of the culvert.*) It can be seen that due to the residual effects of the peaking, the bending moments at the crown are positive under dead-load conditions, but the applied live load tends to generate negative bending moments. These moments increased from a maximum dead load value

TABLE 2 Results of the Nonlinear Analysis

	LOAD CASE DESCRIPTION	LIVE LOAD (N/m x 10^3)	FACTOR OF SAFETY	
			Thrust	Plastic Hinge
1.	Good soils; Half-section.	0	6.7	5.4
		88	5.5	4.5
2.	Average soils; Half-section.	0	6.6	5.1
		88	5.7	4.3
3.	Poor soils; Half-section.	0	6.2	4.6
		44	5.8	4.3
		88	5.3	3.8
4.	Good soils; Full-section	0	6.5	3.8
		88	5.3	3.2
5.	Poor soils; Full-section.	0	6.3	4.7
		88	5.4	3.9

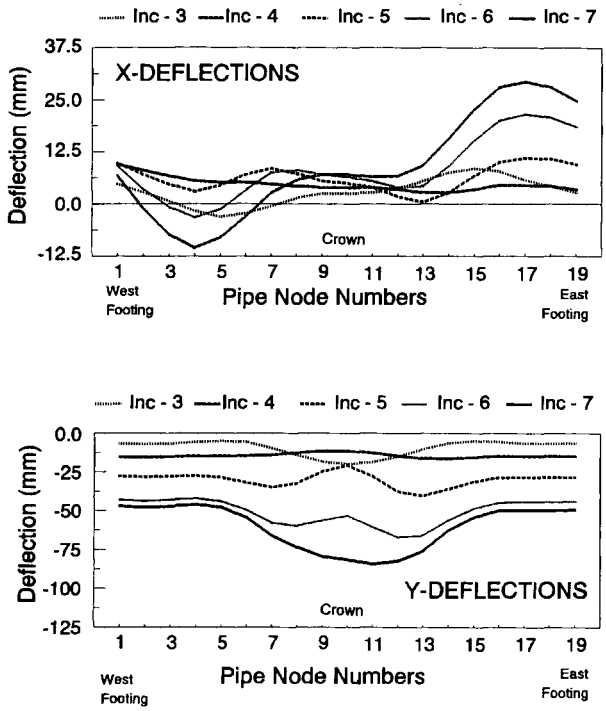

FIGURE 5 Horizontal and vertical deflections for good soil (full section).

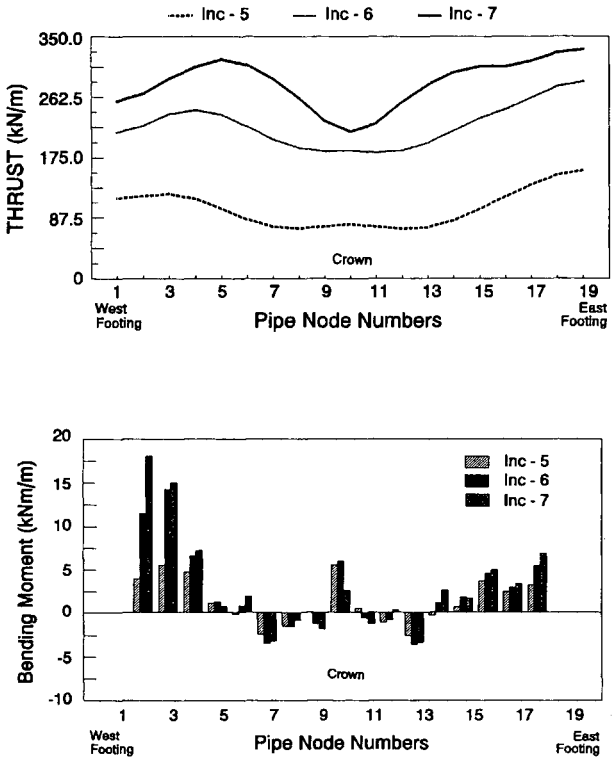

FIGURE 6 Thrust forces and bending moments for good soil computed by finite element analysis (full section).

of 14 195 N·m/m (node 3) to 17 980 N·m/m (node 2) with the application of the live load. The bending moments induced by the live load are significant for this case, with a predicted 57 percent increase at the west springline (node 2). However, this bending moment is not expected to cause any instabilities because there is an FOS of 3.2 against formation of a plastic hinge. The live load effects on the east side are less pronounced and increase bending moments by only a small amount.

Poor Soil Conditions

Results of the final analysis using the full-section mesh and poor soil condition parameters are presented in Figures 7 and 8. For this case, the contrast between the poor soils and the soft layer was marginal, and only a small amount of differential settlement was predicted by the finite element analysis. The peaking effects were successfully simulated during the construction sequence. The x-deflections are again difficult to interpret, but there is a reasonable symmetry between the predicted deformations at the east and west nodes of the culvert.

The computed thrust forces are similar to the previous case and ranged from 183 kN/m, close to the crown, to a maximum value of 286 kN/m at the east footing level for the dead-load case (Inc −6). The predicted bending moments are smaller than the good soils case with maximum values of 8 188 N·m/m and 12 149 N·m/m for the dead load and live load cases. Again the application of live loads was significant, leading to a 48-percent increase in the bending moment at the west springline.

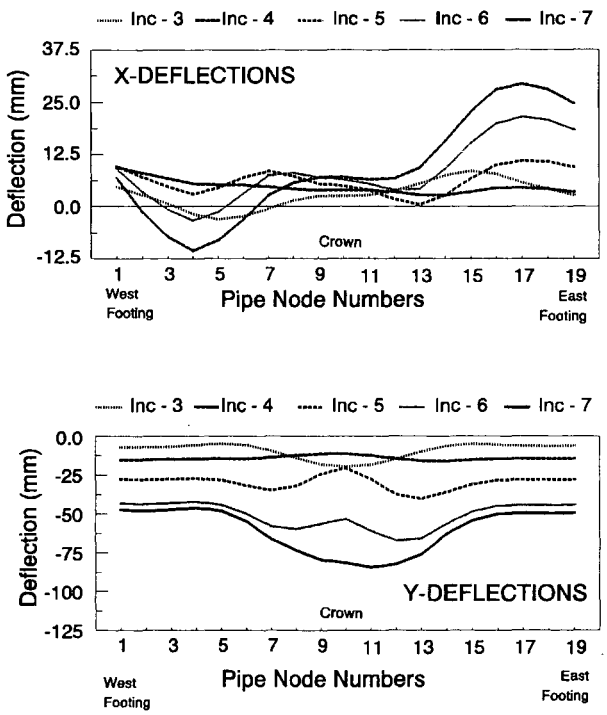

FIGURE 7 Horizontal and vertical deflections for poor soil (full section).

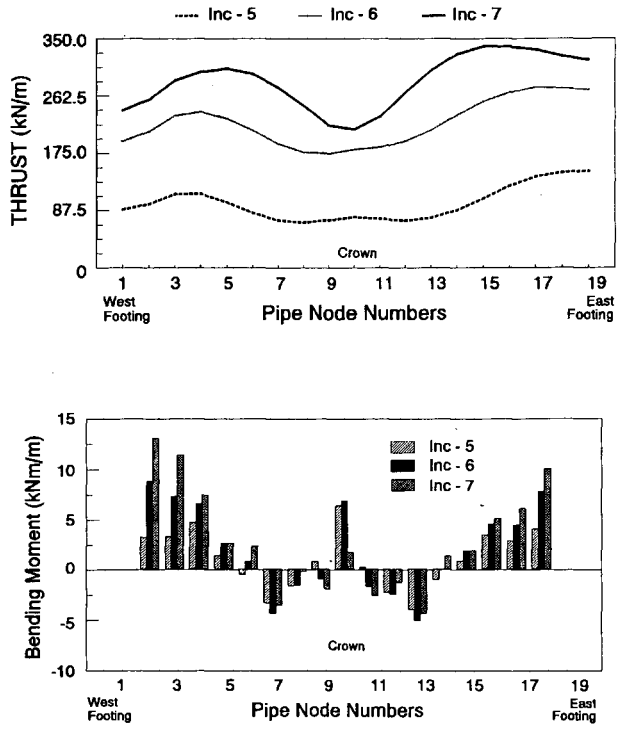

FIGURE 8 Thrust forces and bending moments for poor soil computed by finite element analysis (full section).

SUMMARY OF RESULTS

On the basis of the finite element analysis of the Hayden Creek culvert, the following minimum factors of safety were determined from several cases:

	Factor of Safety	
	Thrust	*Plastic Hinge Formation*
Dead load only	6.2	3.8
Live load = 88 kN/m	5.3	3.2

The values given for a live load of 88 kN/m represent a conservative estimate of the HS-20-44 wheel loading. Minimum values for the design live load represented by a HS-20-44 wheel are likely to be less than 88 kN/m and can be expected to result in larger factors of safety than reported above. These values are greater than the design factors of safety recommended by AASHTO.

The deformations computed by the finite element analysis were smaller than the maximum observed values. The computed values of 75 to 100 mm vertical deformation at the crown (from Figures 7 and 8) were considerably less than the reported value of 175 mm. Similarly, the calculated footing settlements of 50 to 60 mm were less than the reported value of 100–125 mm. The relative displacement of the crown with respect to the footings was reported within the range of 50 to 75 mm. This relative deformation appears to be in close agreement with the values predicted by this analysis.

CONCLUSIONS

The following points summarize the finite element analyses:

- Slight deformations in the shape of the culvert are not expected to significantly affect the stability of the culvert as the factors of safety are likely to be greater than 2.0.
- Although direct comparisons are not really possible, the factors of safety determined using the linear soil properties were greater than those of the nonlinear soil analyses.
- For the half section, nonlinear analysis, the poor soil condition parameters generated the lowest FOS.
- For the full section, nonlinear analysis, the contrast between the good soil conditions and the soft layer under the west footing gave the lower factors of safety.
- The finite element analysis was unable to predict deformations that closely agreed with observations. However, the relative deformations with respect to the footing elevation were predicted within reasonable accuracy.

Finally, it should be recognized that the large amount of processing time required by a linear or nonlinear finite element analysis can be readily provided by desktop computers. In view of the tremendous decrease in computational expenses, the finite element approach can be used to analyze the deformation behavior of culverts. However, considerable effort is still required to determine the subsoil conditions and assign the appropriate parameters for the constitutive model. It is hoped that the knowledge gained with this increased familiarity will lead to increased understanding of the behavior of culverts.

ACKNOWLEDGMENTS

The Idaho Transportation Department and the University of Idaho supported this study. The finite element computer analysis was performed by Li Jing, a doctoral student in the Department of Civil Engineering, University of Idaho. This support and help are gratefully acknowledged.

REFERENCES

1. *SYRO Long Spans*. Syro Steel Company, Centerville, Utah, 1984.
2. Leonards, G. A., and M. B. Roy. Predicting performance of pipe culverts buried in soil. Report No. JHRP–76–15, Purdue University, West Lafayette, Ind., May 1976.
3. Duncan, J. M., et al. *Soil structure interaction program, SSTIP*. University of California, Berkeley, undated.
4. Duncan, J. M., et al. Nonlinear soil structure interaction program, NLSSIP. University of California, Berkeley, undated.
5. Katona, M. G., and J. M. Smith. *CANDE User Manual*. Report No. FHWA–RD–77–6. FHWA, Washington, D.C., Oct. 1976.
6. Katona, M. G., J. M. Smith, R. S. Odello, and J. R. Allgood. *CANDE—A modern approach for the structural design and analysis of buried culverts*. Report No. FHWA–RD–77–5. FHWA, Washington, D.C., 1976.
7. Katona, M. G. Analysis of long-span culverts by the finite element method. In *Transportation Research Record 678*, TRB, National Research Council, Washington, D.C., 1978, pp. 59–66.
8. Katona, M. G., P. D. Vittes, C. H. Lee, and H. T. Ho. *CANDE–1980: Box culverts and soil models*. Report No. FHWA/RD–80/172. FHWA, Washington, D.C., 1981.

9. Leonards, G. A., T. H. Wu, and C. H. Juang. *Predicting performance of buried culverts*. Report No. FHWA/IN/JHRP-81-3. Purdue University, West Lafayette, Ind., 1982.
10. Leonards, G. A., C. H. Juang, T. H. Wu, and R. E. Stetkar. Predicting performance of buried metal culverts. In *Transportation Research Record 1008*, TRB, National Research Council, Washington, D.C., 1985, pp. 42-52.
11. Katona, M. G. Effects of frictional slippage on soil-structure interfaces of buried culverts. In *Transportation Research Record 878*, TRB, National Research Council, Washington, D.C., 1982, pp. 8-10.
12. McVay, M. C., and E. T. Selig. Performance and analysis of a long-span culvert. In *Transportation Research Record 878*, TRB, National Research Council, Washington, D.C., 1982, pp. 23-29.
13. Duncan, J. M. *Behavior and design of long-span metal culverts*. ASCE, Vol. 105, No. GT3, Mar. 1979, pp. 399-418.
14. Duncan, J. M., P. Byrne, K. S. Wong, and P. Mabry. *Strength, stress-strain and bulk modulus parameters for finite element analyses of stresses and movements in soil masses*. Report No. UCB/GT/80-01, University of California, Berkeley, Aug. 1980.
15. Duncan, J. M., and C. Y. Chang. Nonlinear analysis of stress and strain in soils. ASCE, Vol. 96, No. SM5, Sept. 1970, pp. 1,629-1,653.

The conclusions and opinions expressed in this paper were reached after interpreting and analyzing the data provided by the Idaho Transportation Department. The conclusions and opinions are solely those of the authors and do not necessarily reflect the views of the Idaho Transportation Department.

Publication of this paper sponsored by Committee on Subsurface Soil-Structure Interaction.

Long-Term Behavior of Large-Span Culverts in Cohesive Soils

M. C. McVay, P. Papadopoulos, D. Bloomquist, and F. C. Townsend

The long-term (after end of construction) behavior of large-span culverts buried in cohesive soils is presented. Nine centrifuge tests encompassing three different culvert shapes and three soils of varying degrees of plasticity were conducted. Backfill depth over the crown was fixed at 4.8 m to minimize the effect of vehicular live loads and to represent field conditions. The results show that the culvert's original shape controls its deformed shape and possible failure mode. For instance, the crowns of the semicircular culverts were rising, whereas the crowns of the low-profile arches were subsiding. The soil's plasticity was related to the magnitude of stress and deformation increase, and a linear relationship between bending moment and soil plasticity was discovered. In general, axial stress increases of 10 to 50 percent and bending moment increases of 50 to 100 percent, depending on soil plasticity, were recorded. It is suggested that long-term stress changes be accounted for in the future design of cohesive soils.

As small bridges and grade crossings have become old and in need of replacement, alternatives such as large-span steel or aluminum culverts have become economical substitutes for the more traditional bridge deck structures. Among the reasons for their increased use are simplicity of construction (may use unskilled labor), shorter installation times, minimum foundations requirements, and lower costs of construction materials. Typically assembled of corrugated metal plates of wall thicknesses varying from 0.25 to 1.25 cm, the complete structure may have a span (diameter) of 4 to 15 m and a backfill cover ranging from a few meters to 100 m (*1*).

The present AASHTO design (*2*) considers dead and live loads in sizing the plate. Special features such as thrust beams to promote arching and rib stiffeners to increase the cross-sectional moment of inertia of the section are also required. A select granular fill (Unified Soil Classification, GW), compacted to 90 percent AASHTO T180, extending 1.8 m from the side and 1.2 m above the structure, is compulsory. The code does not prohibit the use of cohesive (plastic) borrow soil as embankment material around the granular zone. This material is generally used if granular soils are unavailable on the site for economical reasons.

Long-term movements of the structure have been noted at a number of sites. Deflection increases on the order of 50 percent (*3*) and even catastrophic failures (*4*) have been recorded after a number of years. Currently the four most commonly cited causes of long-term soil-culvert stress and deflection reapportionment (*5*) are time rate consolidation, secondary compression, dynamic vehicular loads, and seasonal temperature and moisture variations associated with the environment.

Department of Civil Engineering, University of Florida, 345 Weil Hall, Gainesville, Fla. 32611.

The objective of the research reported here was to determine the influence of culvert shape (geometry) and soil plasticity on the long-term stresses and deflections within the structure due to consolidation. The study was performed in a large [117-cm (46-in.) radius] geotechnical centrifuge. It has been shown (*6*) that by properly modeling the construction sequence, soil type, and structural geometry, the end of construction and the long-term response of the prototype soil-culvert system can be simulated. Combinations of three frequently used culvert sections with three ranges of soil plasticity (plasticity indexes of 6 percent, 16 percent, and 31 percent) were investigated for a total of nine cases. The height of backfill over the crown (top) was constant (5 m) and was obtained from median field values reported in the literature. All culverts were instrumented with strain gauges and linear variable differential transformers (LVDTs) to measure deformation, a grid of sequins to measure soil deformation, and a pore pressure transducer to monitor the clay's fluid pressures.

Results of the experiments reveal that the culvert's initial shape controls both the end of construction as well as the long-term deformation of the structure. The soil type controlled the magnitude of both the long-term thrust and the bending stresses. Ring compression theory (*2*) can predict very well the thrust stress in the culvert wall at end of construction. However, depending on soil type, increases on the order of 50 percent may develop in the long term for very plastic soils. A linear relationship was found between bending stress and the plasticity index. The latter is important in estimating collapse, that is, the formation of plastic hinges.

LABORATORY EQUIPMENT AND MATERIALS

The containment vessel used to house the soil-culvert model in the centrifuge is shown in Figure 1. The inside dimensions of the container are 25.4 by 30.5 by 25.4 cm deep. The size ensured that the acceleration field within the bucket did not vary by more than 10 percent. The four walls of the box are 2.54-cm-thick Plexiglass and covered with an indelible 1.25-by 1.25-cm grid for determining soil strains using Avgherinos' photographic technique (*7*). The bottom of the container is removable, facilitating the placement of the culvert and instrumentation. The top of the bucket was slotted for the use of the inflight soil compactor (*6*).

The three long spans studied were the low-profile, semicircular, and high-profile arches because they are the most

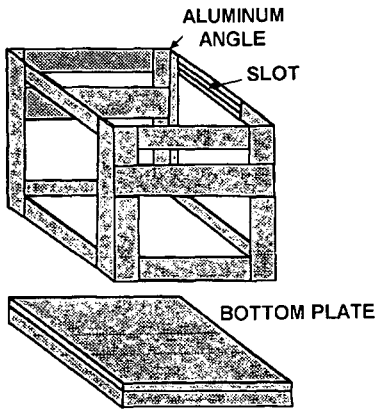

FIGURE 1 Containment vessel housing soil-conduit system.

commonly used shapes. The low-profile and high-profile arches have a larger radius of curvature at the crown than the semicircular shape and a smaller one from the thrust beams to the springline (side). The high-profile arch differs from the low profile arch in that the angle subtended in the former is much greater than that of the latter.

The clay backfill was selected to provide a large variability in terms of compressibility and permeability. Table 1 presents the properties of the three soils used and their classification. The compressibility of the green clay is greater than that of the red clay, which is greater than that of the orange clay; the permeability of the orange is greater than that of the red clay, which is greater than that of the green clay. All clay backfill was placed at optimum moisture content (Table 1) and compacted in flight (*6*).

The depth of backfill over the crown (top) of the culvert was selected to minimize the influence of vehicular loading and yet characterize a typical site. From a literature review, a total backfill depth of 4.8 m was selected. The AASHTO (*2*) specifications stipulate a granular zone of fill, 0.7 m above and 1.8 m alongside the culvert. Figure 2 shows the three prototype structures and backfill depths. All three culverts had the same depth of backfill over the crown because the study was concerned with only the influence of culvert geometry and soil type.

The centrifuge tests were conducted at the maximum *g*-level that would limit the stress variation within the bucket (Figure 1) to 10 percent (55 *g*'s). All three culvert models were made from 0.64-mm-thick aluminum plate and cold rolled. The wall thickness was selected from similitude of bending stiffness (EI/C, where E = Young's modulus, I = moment of inertia, and C = distance from neutral axis to outside fiber) between models and the suggested AASHTO design (15.2-by 5.1-cm corrugations with 0.55 wall thickness). Table 2 provides the complete model geometries for the three structures (Figure 2) under study.

Each model had pairs of strain gauges epoxied to the inside and outside of the culvert at its springline, thrust beam, and crown locations. For redundancy, wear, and tear, each location had three sets of strain gauges for a total of 18 gauges on each model. For a given pair (inside and outside), the average strain may be equated to the thrust stress, and the average of the difference to the bending stress in the wall.

Deformations of the crown of the culverts were determined using an LVDT and subsequently converted to prototype movements by multiplying them by the *g*-level of the test (55 *g*). Figure 3 shows an instrumented model culvert with the AASHTO (*2*) special feature, that is, thrust beams.

The soil was instrumented with a Druck miniature 1-bar (100-kPa) PDCR–81 pore pressure transducer. McVay et al. successfully used a similar device (*6*) to measure pore pressures at different scale sizes to confirm the pore pressure dissipation was *g*-level squared, that is, classical consolidation theory. The transducer was placed 4.1 cm outward from the springline in the clay backfill. To measure soil strains, straight pins with flat heads were placed with each soil lift, touching the grid-lined Plexiglass. A Swiss Kern DSR–1 device, which is accurate to 1 micron, was used to measure the relative movements of the markings.

TEST RESULTS

Deflections

The deflections of the three culverts versus model time with different backfill types are shown in Figure 4. Model time may be converted to prototype time by multiplying it by $(55)^2$, which is the scaling relationship for viscous consolidation time (*6*). In Figure 4, time zero represents no backfill (i.e., start of construction) followed by the end of construction (EOC) (20-min model or 42-day prototype time) and afterwards for a total of 320 min (1.8-year prototype). All structures experienced crown peaking at 10 min (21-day prototype) because backfilling reached the culvert's crown at this point, followed by subsidence as backfilling occurred from the crown (10-min

TABLE 1 Clay Backfill Properties

	Low Plasticity Orange Clay	Med. Plasticity Red Clay	High Plasticity Green Clay
Maximum Dry Density (kN/m^3)	18.69	17.28	12.72
Optimum Moisture Content	13%	21%	36%
Liquid Limit	21%	33%	71%
Plasticity Index	6%	16%	31%
Classification*	CL-ML	CL	MH

* Based on Unified Soil Classification System

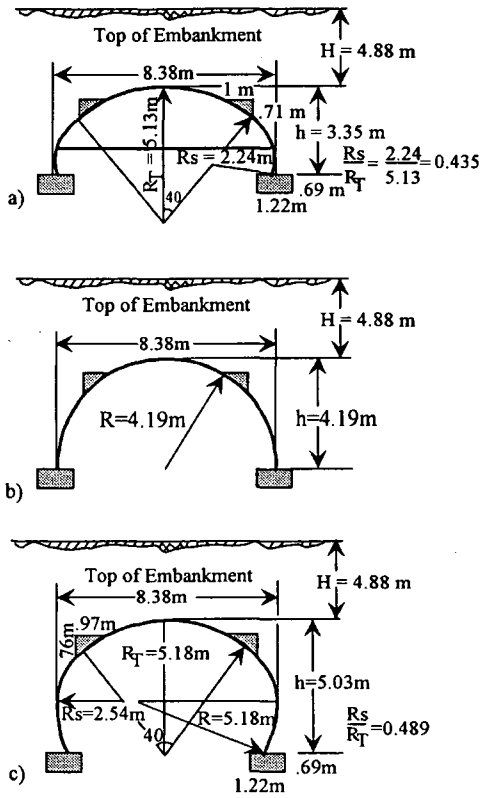

FIGURE 2 Culvert geometries and backfill depths: (*a*) low-profile arch; (*b*) semicircular arch; (*c*) high-profile arch.

model) to its final depth, that is, EOC (20-min model or 42-day prototype time).

As expected, the order of crown peaking due to depth of backfill at the crown after the 10-min mark (21-day prototype) was the high profile, then the semicircle, followed by the low-profile arch. Also, for a given shape, the crown peaking appears to be influenced by the soil's plasticity (Figure 4). The latter may be explained from the compaction induced stresses which, according to Duncan and Seed (*8*), approach passive values. For shallow depths, the passive pressure is controlled more by the soil's cohesion than its angle of internal friction. For instance, Table 3, which presents the resultant passive force (Pp1) on the low-profile arch, shows the high-plasticity green clay to have the greatest passive force. Consequently, a structure will tend to flex inward to a larger extent when interacting with a very plastic soil (higher cohesion) than with a less cohesive soil. All three structures displayed this phenomenon.

Backfilling over the crown (10 min) to the end of construction (20 min) resulted in crown subsidence from overburden weight. Also, the more plastic the clay, the more the subsidence. The latter is due to the lower passive resistance for the green clay compared to its orange counterpart. Because for moderate depths and deeper, Rankine passive pressure coefficient (Kp) times depth (z) is more significant than the cohesion term. Table 3 presents the resultant passive force (Pp2) on the side of the low-profile culvert at the end of construction for all three clays.

Displacement of the structures from EOC onward is due to the long-term dissipation of excess pore water pressures (consolidation). As expected, the low- and high-profile arches displaced downward due to the consolidation of the clay soil alongside the culvert. However, the semicircular arch's crown moved upward. This unexpected result may be explained from its shape at EOC as shown in Figure 5(*b*) for the high-plasticity clay. Clearly displayed is the concave outward curvature at its thrust beam (shoulder) location compared to the inward curvature of the other structures [Figures 5(*a*) and 5(*c*)] at EOC. From the end of construction onward (long term), these curvature changes are accentuated as shown in Figure 5 for all structures. The long-term consolidation deformations of the high-plasticity clays around the semicircular arch support these findings (Figure 6). The structure is moving inward more at its shoulder than outward at its springline, resulting in the crown rising.

These results agree very well with the long-term failure of a semicircular arch reported in *Engineering News Record* (*4*), in which it was stated that the crown was rising and the shoulders (thrust beam) were subsiding just before failure.

It should be noted that the semicircular arch was the only structure studied that did not have a reentrant angle at its footing. One way to alleviate the semicircular's outward curvature at its shoulder is to use a reentrant angle at its footing (i.e., instead of 180 degrees, use 200 degrees as in a horseshoe arch). The latter would ensure an increase in the inward curvature at the structure's shoulder when backfilling from the footing to its springline (*9*).

TABLE 2 Model Geometries

Culvert	Low Profile	High Profile	Semicircular
Culvert Wall Thickness	0.64 mm	0.64 mm	0.64 mm
Culvert Width (span)	15.2 cm	15.2 cm	15.2 cm
Culvert Height	6.1 cm	9.1 cm	7.6 cm
Height of Fill over Crown	8.9 cm	8.9 cm	8.9 cm
Total Height of Clay Backfill	15.0 cm	18.0 cm	16.5 cm
Height of Granular Fill over Crown	1.3 cm	1.3 cm	1.3 cm
Width of Granular Fill at Springline	3.3 cm	3.3 cm	3.3 cm

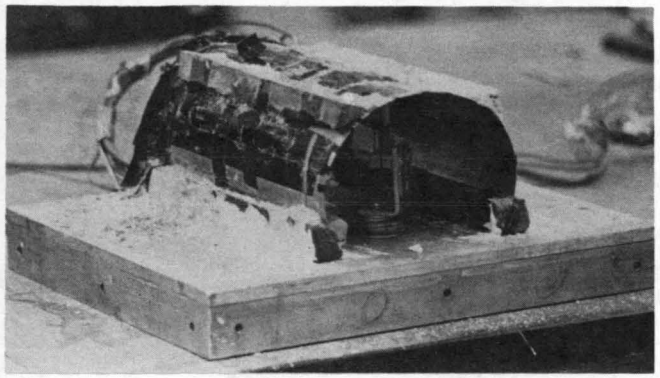

FIGURE 3 Model culvert with attached strain gauges and LVDT.

Stresses

Figure 7(*a*) shows the measured pore pressure in the orange (low plasticity) clay backfill near the springline of the low- and high-profile culverts from the end of construction onward. The decrease in pore water pressure to a constant value (hydrostatic) with time is evident and confirms the consolidation process. Also shown is an estimate of the hydrostatic pore pressure within the clay deposit at the location of the pore pressure transducer. The rise in its value with time is due to the decrease in the clay's void ratio as a result of the consolidation process. The measured pore pressure in the high-profile culvert's backfill starts and ends with higher values than the low-profile value due to its deeper clay deposit (Table 2). Consolidation effects appear to end within 100 min of model time or 210 prototype days.

Figure 7(*b*) shows the measured pore pressure in the red (medium plasticity) clay backfill near the springline of the semicircular and low-profile arches from the end of construction onward. Clearly depicted is a rise in pore pressure and then a decay toward a steady-state hydrostatic value. This rise is believed to be positive arching in which load (overburden weight above culvert) is being transferred to the clay backfill alongside the culvert's springline. This behavior was substantiated by the thrust stresses.

Shown in Figure 7(*c*) is the recorded pore pressures for the green highly plastic clay at the springline of the semicircular and high profile arches. Note the gradual rise and subsequent flattening of the curves. The rise follows the increase in hydrostatic pore pressure (as shown estimated in Figure 7(*c*)) due to a diminishing void ratio (consolidation). The largest excess pore water pressure occurs at the end of construction, suggesting that no arching is occurring. As expected, the higher the plasticity, the greater the amount of time required for dissipation (consolidation) to occur due to the soil's lower permeability.

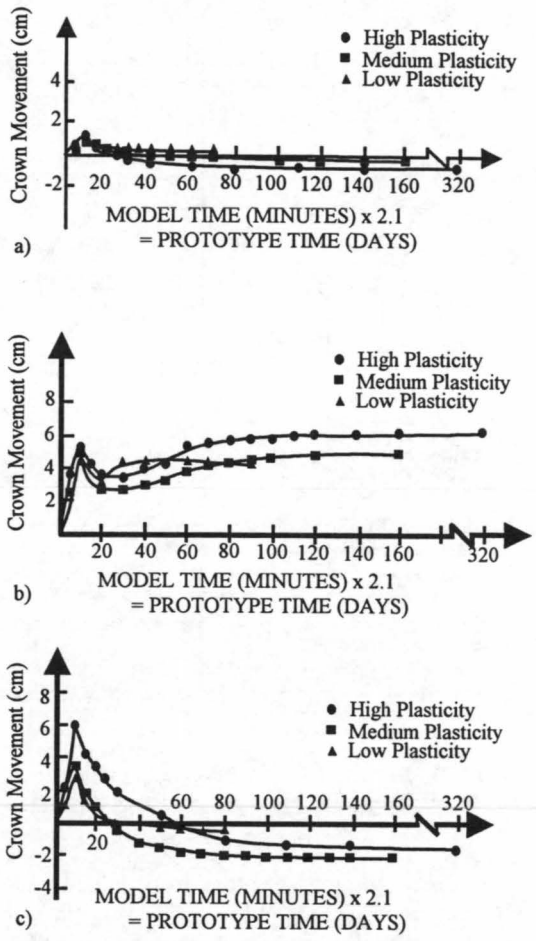

FIGURE 4 Deflection of top of culverts from beginning of construction onward: (*a*) low-profile arch; (*b*) semicircular arch; (*c*) high-profile arch.

Table 4 provides the ratios of the measured EOC and long-term (LT) thrust stresses in the wall of the culverts at their

TABLE 3 Passive Pressures

	ϕ	C (kPa)	γ (kN/m^3)	Kp	At Crown Pp1 (kN/m)	EOC Pp2 (kN/m)
Low Plasticity	38	4.79	21.49	4.20	316.33	1169.61
Medium Plasticity	34	14.36	19.85	3.54	340.31	1097.87
High Plasticity	25	28.73	19.92	2.46	365.90	1023.72

where $Pp = \int_o^H (2C\sqrt{Kp} + \gamma z Kp)\, dz$

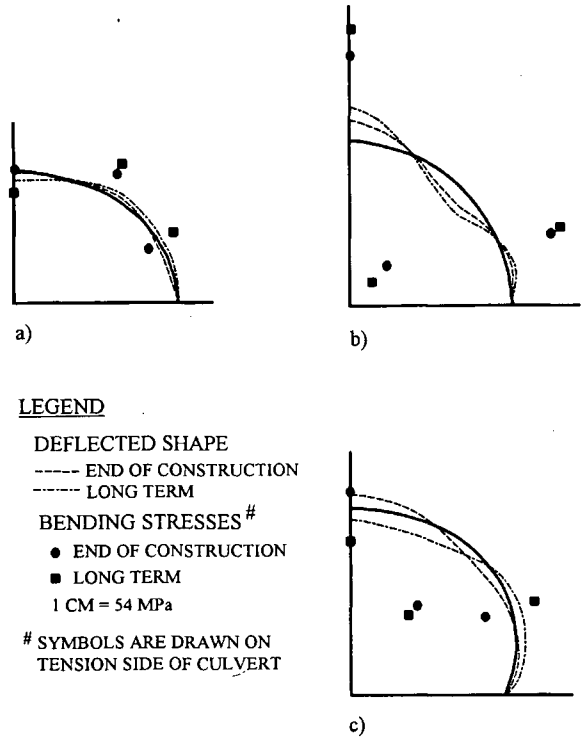

FIGURE 5 Deflected shape and bending moments in culverts: (*a*) low-profile arch; (*b*) semicircular arch; (*c*) high-profile arch.

springlines versus computed values from White and Layer (WL) (*10*) and AASHTO (*2*). White and Layer's thrust stresses are computed by multiplying the unit weight of overburden soil by the depth of fill above the culvert's crown by the culvert span divided by two. In the case of AASHTO, the thrust stress equation is the same as that of White and Layer, except that the span is replaced with twice the top arch radius of the culvert. Figure 8 plots the ratio of LT thrust stresses to those predicted by WL and the AASHTO code (AC) given in Table 4.

As is evident from Table 4, White and Layer's theory predicts very well the thrust stresses at the end of construction (all within 20 percent) and is usually conservative. The AASHTO code is more conservative (25 to 30 percent) for

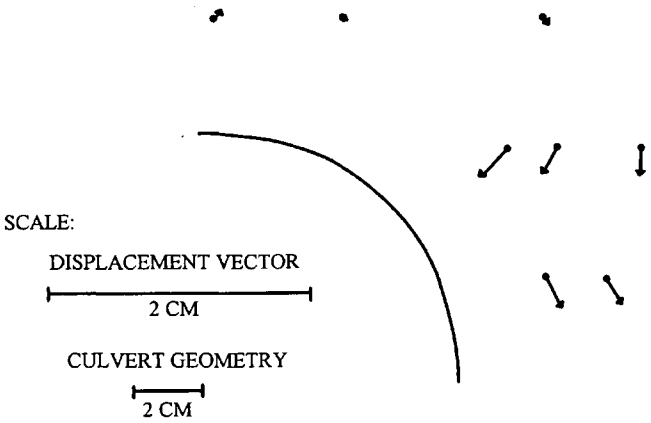

FIGURE 6 Long-term deformations in green backfill clay.

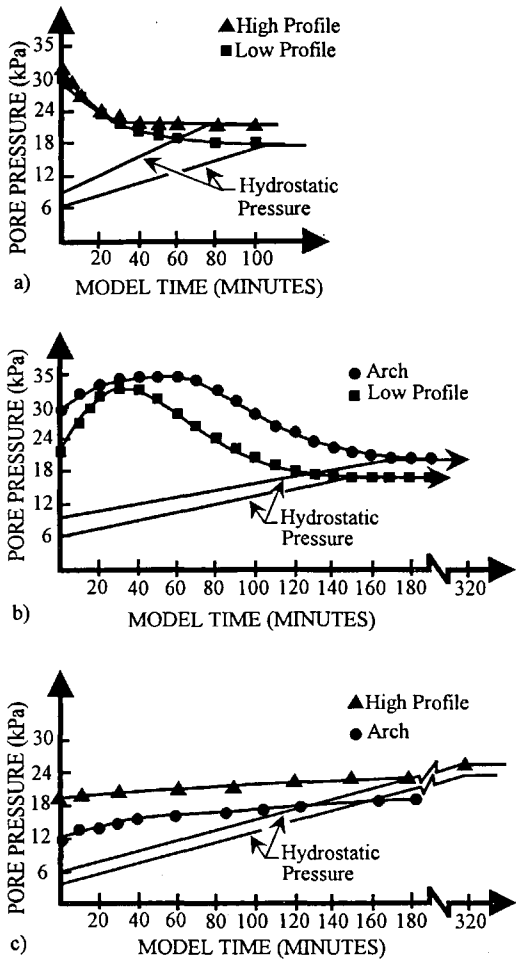

FIGURE 7 Pore water pressure at culvert springline: (*a*) low-plasticity clay; (*b*) medium-plasticity clay; (*c*) high-plasticity clay.

the low- and high-profile culverts at end of construction. Both gave the same result for the semicircular arch (unconservative ≈ 20 percent) because they both use the same radius and/or span of the structure.

In the case of the LT measured to predicted thrust stresses (see Figure 8), White and Layer's predictions for the low- and high-profile culverts were slightly unconservative (15 percent) for the low and medium plasticity clays, but very unconservative (30 percent) for the high plasticity clay. Conversely, the same structures were conservative by 15 percent for the low- and medium-plasticity clays and were within 2 percent for the high-plasticity clays by the AASHTO design. The LT response predicted by White and Layer, as well as the AASHTO code for the semicircular arch, was unconservative by 20 and 30 percent for the medium- and low-plasticity clays and by more than 50 percent for the very plastic clay.

The semicircular arch had the greatest wall thrust stresses of any structure for any soil because of its crown rising with time, which transferred soil load into the structure. As expected from the pore pressure measurements in the red clay [Figure 7(*b*)], definite positive arching occurred, which is reflected by its low thrust stresses compared to the other clays (Figure 8) for all structures.

TABLE 4 Ratio of Measured Axial Forces (EOC, LT) Versus White and Layer (WL) and AASHTO Code (AC) Values and Maximum Bending Moments for Shoulder of Culverts

Case	Struct.	Soil	EOC/WL	LT/WL	EOC/AC	LT/AC	Moment (m-kN/m)
1	low prof	orange	0.935	1.047	0.764	0.855	5311
2	low prof	red	0.923	1.015	0.754	0.829	6628
3	low prof	green	0.963	1.220	0.786	0.997	9643
4	semicirc	orange	1.187	1.305	1.187	1.305	10960
5	semicirc	red	0.848	1.198	0.848	1.198	14412
6	semicirc	green	1.019	1.510	1.019	1.510	17792*
7	high prof	orange	0.998	1.116	0.807	0.902	8994
8	high prof	red	0.831	1.038	0.672	0.840	11405
9	high prof	green	0.872	1.268	0.706	1.025	16048

* reached the yield value

The LT maximum bending moments for all nine cases are provided in Table 4. They are plotted in Figure 9(*a*) versus geometry and in Figure 9(*b*) as a function of soil plasticity (*PI*). *R* is the rise, *S* is the span and R_1/R_2 is the ratio of the culvert's top radius to its springline radius. All the values tabulated or plotted are for the thrust beam location because they were the maximum. Note the linear relationship among bending moment, culvert geometry, and soil plasticity. This latter correlation was expected because the soil's compressibility increases with liquid limit (which affects *PI*, see Table 1).

The semicircular arch had the highest moments (yielded in the case of the green clay), and the low profile had the smallest. Also, the medium plasticity soil, which had the lowest thrust stresses due to arching, had higher bending moments than the low plasticity soil because of its greater deflections due to its higher compressibility.

A comparison between EOC and long-term bending stresses are shown in Figure 5. The following expression may be used to estimate the long-term maximum bending moments given in Table 4:

$$M_b = (1.4 + .0633PI)(R/S)\sqrt{(Rs/Rt)}S^3 \text{ (soil unit wt)} \quad (1)$$

where

R = culvert height,
S = culvert span (width),
Rs = radius of curvature of the culvert side, and
Rt = radius of curvature of the culvert top.

The above expression is accurate to within 5 percent for all nine cases.

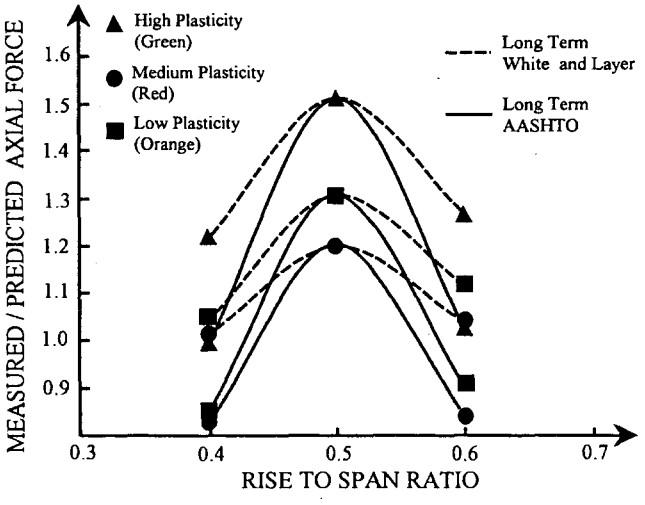

FIGURE 8 Ratio of measured to predicted axial thrust forces.

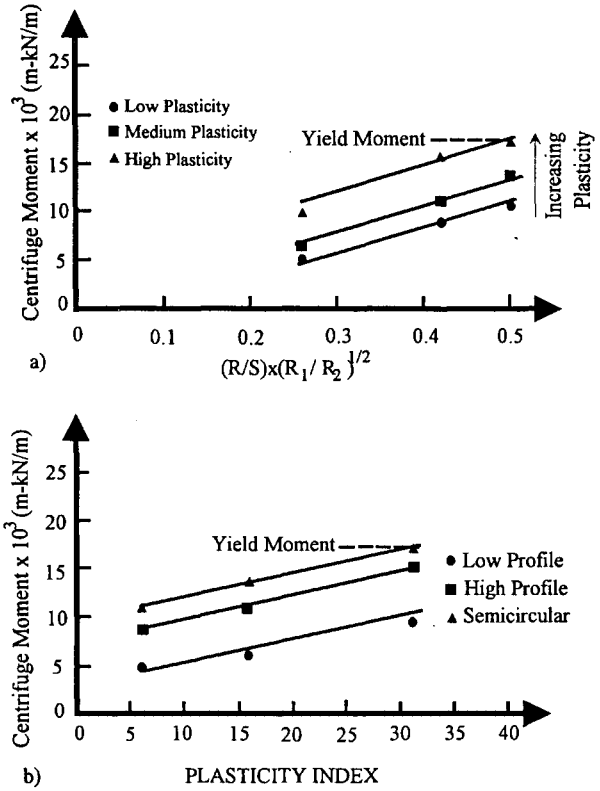

FIGURE 9 Long-term bending moments in the culverts' shoulders: (*a*) function of geometry; (*b*) function of soil plasticity.

CONCLUSIONS

The following results were concluded from this study:

- White and Layer's (*10*) method of determining wall stresses at the culvert's springline predicts very well EOC stresses when cohesive embankment soils are used. The AASHTO (*2*) code is slightly more conservative (25 to 30 percent) at the end of construction for the low- and high-profile culverts.
- The use of cohesive backfill has a definite adverse effect on the long-term response of the soil-culvert system. Maximum increases on the order of 50 percent for axial thrust and 100 percent for bending moments were observed.
- The culvert's initial shape has a significant influence on its long-term deflections and wall stresses (axial and bending).
- Because the semicircular arch has a single radius of curvature without a reentrant angle at its footing, it develops a deflected shape much different than that of the low- or high-profile arches. The long-term deflected pattern of the semicircular arch is inward at the shoulder and outward at the crown and springline (side) of the culvert, respectively. Both the low- and high-profile arches were outward everywhere except at the crown (top) of the culverts. Consequently, the mode of failure and the stresses in the semicircular versus low- and high-profile culverts are different.
- All culverts exhibited the maximum bending moment at their shoulders. The maximum moments were highest for the semicircular culvert, lower for the high-profile culvert, and lowest for the low-profile culvert. A linear relationship between maximum bending moment and plasticity index was measured (for a given culvert shape). A linear relationship also existed between maximum moment and the culvert's geometry (for a given plasticity index).
- The semicircular arch gave the greatest long-term thrust stress increase because its crown was rising (other shapes were subsiding) with time, which transferred more of the clay's overburden weight to the culvert. For a given shape, a unique relationship between soil plasticity and its axial thrust stresses did not exist. The AASHTO code (*2*) predicted conservatively (within 15 percent) the long-term axial thrust for all clays around the low- and high-profile culverts, whereas, White and Layer (*10*) predictions were 30 percent unconservative for the same structures. Both methods gave unconservative thrust stresses, 20 to 50 percent, depending on plasticity, for the semicircular arch.

Overall, the semicircular arch is not recommended when the other two shapes are available or without a reentrant angle (i.e., horseshoe culvert) at its footing in deep plastic clay backfills. Also, the designer should make every effort to use low-plasticity backfill which has high permeability and low compressibility.

Although the significance of soil type and geometry have been identified, the effects of backfill depths and the size of the granular zone around the culvert warrant further investigation before a design procedure may be established. The study should include LT wall stresses (bending and axial) as well as deformation and wall buckling. The centrifuge is an excellent means of conducting the study because of cost and the fact that the *G*-level squared speeds up the consolidation time.

ACKNOWLEDGMENTS

The support of the National Science Foundation is gratefully acknowledged. The authors also wish to express their appreciation to Habib Tabatabai and Phanio Cleanthous for their aid in constructing and recording the soil-culvert systems. Special thanks go to the reviewers, who improved the original text.

REFERENCES

1. Selig, E. T. Large Buried Metal Culvert Design and Construction. *Proc., 11th Ohio River Valley Soil Seminar on Earth Pressures and Retaining Structures*, Clarksville, Ind., 1980, pp. 13–22.
2. *Specifications—Bridges*, American Association of State Highway and Transportation Officials, Washington, D.C., 1989, pp. 186–188.
3. Scheer, A. C., and G. A. Willet. Rebuilt Wolf Creek Culvert Behavior. In *Highway Research Record 262*, HRB, Washington, D.C., 1969, pp. 1–10.
4. Culvert Failure Kills Five. *Engineering News Record*, Jan. 1983, p. 12.
5. Committee on Soil-Structure Interaction on Subsurface Conduits. Minutes. TRB, National Research Council, Washington, D.C., Jan. 1982.
6. McVay, M. C., and P. Papadopoulos. Long-Term Behavior of Buried Large-Span Culverts. *Journal of the Geotechnical Engineering Division*, ASCE, Vol. 112, No. GT4, Apr. 1986, pp. 424–442.
7. Avgherinos, P. J. *Centrifugal Testing of Models Made of Soil*. Ph.D. thesis. University of Cambridge, England, 1969.
8. Duncan, J. M., and B. R. Seed. Compaction-Induced Earth Pressures Under K_0-Conditions. *Journal of the Geotechnical Engineering Division*, ASCE, Vol. 112, No. 1, Jan. 1986, pp. 1–22.
9. Trollope, D. H., A. M. Aust, M. G. Speedie, and I. K. Lee. Pressure Measurements on Tallaroop Dam Culvert. *Proc., Fourth Australia-New Zealand Conference*, Sydney, Australia, 1963, pp. 169–184.
10. White, L. L., and J. P. Layer. The Corrugated Metal Conduit as a Compression Ring. *Proc., Highway Research Board*, Vol. 39, 1960, pp. 389–397.

Publication of this paper sponsored by Committee on Subsurface Soil-Structure Interaction.

Field Performance of Cast-in-Place Nonreinforced Concrete Pipe

CURTISS W. GILLEY AND L. H. GABRIEL

A compilation of case histories of cast-in-place nonreinforced concrete pipe (a continuous monolithic cast underground conduit for irrigation water, storm water, sewage, and industrial waste) is presented. The results of field tests corroborate the value of passive restraint at the springline. Eight field studies dating back to 1954 demonstrate the load-carrying and hydrostatic capabilities of cast-in-place concrete pipe.

The case studies of nonreinforced cast-in-place concrete pipe (CIPCP) presented encompass a period of more than 38 years of in-service field experience.

By American Concrete Institute (ACI) Specification 346 definition, "CIPCP is an underground continuous nonreinforced concrete conduit, having no joints or seams, except as necessitated by construction requirements. It is intended for use to convey irrigation water, storm water, sewage, or industrial waste under a maximum internal operating head of 45 kPa (15 ft.) and external loads . . ." (*1*).

HISTORY OF CIPCP

Although a process for cast-in-place concrete pipe was first patented in 1897, it was not until the early 1920s that the Turlock Irrigation District in California's San Joaquin Valley pioneered its commercial use. Unlike today's machine monolithic casting process, these early pipes were hand (and later, machine) cast in two semicircular segments. Undesirable cold joints appeared at springline where the two segments joined.

The first modern casting machines was used in 1949. Because the function of these pipes in that year was for irrigation water, sizes were limited to 1220 mm (48 in.) in diameter. Application to storm sewer pipelines quickly followed in the early 1950s. Today, sizes with diameters of 610 mm (24 in.) through 3048 mm (120 in.) are routinely constructed. Approximately 3500 km (2,200 mi) of CIPCP has been installed to date, with approximately 22 percent with diameters of 1372 mm (54 in.) or larger. Most of the installations are located in California, Arizona, Texas, New Mexico, Oregon, and Washington. CIPCP has also been installed in Mexico City, Mexico, and Johannesburg, South Africa.

STRUCTURAL PERFORMANCE OF CONCRETE PIPE

The dominating characteristic of a brittle material, such as concrete, is a low threshold of tensile capability. For the reliable performance of concrete pipe, either the internal tensile forces must be transferred, through bond, to tough, ductile, steel reinforcing bars of large tensile capacity or the internal tensile forces must be significantly reduced by developing a compensating force field. Precast reinforced concrete pipe (RCP) is an example of the former; nonreinforced CIPCP is an example of the latter.

When responding to the application of loads, the pipe wall internal reacting forces of shear, in-plane thrust (wall thrust), and bending moment (wall bending) all contribute to the composite stress response. For rigid structures, such as concrete pipe, secondary stress effects due to deflections are assumed negligible; the deformed structure lies well within the bounds of small deflection theory.

The in-plane circumferential stress of wall thrust may be added arithmetically to the flexural stress of wall bending because both forces result in parallel stress fields that track the wall circumference. A properly designed and constructed CIPCP will enjoy an increase in the favorable wall thrust and a decrease in the unfavorable wall bending so as to mask, or nearly mask, the wall-bending tensile stress to which concrete is vulnerable. This is accomplished by the self-induction of passive lateral forces in the vicinity of springline when the lengthening horizontal diameter (under increasing load) engages the stiff walls of the trench which previously served as forms for the casting of the pipe. This is not unlike the way an arch structure develops lateral reaction forces at the supports, which serves to increase internal thrust and decrease internal bending. RCP, which does not enjoy the full benefits of the compensating effects of lateral support at springline, utilizes reinforcement to engage the high tensile stresses that result from wall bending.

CONSTRUCTION PROCEDURES

The first step in the construction process is to excavate a trench with vertical side walls and a round bottom, shaped with a round bottom bucket attached to a tracked excavator or backhoe. [For further information, see the Lynch Manual (*2*) pipe and trench detail, Figure 1, and Table 1.] Alignment is laser controlled.

The pipe casting machine (Figure 2) is placed in the trench, and its motor-driven winch system (Figure 3) is secured to an installed trench anchor. At the start of the process, and continuing in pace with the advancing casting machine, loose metal top forms shaping and containing the upper 270 degrees are positioned to receive concrete. Through a hopper that is integral with the casting machine, a low-slump 25- to 76-mm

C. W. Gilley, Tremont Equipment Co., Inc., 6940 Tremont Road, Dixon, Calif. 95620-9603. L. H. Gabriel, School of Engineering, California State University, 6000 J Street, Sacramento, Calif. 98519-2694.

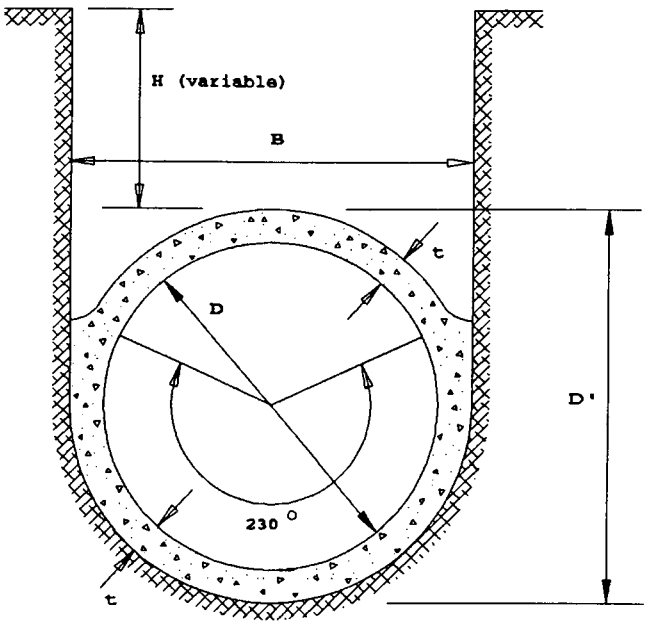

FIGURE 1 Typical cross section of cast-in-place concrete pipe [610–3048 mm (24–120 in.)].

(1- to 3-in.) concrete of modest strength with a minimum 28-day strength of 20.7 MPa (3,000 psi) is placed, tamped, and vibrated to achieve full consolidation. A polyethylene blanket is often used for accelerated curing. Under typical conditions, the production rate ranges from 30 m (100 ft) to 7 m (23 ft) per hour depending on the size, 610-mm diameter to 3048-mm diameter, of the pipe.

After 6 hr, the top forms may be removed. When the concrete achieves a strength of 17.2 MPa (2,500 psi), usually in 2 to 3 days, trench backfilling may begin. Circumferential shrinkage cracks, which are best understood to be joints in the continuously cast pipe, will appear every 7.6 m (25 ft) to 15.2 m (50 ft), or more, depending on curing conditions, the quality of the concrete, and trench moisture conditions. The cracks have no structural significance and need only to be grouted to prevent infiltration, if such is a consideration.

DESIGN CONSIDERATIONS

The following ACI (*1*) engineering design procedure yields a statement of the stress in the pipe wall.

Marston earth loads for the trench conditions are used to define vertical dead loads. Appropriate AASHTO highway loads, FAA aircraft loads, and Cooper rail loads define the live loads. Compensating lateral loads (see section on Structural Performance of Concrete Pipe) are taken conservatively as Rankine active pressures, a significant underestimate of the passive pressures known to be working when the stiff lateral walls are engaged by the pipe. The pipe dead load, the weight of the water in the pipe, and hydrostatic heads may be included as required.

Moments and thrusts may be computed using coefficients developed by Paris (*3*) or Roark compiled by Young (*4*). Stresses at critical points of tension (at crown, invert, and springline) are calculated in appropriate units from the following interaction formula:

$$f = (6M/t^2) - (T/t)$$

TABLE 1 Dimensions of Cast-in-Place Concrete Pipe

NOMINAL DIAMETER (Interior)		OUTSIDE DIAMETER (Depth)		WIDTH OF PIPE/TRENCH (Nominal)		WALL THICKNESS (Minimum)	
D		D'		B		t	
mm	inches	mm	inches	mm	inches	mm	inches
610	24	762	30	787	31	76	3.0
686	27	838	33	864	34	76	3.0
762	30	914	36	940	37	76	3.0
914	36	1092	43	1118	44	89	3.5
1067	42	1270	50	1295	51	102	4.0
1219	48	1473	58	1499	59	127	5.0
1372	54	1651	65	1676	66	140	5.5
1524	60	1829	72	1854	73	152	6.0
1676	66	2007	79	2032	80	165	6.5
1829	72	2184	86	2210	87	178	7.0
1981	78	2362	93	2388	94	191	7.5
2134	84	2540	100	2565	101	203	8.0
2438	96	2896	114	2921	115	229	9.0
2743	108	3277	129	3302	130	267	10.5
3048	120	3658	144	3683	145	305	12.0

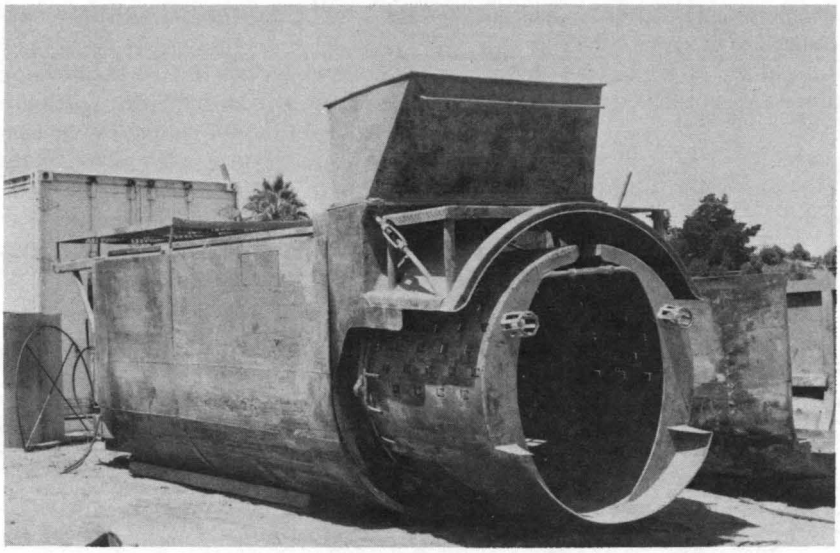

FIGURE 2 Pipe casting machine.

where

M = moment per unit length of pipe (N·m/m),
t = thickness (mm),
T = circumferential thrust per unit length of pipe (m), and
f = stress (MPa).

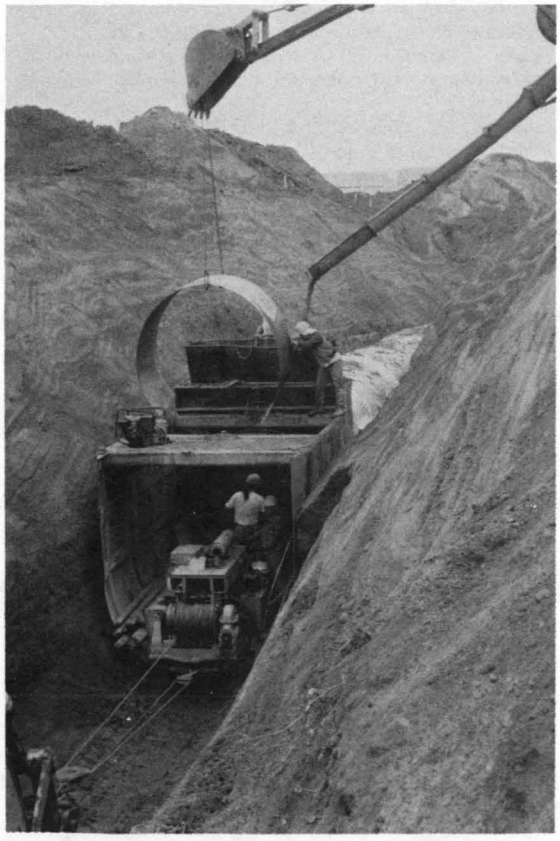

FIGURE 3 Pipe case in prepared trench.

Alternatively, a stress analysis may be obtained from finite element studies, such as CANDE, wherein a round pipe of constant wall thickness may be used to approximate the configuration shown in Figure 1.

FIELD PERFORMANCE STUDIES

The following is a list of studies known to the authors that illustrate the structural performance of CIPCP.

1. Gravity load test performed by Fortier (*5*), 1954, Fresno, California; pipe diameter = 762 mm (30 in.); soil type, sandy loam/silica with cemented hardpan; f'_c = 15.2 MPa (2,200 psi); loading with modified ASTM sand box; visual observation for distress.

Test and results: A 4-ft section was loaded to 288 kN (43,000 lbf). There was no visible cracking.

2. Hydrostatic load test by Fortier (*5*), 1954, Fresno, California; pipe diameter = 762 mm (30 in.); soil type, sandy loam/silica with cemented hardpan; f'_c = 15.2 MPa (2,200 psi); hydrostatic loadings; instrumented with Type IDP marsh gauge with a pressure range of 0 to 0.69 MPa (0 to 100 psi).

Test and results: A 13-ft test section was bulkheaded and hydrostatically loaded. A pipe rupture occurred at 229 kPa (33.2 psi) or 23.4 m (76.7 ft) of head.

3. Shallow burial test by Johnson and Hess (*6*), 1963, Tucson, Arizona; pipe diameter = 1219 mm (48 in.); in situ soil type, cemented sand and gravel; compacted fill around pipe at 100 percent compaction (ASTM T–180), 228 kg/m^3 (143 pcf); cover, 0.15 m (0.5 feet); f'_c = 27.5 MPa (4,000 psi); truck axle and wheel loads; instrumented with strain gauges, dial gauges, and Carlson pressure cells.

Test and results: A maximum wheel load of 125 kN (28,000 lbf) was applied. No distress was observed visually or by instruments.

4. Shallow burial, early live load field test by Gabriel (*7*), 1964, Sacramento, California; pipe diameter = 1830 mm (72 in.); in situ soil type, partially cemented sandy silt; cover, 300

mm (12 in.); 3-day f'_c = 10.3 MPa (1,500 psi); truck axle loads; instrumented with deflection gauges.

Test and results: An axle load of 142 kN (32,000 lbf) was applied after 3 days. No distress was observed visually or by instruments.

5. Field load test by Gabriel (*8*), 1967, Sacramento, California; pipe diameter = 2134 mm (84 in.); in situ soil type, caliche hardpan; f'_c = 20.7 MPa (3,000 psi); early live loads with compaction equipment; instrumented with strain gauges and deflection gauges.

Test and results: Backfilled to 3.7 m (12 ft) and compacted with standard equipment 4 days after pipe was cast. No distress was observed visually or by instruments.

6. Shallow burial load test by Lum (*9*), 1969, Honolulu, Hawaii; pipe diameter = 610 mm (24 in.); in situ soil, stiff red clayey silt; 7-day f'_c = 22.7 MPa (3,292 psi); cover, 0.3 m (1 ft) over CMP, 0.0 to 0.3 m (0 to 1 ft) over concrete pipes; tractor-scraper wheel loads; instrumented with deflection gauges.

Test and results: A 200-kN (45,000-lbf) wheel load was moved over CIPCP, RCP (Class IV), and CMP. No distress was observed in concrete pipes; deflection of RCP was 8 to 10 times that of CIPCP. Large vertical and horizontal deflections of CMP were visually observed.

7. Zero cover static load tests and shallow cover, 0.3 m (1 ft), for dynamic tests by White and Underwood (*10*), Dallas, Texas, 1969; pipe diameter = 2440 mm (96 in.); f'_c = 40.9 MPa (5,920 psi); soil type, clayey sand; sand boxes (static tests) with hydraulic jacks, dynamic loads with falling weights; instrumented with strain and deflection gauges.

Tests and results: Static loads up 912 kN (205,000 lbf) were applied; no cracks were observed visually or by instruments. Dynamic loads up to 65 kN-M (48 ft-kps) were applied; no cracks were observed visually or by instruments.

8. Shallow burial field load test by Gabriel et al. (*11*), 1987–1988, Sacramento, California; pipe diameter = 1830 mm (72 in.); in situ soil type, hard silty clay; f'_c = 27.6 MPa (4,000 psi); cover: 0.5 m (20 in.); compaction equipment loading; instrumented with strain gauges, dial gauges, and pressure cells.

Test and results: Deflections and strains successfully measured the effects of 2+ times H2O loading. Instruments sensed a possible crack; however, none were observed visually.

CONCLUDING REMARKS

The success of CIPCP, as shown in the preceding section, offers evidence that when passive trench wall forces in the vicinity of the springline may be counted upon to develop an archlike response in the pipe to vertical loads, tensile stresses are kept below the cracking threshold. This permits economically efficient use of unreinforced concrete for culverts, pipelines, and other underground structures.

REFERENCES

1. *Recommendations for Cast-in-Place Nonreinforced Concrete Pipe*. ACI 346R–90. American Concrete Institute, Detroit, Mich.
2. *Cast-in-Place Concrete Pipe Process* (Lynch Manual). Tremont Equipment Co., Inc., Dixon, Calif., 1990.
3. Paris, J. M. Stress Coefficients for Large Horizontal Pipes. *Engineering News-Record*, Vol. 87, No. 19, Nov. 10, 1921, pp. 768–771.
4. Young, W. C. *Roark's Formulas for Stress and Strain*, 6th ed. McGraw-Hill Book Co., 1989.
5.* Fortier, E. C. *Tests on 30-inch No-Joint Concrete Pipe*. Unpublished report. Fresno, Calif., June 1954.
6. Johnson, M. A., and J. D. Hess. Load Testing of No-Joint Cast-in-Place Concrete Pipe, In *Highway Research Record 30*, HRB, National Research Council, Washington, D.C., 1963, pp. 20–40.
7.* Gabriel, L. H. *Load Testing of 72-Inch No-Joint Cast-in-Place Concrete Pipe with Shallow Cover*. Unpublished report. Sacramento State College Foundation, Sacramento, Calif., 1964.
8.* Gabriel, L. H. *A Study of Displacements of No-Joint 84-inch Cast-in-Place Pipe Soon After Construction*. Unpublished report. Sacramento State College Foundation, Sacramento, Calif., 1967.
9.* Lum, W. *Report of No-Joint Concrete Pipe Field Test Demonstration—Strength of 24-inch Pipe at Mililani Subdivision*. Unpublished report. Honolulu, Hawaii, Mar. 1969.
10.* White, A., and A. C. Underwood. *Field Sand Box Tests*. Unpublished report. Underwood and Associates, Houston, Tex., 1969.
11.* Gilley, C., L. Gabriel, and R. Standley. Field Test of 72 in.-Diameter Cast-in-Place Nonreinforced Concrete Pipe. Paper No. 26533. *Journal of Transportation Engineering*, ASCE, Vol. 118, No. 1, Jan./Feb. 1992.

**Copies of unpublished reports are available from Tremont Equipment Co., 6940 Tremont Road, Dixon, Calif. 95620-9603.*

Publication of this paper sponsored by Committee on Subsurface Soil-Structure Interaction.

Postfailure Behavior of Buried Pipe

MEHDI S. ZARGHAMEE

A study of the postfailure behavior and the safety of buried pipe is presented. A method based on soil-structure interaction is developed for the postfailure analysis. This method is applied to a deeply buried prestressed concrete pipe after complete loss of prestressing. The analysis is performed at two different cross sections along the pipeline. In one, the pipe is under open water and thus submerged; in the other, the pipe is inland, away from open water. The results of the analysis show that the soil surrounding the buried pipe can provide sufficient support to prevent high compressive stresses and excessive deformations, even after the pipe becomes a mechanism. Consequently, the failed pipe does not collapse.

Deeply buried prestressed and reinforced concrete pipe can fail after installation, and the failed pipe alone may not have the necessary strength to support the design loads. However, the pipe-soil system may be able to support the external loads. The solution to this problem may prolong the use of apparently failed pipelines or ensure the safety of persons working inside to rehabilitate the pipeline.

Buried pipe before failure resists the external loads acting on it by axial and bending strengths. Overload or loss of strength of a buried pipe through loss of prestressing or reinforcing, for example, may result in crack formation in the pipeline. In the case where the cracks first form at the invert and crown of the pipe, the cracking makes the pipe more flexible, and the deflection of the pipe increases. Accompanying the additional deflection of the pipe, the bending moment at the springline increases until cracks are formed at the springline. The pipe, having developed a mechanism, deforms into the soil until either a stable configuration is reached, with the pipe wall stress resultants in the uncracked quadrants below the cracking strength, or new cracks form in these quadrants.

This paper presents a method based on soil-structure interaction to analyze the postfailure behavior of buried pipe and applies the method developed to a practical problem.

METHOD OF APPROACH

The method of approach adopted in this study is based on (*a*) developing a procedure to predict the postcracking behavior of the pipe wall subjected to axial thrust and bending moment and (*b*) developing soil-structure interaction models that can predict the postfailure behavior of the buried pipe. The analysis was performed on a prestressed concrete pipe. The pipe wall construction is shown in Figure 1. The postcracking behavior of prestressed concrete pipe may be predicted using the procedures developed to analyze prestressed concrete pipe and by appropriately modifying the computer program UDP [Unified Design Procedure (*1*)] developed for this purpose. The soil-structure interaction analysis is performed by modifying the finite-element computer program SPIDA [Soil-Pipe Interaction Design and Analysis (*2*)] developed for studying soil-pipe interaction.

UDP computes the stresses and strains in the wall of a prestressed concrete cylinder pipe subjected to combined effects of moments and thrusts. The program considers the tensile softening and cracking of concrete in tension, the nonlinear stress-strain relationship for concrete in compression, cylinder yield in tension, and the nonlinear stress-strain relationship of prestressing wire in tension.

SPIDA discretizes the pipe into beam elements and both the in situ soil and the constructed backfill around the pipe into quadrilateral and triangular elements. The program performs an incremental analysis as backfill is placed in layers. Each soil element has a hyperbolic stress-strain relationship (*3*) that expresses the behavior of the soil up to failure. The values of soil parameters used in the model for each soil type are based on the experimental study of Selig (*4*). The validity of the model has been checked by comparing the calculated horizontal and vertical pipe deflections with the available test results on concrete pipe. [The model with Selig soil parameters was used to develop a new installation design basis for buried concrete pipe (*5*).] The soil types were selected based on the study of the actual soil investigation at the site, including the results of nearly 40 boring logs. The program considers the actual geometry of the trench or embankment, applies the constructed soils in layers, computes the incremental strains and stresses in both the pipe and the soil resulting from each soil layer, and superimposes the increment stresses to obtain the final stresses.

SPIDA was modified to handle postcracking behavior of the previously installed pipe after loss of prestress. Obviously, as the pipe loses prestress, its moment capacity decreases, and cracks develop at its invert, crown, and springline. Consequently, there will be significant redistribution of moments, as well as additional deformation of the pipe wall into the soil at springline. Failure of the pipe-soil system occurs by excessive deformation of the installed pipe.

The following changes were made to simulate the effects of the cracking of the pipe at invert, crown, and springline that may occur after installation is complete and prestress has been lost:

- After the installation of the pipe and introduction of water to the exterior of the empty pipe, if the invert or crown moments exceed the pipe moment capacities, plastic hinges are introduced at the invert and crown. The negative of the dif-

Simpson Gumpertz & Heger Inc., 297 Broadway, Arlington, Mass. 02174-5310.

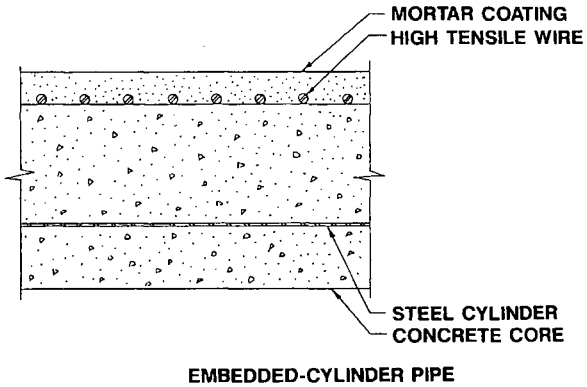

FIGURE 1 Cross section of pipe wall.

ference between the uncracked moment and moment capacity of the section for the existing thrust is applied to the pipe and the pipe-soil system is analyzed. This load increment will increase the springline moment and pipe deflection.

- If the moment at the springline exceeds the pipe moment capacity, new hinges are introduced at the springline and the negative of the difference between the uncracked moment and moment capacity is applied to the pipe in nine load increments and the resulting pipe-soil systems are analyzed. Because the pipe with four hinges is a mechanism, significant soil movement is expected to take place. Under these conditions, the thrusts at the crown and invert will increase as the pipe moves into the soil at the springline; simultaneously, the thrust at the springline will decrease. A large number of increments is used to prevent the numerical problems that result from excessive soil deformation.

In addition to the above changes, SPIDA was modified to incorporate the effect of water outside an empty pipe after the installation. In particular, the following changes were made:

- The soil weight was reduced to account for the buoyancy effect.
- The pipe weight was reduced to account for the buoyancy effect of the solid cross section of the pipe.
- The negative effect of water weight was applied to account for the emptiness of the pipe in water.
- A uniform water pressure was applied to the exterior of the pipe to account for the effect of the water height above the pipe.

APPLICATION

The foregoing procedure was applied to analyze an empty 2743-mm (108-in.) diameter embedded-cylinder prestressed concrete pipe. The pipeline was deeply buried and submerged and passed under a channel. The pipe had a 178-mm (7-in.) thick concrete core, a 16-gauge embedded steel cylinder with an outside diameter of 2858 mm (112.5 in.), and a 25-mm (1-in.) thick mortar coating applied on the exterior of core after prestressing.

The pipeline suffered one or two failures. An inspection of a limited part of the pipeline at the failure site revealed several 1.3-mm (1/20-in.) wide, 0.6-m (2-ft) long longitudinal cracks. Based on these observations, it was concluded that prestressing may have already been lost over a significant part of pipe circumference and length. A 55-m (180-ft) segment of the pipeline under the channel was subjected to internal inspection by a remotely controlled video camera. The inspection revealed a score of 0.6-m (2-ft) long longitudinal cracks at or near the invert, crown, and springline and one circumferential crack.

The pipe was subject to a hypothetical assumption of total loss of prestress, but the embedded steel cylinder was intact and watertight. The pipe, having lost all prestressing, would develop cracks wherever the moment exceeded the moment capacity. The results of analysis for two sections of the pipeline are presented here: one under the open water of the channel (Station A) and the other inland (Station B).

Moment Capacities of Pipe Wall after Loss of Prestress

A prestressed concrete pipe wall cross section at the invert or crown subjected to a fixed axial compressive thrust and a gradually increasing positive bending moment (i.e., producing tension inside the pipe) is considered. The pipe was assumed to have lost all its prestressing wires. The increasing bending moment first causes tension inside the pipe followed by tensile softening and microcracking and finally by visible cracking of the inner core. The steel cylinder, initially under compressive residual stresses resulting from creep and shrinkage of the core, would lose its prestress with increasing bending moment. With sufficient bending moment, the cylinder would go into tension, straighten, and detach from the outer core. From then on, the inner core and the cylinder did not contribute to the stiffness or to the strength of the section. The moment capacity was derived mainly from the eccentricity of the thrust within the pipe wall cross section.

The moment capacities at invert and crown were computed for different compressive axial thrusts at these sections. The variation of the bending moment at the onset of tension in the cylinder and the ultimate strength after the cylinder had pulled away from the outer core were computed and are shown in Figure 2. The variation of the ultimate moment capacity at the springline was computed based on the compressive strength of the inner core, accounting for the tension in the cylinder. The results are shown in Figure 3. The moment capacity increased with the compressive axial thrust at the springline.

Analysis of Submerged Pipe at Station A

The installation condition of the pipe at Station A and the soil types used in the model and compaction levels are shown in Figure 4. The major characteristics of this installation were as follows:

- The pipe invert is at Elevation −22.0 m (−72.0 ft).
- The in situ soil in the trench walls and under the pipe bedding was very stiff clay.
- The bedding consists of crushed stone or processed gravel, or a combination thereof, that was sized to be retained on a 10-mm (3/8-in.) sieve and to pass a 19-mm (3/4-in.) sieve.

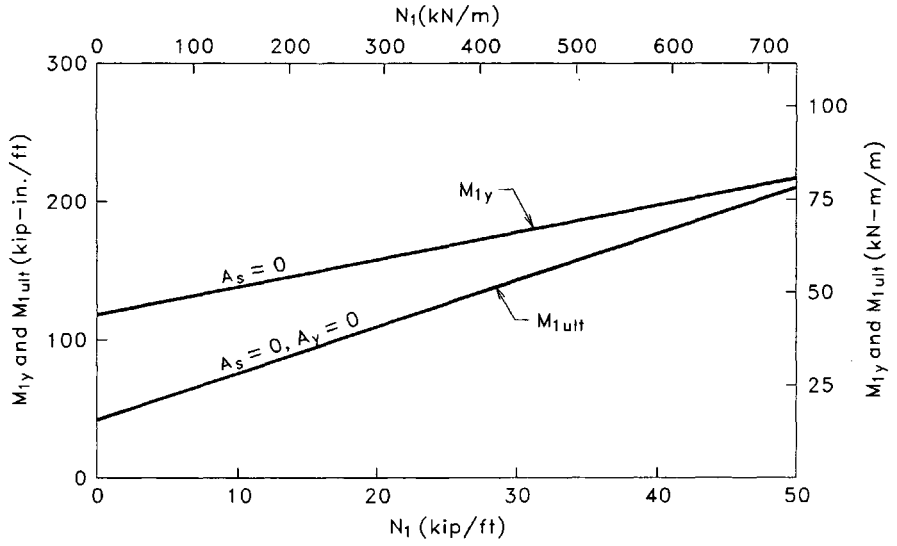

FIGURE 2 Variation of bending moment at onset of tension in steel cylinder, M_{1y}, and ultimate moment capacity, M_{1ult}, with axial thrust at invert and crown, N_1, calculated for the special case of zero wire area, $A_s = 0$, and zero steel cylinder area, $A_y = 0$.

- The backfill in the pipe zone is natural or processed sand with no more than 15 percent passing a No. 200 sieve and 100 percent passing a 10-mm (⅜-in.) sieve.
- A soft soil support was assumed to exist in the haunches of the pipe.
- A 0.15-m (6-in.) thick concrete mat was placed over the backfill.
- The rock fill placed over the concrete mat in the trench was well graded, 25 mm (1 in.) to 305 mm (12 in.) with a minimum of 50 percent to be retained on a 152-mm (6-in.) sieve.
- The bedding, the backfill in the pipe zone, and the rock fill were placed by the tremie method.
- The mud was assumed to extend from the top of rock fill to Elevation −3.0 m (−10.0 ft), that is, about 16 m (52 ft) above the top of the pipe.
- The water level was at Elevation +0.9 m (+3.0 ft).

The results of analysis for the empty pipe with total loss of all prestressing wires are summarized in Tables 1 and 2. The results show that both the invert and the crown of the pipe, after the loss of all prestressing wires, developed cracks. The cylinder would go into tension, straighten, and then separate from the outer core. The installation bending moments in excess of the moment capacity at the invert and the crown would shift to the springline and cause the pipe wall to crack

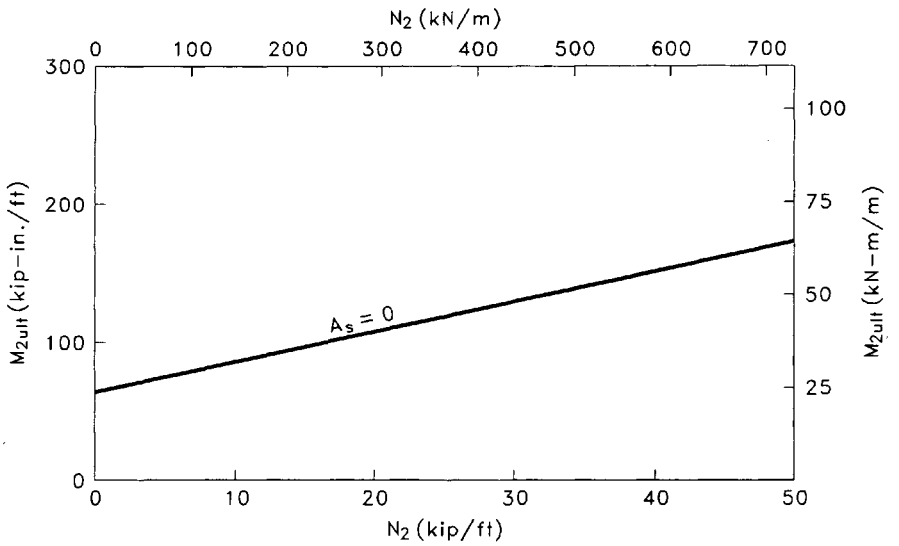

FIGURE 3 Variation of ultimate bending moment capacity, M_{2ult}, with axial thrust at springline, N_2, for the special case of zero wire area, $A_s = 0$.

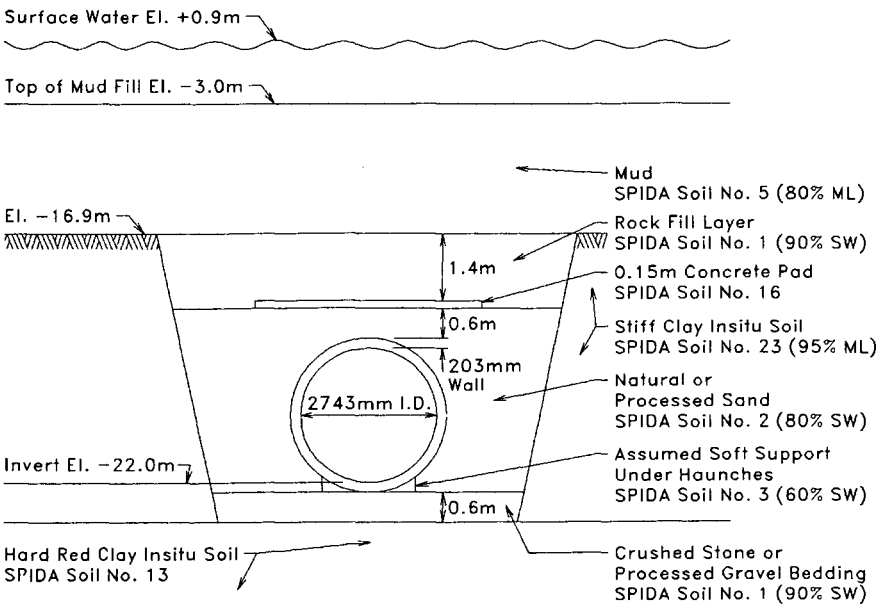

FIGURE 4 Installation condition of submerged pipe at Station A (standard proctor compaction values and soil types are shown in parentheses).

TABLE 1 Calculated Pipe Deformations at Stations A and B Before Cracking (with Prestress) and After Cracking (with No Prestress)

	At Station A		At Station B	
	Vertical mm (in.)	Horizontal mm (in.)	Vertical mm (in.)	Horizontal mm (in.)
Before cracking	14 (0.56)	13 (0.52)	5 (0.21)	5 (0.20)
After cracking				
Without concrete mat	29 (1.13)	101 (4.00)	–	–
With concrete mat	37 (1.46)	64 (2.52)	34 (1.35)	47 (1.85)
After backfill migration into bedding	39 (1.53)	82 (3.21)	–	–
With softer insitu clay for saturation effect	47 (1.85)	74 (2.91)	38 (1.49)	47 (1.86)

TABLE 2 Calculated Pipe Deformations at Stations A and B Before Cracking (with Prestress) and After Cracking (with No Prestress)

	At Station A		At Station B	
	Thrust kN/m (kip/ft)	Moment kN-m/m (kip-in./ft)	Thrust kN/m (kip/ft)	Moment kN-m/m (kip-in./ft)
Before Cracking				
Invert	393 (26.9)	198 (534)	66 (4.5)	70 (188)
Crown	354 (24.2)	149 (399)	115 (7.9)	53 (144)
Springline	703 (48.1)	138 (371)	245 (16.8)	58 (156)
After Cracking				
Invert	454 (31.1)	56 (150)	88 (6.0)	24 (65)
Crown	428 (29.2)	53 (143)	139 (9.5)	28 (75)
Springline	639 (43.7)	60 (162) 71 (132)	240 (16.4)	38 (100)

1 k/ft = 14.612 kN/m; 1 k-in./ft = 0.3711 kN-m/m

at the springline. As cracks developed at the springline, the pipe deformed into the soil; the thrusts at the invert and the crown increased from 393 and 354 kN/m (26.9 and 24.2 kips/ft) to about 454 and 427 kN/m (31.1 and 29.2 kips/ft), respectively, and the thrust at the springline decreased from 703 kN/m (48.1 kips/ft) to about 639 kN/m (43.7 kips/ft). In this process, the pipe underwent diametrical deformation of about −37 mm (−1.46 in.) vertically and +64 mm (+2.52 in.) horizontally. (The plus sign indicates an increase in the diameter of the pipe.) Note that the calculated pipe deflections do not account for the creep of pipe material, the creep of backfill and in situ soil, and the migration of backfill material. The effect of the creep of pipe is expected to be negligible. The backfill is sand and is not expected to creep. A discussion of the effect of migration of the backfill into the gravel bedding follows separately.

The moment capacity at the invert, with a thrust of 454 kN/m (31.1 kips/ft), was about 56 kN-m/m (150 kip-in./ft). The moment capacity at the crown, with a thrust of 427 kN/m (29.2 kips/ft), was 53 kN-m/m (143 kip-in./ft). The moment capacity at the springline, with a thrust of 639 kN/m (43.7 kips/ft), was about 60 kN-m/m (162 kip-in./ft). After moment redistribution, the bending moment just below the springline was 71 kN-m/m (192 kip-in./ft) and therefore exceeded the moment capacity of 60 kN-m/m (162 kip-in./ft). Additional cracking was expected just below the springline. The additional redistribution and the resulting increase in the horizontal diameter of the pipe are not reported here for the sake of brevity.

The gravel bedding may allow the sand backfill to migrate away from the soil and loosen the sand support underneath the pipe. To investigate the sensitivity of the installed pipe to migration of backfill underneath the pipe into the gravel bedding, the compaction level of the column of the soil underneath the pipe and just outside of the assumed standard soft haunches was reduced to 60 percent of the maximum density, as tested by the Standard Proctor method (ASTM D698-64T). The results show that under such a condition, the diametrical deformation of the pipe increased in magnitude from −37 mm (−1.46 in.) to −39 mm (−1.53 in.) vertically and from +64 mm (+2.52 in.) to +82 mm (3.21 in.) horizontally.

The concrete mat over the pipe played a very important role in diverting the earth load away from the pipe. In the absence of the concrete mat, the diametrical deformation of the pipe would be −29 mm (−1.13 in.) vertically and +102 mm (+4.00 in.) horizontally. Note that by omitting the concrete mat, the resulting increase in the horizontal deformation would have been 59 percent.

Because the saturated condition in the stiff clay may lower the soil modulus, a sensitivity analysis was performed by reducing the in situ soil modulus from that which corresponds to 95-percent maximum density, as tested by the Standard Proctor method to 90 percent, while the constructed soil moduli remained unchanged. The results show that the deflection of the pipe increased in magnitude from −37 mm (−1.46 in.) to −47 mm (−1.85 in.) vertically and from 64 mm (2.52 in.) to 74 mm (2.91 in.) horizontally. Note that the increase in the horizontal diametrical deformation is 15 percent.

Analysis of Inland Pipe at Station B

A second pipe installation along the same pipeline was analyzed. In this installation because the pipe was under groundwater but not under open water, a rupture of the pipe would not cause a rapid inflow of water, thus endangering personnel in the pipe.

The installation condition at Station B and the soil types used in the model and compaction levels are shown in Figure 5. The major characteristics of this installation were as follows:

- The pipe invert was at Elevation −4.7 m (−15.5 ft).
- The in situ soil in the trench walls and under the pipe bedding was sandy clay or soft sandy clay with silt seams, and organic with clay seams.
- The bedding was 0.9 m (3 ft) total below the pipe invert and consisted of 0.45 m (1.5 ft) of cement-stabilized sand. The cement-stabilized sand consisted of a mixture of 3.2 sacks

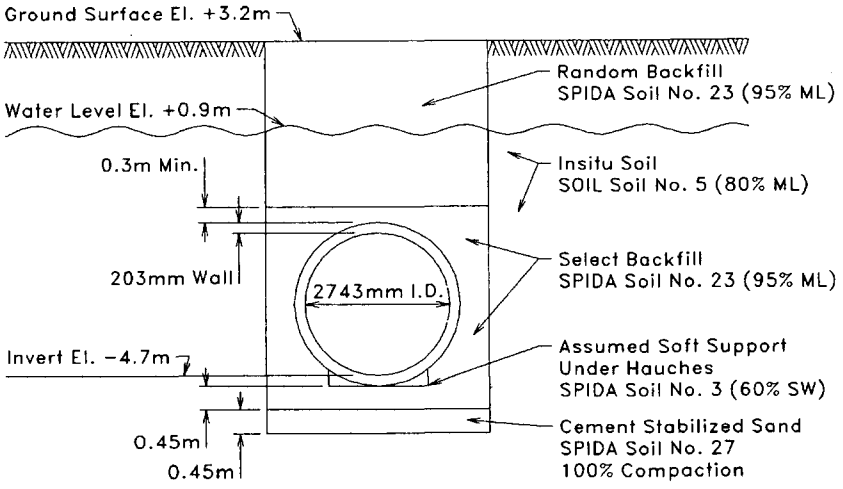

FIGURE 5 Installation condition of in-land pipe at Station B (standard proctor compaction values and soil types are shown in parentheses).

of cement/m³ (2.5 sacks of cement/yd³) of natural sand with liquid limit (LL) of 25 or less, plasticity index (PI) of 4 or less, and with less than 50 percent passing a No. 200 sieve. The cement-stabilized sand was applied over the undisturbed trench bottom. The remaining thickness of bedding consisted of select backfill material with LL, PI, and the gradation as described above.

- The backfill in the pipe zone was natural sand with LL, PI, and gradation as described above.
- A soft support was assumed to exist in the haunches of the pipe. This was a conservative assumption made to simulate the probable lack of adequate compaction in the haunches of the pipe, even though the installation was in a dry trench.
- The bedding and backfill material in the pipe zone were placed in loose lifts of 0.2 m (8 in.) or less and were compacted to 60 percent relative density (ASTM D2049-64T) or to 95 percent of maximum density as tested by the Standard Proctor method.
- The random backfill applied over the backfill in the pipe zone consisted of clays, sandy clays, and clayey sands obtained from the material excavated and compacted to 95 percent of maximum density as tested by the Standard Proctor method.
- The water level is at Elevation +0.9 m (+3.0 ft). Below this elevation, the soil weight and the pipe weight were reduced for the buoyancy effect and the external water pressure was applied to the pipe. Above this elevation, the actual weights of the random fill were used.

The results of the analysis for the empty pipe after loss of all prestressing wires are summarized in Tables 1 and 2. The results show that the pipe cracked at the invert and the crown. The cylinder at the invert and the crown went into tension and thus pulled away from the outer core. The installation bending moment in excess of capacity at the invert and the crown shifted to the springline and cracked the pipe wall at the springline. The cracked pipe deformed into the backfill. The thrust at the crown and invert increased from 66 to 115 kN/m (4.5 and 7.9 kips/ft) to 88 and 139 kN/m (6.0 and 9.5 kips/ft), respectively, and the thrust at the springline decreased from 245 to 240 kN/m (16.8 to 16.4 kips/ft).

The moment capacities at the crown and the invert were about 24 and 28 kN-m/m (65 and 75 kip-in./ft), corresponding to the thrusts of 88 and 139 kN/m (6.0 and 9.5 kips/ft), respectively. The moment capacity at the springline, which was about 37 kN-m/m (100 kip-in./ft) for a thrust of 240 kN/m (16.4 kips/ft), was also exceeded. The diametrical deformation of the pipe was −34 mm (−1.35 in.) vertically and +47 mm (+1.86 in.) horizontally. No other cracks were expected to form in the pipe wall between the invert and the springline.

The signs of distress at this station were expected to be similar to those described for pipe at Station A. However, because the compressive thrusts were much less than those at Station A, cracks formed during the service operation may remain open, that is, the compressive thrusts may not be large enough to close these cracks.

To account for the lower modulus of saturated clay, a sensitivity analysis was performed for this installation by reducing the in situ soil modulus from 80 percent of maximum density as tested by the Standard Proctor method to about 65 percent while maintaining the constructed soil moduli. The results show that the diametrical deformation of the pipe increased in magnitude from −34 mm (−1.35 in.) to −38 mm (−1.49 in.) vertically, but remained the same horizontally at 47 mm (1.86 in.).

DISCUSSION OF RESULTS

Pipe deflection; longitudinal cracks at the invert, the crown, and near the springline; and possible separation of cylinder from the outer core at the invert and the crown are the expected signs of distress.

The following types of distress signs are not predicted by this analysis and indicate that the pipeline may be in danger of collapse and that additional safety measures should be considered:

- Increase in horizontal diameter or decrease in vertical diameter that are more than the calculated value of 64 mm (2.5 in.).
- Leakage or water flowing in the pipe, except at joints.
- Cracks or distress on the inside wall of the pipe at the springline in the form of multiple circumferential (vertical) fine cracks that indicate a very high compressive strain.
- Hollow sounds, when the liner is tapped with a hammer near the cracked crown and invert, extending circumferentially for significantly more than 305 mm (12 in.), accompanied by a large vertical deformation. These signs may indicate that water under external pressure is behind the steel cylinder. The buckling process, if it occurs, could lead to rupture.

CONCLUSION

A method based on soil-structure interaction was developed for the postfailure analysis of buried pipe. The failed pipe, having only a limited capacity for bending, may crack and produce a mechanism. The soil surrounding the pipe supports the pipe against excessive deformation and collapse. This method was applied to a deeply buried prestressed concrete cylinder pipe after complete loss of prestressing at two sections along the pipeline: one under open water, the other inland. The results of the analysis show that the soil surrounding the buried pipe can provide sufficient support to prevent the excessive deformation, the high compressive stresses in concrete core, and the collapse of the pipe.

REFERENCES

1. Zarghamee, M. S., K-L Fok, and E. S. Sikiotis. Limit-States Design of Prestressed Concrete Pipe, II: Procedure. *Journal of Structural Engineering*, ASCE, Vol. 116, No. 8, Aug. 1990, pp. 2,105–2,126.
2. Heger, F. J., A. A. Liepins, and E. T. Selig. SPIDA: An Analysis and Design System for Buried Concrete Pipe. *Proc., International Conference on Advances in Underground Pipeline Engineering*, ASCE, Aug. 1985.

3. Duncan, J. M., and C.-Y. Chang. Nonlinear Analysis of Stress and Strain in Soils. *Journal of Soil Mechanics and Foundation Division*, ASCE, Vol. 96, No. SM5, Sept. 1970, pp. 1,624–1,653.
4. Selig, E. T. Soil Parameters for Design of Buried Pipelines. *Pipeline Infrastructures* (B. A. Bennett, ed.). ASCE, *Proc.*, Boston, Mass., Conference June 1988, pp. 99–116.
5. Heger, F. J. New Installation Designs for Buried Concrete Pipe. *Pipeline Infrastructures* (B. A. Bennet, ed.), ASCE, *Proc.*, Boston, Mass., Conference June 1988, pp. 117–135.

Publication of this paper sponsored by Committee on Subsurface Soil-Structure Interaction.

Load Reduction on Rigid Culverts Beneath High Fills: Long-Term Behavior

JAN VASLESTAD, TOR HELGE JOHANSEN, AND WILLY HOLM

Three full-scale tests with the imperfect ditch method are described. The imperfect ditch method involves installing a compressible inclusion above rigid culverts to reduce the vertical earth pressure. Superlight expanded polystyrene blocks are used as the compressible material. In the first test, the instrumented culvert was a 1.95-m diameter concrete pipe beneath a 14-m-high rockfill embankment. In the second test, a 1.71-m diameter concrete pipe was used beneath a 15-m-high rock fill, and in the third, the culvert is a cast-in-place concrete box culvert with a 2.0-m width beneath 11 m of silty clay. The culverts were built between 1988 and 1989, and the instrumentation measured earth pressure, deformation, and temperature. The full-scale measurements show considerable reduction in the vertical earth pressure: that on top of the pipes in the granular fill was reduced to less than 30 percent of the overburden and that on the box culvert beneath the clay fill was reduced to less than 50 percent of the overburden. The deformation of the expanded polystyrene was 27 percent in the rock fill and 42 percent in the clay. The long-term observations show that there is no increase in earth pressure on and deformation of the pipes beneath the rock fill. There is a slight increase in deformation of the expanded polystyrene in the clay. Use of this method in Norway has realized cost reductions of the order of 30 percent and has made it possible to use concrete pipes beneath higher fills.

The problem of earth pressure on buried structures is of great practical importance in constructing highway embankments above pipes and culverts. Both the magnitude and the distribution of earth pressure on buried culverts are known to depend on the relative stiffness of the culvert and the soil. Current design methods distinguish between a rigid culvert and a flexible culvert. The vertical earth pressure on a rigid culvert is greater than the weight of the soil above the structure (negative arching). The vertical earth pressure on a flexible culvert is less than the weight of the soil above the culvert (positive arching).

Spangler (*1*) stated that in some of Marston's early experiments, the loads on rigid embankment culverts were 90 to 95 percent greater than the weight of the soil directly above the structure. An attempt to avoid this increase in load on the structure led to the development of the imperfect ditch method (sometimes called the induced trench method) of construction.

Penman et al. (*2*) measured the earth pressure on a rigid reinforced concrete culvert below 53 m of rockfill. The measured vertical earth pressure on the culvert crown was about two times the overburden. Höeg (*3*) performed model tests on a rigid pipe and reported that the crown pressure was about 1.5 times the applied surcharge.

Norwegian Road Research Laboratory, Public Road Research Administration, P.O. Box 6390 Etterstad, N-0604 Oslo 6, Norway.

The most common type of compressible material used in the imperfect ditch method is organic (baled straw, leaves, hay, compressible soil). Old tires are used in France (*4*).

The traditional imperfect ditch method involves installing a compressible layer above the culvert within the backfill. As the embankment is constructed, the soft zone compresses more than the surrounding fill and thus induces positive arching above the culvert. The construction procedure is shown in Figure 1.

CHOICE OF COMPRESSIVE MATERIAL

Although the artificially induced arching action is desirable, experience has shown that considerable care should be exercised in designing the compressible layer if the desired loading is to be realized. Indeed, some arrangements of compressible layers have led to serious stress concentration problems.

In addition, the compressible materials are often organic in nature, and they manifest a number of disadvantages, such as the difficulty of specifying their compressibility characteristics and the possibility of their decomposition.

Structural distress has been observed in some imperfect ditch full-scale tests because of the decomposition of the organic material with time as described by Rude (*5*) and Krizek et al. (*6*). This can lead to an unsatisfactory load distribution on the culvert. The reason for the observed structural distress in some imperfect ditch installations could also be attributed to the use of low-quality cohesive material at the sides of the culvert.

From the definition of the mechanisms of positive arching by Terzaghi (*7*), it is clear that positive arching involves two phases: a reduction of the earth pressure on a yielding part of the structure and an increase of the earth pressure on the adjacent nonyielding areas. Also Bjerrum et al. (*8*) noted that the increase in pressure on the adjacent nonyielding areas is equal to or larger than the reduction in pressure on the yielding part.

A zone of maximum shear stress will develop at the sides of the culvert due to the arching phenomena. The soil in the zone of higher shear stress may yield with time if it is a low-quality cohesive soil. Therefore it is important to use high-quality well-compacted granular soil at the sides of an imperfect ditch culvert. If the backfilling material is stable with time, equilibrium will be reached and the active arching will be a permanent state of stress.

Katona et al. (*9*) pointed out that very little quantifiable data are available about the stress-strain properties of the soft

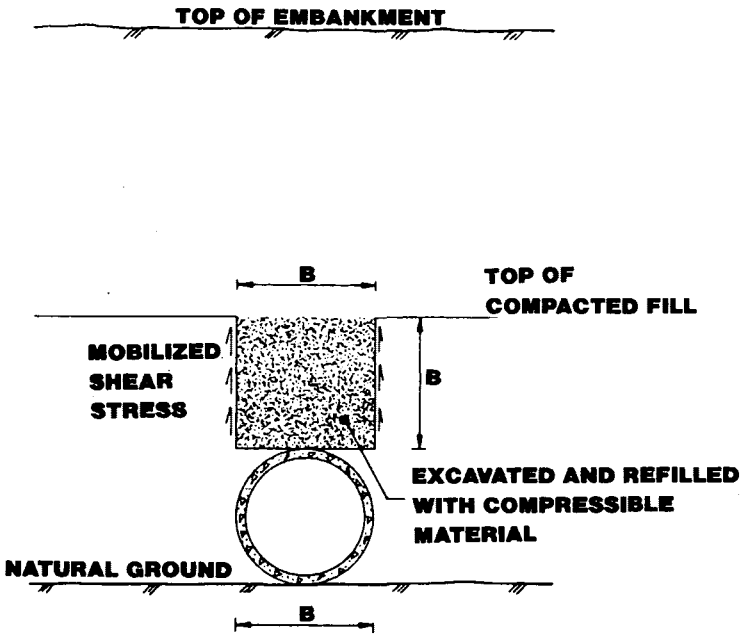

FIGURE 1 Imperfect ditch culvert—traditional installation.

organic materials used to promote arching in imperfect ditch installations. The long-term stability of the organic material was also questioned. A survey was conducted on potential soft materials for which the stress-strain properties are available. Expanded polystyrene (EPS) was identified as a possible material for culvert installations.

Hoff (*10*) conducted tests on a wide range of possible materials that could be used to promote arching. He concluded that foamed or cellular materials (like EPS) exhibited the desirable elastic-plastic behavior. The ideal stress-strain curve for an elastic-plastic material was shown, and the curve was very similar to the one shown by Katona et al. (*9*).

Expanded polystyrene is also used to reduce lateral earth pressure on rigid walls (*11*). The function of the expanded polystyrene is to allow controlled horizontal deformation of the retained soil and induce soil yielding. This concept is analyzed with numerical modeling (*12,13*).

Expanded polystyrene is used as compressible material in imperfect ditch installations in Norway. The typical stress-strain curve for EPS is very similar to the ideal stress-strain curve indicated by Katona et al. (*9*) and Hoff (*10*). A typical stress-strain curve for EPS with a density of 20 kg/m^3 is shown in Figure 2.

Trade qualities of EPS are superlight (20 kg/m^3), and standard block dimensions are 0.5 × 1.0 × 2.0 m with a volume of 1 m^3 and a weight of 20 kg. The compressive strength can be determined using an unconfined compression apparatus. The test specimens are 50 × 50 × 50 mm, and an average strength of minimum 100 kN/m^2 at 5 percent compression (2.5 mm) is required according to Norwegian specifications.

The blocks are easy to handle and are widely used in Norway for solving soft ground problems, Frydenlund (*14*). Overall long-term performance is good, as reported by Aabøe (*15*). The moisture pickup is less than 1 percent of a volume basis for drained conditions. Precautions must be taken against solvents, such as petrol, that can dissolve EPS.

The long-term serviceability of imperfect ditch installations is an important concern. Only full-scale tests and field observations can provide the information required to evaluate the time effects of an imperfect ditch installation.

INSTRUMENTED FIELD INSTALLATIONS

Field Installation at Eidanger

The structure was situated below a 14-m-high rock-fill embankment and served as a drainage pipe for new Euroroad 18 in Telemark County, Eidanger. The concrete pipe had an inner diameter of 1.6 m, a concrete thickness 0.176 m, and an outer diameter of 1.952 m. The pipe was reinforced with two layers of reinforcing steel. The steel bars were 12 mm in diameter and were laid with a center-to-center distance of 51 mm.

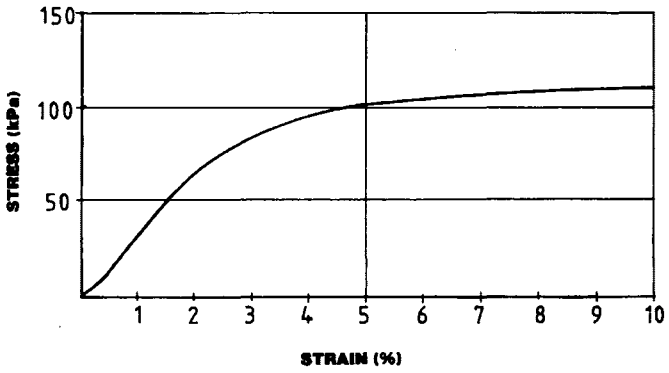

FIGURE 2 Typical stress-strain curve for EPS with density of 20 kg/m^3.

The yield strength of the steel was 500 MPa. The compressive strength of the concrete was 50 MPa. The concrete pipe was made of sections 1.5 m in length, with a total length of 70 m. A cross section of the installation with instrumentation is shown in Figure 3.

Standard EPS blocks 0.5 × 1.0 × 2.0 m were used. Six test specimens of EPS were tested in the laboratory and showed an average compression strength of 98.3 kPa. The measured density was 20.3 kg/m^3. The EPS blocks were placed when the backfill had reached 0.5 m above the top of the pipe. Laying the blocks was very fast and simple, and there was no need to excavate a ditch above the pipe.

The in situ soil was excavated to about 0.5 m below the invert elevation, down to bedrock, and replaced by 0 to 16 mm of sandy gravel. The same material (0 to 16 mm of sandy gravel) was used for backfill, with an optimum dry density of 21.5 kN/m^3 and an optimum moisture content of 9.3 percent. A minimum of a 97 percent Standard Proctor was required. Nuclear field density tests showed an average of 100 percent Standard Proctor (15 tests). The backfill was compacted in 20-cm-thick layers.

The backfill extended 1 m from the springline and 0.5 m over the top of the pipe. The remaining fill in the embankment was rock fill that was placed in 3-m-thick layers and compacted with 6 to 8 passes of a 6-ton vibratory roller. From field experience, this equals 95 to 97 percent Standard Proctor. The construction began in August 1988 and was completed in June 1989.

To evaluate the performance of the pipe and the EPS during construction and on a long-term basis, the pipe and the surrounding backfill were instrumented with hydraulic earth pressure cells of the Glötzl type. In addition, settlement tubes were installed on top of the pipe and on top of the EPS to measure the vertical deformation. The Glötzl cells were 20 × 30 cm; four cells were used. The location of the cells is shown in Figure 3.

One cell was placed in the springline to measure the horizontal earth pressure on the pipe (Cell 1). Two cells were placed 20 cm over the top of the pipe to measure the vertical earth pressure, one cell in the centerline (Cell 2) and one cell over the springline (Cell 3). The last cell (Cell 4) was placed in the centerline 2 m over the top of the pipe to measure the vertical earth pressure in the embankment. The temperature in the soil at the cell locations was measured with thermistors, and temperature corrections were made. Earth pressure and deformation measurements during construction are described by Vaslestad (*16*).

The measured earth pressure on Cell 2 at the top of the pipe is shown in Figure 4. The earth pressure on Cell 2 increased to 72 kPa in September 1988 when the fill height was

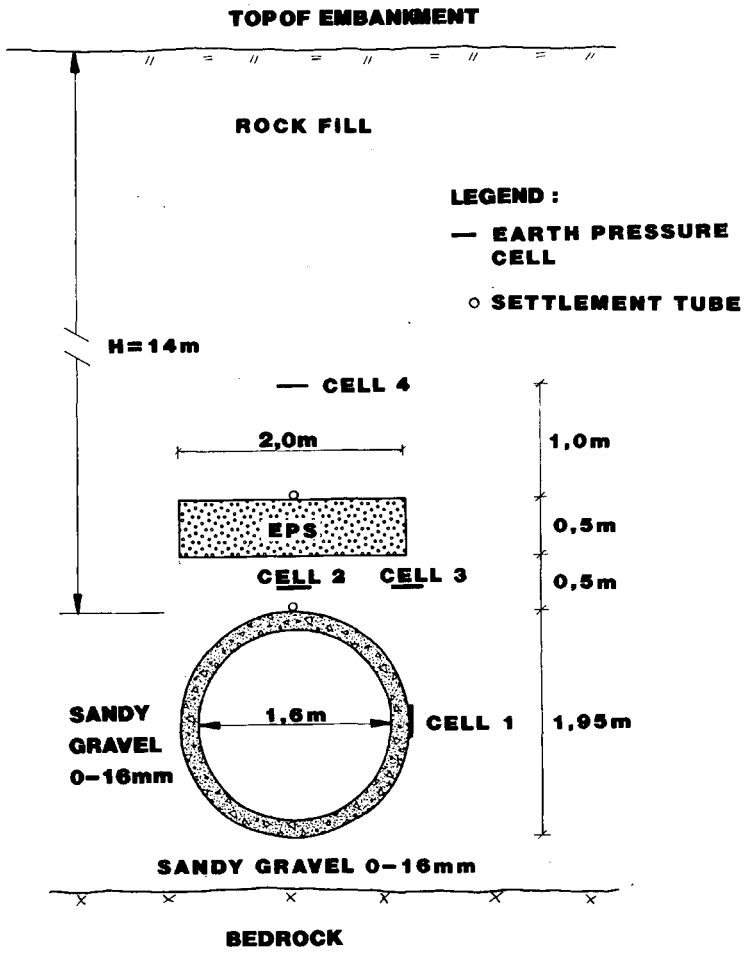

FIGURE 3 Geometry of instrumented cross section (Eidanger).

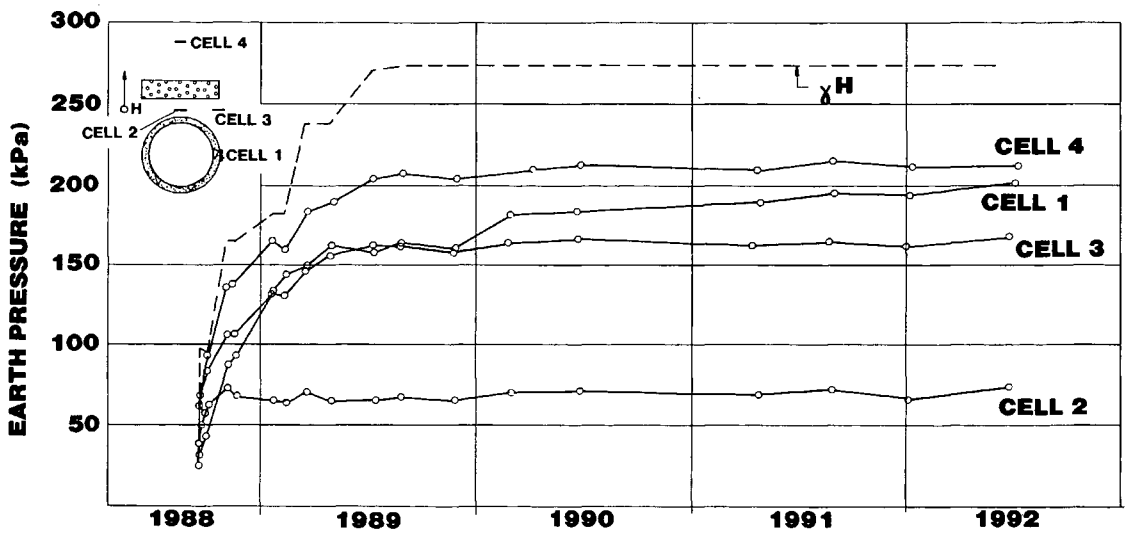

FIGURE 4 Measured earth pressure cells 1, 2, 3, and 4 (Eidanger).

8.3 m. A further increase in the fill height to 13.7 m did not increase the earth pressure on Cell 2. From the end of construction in July 1989 until June 1992, the earth pressure on the top of the pipe was relatively constant around 65 to 75 kPa, which is 25 to 27 percent of the overburden.

The earth pressure on Cell 3 at the end of construction was 161 kPa (see Figure 4). The earth pressure varied between 161 and 167 kPa over the next 3 years. This was 61 to 63 percent of the overburden. Only half of this cell was covered with EPS, explaining why the earth pressure was larger than that on Cell 2.

The measured horizontal earth pressure on the pipe (Cell 1) springline is shown in Figure 4. At the end of construction it was 164 kPa and increased slowly. After almost 3 years, the horizontal earth pressure was 201 kPa, 62 percent of the overburden.

The horizontal earth pressure was 2.7 times the measured vertical earth pressure on top of the pipe. This is not desirable and shows that it is necessary to increase the width of the EPS to decrease the horizontal earth pressure to a value more equal to the vertical earth pressure. In spite of the relatively large horizontal earth pressure, the pipe showed no sign of distress.

The earth pressure on Cell 4 above the EPS is shown in Figure 4. It was 204 kPa at the end of construction and slowly increased until June 1992 to 212 kPa, which was 90 percent of the overburden.

The measured vertical compression of the EPS is shown in Figure 5. The vertical deformation was 13.6 m at the end of construction, which was 27 percent of the initial EPS thickness. The compression was relatively constant in the measured 3-year period, and there was no increase in compression in this period.

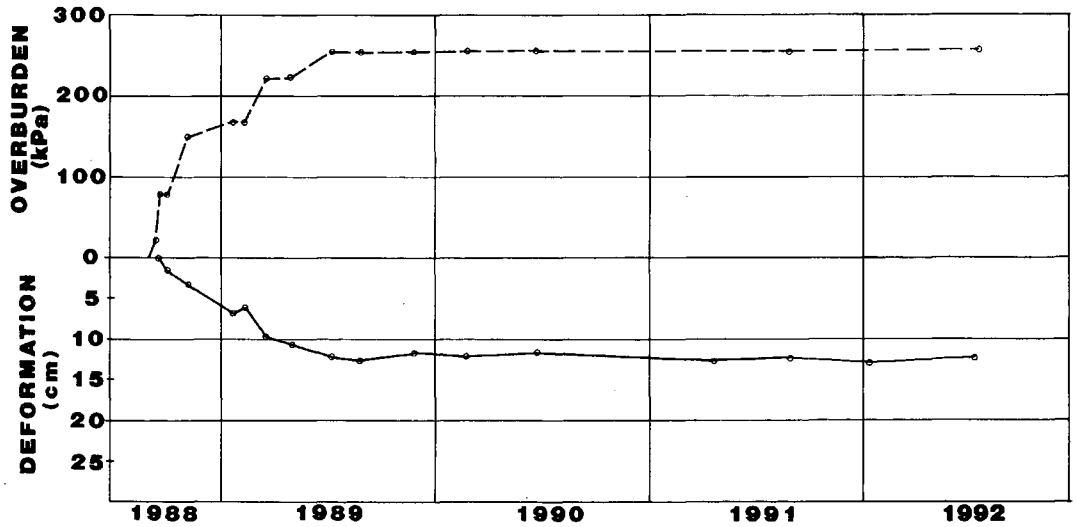

FIGURE 5 Measured deformation of EPS (Eidanger).

Field Installation at Sveio

The culvert was a concrete pipe with an inner diameter of 1.4 m and an outer diameter of 1.714 m. The embankment above the pipe consisted of 15 m of rock fill. The total length of the culvert was 75 m. A cross section of the pipe is shown in Figure 6.

Based on the experience from the field installation at Eidanger and parameter studies with the CANDE program (*17*), the width of the compressible layer increased to at least 1.5 times that of the outer diameter of the pipe (*18*). Increasing the width of the EPS to 1.5 times the width of the pipe had a positive effect on the structural response of the pipe. This was also in accordance with the findings of Sladen and Oswell (*19*) and Leonhardt (*20*). This decreased the horizontal earth pressure on the pipe. The ideal situation is for the horizontal earth pressure to equal the vertical earth pressure. For practical reasons, the width of EPS was 3.0 m, and blocks with a thickness of 0.5 m were used. The EPS had a compression strength of 100 kPa and a density of 20 kg/m^3.

The in situ soil consisted of dense moraine. Well-graded sandy gravel (GW) at a thickness of 400 mm was used as the bedding. As proposed by Heger (*21*), the bedding was compacted to a minimum of 95 percent Standard Proctor and loosened below the invert over a width of one-third of the pipe's outside diameter. This reduced the moments and shears at the invert and increased the structural capacity of the pipe.

Well-graded sandy gravel (0–16 mm) was also used for backfill. The backfill was compacted in 20-cm-thick layers, and nuclear field density tests showed an average of 98.5 percent Standard Proctor compaction. The backfill extended 1 m from the springline and 0.5 m above the EPS. The remaining fill in the embankment was rock. The average unit weight of the soil was $\gamma = 20$ kN/m^3. The construction began in November 1989, and in February 1990 the embankment had reached 13.7 m above the pipe. The remaining fill was placed at the beginning of 1992.

The pipe and the backfill were instrumented with five hydraulic earth pressure cells of the Glötzl type. Two settlement tubes were installed on top of the EPS to measure the vertical deformation. The instrumentation is shown in Figure 6.

The measured earth pressure on Cells 1, 2, and 3 is shown in Figure 7. Unfortunately, no earth pressure readings were taken before the fill had reached 12 m above the top of the pipe.

The measured earth pressure on Cell 1 at the top of the pipe was 57 kPa when the fill had reached 13.7 m above the

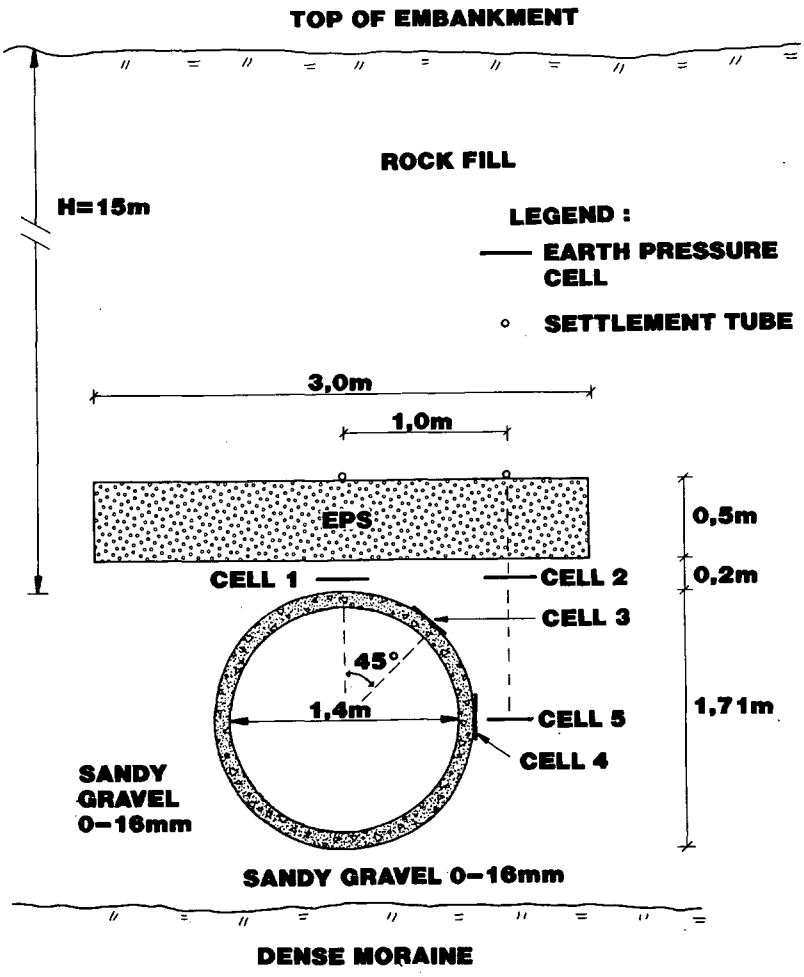

FIGURE 6 Geometry of instrumented cross section (Sveio).

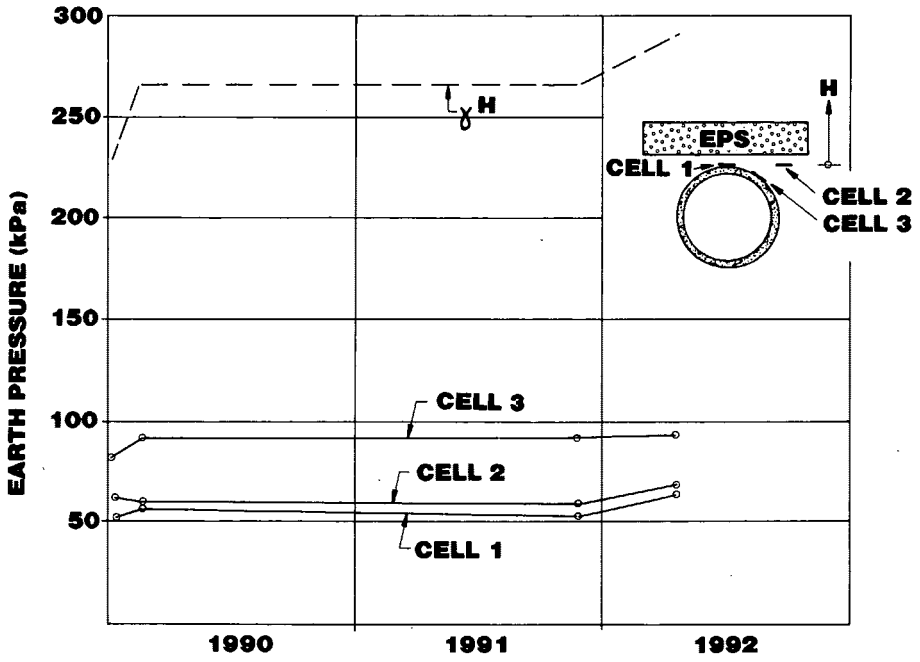

FIGURE 7 Measured earth pressure cells 1, 2, and 3 (Sveio).

pipe. This was 22 percent of the overburden. This value showed a small decrease from February 1990 to November 1991.

The earth pressure on Cell 2 was slightly larger, and the earth pressure on Cell 3 was 97 kPa during this period. The average earth pressure on these cells was 29 percent of the overburden.

The horizontal and vertical earth pressure on the pipe's springline (Cells 4 and 5) is shown in Figure 8. The horizontal earth pressure decreased from 52 to 41 kPa from February 1990 to November 1991.

The vertical earth pressure at the same level (Cell 5) was between 139 and 152 kPa during this period. The average measured horizontal earth pressure coefficient was $K = \sigma_H/\sigma_V = 0.32$ at the pipe's springline.

Compared with the measured vertical earth pressure at the top of the pipe, the average horizontal earth pressure was 89

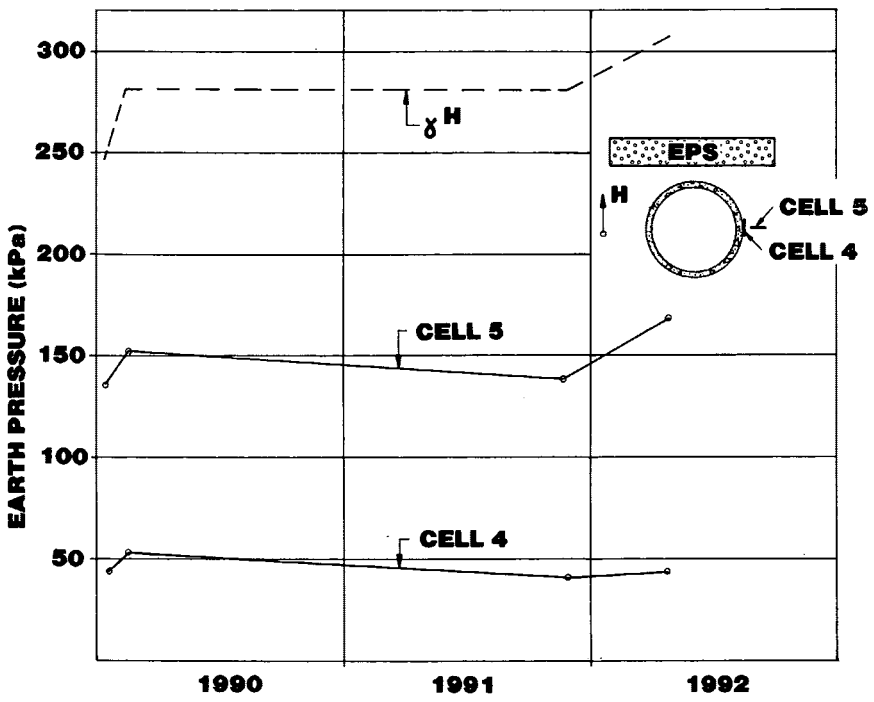

FIGURE 8 Measured earth pressure cells 4 and 5 (Sveio).

percent. This implies that the moments in the pipe were very small. This shows that increasing the width of the EPS reduced the horizontal earth pressure.

The measured vertical compression of the EPS is shown in Figure 9. The deformation was 6.5 m at a full height of 12 m and increased to 8.8 cm at a fill height of 13.7 m. From February 1990 to November 1997 the deformation increased slightly from 8.8 to 9.2 cm. When the remaining fill up to 15.0 m was placed, the deformation increased to 13.1 cm. This was 26 percent of the initial thickness of 50 cm of the EPS.

Field Installation at Hallumsdalen

The culvert was a cast-in-place box culvert with a width of 2.0 m and a height of 2.55 m. The culvert was continuous, had a total length of 385 m, and crossed a valley beneath an embankment of compacted dry crust clay up to 23 m in height.

The subsoil consisted of overconsolidated silty clay with a water content of 25 to 30 percent and undrained shear strength of 35 to 70 kPa. The culvert was instrumented with strain gauges to measure the tension in the culvert due to horizontal shear strain and settlement (*22*).

To investigate the time effects on the earth pressure in a cohesive fill using the imperfect ditch method, EPS was placed above the culvert at a length of 20 m. This section of the culvert was situated in the counterfill that was built up with silty clay. The unit weight of the silty clay was $\gamma = 20$ kN/m^3. EPS with a thickness of 0.5 m and a width of 2.0 m was placed above the culvert as shown in Figure 10.

The section was instrumented with two hydraulic earth pressure cells of the Glötzl type. The deformation of the EPS was measured using a settlement plate. To compare the earth pressure on the imperfect ditch section with a conventional section, one earth pressure cell was placed above the culvert in a cross section without EPS (see Figure 10).

The construction of the embankment began in July 1989. The measured earth pressure on Cell 1 at the top of the culvert is shown in Figure 11. At completion of the fill in February 1990, the fill height was 10.8 m above the cell level, and the overburden was 206 kPa. The measured earth pressure was 132 kPa at this fill height, which was 63 percent of the overburden. The earth pressure decreased slightly to 123 kPa in April 1991. There was a further decrease to 88 kPa in December 1991. This was probably due to stability problems and movements in the counterfills that occurred in April 1991.

The measured earth pressure on Cell 2, which was located in the fill 1 m above the EPS, is shown in Figure 12. At completion of the fill in February 1990, the earth pressure was 144 kPa, which was 81 percent of the overburden. The earth pressure decreased to 128 kPa in July 1992.

The earth pressure on Cell 3, which was located on top of the culvert in a section without EPS, is shown in Figure 13. The fill height above the culvert was 9.8 m. At completion of the fill in February 1990, the measured earth pressure was 244 kPa. The overburden was 196 kPa, and the measured earth pressure was 1.24 times the overburden. Based on extensive finite element modeling, Tadros et al. (*23*) proposed an expression for calculating the earth pressure on concrete box culverts. For silty clay soil, this expression gives an earth pressure of 1.17 times the overburden on top of the culvert.

The measured deformation of the EPS is shown in Figure 14. The deformation was 6 cm when the overburden was 100 kPa, which corresponded to the compression strength of the EPS. The deformation increased to 18.5 cm at completion of fill, when the overburden was 196 kPa. From February 1990 to May 1990, the deformation increased to 19.8 cm. For the next 2 years, the deformation slightly increased to 20.9 cm,

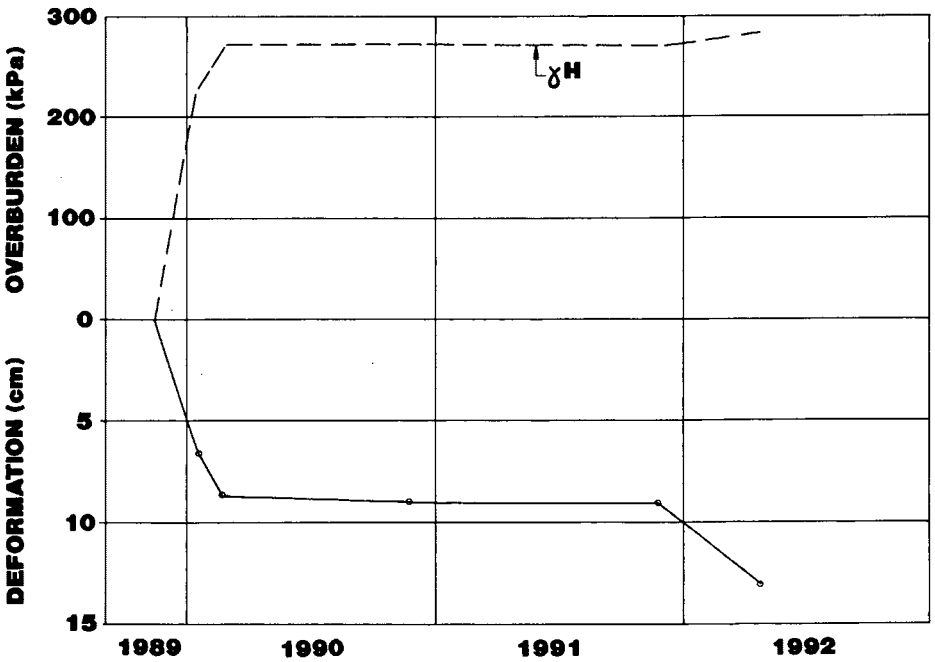

FIGURE 9 Measured deformation of EPS (Sveio).

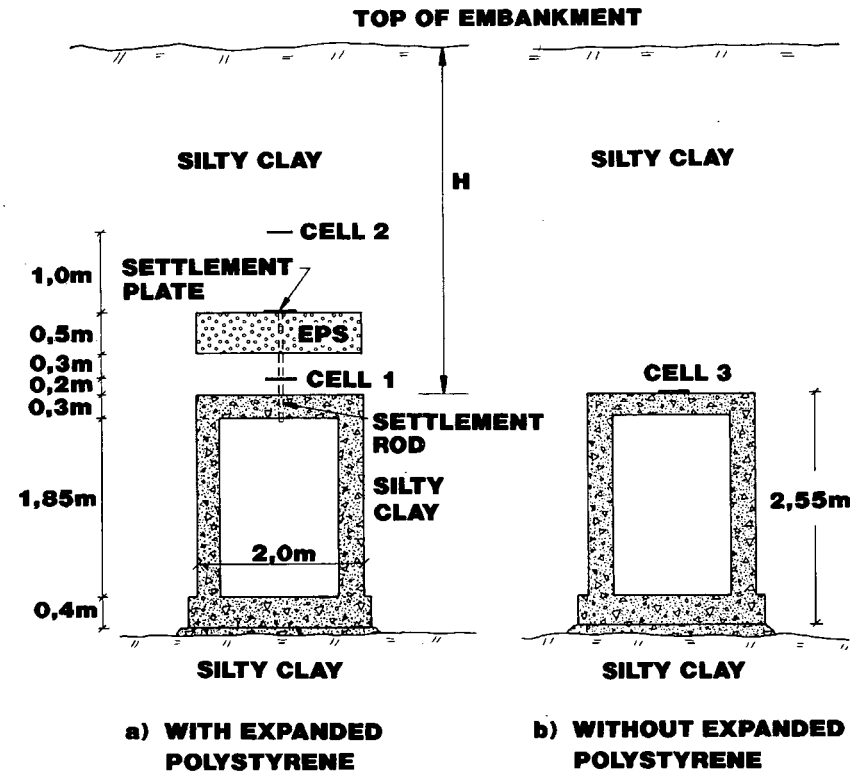

FIGURE 10 Geometry of instrumented cross section (Hallumsdalen).

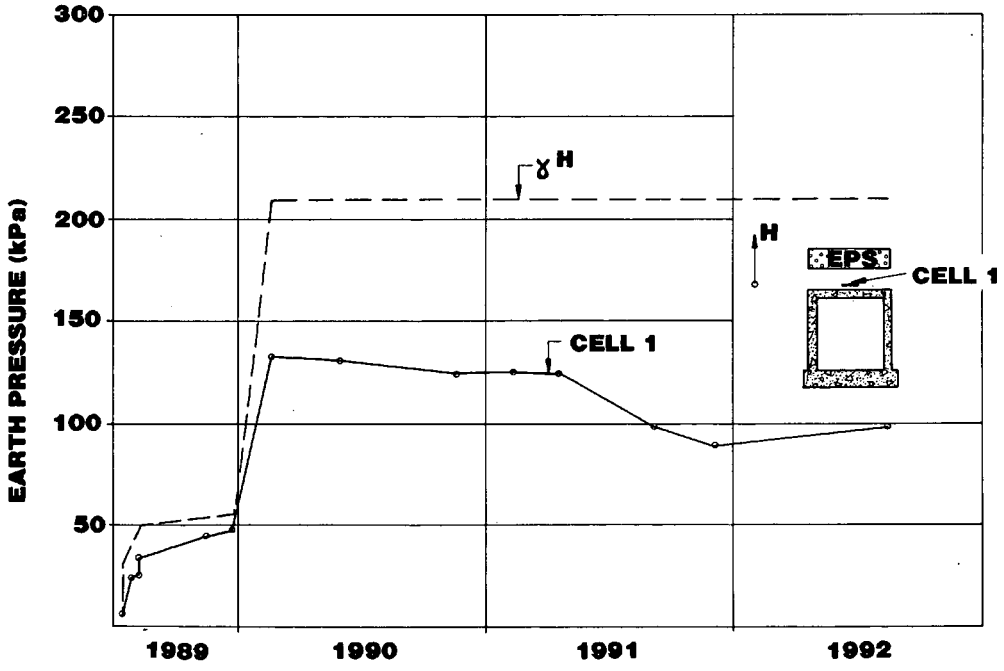

FIGURE 11 Measured earth pressure cell 1 (Hallumsdalen).

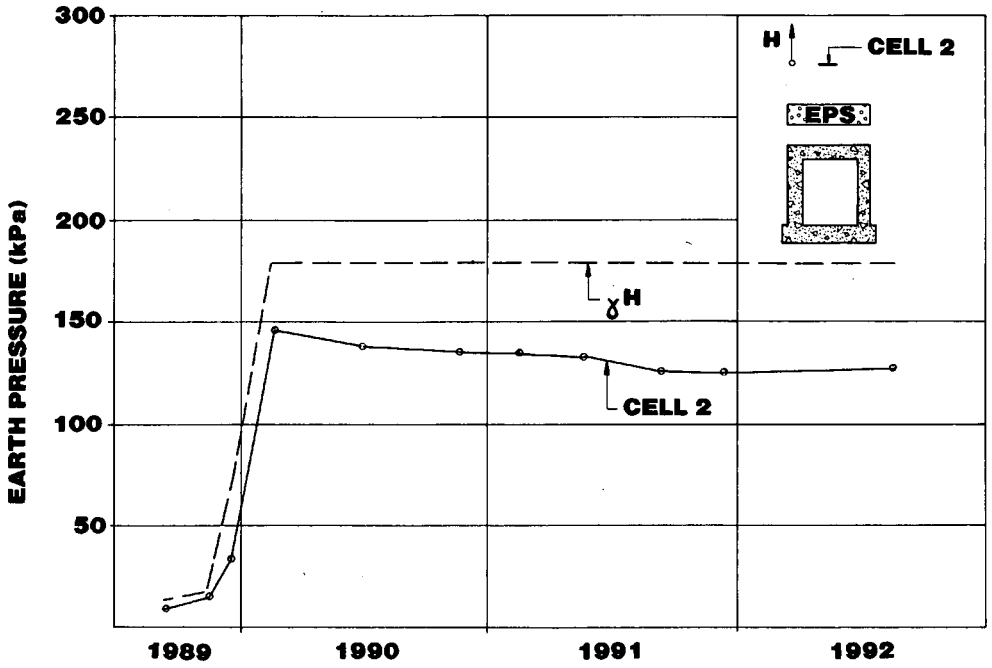

FIGURE 12 Measured earth pressure cell 2 (Hallumsdalen).

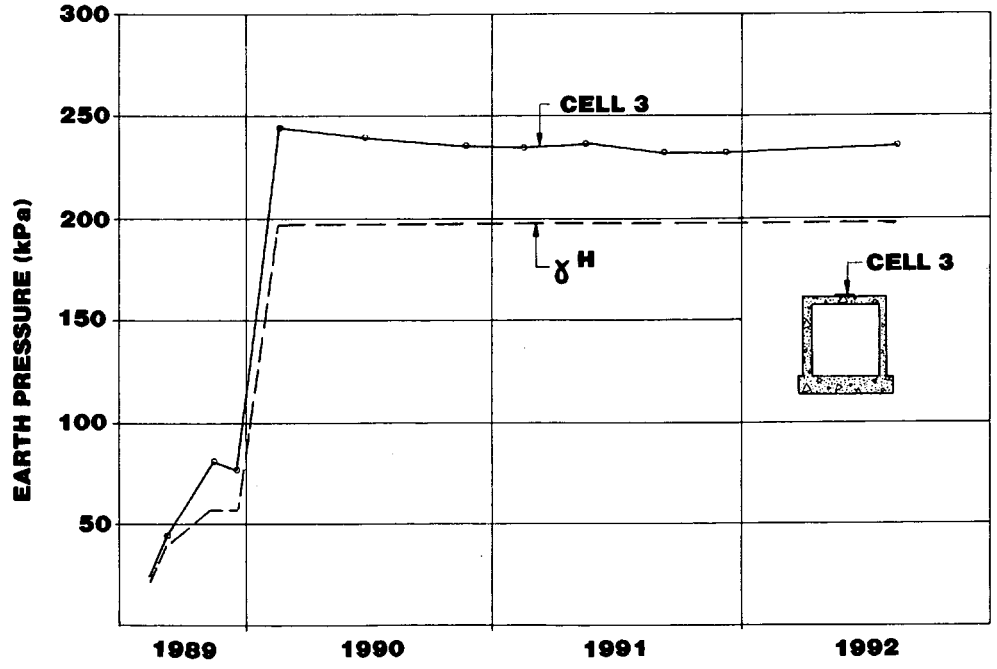

FIGURE 13 Measured earth pressure cell 3 (Hallumsdalen).

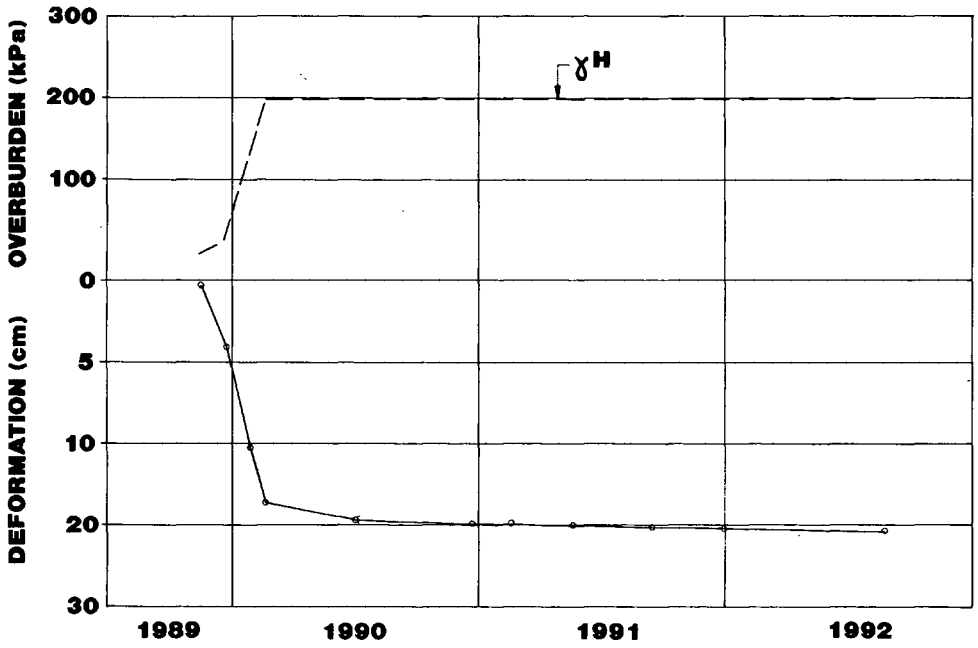

FIGURE 14 Measured deformation of EPS (Hallumsdalen).

which was 42 percent of the initial thickness of the EPS. This shows that the deformation of the EPS in a cohesive fill is greater than that in granular fills. The observed settlement of the culvert was 7 to 11 cm in the instrumented sections during the observation period.

SUMMARY AND CONCLUSIONS

The full-scale tests described show that the imperfect ditch method can be used to reduce the vertical earth pressure on rigid culverts. The EPS blocks used as the compressible material are superlight and easy to handle, and they simplify the construction procedure. Use of organic material in imperfect ditch culverts is not recommended because of the possibility of decomposition and the difficulty of specifying the material characteristics.

Two full-scale tests on concrete pipes backfilled with well-compacted sandy gravel beneath high rock fills show that the vertical earth pressure on top of the pipes was reduced to less than 30 percent of the overburden. The compression of the expanded polystyrene was 26 to 27 percent. Long-term measurements over a period of 3 years show that there was no marked increase in vertical earth pressure and compression after end of construction. Based on the full-scale tests and finite element analyses, it is recommended that a width of the EPS be used that is 1.5 times the outer diameter of the pipe.

One full-scale test was performed on a concrete box culvert backfilled with silty clay and situated below a silty clay embankment. One section with EPS and one section without EPS were instrumented.

The vertical earth pressure in the section with EPS was reduced to less than 50 percent of the overburden. The vertical earth pressure on the section without EPS was 1.24 times the overburden. The measured compression of the EPS was 42 percent of the initial thickness of 50 cm. Long-term measurements show that there was a slight increase in deformation with time.

Based on these full-scale tests and theoretical analyses, recommendations have been made for using the imperfect ditch method in Norway, where it has shown cost reductions of the order of 30 percent and has made it possible to use concrete pipes beneath higher fills (*24*).

ACKNOWLEDGMENTS

Financial support for these projects was provided by the Norwegian Public Roads Administration and the county roads offices in Telemark, Hordaland, and Buskerud. The authors acknowledge these county roads offices for making it possible to perform instrumentation on the field installations. Special thanks to Eli Kolås for drawing the figures and to Jan Faye Braadland for typing the manuscript.

REFERENCES

1. Spangler, M. G. A Practical Application of the Imperfect Ditch Method of Construction. *HRB Proc.*, Vol. 37, Washington, D.C., 1958.
2. Penman, A. D. M., J. A. Charles, J. K. Nash, and J. D. Humphreys. Performance of Culvert under Winscar Dam. *Géotechnique*, Vol. 25, No. 4, 1975, pp. 713–730.
3. Höeg, K. Stresses against underground Structural Cylinders. *Journal of the Soil Mechanics and Foundation Division*, ASCE, Vol. 94, No. SM4, 1968, pp. 833–858.
4. Jean, P. A., and N. T. Long. Creation of Arching (Pneusol and other techniques): Geotechnical Instrumentation in Practice. *Proc., Institution of Civil Engineers*, Nottingham, 1990, pp. 663–670.
5. Rude, L. C. *A Study of the Imperfect Ditch Method for Rigid Culverts*. Ph.D. thesis. University of Virginia, Charlottesville, 1979.
6. Krizek, R. J., R. A. Parmelee, J. N. Kay, and H. A. Elnaggar. *NCHRP Report 116: Structural Analyses and Design of Pipe Cul-*

verts. HRB, National Research Council, Washington, D.C., 1971.
7. Terzaghi, K. *Theoretical Soil Mechanics*. John Wiley and Sons, Inc., 1943.
8. Bjerrum, L., C. J. Frimann Clausen, and J. M. Duncan. Earth Pressures on Flexible Structures—A State-of-the-Art Report. *Proc., 5th European Conference on Soil Mechanics and Foundation Engineering*, Madrid, Vol. 2, 1972, pp. 169–196.
9. Katona, M. G., et al. *Structural Evaluation of New Concepts for Long-Span Culverts and Culvert Installations*. Report FHWA–RD–79–115. FHWA, U.S. Department of Transportation, 1979.
10. Hoff, G. C. *Shock Absorbing Materials*. Technical Report 6–763. U.S. Army Engineer Waterways Experiment Station, Vicksburg, Miss., 1967.
11. Parlos, A. M., and P. M. Karananiwsky. Geoboard Reduces Lateral Earth Pressures. *Proc., Geosynthetics '87*, pp. 638–639.
12. Horvath, J. S. Using Geosynthetics To Reduce Earth Loads on Rigid Retaining Structures. *Proc., Geosynthetics '91*, IFAI, pp. 409–424.
13. Karpupapu, R., and R. J. Bathurst. Numerical Investigation of Controlled Yielding of Soil-Retaining Wall Structures. *Geotextiles and Geomembranes*, Vol. 11, 1992, pp. 115–131.
14. Frydenlund, T. E. Soft Ground Problems. *Meddelelse*, No. 61, Norwegian Road Research Laboratory, 1987.
15. Aabøe, R. 13 Years of Experience with Expanded Polystyrene as a Lightweight Fill Material in Road Embankments. *Meddelelse*, No. 61, Norwegian Road Research Laboratory, 1987.
16. Vaslestad, J. Load Reduction on Buried Rigid Pipes Below High Embankments. *Proc., Pipeline Crossings*, Pipeline Division, ASCE, Denver, 1991, pp. 47–58.
17. Katona, M. G., et al. *CANDE—A Modern Approach for Structural Design and Analyses of Buried Culverts*: User Manual; System Manual; and Reports FHWA–RD–77–5, 77–6, and 77–7. U.S. Naval Civil Engineering Laboratory, 1977.
18. Vaslestad, J. *Soil Structure Interaction of Buried Culverts*. Ph.D. thesis. The Norwegian Institute of Technology, 1990.
19. Sladen, J. H., and J. M. Oswell. The Induced Trench Method—a Critical Review and Case History. *Canadian Geotechnical Journal*, Vol. 25, 1988, pp. 541–549.
20. Leonhardt, G. Die Abmindering der Erdlast durch Anordnung von Deformationsschicten bei Rohren grosser Steifigkeit. *Steinzeuginformation*, 1978.
21. Heger, E. J. New Installation Designs for Buried Concrete Pipe. *Proc., Conference on Pipeline Infrastructure*, ASCE, Massachusetts, 1988, pp. 117–135.
22. Baardvik, G., T. H. Johansen, and F. Oset. Measurement of Tension in Culverts Under High Fills. *Proc., Field Measurements in Geomechanics*, Oslo, 1991, pp. 729–733.
23. Tadros, M. K., J. V. Benak, A. M. Abdel-Karin, and K. Bexten. Field Testing of a Concrete Box Culvert. In *Transportation Research Board 1231*, TRB, National Research Council, Washington, D.C., 1989, pp. 39–54.
24. *Foundation Engineering in Road Construction: Code of Practice* (in Norwegian). Handbook 016. Norwegian Public Roads Administration, 1990.

Publication of this paper sponsored by Committee on Subsurface Soil-Structure Interaction.

Evaluation of Nondestructive Test Methods for Length, Diameter, and Stiffness Measurements on Drilled Shafts

GLENN J. RIX, LAURENCE J. JACOBS, AND CLAY D. REICHERT

Sonic echo, sonic mobility, dynamic impedance function, and impedance log tests were used to estimate the length, diameter, low-strain stiffness, and existence of defects for two drilled shafts. An overview of the data acquisition, processing, and interpretation procedures for each test is presented. The length measurements agreed well with the design length of one shaft but underestimated the length of the second shaft, possibly because the shaft was socketed into rock. Impedance log tests provided the most accurate diameter measurements that agreed remarkably well with the diameters backcalculated from the volume of concrete. Values of the low-strain axial stiffness were nearly the same for both shafts, but were higher than the stiffnesses observed in the static load tests because of the different strain levels involved in each test.

Nondestructive integrity tests offer a cost-effective means of assessing the depth, diameter, existence of defects, and low-strain stiffness of deep foundations. These tests are frequently used as quality control tests to check for defects arising from drilling, casing, slurry, or concreting problems that could adversely affect the performance of the shaft.

The purpose of this paper is to compare results obtained using four integrity tests on two drilled shaft foundations. The shafts were part of a static load test program cosponsored by the American Society of Civil Engineers (ASCE), Association of Drilled Shaft Contractors (ADSC), Georgia Tech's School of Civil Engineering, and the Federal Highway Administration (FHWA). The primary intent of the drilled shaft load test program was to study load transfer characteristics of drilled shafts in residual soils and to evaluate methods of predicting capacity using laboratory and in situ tests.

The following sections present the essential aspects of data acquisition, processing, and interpretation for each of the four methods. Results are presented, and comparisons between the nondestructive methods and the static load tests are discussed.

SITE DESCRIPTION AND SOIL PROPERTIES

An important criterion for the site of the load tests was that there be a sufficient thickness of residual soil to study load transfer characteristics in these soils. A site on the Georgia Tech campus where the depth to partially weathered rock (PWR) is 18–21 m (60–70 ft) was selected. The general soil profile consists of about 1 m (3 ft) of fill underlain by silty fine sands extending down to the PWR. A log from one of the soil borings at the site is shown in Figure 1. The Standard Penetration Test (SPT) blow counts generally range between 10 and 20 for the residual soils and upwards of 50 in the PWR.

A spectral analysis of surface waves (SASW) test was performed at the site to measure the shear wave velocity profile. Using the shear wave velocities, values of initial tangent shear modulus (G_{max}) were calculated to use in predicting the small and intermediate-strain level behavior of the shafts in axial loading. The shear wave velocity profile is presented in Table 1. Cone penetrometer, dilatometer, and pressuremeter tests were also performed at the site. The laboratory testing phase of the project includes index, consolidated-undrained ($\overline{CU}$), incremental consolidation, and resonant column/torsional shear tests.

Six drilled shafts were installed at the site, three test shafts and three reaction shafts, in a triangular pattern. All of the shafts were constructed "dry." One of the three test shafts was an "end bearing only" shaft and was not filled with concrete. The two remaining test shafts, C1 and C2, were used in this study to evaluate the four nondestructive test methods. Figure 2 shows a schematic illustration of the shafts. Shaft C1 was 21.4 m (70.2 ft) long with the tip in PWR, and Shaft C2 was 16.9 m (55.5 ft) long with its tip in residual soil. Both shafts had a nominal diameter of 762 mm (30 in.). Shafts C1 and C2 and one of the 1220-mm (48-in.) diameter reaction shafts were fully instrumented. Harris (*1*) provides a complete description of the load test program and results.

NONDESTRUCTIVE TEST METHODS AND RESULTS

The four nondestructive methods that were used in this study are the (a) sonic echo, (b) sonic mobility, (c) dynamic impedance function, and (d) impedance log tests. All four methods share the same basic equipment configuration and test procedure in the field. This configuration is shown in Figure 3. A transient force is applied to the top of the shaft by an instrumented 5.4-kg (12-lb) sledge hammer. The force applied to the shaft is measured by a dynamic force transducer in the face of the hammer. The response of the pile to the impact is measured by a piezoelectric accelerometer attached to the shaft with mounting wax. Both force and acceleration are recorded by a Fast Fourier Transform (FFT) analyzer capable of processing data in either the time or frequency domain. The four methods differ in the way that the force and accel-

School of Civil Engineering, Georgia Institute of Technology, Atlanta, Ga. 30332–0355.

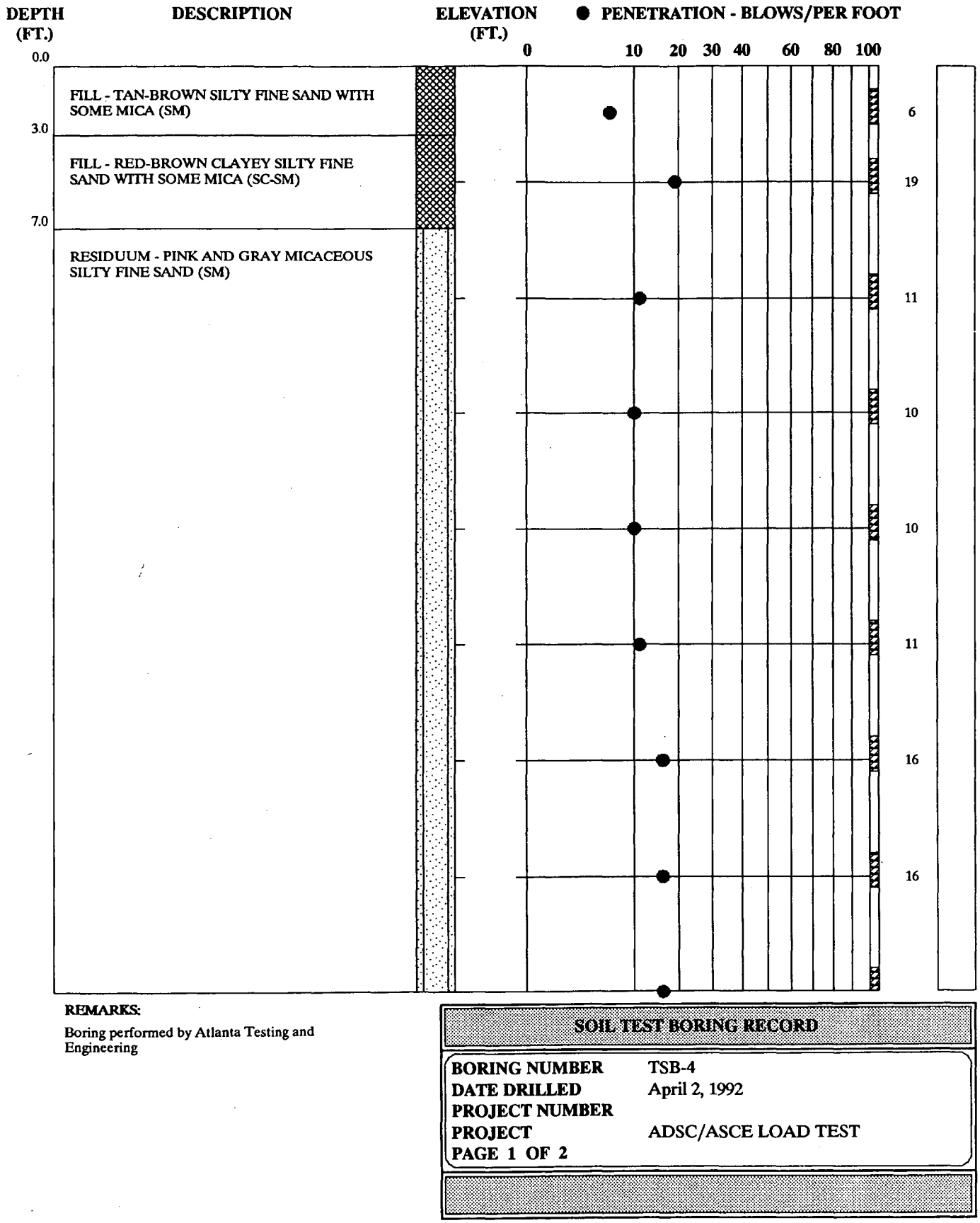

FIGURE 1 Boring log from load test site (*continued on next page*).

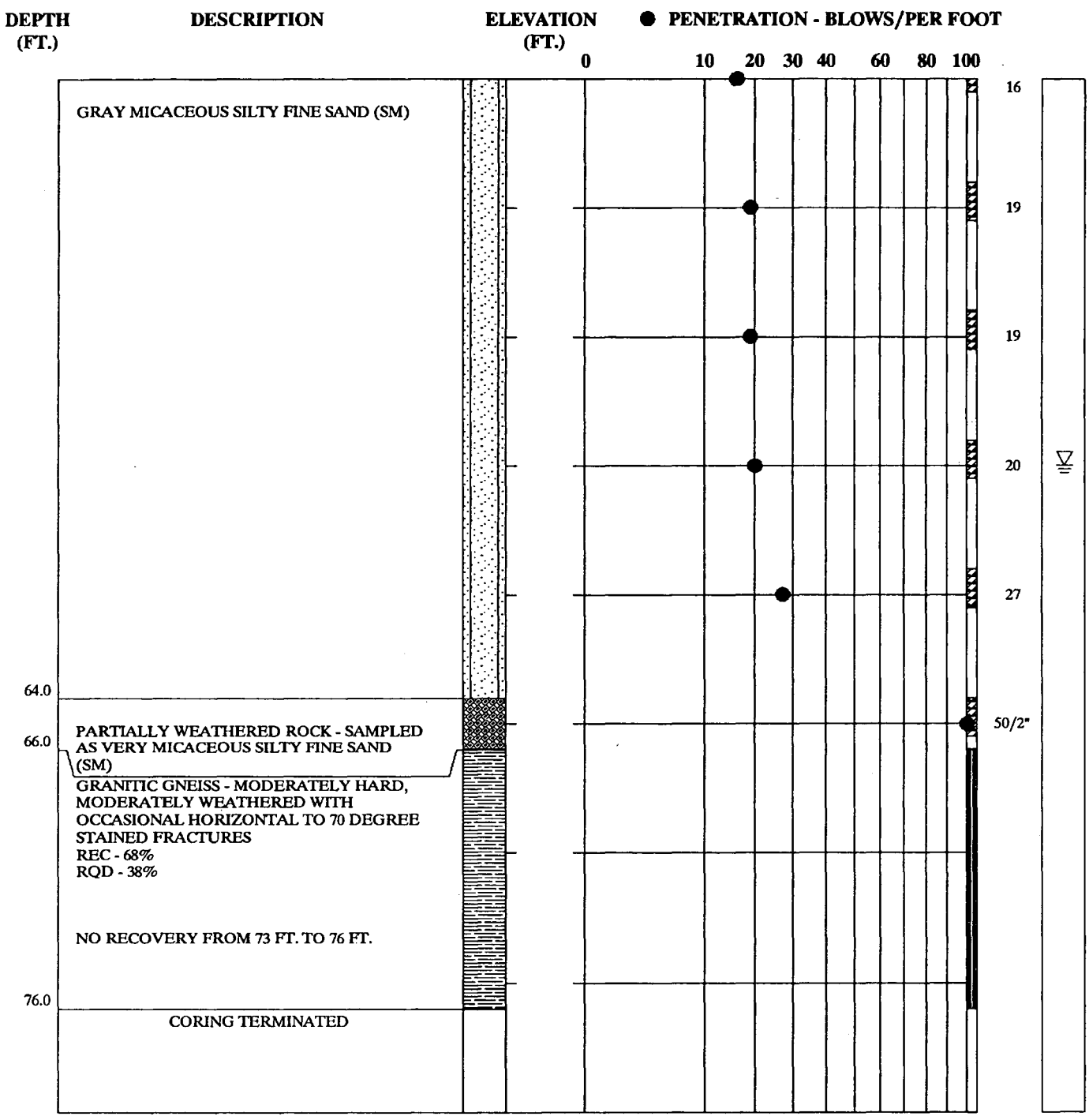

REMARKS:

Boring performed by Atlanta Testing and Engineering

SOIL TEST BORING RECORD

BORING NUMBER	TSB-4
DATE DRILLED	April 2, 1992
PROJECT NUMBER	
PROJECT	ADSC/ASCE LOAD TEST
PAGE 2 OF 2	

FIGURE 1 (*continued*)

TABLE 1 Summary of Spectral Analysis of Surface Wave Test Results

Layer No.	Layer Thickness (m)	Layer Depth (m)	Shear Wave Velocity (m/sec)
1	3.05	3.05	168
2	3.05	6.10	240
3	3.05	9.15	284
4	3.05	12.20	323
5	3.05	15.25	356
6	6.10	21.35	387

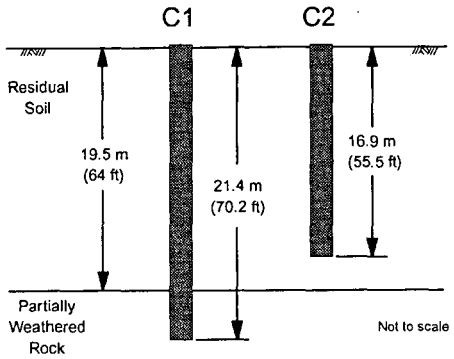

FIGURE 2 Schematic illustration of drilled shafts.

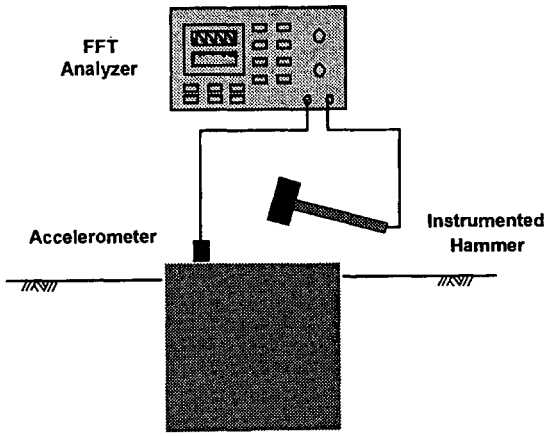

FIGURE 3 Configuration of equipment used for nondestructive tests.

eration time histories are processed. The following sections summarize the methods of interpretation and present the results of each test method for Shaft C2.

Sonic Echo

Conceptually, the sonic echo method is the simplest of the four. The end of the shaft and any defects that exist along its length cause reflections of the seismic waves as they propagate downward through the shaft. By observing the time required for these reflections to return to the top of the shaft, the depth to the reflector can be determined:

$$z = \frac{v_c \cdot \Delta t}{2} \quad (1)$$

where

z = depth to the reflector (a defect or the bottom of the shaft),
v_c = compression wave velocity in concrete, and
Δt = travel time of the reflected wave.

Because Δt is a two-way travel time, the numerator in Equation 1 must be divided by two. Hearne et al. (*1*), Stain (*2*), and Olson and Wright (*4*) provide complete descriptions of the method.

The acceleration time history recorded at the top of Shaft C2 is shown in Figure 4. There was a clearly-identified reflection that occurred 9.47 msec after the initial impact. The compression wave velocity of the concrete measured on 15- × 30-cm (6- × 12-in.) test cylinders was equal to 3700 m/sec (12,130 ft/sec). Using the observed travel time and compression wave velocity, the depth to the reflector was calculated to be 17.5 m (57.4 ft). The depth agreed well with the design length of 16.9 m (55.5 ft). No other reflections could be identified in the acceleration record. Although very simple to apply, the disadvantage of the sonic echo method is that the diameter and low-strain axial stiffness of the shaft cannot be determined.

Sonic Mobility

In the sonic mobility method, the force and acceleration time histories are transformed to the frequency domain using the FFT analyzer. The results are the spectra, $P(f)$ and $A(f)$, of

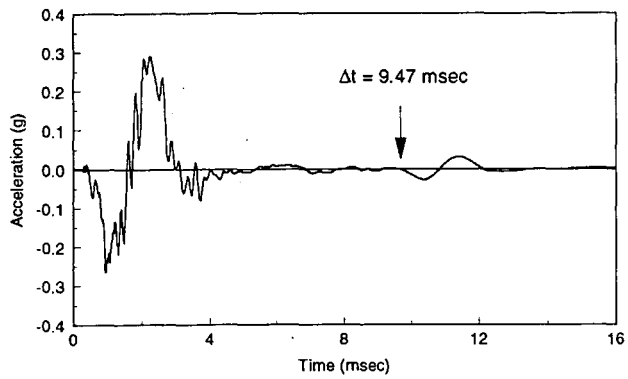

FIGURE 4 Acceleration time history observed at the top of Shaft C2.

the force and acceleration, respectively. The mobility is a frequency response function defined as the particle velocity observed at the top of the shaft normalized by the force:

$$\text{Mobility} \equiv \frac{V(f)}{P(f)} = \frac{A(f)}{i\omega P(f)} \tag{2}$$

where

$V(f)$ = the particle velocity spectrum,
$\omega = 2\pi f$ is the circular frequency, and
$i = \sqrt{-1}$.

The particle velocity spectrum is obtained by integrating the particle acceleration spectrum in the frequency domain as shown in the right-hand term of Equation 2. The mobility is a complex quantity, but typically only the magnitude is plotted. Figure 5 shows the mobility curve measured for Shaft C2. The shaft length and depth to defects, average diameter, and stiffness are determined from the curve using the following interpretive procedures (*3,5*).

The length of the shaft and the depth to any defects are determined from the spacing between peaks, Δf:

$$z = \frac{v_c}{2 \cdot \Delta f} \tag{3}$$

In Figure 5, the spacing between adjacent peaks is 107.5 Hz. This corresponds to a shaft length of 17.2 m (56.4 ft), which also agrees well with the design length of 16.9 m (55.5 ft). Defects in the shaft would appear as more-widely-spaced peaks with larger amplitudes. No other peaks are evident in Figure 5, indicating that the shaft has no major defects.

The average impedance of the shaft can be determined using the average value of the mobility at higher frequencies:

$$N = \frac{1}{\rho_c \cdot A_c \cdot v_c} \tag{4}$$

where

N = the average value of the mobility,
ρ_c = the mass density of concrete, and
A_c = the average cross-sectional area of the concrete.

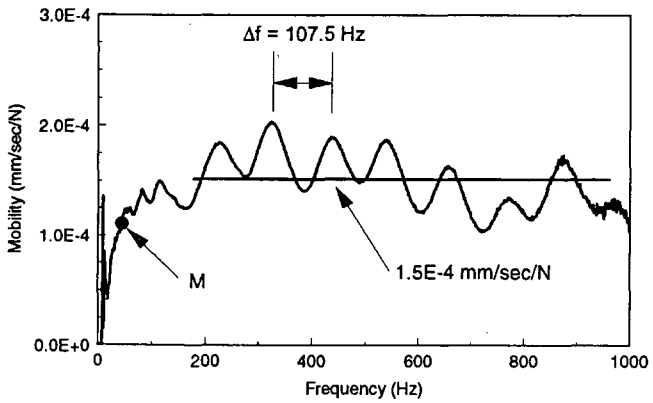

FIGURE 5 Mobility curve for Shaft C2 showing interpretation for length, diameter, and stiffness.

Because the mass density and compression wave velocity can be measured or assumed with little error, Equation 4 can be used to calculate the average cross-sectional area (or diameter) of the shaft. In Figure 5, the average value of the mobility from 200 to 1,000 Hz is identified by the horizontal line at 1.5×10^{-4} mm/sec/N. Using the measured v_c and a measured unit weight of 23.5 kN/m³ (150 pcf), the average diameter of the shaft was 979 mm (38.5 in.).

The low-strain stiffness was calculated from the slope of the initial portion of the mobility plot:

$$K_{\text{mob}} = \frac{2\pi f_M}{\left|\frac{V(f)}{P(f)}\right|_M} \tag{5}$$

where K_{mob} is the low-strain stiffness, f_M is the frequency of a point on the initial slope of the curve, and the term in the denominator is the magnitude of the mobility at that frequency. The low-strain stiffness varied depending on the frequency used in Equation 5. For Shaft C2, the stiffness varied from 2.0 to 2.7 MN/mm (11,421 to 15,420 kips/in.) when frequencies from 25 to 50 Hz were used in Equation 5.

The low-strain stiffness is often several times larger than the working load stiffness because of the difference in strain levels. For this reason, the low-strain stiffness is often used as a relative measurement. Once a typical value is established for the shafts at a site, shafts that have stiffnesses that differ significantly from the typical value can be identified as suspect.

Dynamic Impedance Function

This approach is frequently used to predict the response of foundations to dynamic loads (*6,7*). Although it has not been widely used for integrity tests, it provides another means of calculating the dynamic stiffness of the shaft or other deep foundation. The dynamic stiffness (K^*) of the pile can be expressed as a complex impedance function:

$$K^* = \frac{P(f)}{U(f)} = K_r + iK_i \tag{6}$$

where $U(f)$ is the particle displacement spectrum. The real part of the complex number reflects the stiffness of the foundation system and the imaginary part reflects the damping. The complex stiffness is easily obtained from the mobility plot previously described by integrating in the frequency domain to convert the velocity to a displacement and taking the inverse:

$$K^* = \left(\frac{V(f)}{i\omega P(f)}\right)^{-1} = \left(\frac{-A(f)}{\omega^2 P(f)}\right)^{-1} \tag{7}$$

In many cases, the real part of the stiffness can be considered independent of the frequency and approaches the static stiffness at low frequencies (*7*). Figure 6 shows the real part of the complex impedance function for Shaft C2. Data at frequencies less than 20 Hz were contaminated by noise and have been removed from the plot. The average value of the stiffness between 20 and 100 Hz is 1.8 MN/mm (10,278 kips/in.).

The low-strain stiffness from the dynamic impedance function is about 10 to 30 percent lower than the stiffness from

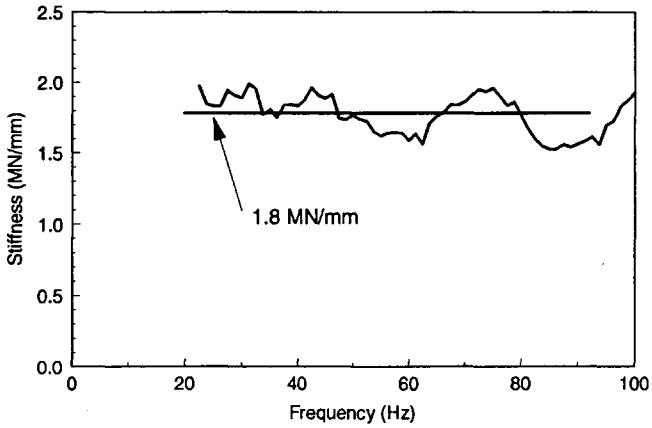

FIGURE 6 Real part of the dynamic impedance function for Shaft C2 showing interpretation of stiffness.

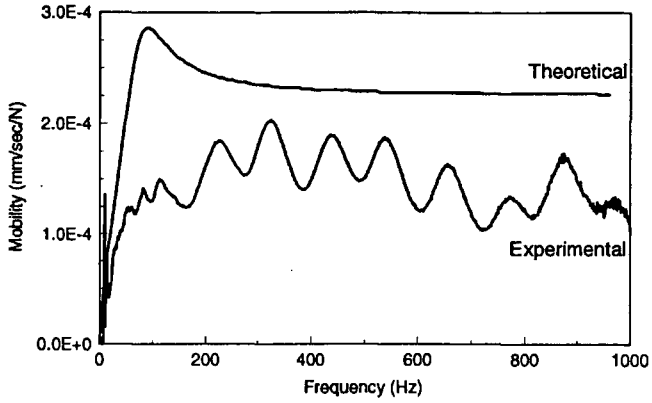

FIGURE 7 Experimental and theoretical mobility curves for Shaft C2.

sonic mobility measurements, depending on the frequency used in Equation 5. In the dynamic impedance function approach, the stiffness is calculated using only the real part of the complex stiffness. However, the definition of K_{mob} in Equation 5 includes both the real and imaginary parts of the complex stiffness because the magnitude of the mobility is used to calculate K_{mob}. As a result, the definition of K_{mob} includes the contribution of damping as well as stiffness. Because damping generally increases with frequency for deep foundations (*7*), K_{mob} will increase with frequency and will exceed K_r. If one of the goals of using nondestructive tests is to estimate the low-strain static stiffness of a drilled shaft, K_r provides a better estimate because the influence of damping is excluded.

Impedance Log

The impedance log is a relatively new nondestructive testing method (*8*). The basic idea of the approach is that reflection coefficients associated with changes in impedance along the length of the shaft can be determined by processing the velocity time history observed at the top of the shaft. Using these reflection coefficients, the changes in impedance can be backcalculated.

The first step in processing the velocity time history is to isolate reflections caused by changes in impedance along the shaft by subtracting the motion at the top of the shaft due to the impact of the hammer and the soil reaction along the length of the shaft. This is performed by calculating a theoretical mobility plot for a defect-free, infinitely long shaft with the nominal diameter. The soil is assumed to be homogeneous. For this study, the Spectral-Analysis of Surface Waves (SASW) test results were used to calculate an average shear wave velocity in the upper 6 m (20 ft). Because there are no defects or shaft end to cause reflections, the theoretical mobility can only be the result of the initial impact and the reaction of the soil. The theoretical mobility plot for a 762-mm (30-in.) diameter, infinitely long shaft is shown in Figure 7. The experimental mobility curve is also plotted in Figure 7 for comparison. Because there are no reflections from defects or the end of the shaft, the portion of the theoretical curve from 200 to 1,000 Hz is free of the oscillations that are present in the experimental curve. The difference between the experimental curve and the theoretical curve is the desired result: a mobility plot that contains only the effect of reflections from defects and the end of the shaft.

$$\left(\frac{V(f)}{P(f)}\right)_{\text{Reflected}} = \left(\frac{V(f)}{P(f)}\right)_{\text{Experimental}} - \left(\frac{V(f)}{P(f)}\right)_{\text{Theoretical}} \quad (8)$$

The next step is to calculate the impulse response in the time domain by taking the inverse FFT of the "reflected" mobility. The result is a "relative reflectogram" that is a time history of the reflections that return to the top of the shaft. Next, the relative reflectogram is scaled to calculate the reflection coefficients corresponding to changes in impedance along the length of the shaft. With the reflection coefficients now determined, the impedance as a function of time is backcalculated using

$$Z(t) = Z(0) \cdot \exp\left[2 \cdot \int_0^t r(t)dt\right] \quad (9)$$

where

$Z(t)$ = impedance as a function of time,
$Z(0)$ = nominal impedance at the top of the shaft, and
$R(t)$ = reflection coefficients from the scaled relative reflectogram.

Finally, the impedance as a function of depth (the impedance log) is obtained from $Z(t)$ by converting time to depth using the compression wave velocity. As in the sonic mobility method, if the mass density and compression wave velocity are known, changes in impedance correspond to changes in the cross-sectional area or diameter of the shaft.

The impedance log for Shaft C2 is shown in Figure 8. The gray area in the figure is a vertical section through the shaft. The black rectangle is the nominal diameter and depth of the shaft. The impedance log underpredicts the length of the shaft by 1.2 m (3.9 ft). The impedance log also shows that the diameter of the shaft in the upper 5 m (16.4 ft) was close to the nominal diameter, 762 mm (30 in.). However, over the remaining 10 m (32.8 ft) of shaft, the impedance log shows that the actual diameter was larger than the nominal diameter.

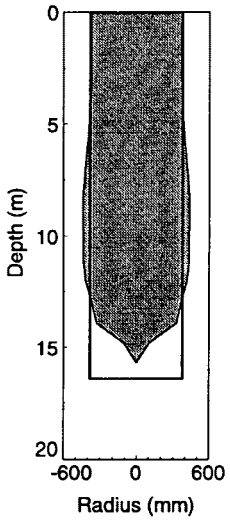

FIGURE 8 Impedance log for Shaft C2.

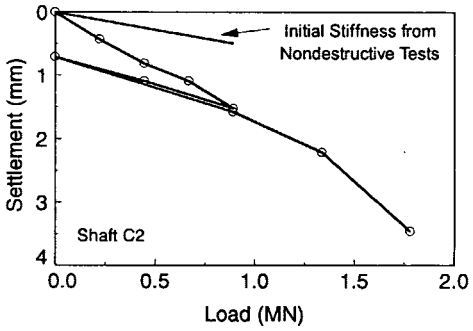

FIGURE 9 Early portion of the load versus settlement curve for Shaft C2.

The maximum diameter from the impedance log is 876 mm (34.5 in.). This enlargement is consistent with the concrete volumes used in Shaft C2. Field notes taken during construction of the shaft indicate that 6.9 m^3 (9 yd^3) of concrete was placed in the lower 11.4 m (37.4 ft) of the shaft. The average diameter of the shaft over this 11.4 m (37.4 ft) must then be 878 mm (34.6 in.). The agreement between the predicted diameter and actual average diameter is remarkable.

COMPARISON OF TEST RESULTS

Static load tests were performed on Shafts C1 and C2. For both shafts, the load was increased to 0.89 MN (100 tons) in 0.22-MN (25-ton) increments. The shafts were unloaded and then reloaded to failure. Figure 9 shows the early portion of the load versus settlement curve for Shaft C2. The stiffness of the shaft for the initial loading part of the curve [0 to 0.89 MN (0 to 100 tons)] was 0.6 MN/mm (3,426 kips/in.). The stiffness associated with the unload-reload hysteresis loop was 1.0 MN/mm (5,882 kips/in.). Similar calculations for Shaft C1 yielded an initial stiffness of 0.5 MN/mm (2,941 kips/in.) and a stiffness of 1.2 MN/mm (6,666 kips/in.) from the unload-reload loop.

Tables 2 and 3 summarize the results of the nondestructive integrity tests and the static load tests. For Shaft C1 all of the methods underestimated the length of the shaft. The difference was particularly large for the impedance log method. A likely explanation is that the nondestructive methods were more sensitive to the impedance change associated with the socketing of the shaft into partially weathered rock at a depth of approximately 19.5 m (64 ft) than the end of the shaft. Similar results have been noted by others performing tests on socketed shafts (*4*). Two of the methods provide an estimate of the actual diameter of the shaft. The average diameter from the sonic mobility test was 851 mm (33.5 in.). The impedance log approach gives the diameter as a function of depth. Values ranged from 742 mm (29.2 in.) in the upper 5 m (16.4 ft) of the shaft to a maximum of 925 mm (36.4 in.) in the

TABLE 2 Summary of Nondestructive and Static Load Tests for Shaft C1

Method	Length (m)	Diameter (mm)	Stiffness (MN/mm)
Sonic Echo	17.3	NA	NA
Sonic Mobility	18.2	851	2.0 to 2.5
Dynamic Impedance Function	NA	NA	1.8
Impedance Log	14.9	742-925	NA
Design/Actual	21.4	762	0.5[a] 1.2[b]

[a] from initial loading
[b] from unload-reload loop

TABLE 3 Summary of Nondestructive and Static Load Tests for Shaft C2

Method	Length (m)	Diameter (mm)	Stiffness (MN/mm)
Sonic Echo	17.5	NA	NA
Sonic Mobility	17.2	979	2.0 to 2.7
Dynamic Impedance Function	NA	NA	1.8
Impedance Log	15.7	740-876	NA
Design/Actual	16.9	762	0.6[a] 1.0[b]

[a] from initial loading
[b] from unload-reload loop

lower 10 m (32.8 ft). As with Shaft C2, records made at the time or pouring indicate that 6.9 m^3 (9 yd^3) of concrete was placed in the lower 11.6 m (38 ft) of the shaft. This corresponds to an average diameter of 869 mm (34.2 in.) in the lower two-thirds of the shaft. The agreement between the diameter estimates from the two nondestructive tests and the independent calculation based on volume of concrete is excellent.

The low-strain stiffness from dynamic impedance function measurements are less than the sonic mobility stiffness by about 10 to 30 percent for Shaft C1. The difference is due to the inclusion of damping in K_{mob}. Both stiffnesses are larger than those measured during the initial loading and unload-reload portions of the static load test. The reason for the differences is the strain level associated with each stiffness. The nondestructive tests measure the stiffness at small strains ($<10^{-3}$ percent) where the soil surrounding the shaft behaves as a linear elastic material. The static load test involves larger displacements and strains with a corresponding decrease in the stiffness of the soil. Similar differences between the stiffnesses from nondestructive tests and static load tests have been noted elsewhere (*9*).

The results of the nondestructive tests on Shaft C2 have been presented in the previous section, but it is useful to summarize them here. The three methods that provide length estimates all yielded estimates that agree well with the design length. Both the sonic echo and sonic mobility approaches slightly overestimated the length; the impedance log underestimated the length by 7 percent. The impedance log accurately measured the variation in the diameter of Shaft C2 with depth. In the upper 5 m (16.4 ft) of the shaft, the 740-mm (29.1-in.) diameter is close to the nominal diameter and the enlarged diameter in the lower 10 m (32.8 ft) is consistent with the average diameter calculated using concrete volume. The average diameter of 979 mm (38.5 in.) from the sonic mobility test overestimates the apparent actual diameter of the shaft. Finally, the low-strain stiffnesses from the mobility and impedance function tests exceed the initial loading and unload-reload stiffnesses from the static load test as shown in Figure 9. The difference is caused by the difference in strain levels between the nondestructive tests and the static load tests.

It was mentioned earlier that the low-strain stiffnesses from nondestructive tests are frequently used as a relative measurement of foundation performance. The low-strain stiffnesses for Shaft C1 and C2 agree well. When used as a relative measurement, the low-strain stiffnesses accurately predicted that both Shafts C1 and C2 would have approximately the same static stiffness.

CONCLUSIONS

Each of the four nondestructive methods has strengths and weaknesses. The sonic echo method is the simplest of the methods to perform and also the simplest to process and interpret. The method is limited in that only the length of the shaft and depths to defects can be determined. The sonic mobility approach requires more sophisticated, frequency domain processing and interpretation. However, its ability to determine the shaft length, depth of defects, average cross-sectional area, and low-strain stiffness makes it more versatile than the other methods. The dynamic impedance function approach provides only an estimate of the low-strain stiffness of the shaft. However, the value of stiffness more accurately reflects the true low-strain static stiffness because the influence of damping is excluded from the definition of stiffness. The strength of the impedance log is in its ability to determine the variation of a cross-sectional area or diameter along the length of the shaft. The ability to produce a "picture" of a vertical section through the shaft is the most persuasive form of output from the four test methods.

It is important to note that all four methods complement one another. Acquisition of data in the field is the same for each method. The differences are in the way the data are processed and interpreted. It is possible, therefore, to use more than one method to complement and/or confirm the results without the need for different field test procedures or equipment.

The ability to use several of these methods to complement one another becomes particularly important if nondestructive methods are used for the unknown foundation problem. In these cases, the interpretation of test results may be more difficult due to the deterioration of the shaft. The impedance log is valuable because it produces the most complete visual representation of the shaft. The low-strain axial stiffness from either the sonic mobility or the dynamic impedance function approach is a measure of the performance of the shaft under load. The stiffness value is potentially useful in rapidly and nondestructively assessing the ability of a deteriorated shaft to carry additional load.

ACKNOWLEDGMENTS

The authors wish to thank the following organizations for their participation and support of the load test program: ASCE Georgia Section Geotechnical Committee, ATEC Associates, Atlanta Testing and Engineering, Brainard Kilman, Inc., Case International, Dames and Moore, Georgia Department of Transportation, Georgia Tech's Office of Facilities, Geo-Syntec Consultants, Golder Associates, Johnson Drilling Co., Law Engineering, Long Foundation Drilling Co., McKinney Drilling Co., Russo Corporation, Tensar Corporation, and Turner Engineering Consultants. The financial support of the Federal Highway Administration is also gratefully acknowledged.

REFERENCES

1. Harris, D. *Load Tests of Two Drilled Shafts Constructed in Piedmont Residuum*. Master's thesis. Georgia Institute of Technology, 1992.
2. Hearne, T. M., K. H. Stokoe II, and L. C. Reese. Drilled Shaft Integrity by Wave Propagation Method. *Journal of Geotechnical Engineering*, ASCE, Vol. 107, No. GT10, Oct. 1981, pp. 1327–1344.
3. Stain, R. T. Integrity Testing. *Civil Engineering*, April 1982, pp. 54–59.
4. Olson, L. D., and C. C. Wright. Nondestructive Testing of Deep Foundations with Sonic Methods. *Foundation Engineering: Current Principles and Practices*, ASCE, Vol. 2, 1989, pp. 1173–1183.
5. Paquet, J. Étude Vibratoire Des Pieux En Béton, Réponse Harmonique Et Impulsionelle: Application Au Controle (in French).

Annalles de l'Institut Technique du Batiment et des Travaux Publics, No. 245, May 1968, pp. 788–803.
6. Gazetas, G. Analysis of Machine Foundation Vibrations: State of the Art. *Soil Dynamics and Earthquake Engineering*, Vol. 2, No. 1, 1983, pp. 2–42.
7. Novak, M. Piles Under Dynamic Loads. *Proc., Second International Conference on Recent Advances in Geotechnical Earthquake Engineering and Soil Dynamics*, St. Louis, Vol. 3, March 1991, pp. 2433–2456.
8. Paquet, J. A New Method for Testing Integrity of Piles by Dynamic Impulse: The Impedance Log (in French). *International Colloquium on Deep Foundations*, Paris, March 1991, pp. 1–10.
9. Baker, Jr., C. N., E. D. Drumwright, F. Menash, G. Parikh, and C. Ealy. Dynamic Testing to Predict Static Performance of Drilled Shafts: Results of FHWA Research. *Geotechnical Engineering Congress 1991*. Geotechnical Special Publication No. 27, ASCE, Vol. 1, 1991, pp. 491–504.

Publication of this paper sponsored by Committee on Soil and Rock Properties.

Dynamic Response Measurements and Identification Analysis of a Pavement During Falling-Weight Deflectometer Experiments

STEPHEN A. KETCHAM

Falling-weight deflectometer (FWD) experiments were conducted on an airport taxiway pavement using techniques of experimental dynamics to obtain compliance frequency response functions of the pavement, which are functions in the frequency domain that represent the pavement displacement response at a given location to the FWD load. The compliance functions reveal that at certain locations the pavement responded to the FWD load with a significant resonant amplification at approximately 30 Hz. To understand this response and to develop appropriate techniques for backcalculation when dynamic behavior should not be ignored, the compliance data were used to backcalculate selected pavement properties using a minimization algorithm and a wave propagation model applicable to pavement systems. The backcalculations provide a credible explanation of the observed pavement behavior. They also demonstrate the utility of the minimization algorithm and wave propagation model to estimate pavement system properties using dynamic response data from FWD tests.

A falling-weight deflectometer (FWD) is an apparatus for testing pavements. FWD experiments are performed by dropping a mass onto a circular pad, measuring the force history of the drop, and measuring the vertical velocity response of the pavement surface at several distances from the load center. Peak-load and peak-displacement values are calculated from the measured transient load and velocity histories of an experiment. These values are often used by pavement engineers as quasi-static response data to match in elastic modulus identification calculations using a static model of the pavement system. This process is generally referred to as "backcalculation."

Several investigators have suggested that the inertial and dissipative responses can contribute significantly to the load and velocity responses measured during FWD experiments; that is, the dynamics of an FWD test can be important. Roesset and Shao (*1*), Sebaaly et al. (*2*), Anderson (*3*), Magnuson et al. (*4*), and Chang et al. (*5*) have conducted studies of the dynamic response of pavements to understand the implications of the static assumption on backcalculation results. Roesset and Shao (*1*) and Chang et al. (*5*) have shown that a pavement system with a bedrock or other relatively hard layer at shallow depth can have resonant vibration modes that may be excited during FWD experiments. They have suggested that the use of static backcalculation techniques can lead to erroneous results because of their inability to account for an amplified, dynamic response. Their studies indicate that the quasi-static assumption inherent in conventional FWD backcalculation practice should be further evaluated.

This paper presents results from FWD experiments of a pavement that responded at a number of locations with a significant resonant vibration at approximately 30 Hz, and at other locations without this distinct resonance. To quantify the dynamic response, the experiments were conducted with supplemental instrumentation and the data were analyzed using conventional signal processing techniques of experimental dynamics. A minimization algorithm (*6*) together with a wave propagation model applicable to pavements (*7,8*) were used to backcalculate selected pavement layer properties from the experimental data sets. The identified models provide a credible explanation of the resonant response behavior of the pavement, and the analysis demonstrates that the method is appropriate for backcalculation when rigid or relatively hard layers underlie the pavement structure.

EXPERIMENTAL TECHNIQUE AND RESULTS

The tests reported here were conducted April 11, 1991, at the Lebanon, New Hampshire, Airport at three locations on taxiway B. A Dynatest 8000 FWD with a 30-cm-diameter load plate was used as the loading system together with an array of accelerometers and a dynamic data acquisition system as the response measurement system. Experiments were conducted by recording the load cell and displacement histories provided by the FWD system and the response histories of the accelerometers.

Pavement System and Experimental Configuration

The taxiway pavement was 15.2 m wide and consisted of 12.7 cm of asphalt concrete surface course over 15.2 cm of crushed aggregate base course, approximately 1 m of subbase course, and subgrade. Instrumentation at the site indicated that the pavement soil was unfrozen and had thawed completely several weeks prior to the test date. The design thickness of the subbase course was 94 cm, but the constructed thickness was

U.S. Army Engineer Cold Regions Research and Engineering Laboratory, 72 Lyme Road, Hanover, N.H. 03755-1290.

slightly greater at some locations according to construction documents. The additional depth was unknown at the test locations.

The tests were conducted along the center line of the taxiway at locations 60 m apart. The taxiway runs approximately southwest to northeast. The test location furthest to the southwest was designated station 18-00 on the taxiway construction drawings; the middle location was designated 20-00; and the location furthest to the northeast was designated 22-00. (These designations were based on the distance in feet from the beginning of the taxiway.) Information from a site investigation pit close to the 20-00 location that was excavated prior to construction indicated that the subgrade was a "very dense gravelly silty sand." The depth of the pit was 3.6 m. Information from borings much further from the test locations indicated that the depth to bedrock was likely to be greater than 10 m at the sites.

The accelerometers were attached to the pavement surface at the radial distances 0.30, 0.45, 0.75, 1.05, and 2.25 m from the load pad center, and the geophones of the FWD system were located at distances of 0, 0.305, 0.61, 0.91, 1.22, 1.52, and 1.83 m. All were oriented to measure vertical responses.

Data Analysis

A set of specifications for a digitally sampled signal is the sampling interval Δt, which is the time domain resolution, and the duration of sampling T. The number of samples (N) is

$$N = \frac{T}{\Delta t} \tag{1}$$

The highest frequency that will appear in the sampled data (f_c) is called the Nyquist frequency. The Nyquist frequency is

$$f_c = \frac{1}{2\Delta t} \tag{2}$$

The frequency domain resolution is the bandwidth Δf, that is,

$$\Delta f = \frac{1}{T} = \frac{1}{N\Delta t} \tag{3}$$

The sampling rate is the frequency $1/\Delta t$, which is twice the Nyquist frequency. The sampling rate used for this study (5,000 Hz) was dictated by the sampling rate of the FWD load cell output, which was not adjustable. The Nyquist frequency corresponding to this sampling rate is 2,500 Hz. The number of values of the accelerometer data sequences is 2,048, which corresponds to a sample duration of approximately 0.41 sec and a frequency resolution of approximately 2.44 Hz. The number of values and the sample duration of the FWD data acquisition system were 300 and 0.06 sec, respectively, and these were not adjustable. The accelerometers and the dynamic data acquisition system were used as an alternative to the FWD geophones and measurement system specifically because the 0.06 sec sample duration of the FWD system was not long enough to capture the complete response of the pavement and would have been unnecessary if the FWD sample duration could have been set to a sufficient duration.

The load and acceleration histories of the repetitions were used to calculate frequency response and impulse response functions between the load and response, according to conventional linear systems-based analysis techniques for dynamic testing of structures (*9,10*). An impulse response function $h(t)$ of a structure relates a structural response $y(t)$ to a loading history $x(t)$ by the convolution integral

$$y(t) = \int_{-\infty}^{\infty} h(\tau)x(t - \tau)d\tau \tag{4}$$

and a frequency response function $H(f)$ relates the Fourier transform of the structural response $Y(f)$ to the Fourier transform of the loading history $X(f)$ by the multiplication

$$Y(f) = H(f)X(f) \tag{5}$$

where t and f denote the time and frequency domains, respectively. Frequency response and impulse response functions make up a Fourier transform pair. For digital signals, discrete versions of Equations 4 and 5 apply.

A frequency response function is complex valued. It can be illustrated by plotting the real and imaginary components of the function versus frequency as well as by plotting the amplitude (termed gain) and phase angle versus frequency. The physical significance of a frequency response function can be thought of as follows: If a linear system were excited with a sinusoidal input of unit amplitude, the response would be sinusoidal with the same frequency as the input, and it would have an amplitude that is given by the gain value and a phase lag that is given by the phase angle. The static response of the system would be given by the 0-Hz value of the amplitude or the real component.

For a pavement system excited with an FWD load, a frequency response function for a given measurement location can be calculated simply as the Fourier transform of the response signal divided by the Fourier transform of the load signal, as suggested by Equation 5. However, considering the influence of measurement noise and the random error that is inherent in frequency response estimates, an equation for an optimal calculation of a frequency response function for the pavement system, using averaged results from a number of FWD experiments, is (*9*)

$$H(f) = \frac{\bar{S}_{xy}(f)}{\bar{S}_{xx}(f)} \tag{6}$$

where

$\bar{S}_{xy}(f)$ = averaged energy cross-spectral density function between load input signals (subscript x) and motion output signals (subscript y),
$\bar{S}_{xx}(f)$ = averaged energy autospectral density function of the load input signals, and
f = discrete frequency sequence.

For a single test record, these functions are related to the Fourier transforms of the load input and motion output sig-

nals, $X(f)$ and $Y(f)$, respectively, by

$$S_{xy}(f) = X^*(f)Y(f) \tag{7}$$

and

$$S_{xx}(f) = X^*(f)X(f) \tag{8}$$

where the asterisk indicates the complex conjugate. For n FWD test repetitions, the averaged functions are calculated by

$$\bar{S}_{xy}(f) = \frac{1}{n}\sum_{i=1}^{n} S_{xy_i}(f) \tag{9}$$

and

$$\bar{S}_{xx}(f) = \frac{1}{n}\sum_{i=1}^{n} S_{xx_i}(f) \tag{10}$$

Eight FWD test repetitions were conducted for the experiments reported here so that the averaging technique of these equations could be followed.

Because the measured signals in this study were force and acceleration histories, "accelerance" frequency-response functions, that is, frequency-response functions relating force inputs and acceleration outputs, were calculated directly from the experimental results. However, of greater interest for the pavement response interpretations in this study were "compliance" functions, or frequency-response functions relating force inputs and displacement response outputs. Compliance functions are inverses of "dynamic stiffness," and reflect the mass, damping, and stiffness response characteristics of a structure. These functions were calculated from the accelerance functions by frequency domain integration. Although the frequency response function calculations are based on linear systems theory, the material responses of pavement systems are inherently nonlinear. For transient excitations such as FWD loads, using Equation 6 results in an equivalent linear estimate of the accelerance or compliance function at a given load level (*11*).

Measurements and Pavement Response Functions

Measurements and data analysis results from the tests at station 20–00 are presented in Figures 1, 2, and 3. The measurements are from the first repetition of the tests. Force and displacement histories from the FWD data acquisition system are presented in Figure 1, and acceleration histories are presented in Figure 2. Although the acceleration signals are shown only to 0.1 sec, the 0.41-sec sample duration allowed the full response transient of the initial FWD load "bounce" to be captured. Of particular interest in this study are the damped oscillations of the displacement and acceleration signals after the load is completely removed. These oscillations indicate that the dynamic response of the pavement is significant.

Compliance functions that were calculated from the load and acceleration measurements are depicted in Figure 3 over the 7- to 200-Hz bandwidth. The functions are presented in a gain and phase format. Data below 7 Hz were unavailable because the test was a dynamic loading test such that the low frequency loading and response of the pavement system was small. The experimental consequence was a low signal-to-

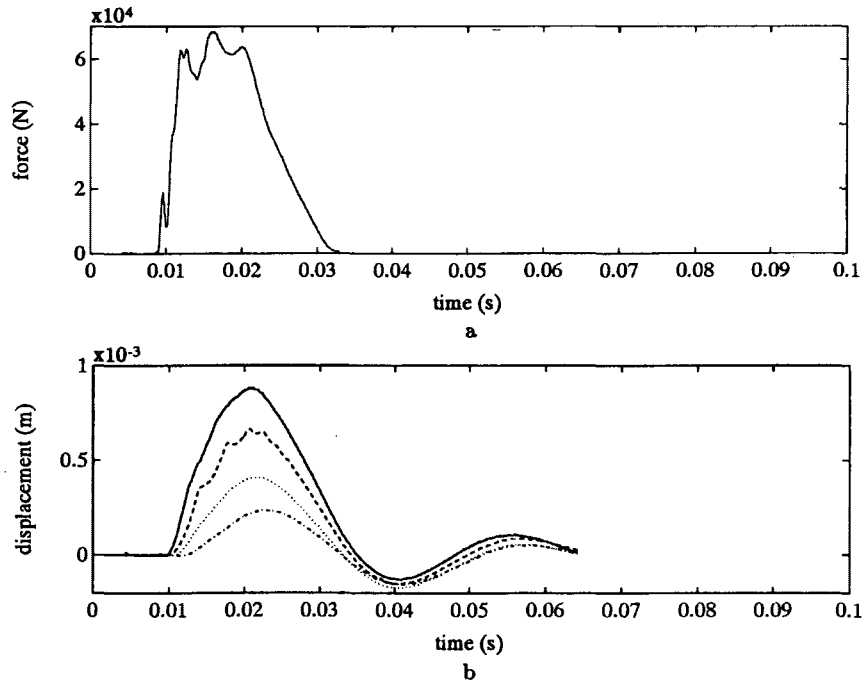

FIGURE 1 Data of first test at location 20-00: (*a*) FWD force history; (*b*) FWD displacement histories from geophones located at 0 m (*solid line*), 0.305 m (*dashed line*), 0.61 m (*dotted line*), and 0.91 m (*dash-dot line*) from load center.

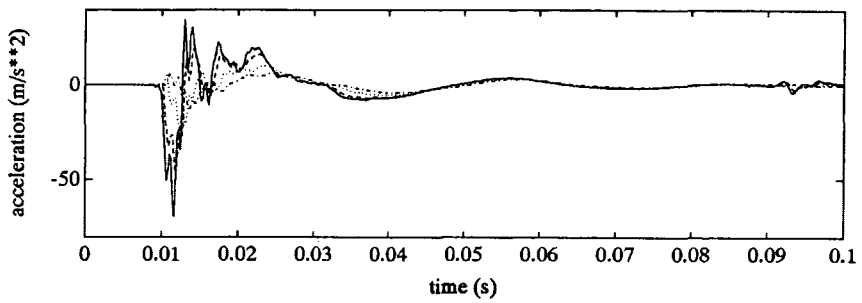

FIGURE 2 Data of first test at location 20-00, acceleration histories from accelerometers located at 0.30 m (*solid line*), 0.45 m (*dashed line*), 0.75 m (*dotted line*), and 1.05 m (*dash-dot line*) from FWD load center.

noise ratio below 7 Hz, which produced errors in the calculated spectral quantities in this bandwidth. The gain spectra contained appreciable peaks around 30 Hz, which indicated that the FWD load excited a resonance of the pavement system. The dominance of the resonance, together with the damped oscillations of the displacement and acceleration histories after the load is zero, provided an experimental indication that the dynamic response of this pavement system should not be ignored for backcalculation of properties.

Bias errors were present in the compliance function estimates as a result of the experimental technique. In particular, the load and accelerometer signals were not synchronous because they were measured using different data acquisition systems, and this introduces an unknown error into the compliance function estimates. An improved measurement system would allow synchronous measurements while providing complete motion responses. In addition, because the tires of the FWD trailer are unloaded when the weight is dropped, the measured load is not the entire disturbance of the pavement.

Compliance functions calculated from measurements of the tests at locations 18-00 and 22-00 are shown in Figure 4 together with a compliance function from location 20-00. These functions reveal a pavement response behavior that is similar to the behavior at station 20-00. The nature of this behavior is examined in the following section.

SYSTEM IDENTIFICATION TECHNIQUE AND RESULTS

A system identification technique based partly on the method presented by Luco and Wong (*12*) for estimating soil properties from dynamic responses of foundations was used for this study. With this technique, pavement system properties were

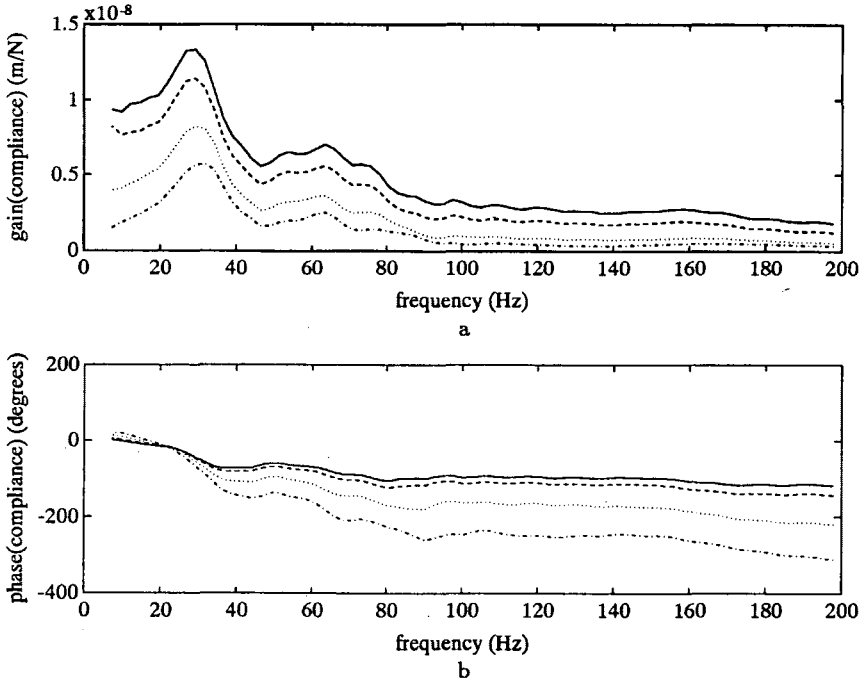

FIGURE 3 Compliance functions for location 20-00 corresponding to locations at 0.30 m (*solid line*), 0.45 m (*dashed line*), 0.75 m (*dotted line*), and 1.05 m (*dash-dot line*) from FWD load center: (*a*) gain spectra; (*b*) phase spectra.

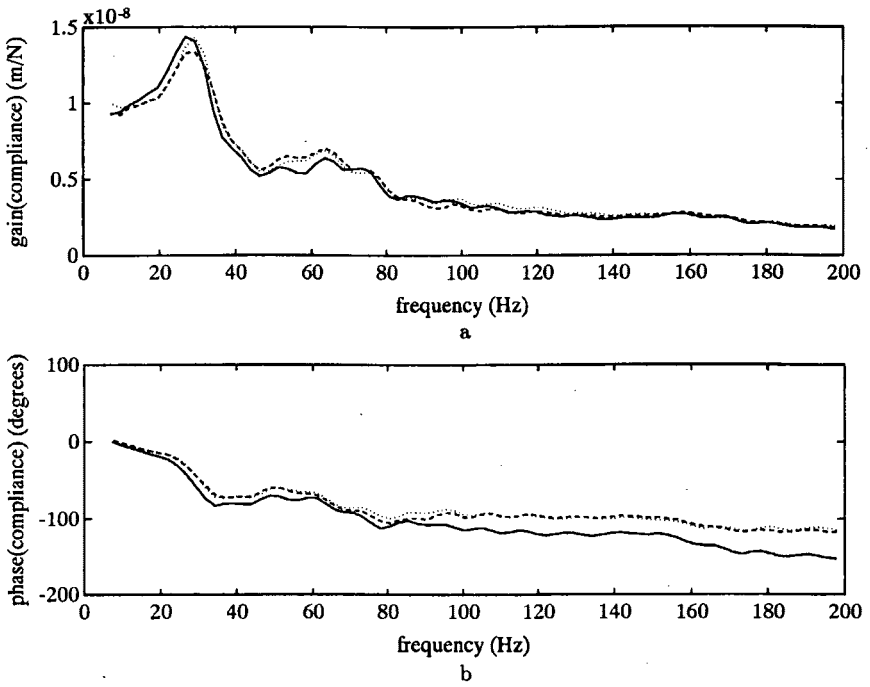

FIGURE 4 Compliance functions for stations 18-00 (*solid line*) and 22-00 (*dotted line*) together with a compliance function from station 20-00 (*dashed line*) for a location 30 cm from FWD load center: (*a*) gain spectra; (*b*) phase spectra.

estimated by minimizing a relative error function that quantifies the difference between compliance function data predicted by a wave propagation model for an FWD test and the experimentally derived compliance functions presented above. The minimization was performed using a "quasi-Newton" algorithm (*6,13*) to vary selected input properties of the model. Real and imaginary data components of the experimental and model compliance functions at selected frequencies were used to calculate the error measure. The wave propagation model is the "thin layer method" described by Kausel and Peek (*7*) and Seale and Kausel (*8*).

The thin layer method is an algorithm for modeling the response of a layered elastic system with hysteretic damping to a dynamic load. It assumes layering of infinite horizontal extent. It has been used by several investigators (*1–3,5*) for FWD pavement response predictions. The thin layer method is a state-of-the-art technique for modeling dynamic pavement response.

Software implementation of the thin layer algorithm (*14*) includes coding of (*a*) the input of elastic constants, mass density, hysteretic damping ratio, thickness for each layer, and the harmonic loading frequency; (*b*) the formation of a wavenumber domain stiffness matrix for the system; (*c*) the solution of the eigenproblem, which provides modes of wave propagation in the form of eigenvalues and eigenvectors; and (*d*) the superposition of the modal solutions for a given load configuration (*7*) for each output location, which may be at any specific radius and layer interface combination. Step d provides the compliance values at the input frequency, and steps b, c, and d are repeated for each harmonic of interest to obtain compliance spectra. The software implementation used for this study is the program PUNCH written by Kausel (*15*). This program can be used to model a vertical, circular, and uniform load in an axisymmetric context, which is applicable to the loading and displacement response of an FWD experiment. The halfspace approximation of Seale and Kausel (*8*) is incorporated so that models of a pavement system over a halfspace can be analyzed.

Analysis and Results

Using the compliance data from location 20-00, an identification analysis was conducted by assuming that an idealized thin layer model of the loading and pavement system could capture predominant features of the experimental compliance functions. In particular, it was assumed that the FWD load was uniform over the area of the loading pad, that the pavement surface course, base course, subbase course, and subgrade are each homogeneous in material properties, and that the material properties do not change significantly across the dominant frequency bandwidth of the FWD load. It was also assumed that the subgrade could be represented by a halfspace. Results from a single analysis are presented here. In the analysis, 13 pavement system properties were selected for identification: the shear moduli, hysteretic damping ratios and Poisson's ratios of the four pavement layers, and the thickness of the subbase course. The subbase thickness was allowed to vary because, as mentioned, the actual constructed thickness is unknown and because the thickness as well as the shear modulus of the subbase course was expected to have predominantly influenced the observed resonant behavior. Maximum and minimum constraints were imposed on the varying properties. Other system properties were held constant throughout the identification iterations.

Compliance function data from the five accelerometer locations and at eleven frequencies were used for the identification analyses. The frequencies that were selected are 9.8, 12.2, 14.6, 17.1, 22.0, 26.8, 31.7, 41.5, 56.1, 75.7, and 100.1 Hz, which are concentrated primarily at the lower frequency end of the spectra and around the resonant feature. The initial property guesses and assumed system constants for the analysis are presented in Table 1. Identification results are presented in Table 2 and in Figures 5, 6, 7, and 8. In Figure 5, compliance values of the model that were based on the initial guesses and assumed constants of Table 1 are shown relative to the experimental functions. The bandwidth of the spectra in this figure is 7 to 117 Hz. It is clear from Figure 5 that the initial guesses are not a good set of properties for this pavement.

In Figure 6 the variations of layer shear moduli, hysteretic damping ratios, Poisson's ratios, and subbase thickness with iteration number are shown. The maximum and minimum constraints were reached only in the variation of the subbase thickness, and these were 1.17 m and 0.94 m, respectively. As indicated in Figure 6, the Poisson's ratios were held constant until Iteration 24.

In Figure 7 the variation of the relative error measure is shown. The relative error was calculated at the sum of the squares of the differences between the model and experimental compliance values, divided by the sum of the squares of the model values. The relative error reached a minimum at Iteration 23 with the Poisson's ratios held constant, and at Iteration 47 with all properties varying.

Figure 8 illustrates the final compliance values of the model relative to the experimental functions. It can be observed that the dominant resonant feature of the compliance functions is captured by the identified model, even though a simple layered system underlain by a halfspace was used to represent the pavement. The estimated values for the varied properties are given in Table 2. Of particular interest for understanding the resonant response are the shear moduli and the subbase thickness. The subbase thickness is a reasonable value close to the design thickness and the shear moduli appear to be reasonable values as well. The latter values quantify the modulus of the "very dense, gravelly silty sand" subgrade, relative to the base and subbase moduli, that is required to cause the resonance.

The compliance spectra of the identified model are shown together with the experimental compliance spectra in Figure 9. The model spectra were calculated using the thin layer method and the identified pavement system properties. The comparison reveals that, as should be expected, the identified model does not capture all features of the experimental compliance spectra. To illustrate the significance of the difference, the identified model was used to predict the pavement displacement response to the FWD load history shown in Figure 1. A comparison of the predicted displacement history for the

TABLE 1 Initial Guesses and Assumed Constants for Identification Analysis, Pavement Location 20-00

layer	h (m)	ρ (kg/m^3)	G (GPa)	ν	D
surface	0.127	2300	(1)	(0.3)	(0.02)
base	0.152	2200	(0.01)	(0.3)	(0.02)
subbase	(1)	1900	(0.01)	(0.3)	(0.02)
subgrade	∞	2100	(0.1)	(0.3)	(0.02)

Symbols: h = layer thickness; ρ = mass density; G = shear modulus; ν = Poisson's ratio; D = hysteretic damping ratio.

Notes: Initial guesses of varying properties are shown in parentheses; Poisson's ratio was not allowed to vary until iteration 24; one discrete layer each was used to model the surface course and the base course; four discrete layers were used to model the subbase course; the subgrade was modeled as four discrete layers in the upper 2 m over a halfspace approximation.

TABLE 2 Backcalculated Values of Pavement System Properties, Pavement Location 20-00

layer	h (m)	G (GPa)	ν	D
surface		3.2	0.30	0.024
base		0.039	0.31	0.021
subbase	0.96	0.018	0.37	0.036
subgrade		0.085	0.43	0.018

Symbols: h = layer thickness; G = shear modulus; ν = Poisson's ratio; D = hysteretic damping ratio.

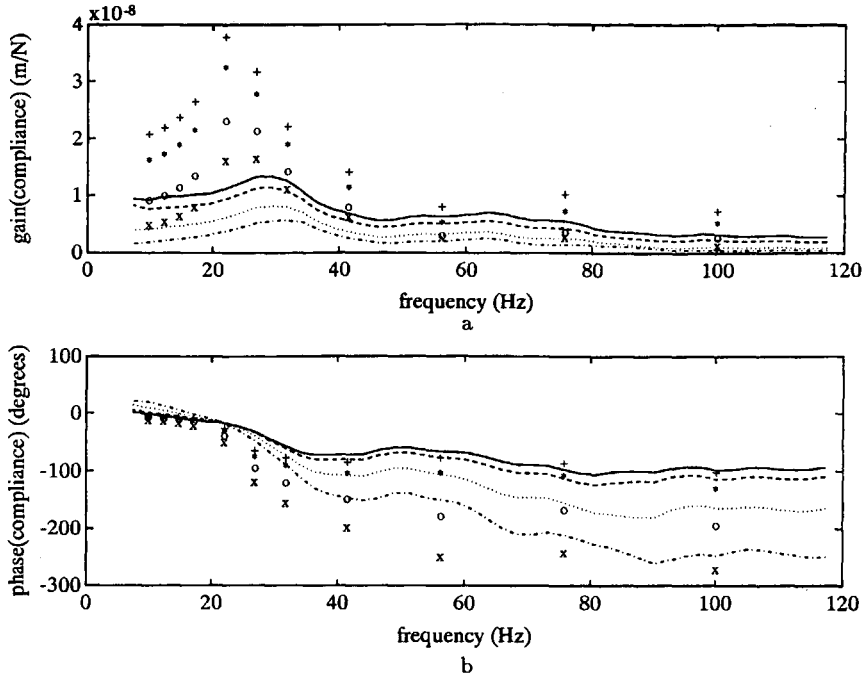

FIGURE 5 Initial compliance values of model relative to experimental compliance spectra for locations at 0.30 m (+, model; *solid line*, experimental), 0.45 m (*, model; *dashed line*, experimental), 0.75 m (○, model; *dotted line*, experimental), and 1.05 m (×, model; *dash-dot line*, experimental) from FWD load center: (*a*) gain spectra; (*b*) phase spectra.

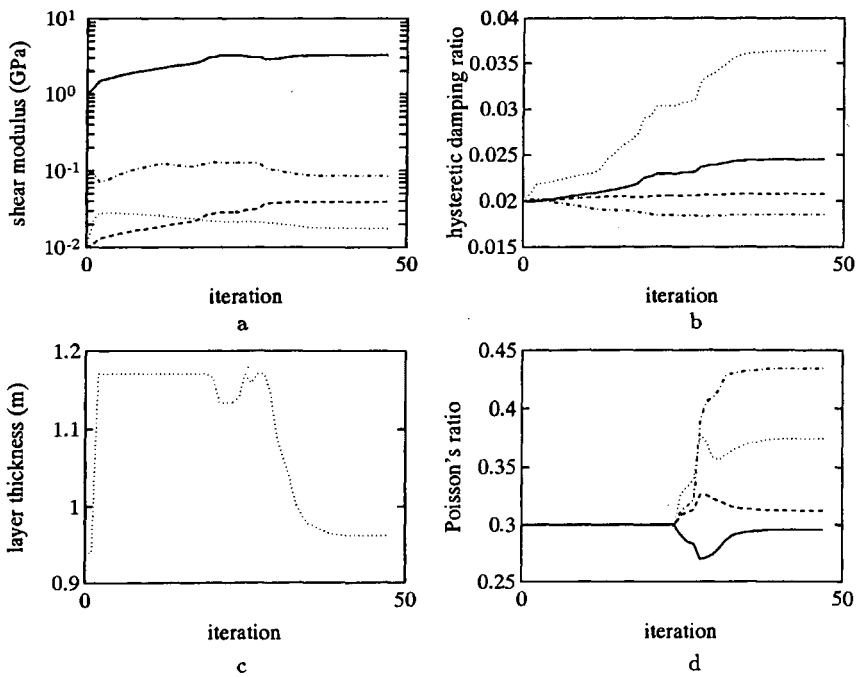

FIGURE 6 Variation of (*a*) shear moduli, (*b*) hysteretic damping ratios, (*c*) layer thickness, and (*d*) Poisson's ratios with iteration number during identification analysis. *Solid line*, surface course; *dashed line*, base course; *dotted line*, subbase course; *dash-dot line*, subgrade.

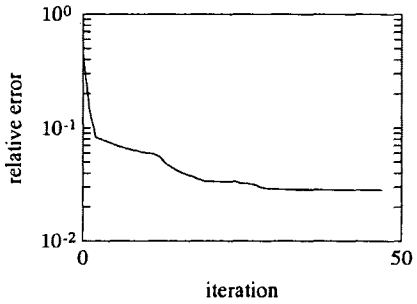

FIGURE 7 Variation of relative error with iteration number.

radial distance 30 cm from the load center with the measured history from the FWD geophone at 30.5 cm is shown in Figure 10. Also shown in this figure are the predicted and measured load versus displacement responses. The comparisons are very favorable and show that the identified model can capture the pavement displacement response to an FWD load, including the damped oscillations after the load is removed, and do so over the complete duration of the transient response. The accuracy of the predictions demonstrates that the identified model is indeed a credible model of the pavement system.

The identified model was further used to predict the static compliance of the pavement as a function of the radial distance from the load center; i.e., the static "deflection basin." This prediction is shown in Figure 11 together with the deflection basin values calculated from the peak load and displacement values from the load cell and geophone data of an FWD test. The figure shows that the deflection basin calculated from the FWD test data is significantly and consistently greater than the static deflection basin calculated from the identified model of the pavement. The comparison suggests that, for this pavement system, the FWD deflection basin should not be used to backcalculate properties using a static pavement system model.

CONCLUSION

The experiments and identification analysis described here comprise the steps of a backcalculation technique that incorporates the dynamic response of the pavement to the FWD load. In practice, this or a similar technique would be a valid backcalculation technique when the peak dynamic displacement during an FWD test is not a good estimate of the static pavement response, that is, when the quasi-static assumption inherent in conventional backcalculation practice is not correct. As several investigators have reported, this can be the case when a pavement is underlain by a rigid or relatively hard layer. This can also be true for cold climate pavements during spring thaw, when a soft thawing soil layer can exist above a hard frozen layer. It is this condition and the need for backcalculation techniques that can be applied to results of FWD tests during spring thaw that have motivated this work. Further developments of FWD backcalculation techniques for cold climate pavements should consider dynamic pavement response and its seasonal variation.

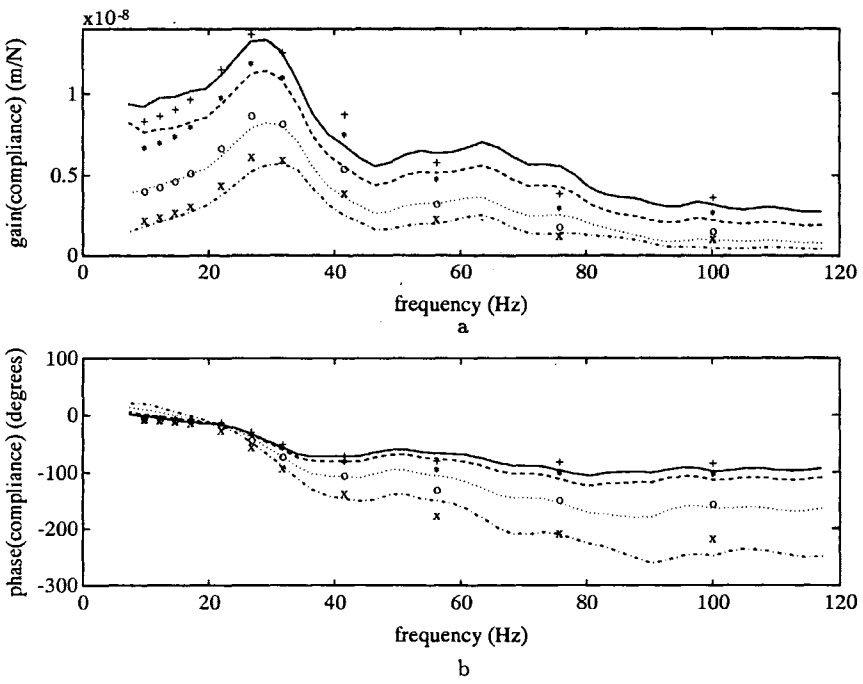

FIGURE 8 Final compliance values of model relative to experimental compliance spectra for locations at 0.30 m (+, model; *solid line*, experimental), 0.45 m (*, model; *dashed line*, experimental), 0.75 m (○, model; *dotted line*, experimental), and 1.05 m (×, model; *dash-dot line*, experimental) from FWD load center: (*a*) gain spectra; (*b*) phase spectra.

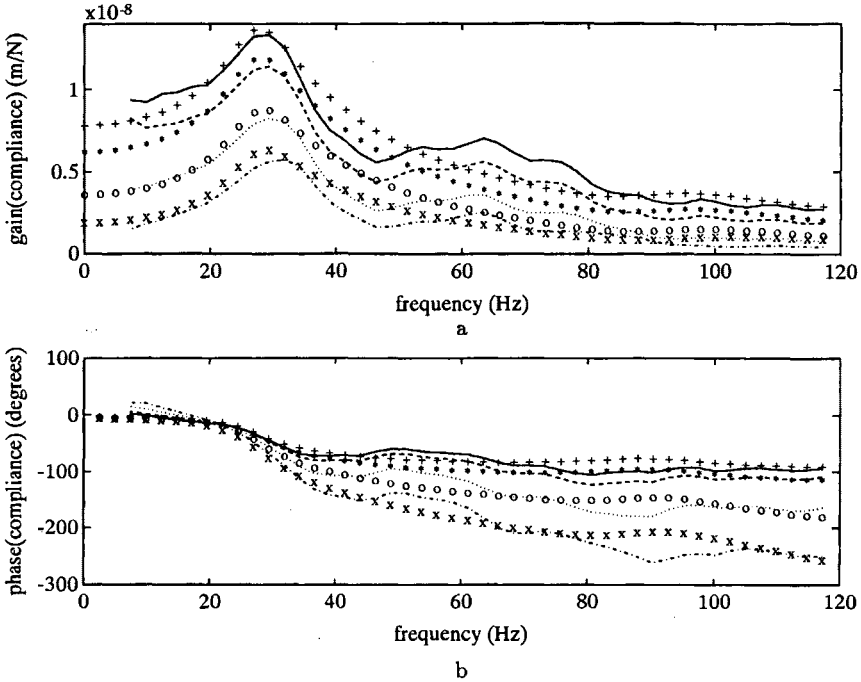

FIGURE 9 Compliance spectra identified model relative to the experimental spectra for locations at 0.30 m (+, model; *solid line*, experimental), 0.45 m (*, model; *dashed line*, experimental), 0.75 m (○, model; *dotted line*, experimental), and 1.05 m (×, model; *dash-dot line*, experimental) from the FWD load center: (*a*) gain spectra; (*b*) phase spectra.

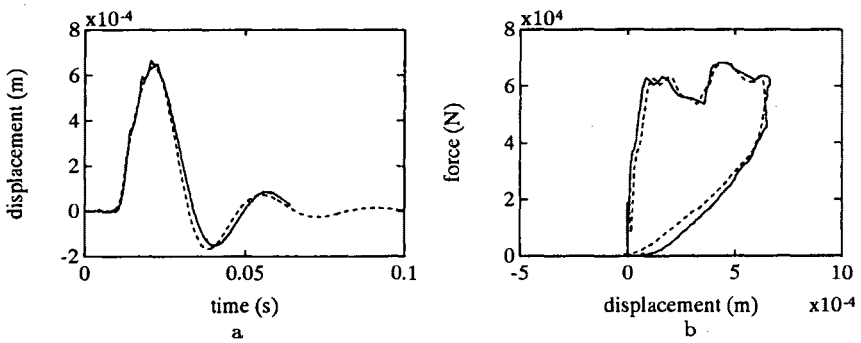

FIGURE 10 Comparison of response predicted using identified model (*dashed line*) for radial distance 30 cm from load center to measured response (*solid line*) at 30.5 cm: (*a*) displacement versus time; (*b*) force versus displacement.

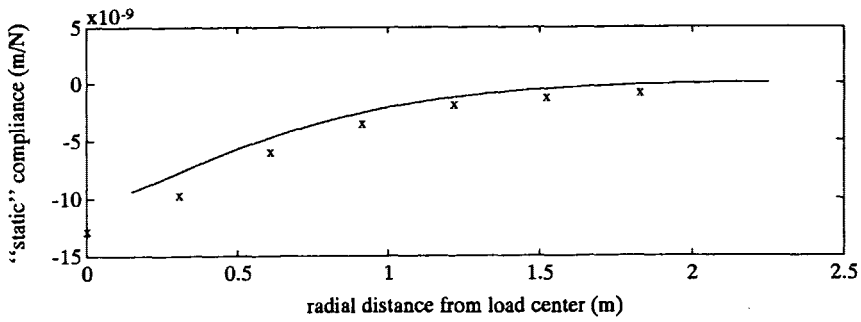

FIGURE 11 Static compliance of pavement as a function of radial distance from load center. *Solid line*: prediction calculated using identified pavement system model; ×, prediction calculated from peak load and displacement values from load cell and geophone data of an FWD test.

ACKNOWLEDGMENTS

E. Kausel of the Massachusetts Institute of Technology provided the software implementation of the thin layer method used for this study. His kind support is sincerely appreciated. Christopher Berini of the U.S. Army Engineer Cold Regions Research and Engineering Laboratory (CRREL) provided capable technical support for the experiments. Funding for this work was provided by the CRREL In-House Laboratory Independent Research Program.

REFERENCES

1. Roesset, J. M., and K.-Y. Shao. Dynamic Interpretation of Dynaflect and Falling Weight Deflectometer Tests. In *Transportation Research Record 1022*, TRB, National Research Council, Washington, D.C., 1985, pp. 7–16.
2. Sebaaly, B., T. Davis, and M. S. Mamlouk. Dynamics of Falling Weight Deflectometer. *Journal of Transportation Engineering*, ASCE, Vol. 110, No. 6, 1985, pp. 618–632.
3. Anderson, M. *Backcalculation of Composite Pavement Layer Moduli*. Technical Report GL-90-15. Army Engineer Waterways Experiment Station, Vicksburg, Miss., 1990.
4. Magnuson, A. H., R. L. Lytton, and R. C. Briggs. Comparison of Computer Predictions and Field Data for Dynamic Analysis of Falling Weight Deflectometer Data. In *Transportation Research Record 1293*, TRB, National Research Council, Washington, D.C., 1991, pp. 61–71.
5. Chang, D-W, Y. V. Kang, J. M. Roesset, and K. H. Stokoe II. Effect of Depth to Bedrock on Deflection Basins Obtained with Dynaflect and FWD Tests. In *Transportation Research Record 1355*, TRB, National Research Council, Washington, D.C., 1992.
6. Dennis, Jr., J. E., and R. B. Schnabel. *Numerical Methods for Unconstrained Optimization and Nonlinear Equations*. Prentice-Hall, Englewood Cliffs, N.J., 1983.
7. Kausel, E., and R. Peek. Dynamic Loads in the Interior of a Layered Stratum: An Explicit Solution. *Bulletin of the Seismological Society of America*, Vol. 72, No. 5, 1982, pp. 1459–1481.
8. Seale, S., and E. Kausel. Point Loads in Cross-Anisotropic Layered Halfspaces. *Journal of Engineering Mechanics*, ASCE, Vol. 115, No. 3, 1989, pp. 509–524.
9. Bendat, J. S., and A. G. Piersol. *Random Data*, 2nd ed. John Wiley and Sons, Inc., New York, 1986.
10. Ewins, D. W. *Modal Testing: Theory and Practice*. John Wiley and Sons, Inc., New York, 1984.
11. Bendat, J. S., and A. G. Piersol. *Engineering Applications of Correlation and Spectral Analysis*. John Wiley and Sons, Inc., New York, 1980.
12. Luco, J. E., and H. L. Wong. Identification of Soil Properties from Foundation Impedance Functions. *Journal of Geotechnical Engineering*, ASCE, Vol. 118, No. 5, 1992, pp. 780–795.
13. Behrens, R. T. *NONLINPK: NESOLVE and UMSOLVE*, Release 1.1. MATLAB User Group Software Archive, NETLIB server, Oak Ridge National Laboratories, 1990.
14. Kausel, E. Wave Propagation in Anisotropic Layered Media. *International Journal for Numerical Methods in Engineering*, Vol. 23, 1986, pp. 1567–1578.
15. Kausel, E. *PUNCH: Program for the Dynamic Analysis of Layered Soils*, Version 3.0. Massachusetts Institute of Technology, 1989.

Publication of this paper sponsored by Committee on Soil and Rock Properties.

Stress-Wave Nondestructive Testing of Tunnels and Shafts

LARRY D. OLSON, DENNIS A. SACK, KENNETH H. STOKOE II, AND KENNETH W. BUCHINSKI

Case histories of the application of stress-wave methods, such as impact echo, impulse response, and spectral analysis of surface waves, to evaluate conditions of concrete-lined tunnels and shafts are presented. These nondestructive evaluation methods provide data on the concrete integrity, the contact condition at the interface between concrete and rock or soil, and the stiffness (velocity, elastic modulus, or both) profile. Conditions such as fractures, void, and comparatively weak materials can all be identified from the test surface without drilling coreholes into the materials. A brief technical description of each nondestructive evaluation method is included along with the respective case history data. In addition, the potential for rapid, near-continuous testing using innovative stress-wave measurement instrumentation with PC-based data acquisition and analysis is discussed.

The evaluation of the condition of tunnel and shaft liners is an area of great concern to both the owners and the users of these structures. Traditional methods of evaluation have been based primarily on visual inspection coupled with destructive coring at selected locations to attempt to relate the visual condition of the liner with the actual conditions. Recent evaluations of tunnel and shaft liners have used nondestructive testing (NDT) techniques based on stress waves to better define the actual in situ conditions of the liner as well as those of the rock or soil behind. The basic advantages of NDT techniques are that they are faster than coring and do not damage the liner material. Thus, a more extensive evaluation of the tunnel and shaft integrity conditions can be undertaken than would be practical with destructive methods. The NDT techniques discussed herein include the spectral analysis of surface waves (SASW), impact echo (IE), and impulse response (IR) methods. Each method was used in a mine shaft liner evaluation case history.

CASE HISTORY BACKGROUND

The mine shaft tested provided vertical access at a potash mine owned by the Potash Corporation of Saskatchewan, Incorporated (PCS Inc.). The shaft was constructed about 25 years ago as the production shaft for one of the PCS Inc. mines in Saskatoon, Saskatchewan, Canada. This NDT investigation was undertaken to evaluate various NDT methods and their overall effectiveness for determining the physical condition of the liners, liner and wallrock interfaces, and, to a lesser degree, the wallrock itself. All testing was conducted under normal field conditions and was subject to the unique constraints associated with a high-production mine shaft. Logistics and effectiveness were assessed to determine the basis for future programs.

The shaft, which was lined with concrete from the ground surface to a depth of 1020 m (3,344 ft), was 4.9 m (16 ft) in diameter. The liner varied in thickness from 0.61 to 1.22 m (2 to 4 ft). The concrete liner thickness in the interval over which the SASW, IE, and IR tests were conducted varied from 0.56 to 0.81 m (22 to 32 in.). Design specification on liner concrete was 34.5 MPa (5,000 psi) minimum, and actual 28-day strengths varied from 37.2 to 48.3 MPa (5,400 to 7,000 psi). Observed concrete conditions were generally good in the shaft, although some mineral deposits had formed on the liner concrete in the lower portions of the shaft, which hindered the testing.

The Prairie Formation, from which sylvinite is mined and that the shaft services, was overlain by 1037 m (3,400 ft) of sediments. Immediately overlying the Prairie Formation was 427 m (1,400 ft) of Devonian carbonates, shales, and evaporites. These layers included the Watrous, Nisku, Duperow, Beaverhill Lake, Upper and Lower Souris River, Davidson, First Red Beds, Dawson Bay, and Second Red Beds. NDT testing was conducted over sections adjacent to the Nisku, Duperow, and Upper and Lower Souris River. The majority of the SASW tests were conducted in the Duperow Formation. The test locations were selected based on a priority list supplied by PCS, which identified those regions that were considered to be most critical and that would give the maximum variety of test conditions to evaluate the various methods. Actual tests were typically performed in a 3.05-m (10-ft) vertical grid within each region for IR and IE tests, with SASW lines interspersed throughout the regions.

NDT TEST METHODS

The NDT methods used included the SASW, IE, and IR methods. Because the majority of the testing was conducted using the first two of these methods, detailed descriptions of these follow. The IR method was used less extensively and proved to be less useful because of the great thickness of the liner concrete [over 0.6 m (2 ft)]. An overview of the IR method is also included because it can be very useful for evaluating thinner concrete liners.

L. D. Olson and D. A. Sack, Olson Engineering, Inc., Golden, Colo. 80401. K. H. Stokoe II, Civil Engineering Department, University of Texas at Austin, Austin, Tex. 78712. K. W. Buchinski, Technical Services, Potash Corporation of Saskatchewan, Inc., Saskatoon, Saskatchewan S7K 7G3, Canada.

Impact Echo Test Method

The IE tests typically involved hitting the surface of the test area at a given location with a small [0.09-kg (0.2-lb)] instrumented impulse hammer to measure the pounds-force of the impact and recording reflected wave energy with an accelerometer receiver mounted with grease on the liner. The IE method was developed at the National Institute of Standards and Technology, Gaithersburg, Maryland, in the 1980s (*1*). A simplified diagram of the method is presented in Figure 1. Because the reflections are more easily identified in the frequency domain, the time domain test data of the hammer and receiver are processed with Fast Fourier Transform (FFT) operations by the dynamic signal analyzer for frequency domain analyses. A transfer function is then computed between the hammer (input) and receiver (output). Reflections or "echoes" of the compression wave energy are typically indicated by pronounced "echo" peaks in the test records that correspond to thickness or flaw depth resonant frequencies. With an echo peak and knowledge of the thickness of the test member, the compression wave velocity can be calculated. Conversely, if the velocity of the concrete is known, the depth of a reflector is calculated from the echo peak frequency. Concrete quality is related to compression wave velocity, and increases in compression wave velocity generally correlate with increased concrete strength and better concrete quality. Correspondingly, poor-quality concrete, damaged concrete, or both result in slower wave velocities that are reflected by lower-frequency echo peaks for a given concrete thickness.

At a concrete-to-air interface, virtually all of the compression wave energy is reflected back into the concrete. This near total energy reflection is due to the large difference in acoustic impedance (Z), which equals velocity (v) times mass density (ρ), between the concrete (high Z) and air (low Z). The geophysical equation governing the amount of energy reflected (R) back into material from an incident wave coplanar with the interface between materials 1 and 2 is as follows:

$$R = (Z_2 - Z_1)/(Z_2 + Z_1)$$
$$= \text{ratio of amount of reflected energy to total energy} \quad (1)$$

In a shaft, if the concrete and rock have similar velocities and densities, very little energy is reflected back into the concrete from the rock interface provided there is good contact (bonding) between the concrete and the rock. In areas where the concrete and rock do not have similar acoustic properties, more energy is reflected from the interface. In the case of cracks, tight cracks produce weaker echoes with deeper echoes still identifiable (if present). An open, air-filled crack completely reflects the energy. A shallow, open crack [typically less than 0.1 to 0.15 m (4 to 6 in.) deep] parallel to the test surface will flexurally resonate and sound hollow and is referred to as a delamination.

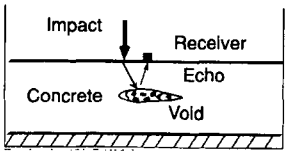

FIGURE 1 Impact Echo test method.

Spectral Analysis of Surface Waves Method

The SASW method is based on the theory of stress waves propagating in layered elastic media. The ratio of surface-wave velocity to shear-wave velocity varies slightly with Poisson's ratio, but it can be assumed to be equal to 0.90 with an error of less than 5 percent for most materials, including concrete and the rock tested in the potash mine shaft. Measurement of the surface-wave velocity with the SASW method similarly allows calculation of compression wave velocity. Knowledge of the seismic wave velocities and mass density of the material layers allows calculation of shear and Young's moduli for low strain amplitudes.

Surface-wave (Rayleigh; R-wave) velocity varies with frequency in a layered system with velocity contrasts, and this frequency dependence of velocity is termed *dispersion*. A plot of surface-wave velocity versus wavelength is called a *dispersion curve*. The SASW tests and analyses are performed in three phases: (*a*) collection of data in situ, (*b*) construction of an experimental dispersion curve from the field data, and (*c*) forward modeling of the theoretical dispersion curve to match the experimental curve and provide the shear-wave velocity versus depth profile.

The SASW field tests consisted of blows to the concrete surface to generate surface-wave energy at various frequencies that was transmitted through the concrete. Two accelerometer receivers were evenly spaced on the surface in line with the impact point to monitor the passage of the surface-wave energy as illustrated in Figure 2. To obtain increasingly deeper data, several tests with different receiver spacings can be performed by doubling the distance between the receivers about the imaginary centerline between the receivers. The tests on the liner were typically conducted with receiver spacings ranging from 11.43 cm to 3.65 m (4.5 in. to 12 ft). For this project, five impacts and the associated receiver responses were typically obtained at each receiver spacing. Also, the impacts were applied typically at each end of a given receiver spacing with the distance from the impact point to the closest receiver about that of the receiver-to-receiver spacing. The

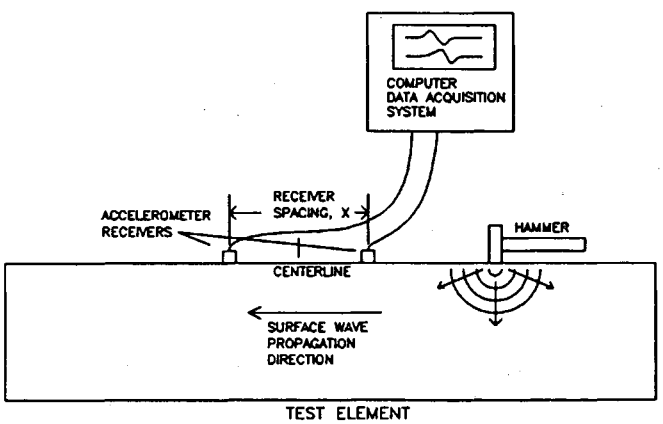

FIGURE 2 SASW test method diagram.

majority of the tests were conducted in the vertical axis of the tunnel to minimize the effects of wall curvature.

A signal analyzer digitizes the analog receiver outputs and records the signals for spectral (frequency) analyses to determine the phase information of the cross power spectrum between the two receivers for each frequency. The dispersion curve is developed by knowing the phase (ϕ) at a given frequency (f) and then calculating the travel time (t) between receivers of that frequency or wavelength by

$$t = \phi/360^*f \quad (2)$$

Surface-wave velocity (Vr) is obtained by dividing the receiver spacing (X) by the travel time at a frequency:

$$Vr = X/t \quad (3)$$

The wavelength (Lr) is related to the phase velocity and frequency by

$$Lr = Vr/f \quad (4)$$

By repeating the above procedure for every frequency, the surface-wave velocity corresponding to each wavelength was evaluated, and the dispersion curve was determined (*2,3*).

Forward modeling is the process of determining the "true" shear-wave velocity profile from the "apparent" velocity of the dispersion curve. The forward modeling process is iterative and involves assuming a shear-wave velocity profile and constructing a theoretical dispersion curve. The experimental and theoretical curves are compared, and the assumed theoretical shear-wave velocity profile is adjusted until the two curves match. The SASW method and an interactive computer algorithm for both two-dimensional and three-dimensional analyses have been developed by Jose Roesset of the University of Texas at Austin to compute a theoretical dispersion curve based on an assumed shear-wave velocity and layer thickness profile.

Impulse Response Test Method

The IR tests were conducted from the surface of the liner. The test equipment included an impulse hammer, a geophone receiver, and a signal analyzer. The tests involved hitting the concrete to generate vibration energy in the liner. The 3-lb impulse hammer had a built-in load cell to measure the force of the impact. The vibration response of the liner to the impact was measured with the horizontal geophone held in contact with the concrete close to the point of impact. The output from the hammer and the receiver was viewed and processed on the signal analyzer. The digital data were stored on magnetic disks for later recall.

The IR test record produced by this test was a plot of mobility (vibration velocity amplitude per pound force) as a function of frequency measured in cycles per second or hertz. The mobility indicates support conditions and stiffness. The greater the mobility, the less stiff is the liner-subgrade system. Support condition evaluation includes two measurement parameters in particular. First, the dynamic stiffness is measured. The slope of the initial straight line portion of the mobility plot indicates the quasi-static flexibility of the system. The low-frequency flexibility provides a general indication of the liner wall stiffness because the inverse of flexibility is dynamic stiffness. The steeper the slope of the line, the more flexible and less stiff is the system. The shape, magnitude, or both, of the mobility at frequencies above the initial straight-line portion of the curve are the second indicators of support conditions. The response curve is more irregular and has a greater mobility for void versus good support conditions because of the decreased damping of the wall vibration response for a void. This factor is not as usable in the case of the mine shaft liner because of the relatively thick cross section of the liner wall. This thick cross section tends to damp vibration responses and thus decreases the difference between the response from void versus sound conditions.

NDT TEST RESULTS

The NDT test results presented include typical results of both the SASW and the IE methods. As stated above, the IR test results were not as meaningful for this application because of the liner thickness and are thus not presented.

Impact Echo Records and Results

The integrity of the concrete liner was nondestructively investigated with the IE method in 86 tests at 77 stations. The IE method is a sonic echo test that measures concrete thickness, evaluates concrete quality, and detects flaws from one surface as detailed previously in this paper.

Representative IE Test Record

A typical IE test record is presented in Figure 3 for the case of a sound concrete liner backed by rock of a slower velocity. The IE test is most sensitive to cracking and interfaces parallel to the test surface because of the test configuration. The top trace in the figure is the coherence of the transfer function data, indicating data quality. A coherence near 1.0 indicates good quality, repeatable data. The bottom trace in the figure is the doubly integrated transfer function between the hammer and the accelerometer, giving vertical axis units of millimeters displacement of the surface per newton input by the hammer. The horizontal axis is linear frequency measured in thousands of hertz. The depth indicated in the sample record was calculated based on a compression-wave velocity of 3813 m/sec (12,500 fps). This value was obtained from the average compression-wave velocity as measured on the cores and corrected for use with the IE method. Note that compression-wave velocities measured with the ultrasonic pulse velocity (UPV) scanning system are typically 10 percent higher than those found using the IE method (*1*). In the record, the clear, single echo peak that corresponds to multiple reflections of the wave energy from the backside of the liner is apparent at 2.35 kHz. Using a velocity of 3813 m/sec, a thickness of about 0.81 m (33 in.) was calculated, which is reasonable considering the potential overbreak. Because no other higher-frequency echo peaks indicative of potential flaws were identified, this IE location is indicated to have sound concrete.

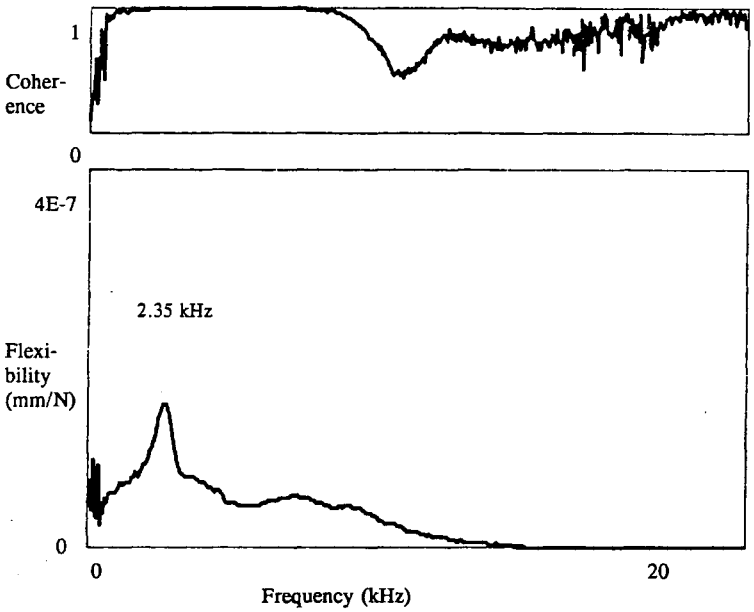

FIGURE 3 Impact Echo test record (sound concrete conditions).

IE Test Results

The IE results were analyzed to identify significant echo peak frequencies and condition ratings assigned according to criteria developed for typical IE data. These IE results showed the ability of the IE method to evaluate concrete liner thickness and integrity conditions, even under the difficult field conditions in the vertical shaft. The results also showed that this method is also useful in giving some indication of the relative velocity and bonding conditions at the rock-concrete interface, although it is not as useful as the SASW method in this type of evaluation.

SASW TEST RECORDS AND RESULTS

The SASW method is comparatively new; it was developed to determine shear modulus profiles with depth in layered systems such as pavements and earth (*4,5*). The method is based on the field measurement of surface-wave velocity as a function of wavelength and subsequent theoretical modeling to determine the shear-wave velocity profile versus depth. The SASW method is capable of determining the "stiffness" and thickness profiles for layered concrete, pavement, soil, and rock systems without drilling borings. (The SASW method was detailed earlier in this paper.)

SASW Phase Record

A sample phase record from the SASW testing is shown in Figure 4, which is an example of a good-quality phase data record. The record plots phase versus frequency. The trace in the plot has the phase difference between the two received signals on the vertical axis in degrees, with phases of less than −180 degrees or greater than 180 degrees being "wrapped" with a vertical line. The horizontal axis is the frequency in hertz. Not shown is the coherence plot for these data, which indicated almost perfect coherence (near 1.0) for the entire frequency range. Note that it is possible that a phase can be accurate, even with poor coherence, if the test results are consistent and enough averages can be obtained. A total of 360 degrees of phase (−180 to 180 degrees) represents one wavelength, which equals the receiver-to-receiver spacing for a given test, and one cycle of surface-wave energy at a given frequency. The calculation of surface-wave velocity for 360 degrees of phase (one wavelength) is determined from the wave frequency at the one wavelength point in Figure 4.

SASW Results of Dispersion Curve and Inversion Analyses

Dispersion curves were calculated from the phase data for each survey line where sufficient quality measurements could be obtained. These curves were then used to determine the layer depths and the condition at each point. The dispersion curves were calculated from the raw data after the data were "masked" to eliminate data in frequency ranges with poor coherence or other obvious "glitches" in the phase data. The SASW phase data measurements were complicated by the existing variety of surface conditions, including the surface deposits present in some parts of the shaft. Nonetheless, SASW measurements were able to provide data on most tested locations.

SASW Inversion Analyses for Shear-Wave Velocity versus Depth Profiles

A typical dispersion curve and the shear-wave velocity profile computed from it are presented in Figures 5 and 6. The dispersion curve plots surface-wave velocity versus wavelength, and the velocity profile plots shear-wave velocity in feet per

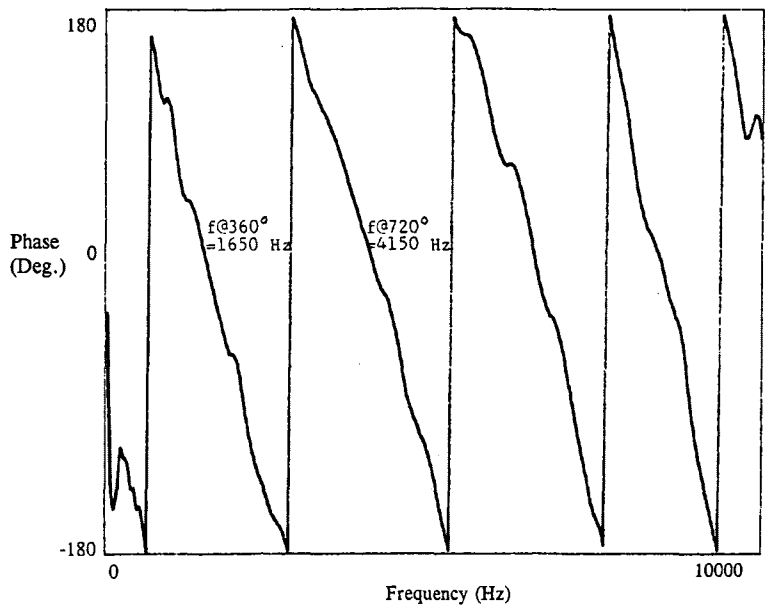

FIGURE 4 Sample phase/frequency plot from an SASW test.

second versus depth into the shaft wall concrete and rock in feet. A total of 11 SASW measurement locations were inverted at the University of Texas at Austin. The theoretical inversion analyses were reviewed by one of the authors (Stokoe). Only one SASW location had insufficient data quality that prevented inversion.

Inversions were performed of representative test locations to compute the theoretical shear-wave velocity versus depth model (inversion) that best matches the field experimental dispersion curve data. The field dispersion curve data and two-dimensional and three-dimensional (more accurate) theoretical inversion analysis produced dispersion curves that present the data in terms of velocity versus wavelength, whereas the final inversion process produced a plot of velocity versus depth. The dispersion curves are typically plotted with velocity on the vertical linear axis scale and wavelength in feet on a horizontal logarithmic (base 10) scale. The shear-wave velocity profiles are plotted on linear scales with velocity on the horizontal axis and depth of each analysis layer on the vertical axis in feet.

The inversion curve presented (velocity versus depth profile) is from station 2110 and shows the constant good velocity [about 3000 m/sec (9,840 fps)] of the liner concrete out to about 0.91 m (3.0 ft), followed by an abrupt transition to the rock velocity of about 2500 m/sec (8,200 fps). Thus, the data for this location showed competent concrete followed by competent but less stiff rock with no appearance of a debonding or void zone between them. In the associated dispersion curve,

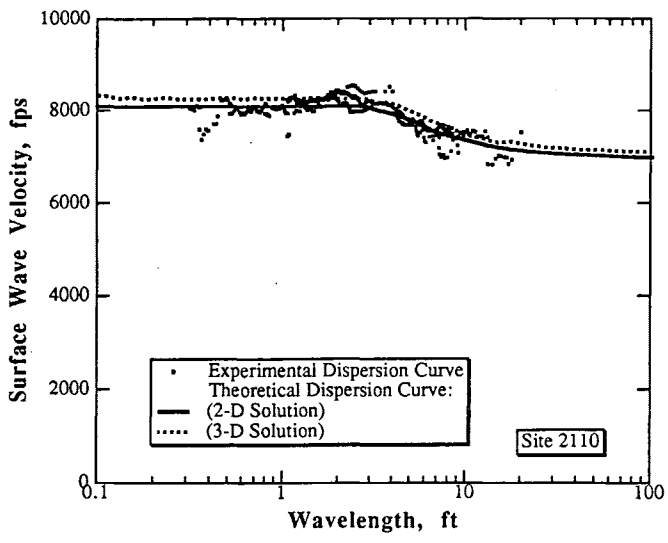

FIGURE 5 SASW dispersion curve (sound concrete over slower rock).

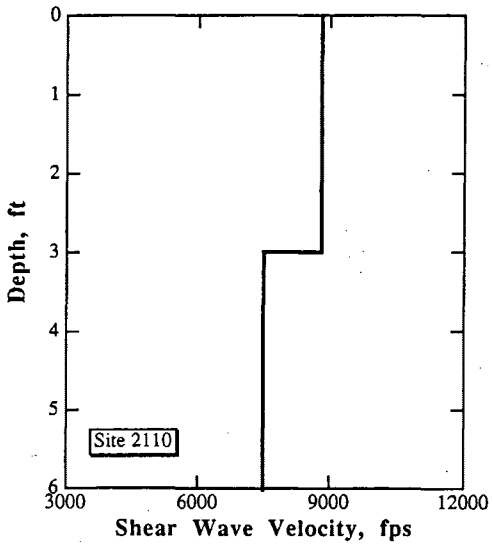

FIGURE 6 SASW velocity profile (sound concrete over slower rock).

the transition is evident as a smooth change from the velocity of the concrete only to that of the rock only as the wavelength increases.

The overall inversion results indicated shear-wave velocities of up to 3048 m/sec (10,000 fps) in the near-surface concrete with underlying rock velocities ranging from 1890 to 3354 m/sec (6,200 to 11,000 fps). The SASW results indicate that 9 of the 12 locations tested had relatively high-velocity (indicating higher quality) concrete with relatively high-velocity, sound rock behind. The remaining points had either poor-quality test data or other anomalies in the results. One important finding from the SASW data was that at every point tested where wavelengths into the rock layer were generated and measured, the rock layer shear-wave velocity was ≥1830 m/sec (6,000 fps). In addition, at locations where the surface-material velocity was slower (degraded surface conditions), the shear-wave velocity continued to improve with depth. These results indicate that, in general, only the surface of the liner has been significantly affected by surface deposits or other conditions at the points tested.

IMPULSE RESPONSE TEST AND RESULTS

Concrete liner support conditions and stiffnesses were nondestructively evaluated with the IR method. The IR tests detect and define the extent of good versus poor support conditions, but do not provide information on the depth of void and may not easily differentiate between back-side voids and near-surface delamination cracking. The method was developed from a forced-response modal vibration test for investigating the integrity of deep foundations and was originally adapted for slabs and tunnels by a European group.

The IR method is useful to determine the support conditions of the material behind a tunnel liner, provided the stiffness of the tunnel liner is not too high. For this investigation, the stiffness of the 0.6- to 0.9-m (2- to 3-ft) thick liner did not allow differentiation between good versus poor substrate support conditions. The method has been used successfully on other tunnel liners and slabs with thinner cross sections.

NDT METHOD EVALUATION

Of the three methods used on this shaft, the IE and SASW methods appear to provide the most useful information as to the condition of the concrete liner, interface, and rock conditions. When performed together, these two methods are able to effectively and fairly quickly evaluate the overall condition of a mine shaft liner, especially if used in conjunction with limited coring to establish overall velocities and other baselines. The results also agreed well with the destructive (coring) results, with the SASW-determined shear-wave velocity agreeing to within 5 percent of the shear-wave velocity in a core at the same point (2885 m/sec from SASW versus 2911 and 2776 m/sec from the cores). The IR method does not appear to be as useful for the thick shaft liner tested, although it should perform much better in thinner-walled linings. The NDT methods used for this investigation are all fairly quick relative to other methods (especially coring), but actual testing time will vary significantly depending on the actual shaft liner conditions. This investigation was carried out in three night shifts. The investigation extended over nearly 305 m (1,000 ft) of the south side of the shaft liner with much of the liner requiring chipping of surface deposits to test.

RECENT NDT TECHNIQUE DEVELOPMENTS

Recent developments in the equipment used for several of the more common NDT methods promise to greatly increase the speed and utility of these methods. One development that will aid in testing tunnel liners is the IE scanning system, which will allow the performance of rapid, close-spaced IE tests on any relatively smooth, continuous concrete or rock surface.

The IE scanning system (patent pending) is diagrammed in Figure 7. It is similar to the UPV scanning system, which was developed in conjunction with this system and uses much of the same hardware. The IE scanner is used from only one surface and requires only one scanner unit, which encompasses both signal source and receiver. The IE scanner is composed of an electrically driven solenoid with an impulse hammer mounted to it and a coated piezoelectric ceramic receiver that is used to pick up the echo signals. The electrical impulses to drive the hammer can be generated automatically based on time or distance, or manually from an operator switch. This allows the maximum flexibility for IE testing at various speeds, locations, and data densities.

The IE test involves impacting the concrete at a point. A surface receiver measures the vibration of the concrete. With the scanning system, the surface receiver rolls while measuring vibration responses to the hammer impacts. An analysis of the return echo resonant frequency peaks of the test results provides information on the condition of the concrete.

An IE scan of a concrete slab on grade is presented in Figure 8. The scan covers about 0.7 m (2.25 ft) of the 127-mm (5-in.) thick slab. The scan is presented as a three-dimensional waterfall plot that is composed of the data records from each of about 10 individual test points. In the plot, the series of peaks at about 1.30 kHz corresponds to echoes from the back side of the slab with a concrete compression-wave velocity of about 3300 m/s (10,800 fps). If a defect were present, it would show as a series of adjacent, matched frequency peaks at a frequency higher than the backside frequency. Due to the close spacing of adjacent test points, intermittent peaks at lower and higher frequencies are indicated because of random noise and frame vibrations. Because the intermittent peaks

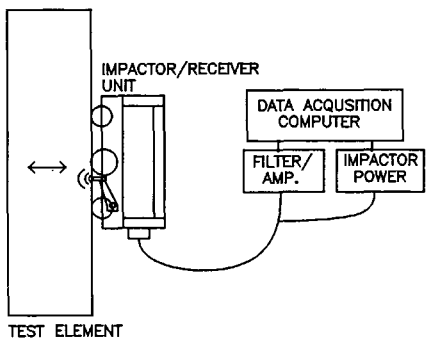

FIGURE 7 Impact Echo scanner system.

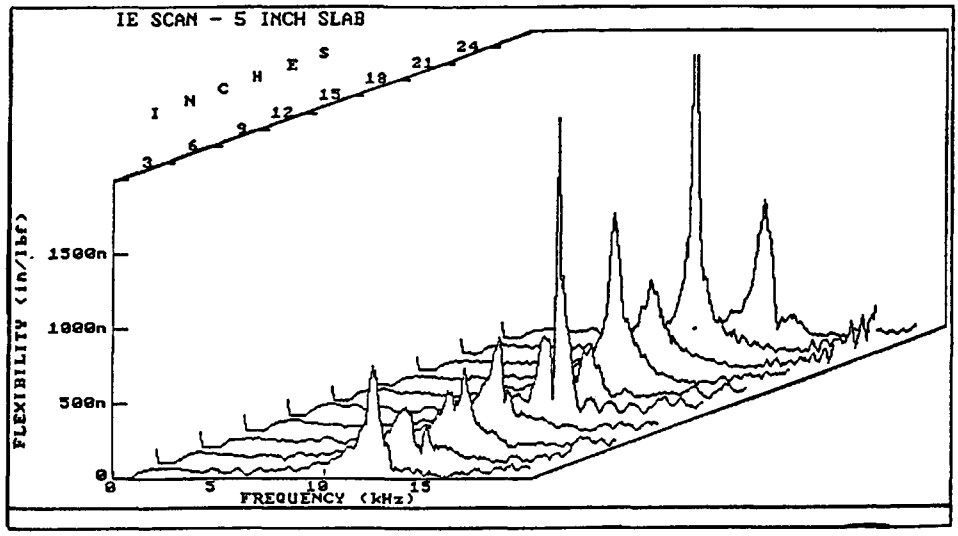

FIGURE 8 Impact Echo scan of a sound concrete slab.

did not repeat in adjacent tests, this indicates that they do not represent structural defects or other elements.

The individual data records that make up the scan are plots of vibration displacement (integrated from the accelerometer output) as a function of frequency. The dominant frequency peaks at 13.0 kHz correspond to the periodic compression wave reflections between the front and back sides of the slab.

As can be seen, the IE scanning system promises to greatly improve the speed and utility of the IE method for field applications, especially for large structures such as tunnel and shaft liners. Currently, efforts are under way to develop such a scanning system for SASW tests as well. These scanning technologies in turn are expected to eventually result in a completely automated pipe-tunnel-shaft liner testing system that would be capable of conducting a complete NDT evaluation of a structure with minimal down time and interaction.

REFERENCES

1. Sansalone, M., and N. J. Carino. *Impact-Echo: A Method for Flaw Detection in Concrete Using Transient Stress Waves*. Report NBSIR 86-3452. National Bureau of Standards, Gaithersburg, Md., Sept. 1986.
2. Roesset, J. M. Nondestructive Testing of Soils and Pavements—The SASW Method. Presented at the International Conference on Analytical and Experimental Methods in Mechanics, May 1989.
3. Nazarian, S., and M. Baker. A New Nondestructive Testing Device for Comprehensive Pavement Evaluation. *Proc., Nondestructive Evaluation of Civil Structures and Materials Conference*, University of Colorado at Boulder, 1992.
4. Bay, J. A., and K. H. Stokoe II. Field Determination of Stiffness and Integrity of PCC Members Using the SASW Method. *Proc., Nondestructive Evaluation of Civil Structures and Materials Conference*, University of Colorado at Boulder, 1990.
5. Nazarian, S. *In Situ Determination of Elastic Moduli of Soil Deposits and Pavement Systems by Spectral-Analysis-of-Surface-Waves Method*. Ph.D. thesis. The University of Texas at Austin, 1984.
6. Nazarian, S., and K. H. Stokoe II. *In Situ Determination of Elastic Moduli of Pavement Systems by SASW Method (Practical Aspects)*. Report 368-1F. Center for Transportation Research, The University of Texas at Austin, 1985.
7. Nazarian, S., and K. H. Stokoe II. *In Situ Determination of Elastic Moduli of Pavement Systems by SASW Method (Theoretical Aspects)*. Report 437-2. Center for Transportation Research, The University of Texas at Austin, 1986.
8. Penderson, C. M., and L. T. Senkowski. Slab Stabilization of PCC Pavements. Presented at the 65th Annual Meeting of the Transportation Research Board, Washington, D.C., 1986.

Publication of this paper sponsored by Committee on Soil and Rock Properties.

Tomographic Imaging Stress Changes in Soil Media

J. C. SANTAMARINA, J. GRAHAM, C. MACDOUGALL, AND V. ROY

The stiffness of particulate media and the velocity of wave propagation are determined by the state of stress. Therefore, boundary measurements of travel time can be inverted to determine the field of velocity and converted to image the state of stress. Results from a simulation study are presented for the cases of footings and tunnels. The underlying assumptions in the simulation are highlighted and difficulties in field implementations are discussed.

The mechanical behavior of soils is determined by the state of stress. The relationship between strength and state of stress is represented in failure criteria such as Mohr-Coulomb. On the other hand, the analysis of particulate arrangements clearly shows the effect of the stress field on deformation parameters (Hertz theory).

It is difficult to measure the state of stress in particulate media. Current technology is based on local measurements with transducers. The presence of the transducer and its relative stiffness affect the measurement. The combined use of stress waves and tomographic inversion to image the field of stress in a medium is discussed. In this case, sources and receivers are mounted on the boundary of the region, with minimum perturbation, and an image of the distribution of the wave velocity is generated by means of mathematical inversion. Finally, velocity (V) is interpreted in terms of stress (σ) by appropriate "constitutive" equations ($\sigma \Leftrightarrow V$).

TOMOGRAPHY

Tomography is an imaging technique based on multiple transmission measurements of time or attenuation. Tomographic reconstruction is the inversion of these spatially averaged boundary measurements, either travel time or amplitude, to determine the field of material parameters in an "unknown space" [see Figure 1 (*a*)].

A possible approach is to discretize the region into pixels [see Figure 1 (*b*)]. Measured travel times are expressed in terms of pixel velocities and travel lengths estimated from assumed ray paths. Assuming a straight ray, the ray path is obtained by joining the source S_a and the receiver R_a; the distance traveled by the ray in pixels 1 and 2 is readily determined (d_{a1} and d_{a2}), and the travel time t_a can be expressed as

$$t_a = \frac{d_{a1}}{V_1} + \frac{d_{a2}}{V_2} \tag{1}$$

where the unknowns are V_1 and V_2. The inverse of the velocity is often referred to as the "slowness" (s). The following equations are written for all the measured travel times [see Figure 1 (*c*)]:

$$\begin{aligned} t_a &= d_{a1} \cdot s_1 + d_{a2} \cdot s_2 \\ t_b &= d_{b3} \cdot s_3 + d_{b4} \cdot s_4 \\ t_c &= d_{c1} \cdot s_1 + d_{c3} \cdot s_3 \\ t_d &= d_{d2} \cdot s_2 + d_{d4} \cdot s_4 \end{aligned} \tag{2}$$

In general, these equations can be written as

$$t_i = \sum_j d_{ij} s_j \tag{3}$$

and the system of Equations 2 can be presented in matrix form,

$$T = D \cdot S \tag{4}$$

where

T = vector of n measured travel times,
D = $n \times m$ matrix of estimated travel lengths, and
S = vector of m unknown pixel slowness.

The goal of inversion is to solve Equation 4 to determine S; then the image is rendered by coloring pixels. For example, gray levels are selected according to the pixels' slowness.

The system of Equation 3 is easily solved for the four unknown values of slowness. In finer grids, normal rays are insufficient; for example, there are six source locations (a–g) yet nine unknown values of pixel slowness in Figure 1 (*d*). Furthermore, not all faces of the unknown region are accessible. In practice, a wave from a source is detected by multiple receivers [see Figure 1 (*e*)]. The result is a system of equations where the number of measured travel times exceeds the number of pixels ($n > m$).

The goal of tomographic reconstruction is to find the best estimate of S. Iterative methods are used to solve the inversion problem and overcome difficulties related to the nature of the problem (e.g., large, sparse, ill-conditioned matrices). Other

J. C. Santamarina, J. Graham, and C. MacDougall, Department of Civil Engineering, University of Waterloo, Ontario N2L 3G1, Canada, V. Roy, Department of Geological Engineering, University of Waterloo, Ontario N2L 3G1, Canada.

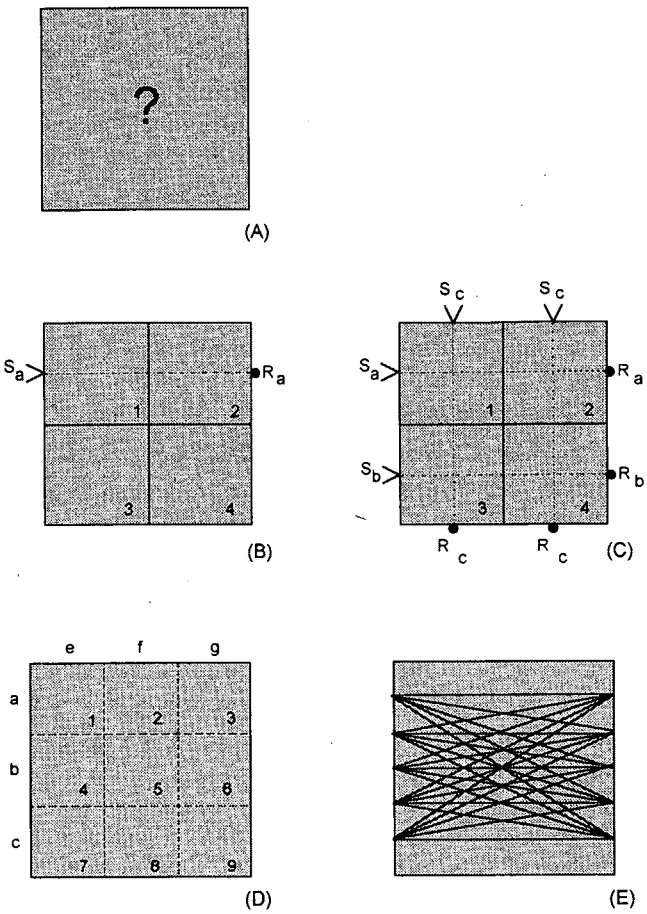

FIGURE 1 Tomographic inversion: (*a*) unknown space; (*b*) discretization into pixels; (*c*) measurement of travel times; (*d*) solution for unknown values of slowness; (*e*) detection by multiple receivers.

solutions include Snell's relations for reflection and refraction, full time series (Fourier slice theorem), and fuzzy logic (norm minimization).

SIMULATION STUDY: PROCEDURE AND ASSUMPTIONS

Step 1: Computation of In Situ and Induced Stresses

The cross section under study is discretized in pixels. At the center of each pixel, the in situ state of stress is computed assuming at-rest conditions, whereas induced stresses are approximated using linear elastic solutions.

Step 2: Computation of Pixel Velocities

Once the state of stress is known, the velocity of wave propagation in the pixel is estimated with constitutive equations that relate stress and velocity ($\sigma \Leftrightarrow V$). Multiple correlations have been proposed between the effective mean confining stress σ'_{mean} and the maximum shear modules G_{max}, shear-wave velocity V_s and compressional wave velocity V_p. However, laboratory experiments in the 1970s and 1980s and simulations with micromechanics have shown that the propagation of P-waves depends primarily on the stress along the direction of propagation (σ_{par}) and that the propagation of S-waves is conditioned by the stresses on the polarization plane (*1*):

$$V_p = \kappa_p \cdot \sigma^{\alpha}_{par} \tag{5}$$

$$V_s = \kappa_s \cdot \sigma^{\beta}_{par} \cdot \sigma^{x}_{nor-1} \cdot \sigma^{\delta}_{nor-2} \tag{6}$$

The constants in these constitutive equations are readily determined in the laboratory. In the case of this study, a true triaxial device was used: a piezocrystal source and sensors were buried in the sample during soil placement, and wave velocities were determined at different states of the stress history. For the purpose of this study, it was assumed that the velocity of propagation V (m/sec) was proportional to the mean stress σ_{mean} (kN/m^2) such that

$$V = 50 + 90 \cdot \sigma^{0.25}_{mean} \tag{7}$$

This corresponds to a nonuniform, vertically heterogeneous isotropic medium, where the velocity increases with depth. A nominal surface velocity of 50 m/sec was used to reduce numerical difficulties related to shallow measurements. In practice, most field cases involve a minimum overburden. (Long and shallow rays should be avoided because of biases induced by excessive ray curvature.)

The exponent $\alpha = 0.25$ corresponded to angular, crushed quartzitic sand. Lower values of α were found in uniform sands with round grains. The higher the α-coefficient, the more significant the effect of stress changes on velocity changes and the lower the effect of noise (such as measurement errors) in the solution. In simulation studies without noise, any realistic value of α can be equally resolved.

Step 3: Computation of Travel Times

Travel times were measured in situ. A digital storage oscilloscope (triggered by a transducer mounted at the source) recorded the source and receiver signals. The relative position of the traces was used to determine travel time. In this study, configurations of sources and receivers simulated real field conditions. Travel times were then integrated along straight rays joining each source and receiver position (Equation 2).

Step 4: Tomographic Inversion

Standard tomographic images were reconstructed using the ART algorithm (*2*). The variation or δ-image was then obtained by subtracting inverted pixel velocities from two consecutive images. In this case, the images obtained were with in situ and combined stresses. The normalized stress change $\Delta\sigma/\sigma_0$ can be obtained from the normalized variation image $\Delta V/V_0$ as

$$\frac{\Delta\sigma}{\sigma_0} = \sqrt[\alpha]{1 + \frac{\Delta V}{V_0}} - 1 \tag{8}$$

SIMULATION CASE STUDIES

Case 1: Strip Footing

The footing was loaded on a semiinfinite medium, characterized by an anisotropic, vertically heterogeneous initial state of stress. Induced stresses were computed using Boussinesq's solution integrated for strip footings. Plane strain was assumed to complete the state of induced stress. The following parameters were used: unit weight of soil $\gamma = 20$ kN/m^3, coefficient of earth pressure at rest $k_0 = 0.4$, Poisson's ratio $\nu = 0.3$, load $q = 100$ kN/m^2, and footing width $B = 2$ m. The imaged cross section was 10 × 10 m. Sources were placed along the right and left sides of the section, and receivers were placed along the left, right, and top sides.

Tomographic reconstruction was based on a 15 × 15 grid. Figure 2 shows (*a*) the image of the in situ state of stress, (*b*) the image of the combined state of stress, and (*c*) the δ-image. Notice the similarity between this image and the stress bulbs predicted by Boussinesq's solution.

Case 2: Multilayer System

A two-layer system loaded with a circular imprint simulates a wheel on a pavement (This problem was first suggested by Stokoe, University of Texas.) In situ stress within the granular layer (Layer 2) was computed using soil $\gamma = 20$ kN/m^3 and an isotropic coefficient $k_0 = 1.0$. Induced stresses were obtained for the two-layer solution (*3*), with $\nu = 0.5$, load $q = 179$ kN/m^2, footing radius $r = 0.3$ m, first-layer thickness $h_1 = 0.3$ m, and relative stiffness $E_1E_2 = 10$.

Tomographic images were limited to the granular base and were generated for the combined state of stress for a 0.6 × 0.6 = m section. Assuming that installation of full instrumentation was possible during construction, travel time data were generated for sources on the left and right sides of the cross section. Sensors were assumed to be installed on left and right sides, between Layers 1 and 2, and within Layer 2 at a depth of 0.6 m.

Simulations with the load (*a*) far from the cross section, (*b*) at the boundary of the cross section, and (*c*) at the center of the cross section were examined (Figure 3). The reconstruction was based on a 12 × 12 grid. In Simulations b and c, the induced stress prevailed over the in situ component, and the field of induced stress became apparent without the need to generate δ-images. The redistribution of stresses within the granular bases by the stiff pavement is clearly shown in the image.

Refracted waves traveling through the faster upper layer were not considered. In field applications, this effect can be minimized by properly selecting the spacing of transducers.

Case 3: Tunnel

For a long circular excavation, stresses were computed by means of Kirsch's solution for an elastic semiinfinite medium and the plane strain condition. The homogenous boundary stresses were estimated assuming that the axis of the tunnel was at a depth of 40 m, soil $\gamma = 20$ kN/m^3, $k_0 = 0.4$, and $\nu = 0.3$. Two tunnels, with diameters of 4 m and 8 m, were modeled. Travel time data were generated simulating the two-borehole tomographic setting with a 20-m spacing. The model assumed 10 sources in one borehole and 10 receivers in the other.

Images were resolved in 10 × 10 pixels, covering the 20- × 20-m region. Images indicated that stresses were low at the crown and the invert of the tunnel but high on the springlines. Although this exercise deviates from reality (e.g., neither support nor plastic regions are involved), the difficulties encountered in this case hint that even greater difficulties will be encountered in real field conditions.

DIFFICULTIES IN FIELD IMPLEMENTATION

Information Content

The images presented previously were generated using different amounts and distributions of information content. The best field setting corresponds to the circular footing on the two-layer medium, where the large number of sources and receivers placed around the cross section led to a high and well-distributed information content. The worst case is the cross-hole configuration used in the tunnels, where most of

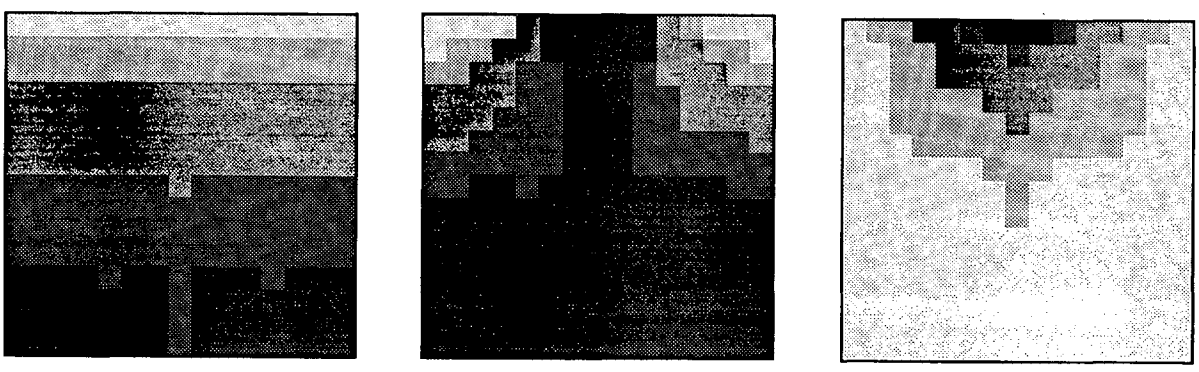

FIGURE 2 Strip load on semiinfinite medium: (*a*) in situ conditions; (*b*) in situ and induced stresses; (*c*) variation image.

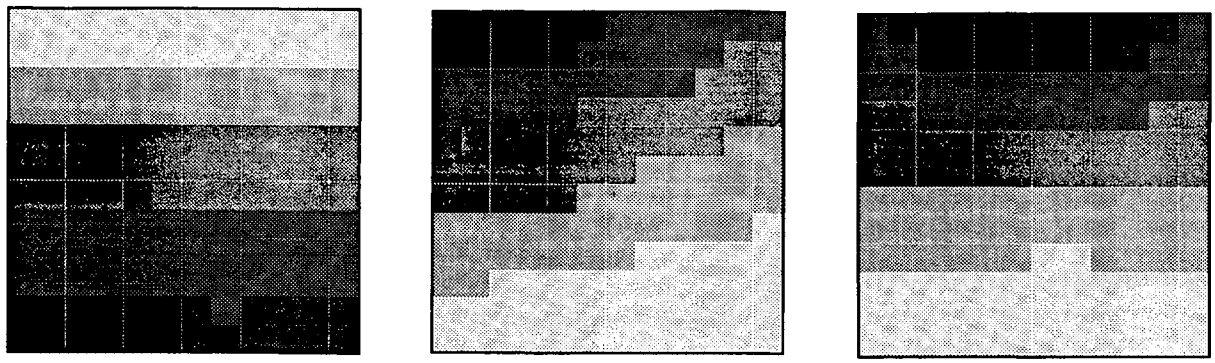

FIGURE 3 Wheel load on two layers (lower layer): (*a*) in situ conditions; (*b*) wheel at the corner; (*c*) wheel at the center.

the limited information is concentrated in the center of the image.

Anisotropy and Vertical Heterogeneity

Wave velocities are related to the stress in the direction of propagation. The state of stress in granular media is heterogeneous and anisotropic; hence the velocity of wave propagation in soil is nonhomogeneous and nonisotropic. Recently, Santamarina and Cesare (*4*) developed a computer program to determine ray paths in anisotropic, vertically heterogeneous media. Figure 4 presents the rays that minimize P-wave travel time in a common geotechnical particulate medium described by the following relationships:

$$V_z^P = 150 \cdot \sigma_z^{0.25} \text{ (vertical heterogeneity)} \quad (9)$$

$$V_x^P = 0.8 \cdot V_z^P \text{ (local anisotropy)} \quad (10)$$

where

V (m/sec) = velocity of propagation in the principal directions x and z,
σ_z (kN/m^2) = vertical effective stress, and
V_x/V_z = 0.8 is an index of anisotropy (often between 0.8 and 1.2).

From an inversion point of view, the deviations from straight rays with changes in depth and inclination (Figure 4), restrict the use of the straight ray assumption.

Diffraction

When the wavelength is in the order of magnitude of the inclusion size, then ray assumptions lose validity, and diffraction must be taken into consideration. In particular, if the inclusion has a lower velocity than the medium, Weilandt (*5*) showed that it may not be detected by inversion algorithms based on travel time. Hence, it follows that imaging a tunnel would be difficult not only from the point of view of angular coverage, which was discussed earlier, but also from the effects of diffraction.

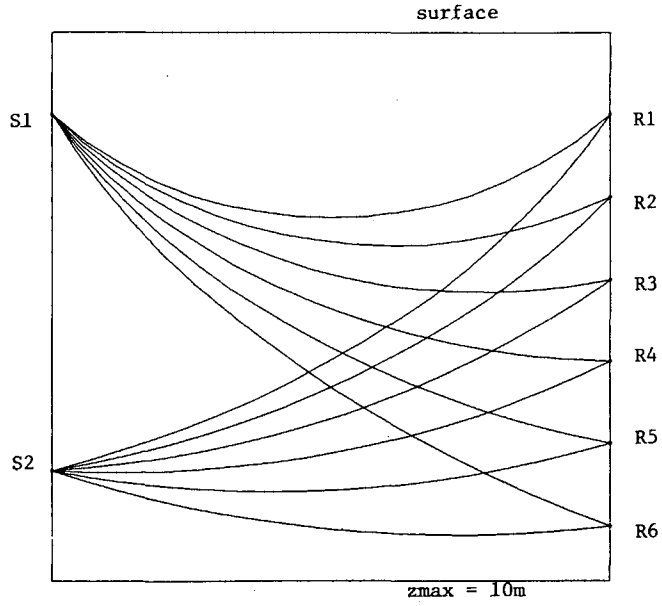

FIGURE 4 Ray paths—anisotropy and vertical heterogeneity.

Field Equipment

Proper selection of adequate sources, receivers, preamplifiers, filters, and digitizers is most important to successfully implementing the proposed technology.

CONCLUSIONS

It is possible to image the state of stress in granular media. Results are enhanced when variation images are produced. An alternative to "variation images" is the "imaging of variations" where changes in measured travel times are inverted (not shown here).

Preliminary results indicate that inverting changes is a more robust approach in cases where the medium is not weakly heterogeneous.

The simple cross-hole tomographic setting is inherently difficult to resolve (such as in the case of deep tunnels).

Small stress changes or stress changes that result in a region of velocity lower than the medium may not be properly detected, particularly if long wavelengths are used and diffraction takes place.

The anisotropy and heterogeneity induced by the in situ state of stress and by the stress changes affect the characteristics of wave propagation, further complicating the inversion problem.

ACKNOWLEDGMENTS

This study was part of a research program on wave-geomedia interaction and applications. Support was provided by the National Science Foundation and the Natural Sciences and Engineering Research Council of Canada.

REFERENCES

1. Knox, D. P., K. H. Stokoe, and S. E. Kopperman. *Effect of State of Stress on Velocity of Low-Amplitude Shear Waves Propagating Along Principal Stress Directions in Dry Sand.* Report GR82-83. University of Texas at Austin, 1982.
2. Tallin, A. G., and J. C. Santamarina. Geotomography in Site Investigations: Simulation Study. *Geotechnical Testing Journal*, Vol. 13, No. 2, 1990, pp. 129–133.
3. Poulos, H. G., and E. G. Davis. *Elastic Solutions for Soil and Rock Mechanics*. John Wiley and Sons, Inc., New York, 1974.
4. Santamarina, J. C., and M. A. Cesare. *Inversion Problems in Anisotropic, Vertically Heterogeneous Media*. Department of Civil Engineering, University of Waterloo, Waterloo, Ontario, Canada, 1992.
5. E. Wielandt. On the Validity of Ray Approximation for Interpreting Delay Times. In *Seismic Tomography* (G. Nolet, ed.), Reidel Publishing Company, Boston, 1987, pp. 85–98.

Publication of this paper sponsored by Committee on Soil and Rock Properties.

Tensioned Wire System for Monitoring Tunnel Movement

THOMAS A. BELLATTY AND RICHARD MAST

The Westway Highway Project was designed to extend from the Bulkhead Line of Manhattan roughly 305 m (1,000 ft) into the Hudson River to the Pierhead Line. The roadway was to be constructed over four existing tunnels crossing under the Hudson River to New Jersey. Two Port Authority Trans-Hudson tubes carry passenger trains, and the two tubes of the Holland Tunnel carry vehicular traffic. The tunnels are old, and all have experienced settlement. It was considered essential that tunnel structures be monitored accurately and frequently throughout the estimated 2-year construction period, but the tunnel environments are extremely hostile to monitoring systems. Closing tunnels frequently for extended periods to monitor tunnel movement was unacceptable. Monitoring systems studied in great detail included optical surveys, lasers, and hydraulic pneumatic settlement devices. Serious problems with each of the systems studied could not be resolved. The Engineering Department of the Port Authority of New York and New Jersey developed the Tensioned Wire System, to monitor horizontal and vertical movement in the tunnels. Several prototype systems were designed and installed to demonstrate their feasibility and gain experience. The wire system was capable of measuring horizontal and vertical movements of tunnels to precisions of 0.8 mm (0.03 in.) at 40 locations in 20 min. The Westway Highway Project was terminated a short time before being sent out for bids, and the Tensioned Wire System was never implemented. Although it was not tested under long-term service conditions, its potential for survival was considered to be very good.

In 1984 a combination of environmental concerns and legal actions caused the Westway Highway Project to be terminated a short time before it was sent out for bids. The project was designed to extend from the Bulkhead Line of Manhattan roughly 305 m (1,000 ft) into the Hudson River to the Pierhead Line. The roadway was to be constructed over four existing tunnels crossing under the Hudson River to New Jersey. Two Port Authority Trans-Hudson (PATH) tubes carry passenger trains, and the two tubes of the Holland Tunnel carry vehicular traffic. The PATH tubes were constructed around 1905, and the Holland Tunnel was constructed in 1927.

Previous monitoring of the tunnels' movement by optical surveys indicated that they had all moved laterally and vertically. Tunnel diameters for the PATH tubes are 4.86 m (16 ft) and 5.78 m (19 ft), and the Holland Tunnel tubes are 8.82 m (29 ft) in diameter. The tunnels are in stable ground at the Bulkhead Line, bedrock at the Pierhead Line, and in soft Hudson River silt for most of the tunnel sections in between. The tunnels are bolted ring construction.

Proposed construction of the Westway protective structure over and adjacent to the tunnels presented serious potential for unavoidable lateral and vertical movement of tunnel sections. Excavation of silt above the tunnels could cause buoyant rise, and excavation adjacent to a tunnel could produce lateral movement in the soft silt. Several hundred 2.1-m (7-ft) diameter caissons were to be constructed about 4.6 m (15 ft) from the tunnels. A "blow" during the installation of a caisson could result in a serious loss of support in the silt surrounding the tunnel.

Tunnel movements were to be monitored with sufficient accuracy to lead to early recognition of unfavorable trends and permit prompt application of remedial measures. Monitoring systems were to be installed in each tunnel before the start of any construction to determine normal movements of the tunnels and verify the accuracy and reliability of the monitoring systems.

TUNNEL ENVIRONMENTS AND CONSTRAINTS

The tunnel environments are extremely hostile to monitoring systems. Ventilation fans in the fresh air ducts below the roadways in the Holland Tunnel (where the monitoring points would be installed) force air through the ducts at 40 m/sec (90 mph). Vehicle emissions create acid rain, and debris falls from the roadway scuppers into the ducts. PATH trains push horizontal columns of air ahead of them as they speed through the tunnels with minimum clearance. All tunnels operate 24 h a day, 7 days a week, and service is interrupted only for maintenance and emergencies. The heavy traffic causes vibration, raises dust, and produces constantly changing and variable conditions of moisture and temperature. As shown in Figure 1, the PATH trains fill the tunnels, and working space is very limited. Working conditions in all the tunnels are unfavorable.

The problems associated with installing, reading, and maintaining an accurate and reliable monitoring system that could be read quickly and frequently were formidable. Worker safety, ease of reading, the time required to obtain data and reduce it, and the need to minimize interruption to service were important considerations. The survival of monitoring systems in the tunnels for more than 2 years was another factor that was considered.

MONITORING SYSTEMS STUDIED

The monitoring system was required to measure horizontal and vertical movements of the tunnels at about 40 locations in a 305-m (1,000-ft) long section of each tunnel. Any monitoring system believed to be potentially feasible was studied in detail. The main systems studied are described briefly.

T. A. Bellatty, Department of Civil Engineering, Manhattan College, Riverdale, N.Y. 10471. R. Mast, Port Authority of New York and New Jersey, 1 World Trade Center, New York, N.Y. 10048.

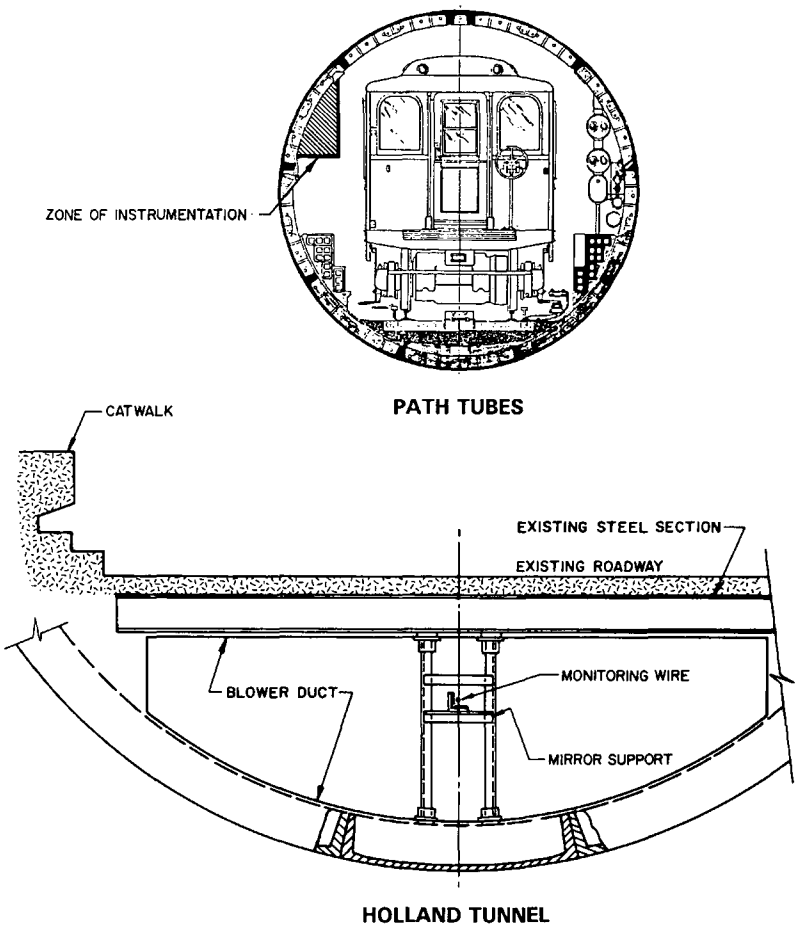

FIGURE 1 Location of instrumentation.

Optical Survey

The optical survey method was important as a backup system to check critical measurements at selected locations, but it was too slow, cumbersome, and limited in accuracy for measurements of tunnel movement on a frequent basis. It had no automatic alarm capability.

Laser System

In 1979 manufacturers of laser equipment believed that suitable equipment could be developed for monitoring 305-m (1,000-ft) lengths of tunnel, but no equipment was available at that time. Unstable moisture and temperature conditions and gradients, vibrations from many sources, dust, smog, and potential damage to workers' eyes were other important problems. After extensive study, laser systems were finally abandoned. Although laser technology today is improved, the problems remain formidable.

Hydraulic-Pneumatic Settlement Device System

The hydraulic-pneumatic settlement device system, which could measure only vertical tunnel movements, was studied extensively. It was abandoned when problems caused by erratic temperature gradients and moving air limited its accuracy and reliability.

Tensioned Wire System

The Tensioned Wire System, to monitor both vertical and horizontal movements of the tunnels, was developed by the Engineering Department of the Port Authority of New York and New Jersey. Measurements of horizontal and vertical movement at 40 monitoring locations could be made in less than 20 min by workers with no special skill or training. The precision of readings could be 0.8 mm (0.03 in.). Data reduction, requiring only basic arithmetic, would be fast and simple. An automatic alarm system, capable of transmitting an electric signal if any tunnel monitoring point moved more than a preset distance, was an important additional feature.

DEVELOPMENT OF TENSIONED WIRE SYSTEM

A prototype of the Tensioned Wire System was installed in the fresh air duct located below the roadway in a 366-m (1,200-ft) section of the Lincoln Tunnel in 1978. The installation was similar to the schematic concept shown in Figure 2. At the

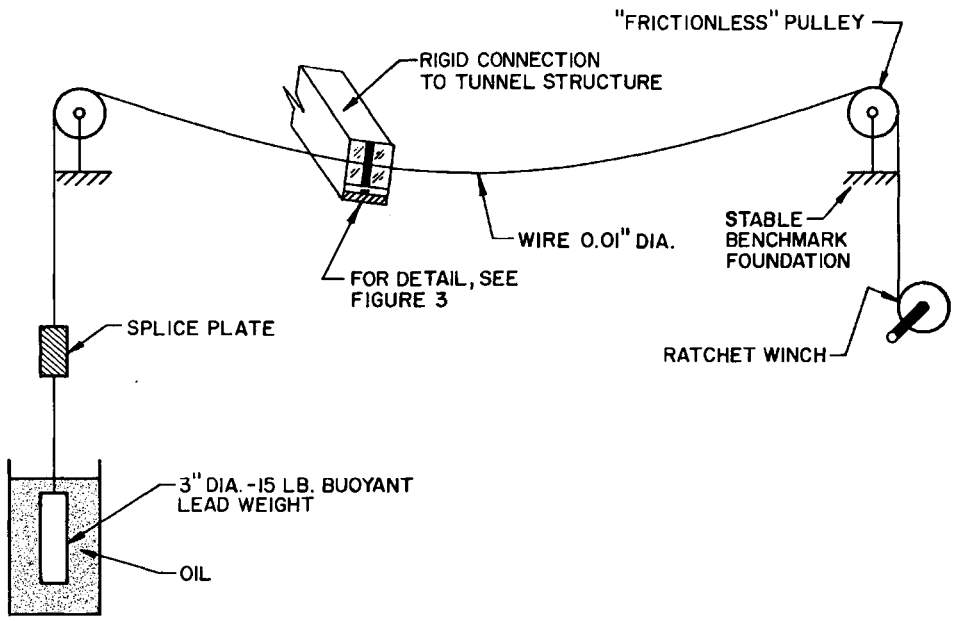

FIGURE 2 Schematic of basic Tensioned Wire System.

locations where the monitoring points were attached to the tunnel wall, the maximum headroom clearance was about 760 mm (30 in.). A stainless-steel wire with a diameter of 0.18 mm (0.007 in.) was suspended between two pulleys roughly 366 m (1,200-ft) apart. The maximum sag in the wire was less than 760 mm (30 in.) under a constant tension of 53 N (12 lb). The tensile stress in the wire was over 2 GPa (300 kips/in.^{2}), not far below its breaking strength. A total of 27 monitoring points were installed. The wire had no protection at all, and it survived for 1 month. During that period, it was subjected to the following:

- Wind velocities of 40 m/sec (90 mph) from blower duct fans,
- Corrosive fluids and debris falling from roadway scuppers leading from the roadway drains to the duct,
- Corrosion caused by salts and acid rain from roadway vapors and engine exhaust, and
- Possible tampering by curious individuals.

The wire was broken by a car side mirror that had fallen from a roadway scupper. When the wire was replaced, the new readings agreed with previous results. After the wire had been replaced several times, it was concluded that the wire system was feasible, but the wire would have to be protected in a tunnel environment.

In 1982 a temporary wire system was installed in a 305-m (1,000-ft) long section of one of the PATH tubes. This prototype installation took about 30 min to complete, and it demonstrated the feasibility of the wire system functioning in the limited working space of the PATH tunnels. Design measurements were made at locations of critical clearances. A special wire with a unique combination of strength and corrosion resistance was obtained. The wire diameter was 0.25 mm (0.01 in.), and it was tensioned to 1.4 GPa (200 kips/in.^{2}), about 70 percent of its breaking strength. In the final design, intermediate pulleys (called saddle points) were added at key locations to provide horizontal clearance from obstructions and to accommodate horizontal alignment curves in some of the tunnels.

DESIGN FEATURES

Basic Concept

As shown in Figure 2, a wire suspended under a constant tension between two fixed benchmark points in a tunnel remains in a stable configuration. The winch is used to take up slack during installation, and the "frictionless" pulleys (which are not completely frictionless) maintain a constant tension regardless of temperature changes or lateral movement of benchmark points. When the wire is tensioned and protected, it is unaffected by changes in temperature or any of the other unfavorable conditions in the tunnels. If the fixed and benchmark points do not move (they were anchored in tunnel locations in bedrock or stable ground), the wire location provides a constant reference for observing tunnel movements by measuring distances between the wire and rulers rigidly attached to the tunnel structure at the monitoring points. The frictionless pulleys were to be fully protected and enclosed to minimize the tendency for any slight changes of wire tension to occur. Small rotations of the pulleys at the time of the readings would free up any friction between the wire and pulley and ensure the correct tension in the wire.

Wire Protection

In the final design, the entire system was enclosed. The wire was suspended inside a 102-mm (4-in.) diameter pipe, and

the other parts of the system were enclosed within larger pipes. In the PATH tubes, the pipe was designed as a handrail to assist personnel in climbing to safety from the tracks.

Readings

Readings were to be made through glass-sealed openings in the pipe at locations of monitoring points. The wire was to be read on machinists' rules set horizontally and vertically as shown in Figure 3. Future changes in readings would indicate horizontal and vertical movement of the tunnel structure because the wire position would remain stable and constant. Locations and elevations of fixed benchmark points and tunnel monitoring points were to be checked by optical survey.

Obtaining and Processing Data

In the PATH tubes, where trains run on 20-min schedules late at night, a flatcar with 20 workers could be brought to a 305-m (1,000-ft) long section of tunnel. Each individual could read two monitoring points and be back on the work car in less than 15 min. Tunnel movements would be known immediately by comparing results and previous readings. In the Holland Tunnel, readings would be made when the fans could be shut down.

Automatic Alarm

Presetting wires rigidly attached to the tunnel structure a selected distance from the tensioned wire and connecting them to an electric source could achieve an automatic alarm system. Contact between the preset wire and the tensioned wire would trigger an alarm and locate the problem for further checking. This feature was never implemented and tested, but it was believed to be feasible.

CONCLUSIONS

After intensive study lasting several years, the Tensioned Wire System was finally selected as the primary monitoring system for the tunnels. It was the only survivor of all the systems studied. Although the Tensioned Wire System was not a "high-tech" solution, it did work when other methods studied had to be abandoned because of the unfavorable conditions and constraints found in the tunnels. However, there was considerable resistance to accepting the Tensioned Wire System.

The Tensioned Wire System has great flexibility and can be adapted to fit a wide range of conditions and situations not discussed here. At locations where tampering is unlikely, for example, the wire would probably not require any protection. It can also be set up and taken down quickly so that the wire would be in place only when measurements were being taken. It could be a portable system, used on an as-needed basis.

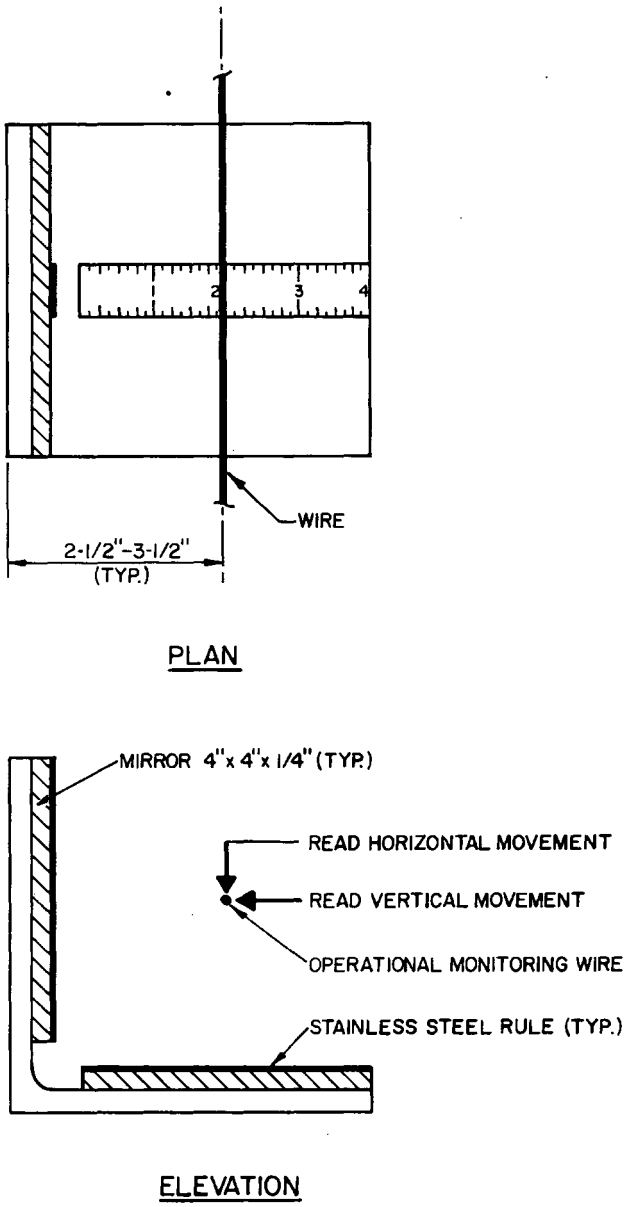

FIGURE 3 Reading horizontal and vertical movements.

The Tensioned Wire System has been patented. Anyone wishing to use the wire system on a project can do so at no charge by requesting written permission from the authors of this paper. Under adverse conditions, the Tensioned Wire System may be the best way to obtain important data.

Publication of this paper sponsored by Committee on Soils and Rock Instrumentation.